

Annual Report 2021

Institut für Kernphysik · COSY
Jül-4429

Annual Report 2021

Institut für Kernphysik / COSY

DIRECTORS AT THE IKP

Experimental Hadron Structure (IKP-1):

Prof. James Ritman

Experimental Hadron Dynamics (IKP-2):

Prof. Hans Ströher

Theory of the Strong Interactions (IKP-3/IAS-4):

Prof. Ulf-G. Meißner

Large-Scale Nuclear Physics Equipment (IKP-4):

Dr. Ralf Gebel (managing director 2020-21)

EDITORIAL BOARD

Dr. Ralf Gebel

Prof. Frank Goldenbaum

Dr. Dieter Grzonka

Prof. Christoph Hanhart

Dr. Volker Hejny

Dr. Andro Kacharava

Dr. Vsevolod Kamberdzhiev

Prof. Andreas Lehrach

Prof. Livia Ludhova

Prof. Thomas Luu

Prof. Ulf-G. Meißner

Prof. James Ritman

Susan Schadmand, Ph.D. habil.

Dr. Thomas Sefzick

Prof. Hans Ströher

Dr. Raimund Tölle

Cover picture: The cover picture shows a selection of various IKP-activities.

The top left picture shows the first HESR-cavity installed for test measurements in the COSY-ring with a sketch of the internal structure on the right side. Key feature is the cooling by air instead of water (lower impedance), allowing solid state amplifiers as drivers.

The middle part is related to a strawtube detector which was build at IKP for an upgrade of the HADES FAIR phase-0 experiment at GSI with in total 704 strawtubes in four double layers. A photo of the installation at HADES is seen on the left side and the color plot on the right side shows the hit distribution of one layer for a beam operation at HADES with illustrates the stable functioning of all strawtubes.

The plot in the bottom right part demonstrates the bunch-selective spin manipulation with the RF Wien filter for EDM studies of the JEDI experiment, shown in the photo on the left side. The COSY-beam was separated into two bunches and the Wien filter was switched on during only one bunch resulting in an oscillation of the beam polarization while the second bunch remains unaffected.

Contents

Preface	v
1 Experimental Activities for FAIR phase-0	1
1.1 Detector Tests fo HADES	1
1.2 Investigation of the Σ^0 Production Mechanism in p+p Collisions	2
1.3 KOALA Experiment	3
1.4 Prospects for Spin-Parity Determination of Ξ Resonances with PANDA	3
1.5 Comparison of Track Finding Algorithms for PANDA	5
2 Storage Ring Based EDM Search	6
2.1 First Detection of Collective Oscillations	6
2.2 First Direct Measurement of Deuteron EDM	7
2.3 The Pilot Bunch Approach	7
2.4 Search for Axion-like Particles at COSY	8
2.5 Results of Beam and Spin Tracking Simulations	10
2.6 Next Steps	11
3 Neutrino Physics	11
3.1 Borexino latest results with neutrinos of solar and astrophysical origin	12
3.2 Towards completion of the JUNO detector	14
3.3 Online Scintillator Internal Radioactivity Investigation System (OSIRIS) of JUNO	16
4 Accelerator Research	17
4.1 Developments at COSY	17
4.2 Progress of the HESR	18
5 Further Activities	20
5.1 LHCb-target Development	20
5.2 Spectroscopy with a Sona Transition Unit	21
5.3 Developments of polarized beams at JuSPARC	22
6 Theoretical Investigations	24
A Beam Time at COSY in 2021	32
B Committees	34
B.1 CBAC – COSY Beam Time Advisory Committee	34
B.2 Committee Service	34
C Publications	36
C.1 Journal Articles	36
D Talks, Colloquia and Proceedings	42
D.1 Conference and Workshop Contributions	42
D.2 Colloquia	48
E Academic Degrees	49
E.1 Dissertation / PhD Theses	49
E.2 Master Theses	50
E.3 Bachelor Theses	50
F Awards	51
G Third Party Funded Projects	52
H Collaborations	53

I	Conferences and Outreach Activities (Co-)Organized by the IKP	54
I.1	EXPO in Dubai	54
I.2	MESON2021	54
I.3	744. WE-Heraeus-Seminar, 29.-31. March, 2021 Towards Storage Ring Electric Dipole Moment Measurements	54
J	Teaching Positions	55
K	Personnel	56
L	Individual Contributions	59
	Accelerator Research	60
	Storage Ring Based EDM Search	74
	FAIR Related Experimental Activities	85
	Neutrino Physics	94

Preface

At the beginning of this year, the formal transition of IKP, with exception of the theory group (IKP-3/IAS-4), from Forschungszentrum Jülich to GSI/FAIR commenced. The implementation of this transition is regulated in a contract called TransFAIR, which has been approved by BMBF and signed by both laboratories. The process itself, and the achievements attained this year are briefly described below.

The TransFAIR contract foresees a multi-year transition period, in which the activities at IKP and the associated resources are incrementally transferred from FZJ to GSI. In a first step, two new departments have been established at GSI, where the IKP activities will be organizationally located at GSI. The experimental activities at IKP-1 and IKP-2 as well as part of the infrastructure activities are foreseen to be transferred into the department FFN (FAIR-Forschung-NRW), the accelerator-related activities plus most of the remaining infrastructure activities are foreseen to be transferred to the department HESR. Two of the IKP institute directors are now employed by GSI in order to lead these departments, i.e., Ralf Gebel for HESR and Jim Ritman for FFN.

A central goal of TransFAIR is for the personnel of IKP to shift to GSI. To this end, by the end of the year already 17 IKP-employees have changed to GSI work contracts, 23 new hires have been made, and a further 15 work contracts have been signed and the employees will begin in early 2022. This process is expected to continue at this high pace, as more of the temporary work contracts at FZJ expire and replacements are hired at GSI, and more of the permanent staff are expected to switch to GSI.

Currently, most of the activities in IKP are physically located at the FZJ site. Nevertheless, both departments FFN and HESR have already located personnel at the GSI/Darmstadt site. As the office and laboratory space in Jülich is successively relinquished, more activities will move to GSI/Darmstadt, or to one of the surrounding universities. For instance, a contract has been signed with the Ruhr-Uni-Bochum to locate part of the FFN activities there. This will be further strengthened if the Network-NRW application (NRW-FAIR) is approved. At the same time, significant parts of IKP-2 are expected to move to the Universität zu Köln, where a process to call a successor for Hans Ströher is currently underway.

The central element unifying IKP is the operation of and experiments with COSY. These are ongoing and are expected to continue to the end of 2024, depending upon the availability of resources. Upon completion of its mission, COSY will be decommissioned and the corresponding resources reallocated to the operation of parts of the FAIR accelerator complex.

The accomplishments shared in this report would not have been possible without the dedication of our technicians and engineers, the service groups, the colleagues of the infrastructure of the FZJ and the students that have advanced the scientific case with their theses. We thank our national and international collaboration partners for their activities, our advisory committees and board of directors and especially our co-workers in Jülich for their ongoing commitment.

Jülich, March 2022

Jim Ritman, Hans Ströher, Ulf-G. Meißner, Ralf Gebel

1 Experimental Activities for FAIR phase-0

1.1 Detector Tests fo HADES

For the HADES experiment at GSI a new trigger scintillator, called the InnerTOF, has been built, which is placed in front of the first MDC layer of HADES. It consists of six trapezoidal modules, as shown in Fig. 1 with three separate scintillators in each module read out by SiPMs. Each scintillator is equipped with 12 SiPMs of the type MFC-60035 with an active area of $6 \times 6 \text{ mm}^2$ attached to the outer scintillator edge. A description of the system is given in an individual contribution in this report. The SiPM-signals are connected to PADIWA-boards to amplify and discriminate the signals and generate LVDS-output signals for TRB3C-boards. The trigger signal generation requires a minimum SiPM-signal multiplicity.

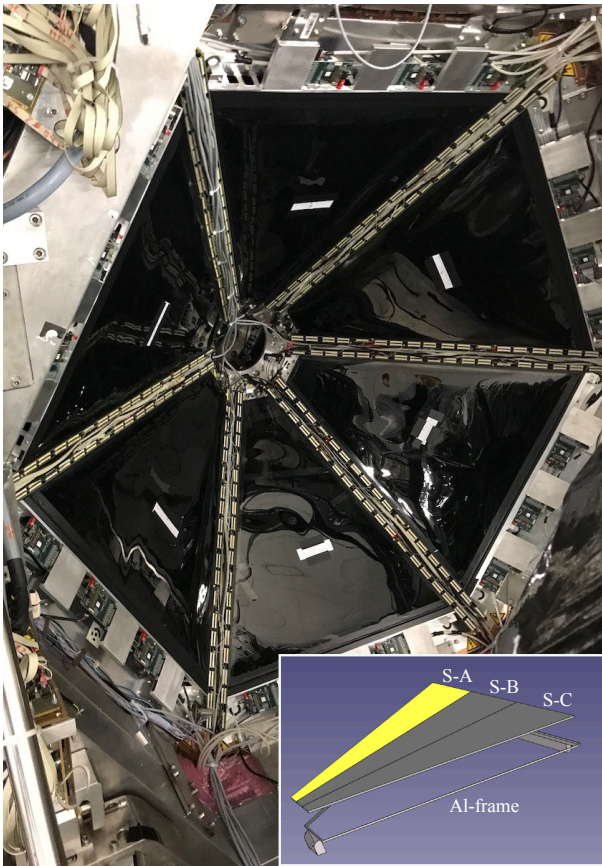


Figure 1: Photo of the InnerTOF modules mounted at the HADES MDC with a sketch of the module-structure in the lower part.

All modules have been tested over the whole scintillator area with ^{90}Sr -source, cosmics and $2.74 \text{ GeV}/c$ proton beam from COSY. For all positions a rather high signal multiplicity was achieved with mostly a signal from all 12 SiPMs in each event. In Fig. 2 the multiplicity distribution for a cosmic measurement is shown where all modules were mounted in a stack that cosmic particles

pass through all modules. Events were selected with a signal multiplicity of 12 for the scintillator in the first and last module to ensure that the cosmics crossed the modules in between. The detailed studies of the modules have shown that a detection efficiency of close to 100% is achieved for minimum ionizing particles.

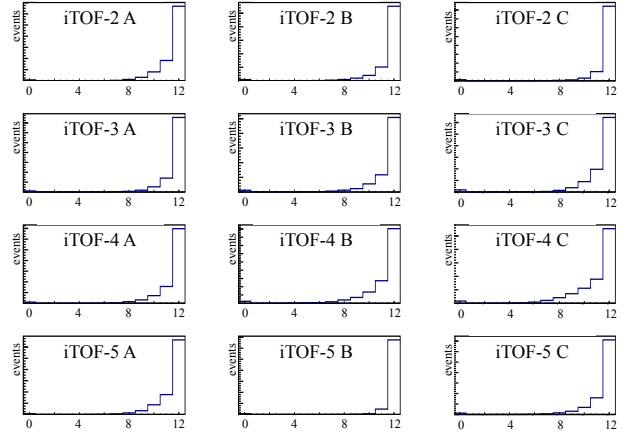


Figure 2: Multiplicity distribution of the SiPM-signals resulting from the passage of cosmic particles through the InnerTOF modules for the units 2 to 4 for the separate scintillators S-A, S-B, S-C. Events with a multiplicity of 12 in modules 1 and 6 were selected for the plot.

The tracking capabilities of the HADES spectrometer for the phase 0 experiment were upgraded by the installation of two straw stations (STS1 and STS2) and a fRPC detector for the time-of-flight measurement of tracks in the polar angle region from about 0.5° up to 7° . The STS1 and STS2 stations each consist of four planar double-layers of straws with different angular orientations. The STS1 layers have vertical and horizontal orientations (0° , 90° , 90° , 0°), whereas the STS2 has four different orientations (0° , 90° , $+45^\circ$, -45°) to resolve ambiguities in the hit association. The STS1 was built at IKP and consists of 704 straw tubes with 10 mm diameter and 766 mm length. The gas mixture in the straws is argon based with a 10% CO_2 admixture as quenching component. The gas overpressure of 1 bar in the tubes sustains the straw wire tension, so that the straws glued together in modules of 2×16 tubes are self-supporting. Each double-layer exhibits a beamhole of $8 \times 8 \text{ cm}^2$ in the center for the direct beam. The signal amplification, shaping and discrimination is performed by frontend boards containing two PASTTREC ASICs for 16 channel readout. The ASIC control and signal readout of leading edge and time-over-threshold time is done by TRB3 boards for the data acquisition.

The STS1 and STS2 were installed by the end of 2020 and a dedicated commissioning proton beamtime with the HADES spectrometer was carried out in February 2021. Proton beam kinetic energy was 2.5 GeV and 4.2 GeV , the latter close to the 4.5 GeV which is foreseen for the next proton production experiment beamtime in

2022. Both straw stations showed a very stable operation without any failure. The STS control and readout was added into the HADES slow control and data-acquisition system. Figure 3 shows the STS1 detector installed in the HADES spectrometer and Fig. 4 a hitmap of all straw channels with increasing hitrates towards the straws in the center. Note the beam hole straws in the middle of each double-layer with reduced hit counts. As can be seen a few channels are missing due to failures in the PASTTREC boards. The identified boards were exchanged in 2021 after the commissioning beamtime. All 704 straws of the STS1 were in operation without any failures, such as broken wire or gas leakage for instance.

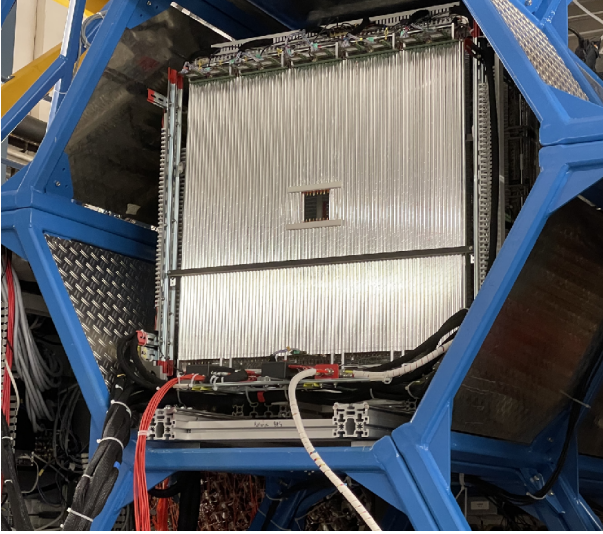


Figure 3: Photo of the STS detector at the HADES experiment. The center area is left open for the beam by splitting the strawtubes.

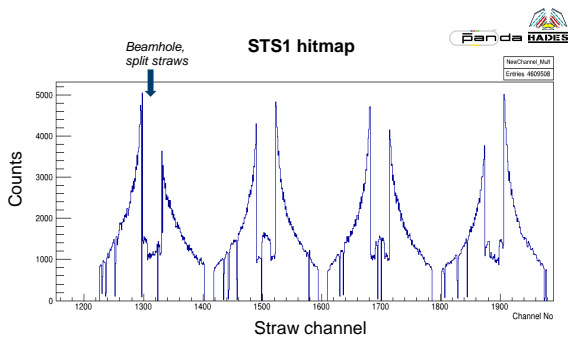


Figure 4: Hitmap of the STS1. The TDC channels for the STS1 with 704 straws start at 1224, with a 17 channels gap between the layers.

Data-taking with different electronic settings of the PASTTREC ASICs were recorded and analyzed to find the best configuration considering low noise level, highest signal detection efficiency and low straw operation voltage. As a result the setting with a high ASIC amplification of about 4 mV/fC turned out to be the best

choice and allowed to lower the high voltage inside the straws from 1800V down to 1700V which reduces the charge load in the straws by about a factor of four. This result is of great importance for the operation of the same straw type and electronic readout later in the PANDA experiment where the particle intensities and accumulated charge loads are higher. We have now proofed for a large straw system under experiment conditions that we can reduce the nominal gas gain from 5×10^4 down to about 1×10^4 in the PANDA straw operation which gives us then the same factor enhancement in the straw detector lifetime by the reduced charge load in the straws.

The data was also taken to develop the calibration and tracking methods for the STS1 and STS2 with in total 1728 straw channels. Details about the STS calibration, including the parametrization of the space-drifttime relation can be found as an individual report. The STS geometry, calibration and track reconstruction methods have been included in the HADES software framework HYDRA.

The STS detector and the InnerTOF modules are now in operation at HADES for a beam time in February 2022 of proton induced hyperon production studies where they will allow a higher selectivity of real events and an improved tracking capability and background reduction.

1.2 Investigation of the Σ^0 Production Mechanism in p+p Collisions

The production of the Σ^0 hyperon in p+p reactions at a beam energy $T = 3.5$ GeV was investigated via the exclusive reaction $pp \rightarrow pK^+\Sigma^0$ with the HADES detector. The total production cross section was determined to be $\sigma = 18.7 \pm 1.0(\text{stat}) \pm 1.7(\text{syst}) \mu\text{b}$.

The dynamics of the $pp \rightarrow pK^+\Sigma^0$ reaction was investigated by studying the angular distributions in the CMS, G-J and helicity reference frames. The angular distributions in the CMS of the Σ^0 hyperon and the proton show anisotropies, where the anisotropy is more pronounced for the proton. This is a clear indication that the reaction proceeds dominantly via the pion exchange mechanism. The G-J angle of the kaon in the $K^+\Sigma^0$ frame tends to be asymmetric, which can be caused by the excitation of nucleon resonances decaying into the $K^+\Sigma^0$ channel. All the helicity angular distributions are non-isotropic, which indicates significant resonant contributions.

In order to provide a better description of the angular distributions and to estimate the contributions of nucleon resonances, the Bonn-Gatchina Partial Wave Analysis (Bo-Ga PWA) tool has been employed. Nucleon resonances (either $I=1/2 N^*$ or $I=3/2 \Delta^*$) with a non-zero measured $K^+\Sigma^0$ branching ratio have been included as resonant components. The Bo-Ga PWA framework performs an unbinned fit, where the fit quality is determined by a log-likelihood value. However, due to the limited statistics, an unambiguous determination of the relative contributions was not possible. Nevertheless, the resonances

$N^*(1710)$ ($J^P = 1/2^+$), $N^*(1900)$ ($J^P = 3/2^+$) and $\Delta^*(1900)$ ($J^P = 1/2^-$) are required by the fit.

The upcoming proton beam time in February 2022 with the upgraded HADES setup including the new forward detector offers the opportunity to improve the mass resolution in the forward detector. In addition, it will provide sufficient statistics to extract quantitative contributions of the different nucleon resonances.

1.3 KOALA Experiment

For a complete understanding of the proton-proton or antiproton-proton hadronic interaction, precise knowledge of the total and elastic cross sections are required. Often the determination of the absolute luminosity is a challenge in order to gain precision data of the interaction being investigated. The concept of the KOALA experiment is to measure the proton-proton or antiproton-proton elastic scattering covering the Coulomb nuclear interference region, in which the Coulomb scattering can be fixed to normalize the luminosity. KOALA was initially proposed for the antiproton-proton elastic scattering measurement at HESR and is currently being commissioned with the proton beam at COSY.

KOALA is an internal fixed target experiment to be operated at a ring accelerator like HESR or COSY and consists of a hydrogen cluster target, a recoil as well as a forward detector to obtain a wide range of four-momentum transfer squared, *i.e.*, $0.0008 < |t| < 0.1$ (GeV/c)². A newly built recoil detector consisting of four semiconductor strip energy sensors measuring the kinetic energy and emission angle of the recoil proton, has been commissioned by measuring proton-proton elastic scattering at COSY. The results of the commissioning experiment validated the experiment principles as well as the detector concept. It has been observed that a limiting factor in reaching the desired t range when only using the recoil detector is the inelastic background at small recoil angle ($\alpha = 90^\circ - \theta$). In order to suppress the inelastic background, a forward detector ($0.37^\circ < \theta < 1.2^\circ$) has been added for the commissioning experiment.

The forward detector consists of four pairs of plastic scintillators located symmetrically in the vertical and horizontal directions close to the beam axis. It detects the elastically scattered beam particles and provides the timing as well as the charge information of the incident particles. With the forward measurement, true elastic events at the lower $|t|$ region can be selected by the correlation of the time of flight between the recoil protons and the forward scattered beam protons. It is noted that the precision of the measurement is significantly impacted by the finite beam emittance.

During the beam test performed in 2021, the fine tuning for the beam, *e.g.* orbit correction and stochastic cooling, has been carried out, and in addition a scintillator detector with larger area has been used to compensate for small imperfection of the beam alignment. Ideal circumstances for the measurement have been attained during



Figure 5: The hit rates on the four scintillator detectors measuring the proton-proton elastic scattering at the beam momentum of $3.0 \text{ GeV}/c$, which the beam was running at the centre of the beam pipe and without evident beam halo.

the commissioning experiment. Figure 5 illustrates the almost equal hit rates on the four scintillator detectors at the beam momentum of $3.0 \text{ GeV}/c$.

For technical details see Reference¹.

1.4 Prospects for Spin-Parity Determination of Ξ Resonances with PANDA

Introduction

In order to deepen our insights into the mechanisms of non-perturbative QCD, it is essential to understand the excitation pattern of baryons. So far, the nucleon excitation spectrum has been subject to systematic studies, while the knowledge on the excitation spectra of double and triple strange baryons is scarce. An example is the lack of information concerning the quantum numbers (QN) of excited Ξ states. In Monte Carlo studies, it has been demonstrated that PANDA will be able to observe the $\Xi^+ \Lambda K^-$ channel with high statistics, and at the same time kinematic constraints will suppress the background to negligible level.

In this study, the feasibility of PANDA to determine the spin and parity of two specific Ξ resonances, $\Xi(1690)$ and $\Xi(1820)$, is investigated by making use of a partial wave analysis (PWA) employing the PAWIAN framework.

Event Generation

The event generator included in PAWIAN has been used to generate events according to the reaction $\bar{p}p \rightarrow \bar{\Xi}^+ \Lambda K^-$ requiring a beam momentum of $p_{\bar{p}} \geq 3.5 \text{ GeV}/c$. In this study, the beam momentum is chosen to be

¹Nuclear Inst. and Methods in Physics Research, A 1019 (2021) 165849.

4.6 GeV/c corresponding to a center-of-mass (c.m.) energy that is about 300 MeV above the production threshold of the final states. This choice allows the population of the two resonances $\Xi(1690)$ and $\Xi(1820)$. The dynamics of the production and decay process are modeled by a Breit-Wigner function.

Various data sets are needed for this study. Since the normalization of the fit uses a Monte Carlo integration, the first data set consists of phase-space distributed events called the continuum data sample in the following. The other data sets, called signal data sets, include events generated according to the following reactions:

- i. $\bar{p}p \rightarrow \bar{\Xi}^+ \Xi(1690)^- \text{ or } \bar{p}p \rightarrow \bar{\Xi}^+ \Xi(1820)^-$
- ii. $\bar{p}p \rightarrow \bar{\Xi}^+ \Xi(1690)^- \text{ and } \bar{p}p \rightarrow \bar{\Xi}^+ \Xi(1820)^-$

Pre-studies showed that about 30,000 events are needed to perform the PWA with PAWIAN. Assuming a reconstruction efficiency of about 5%, resulting from a Monte Carlo study of the $\bar{\Xi}^+ \Lambda K^-$ final state with PANDA, a data sample of about 600,000 generated events is needed to ensure a sufficient number of reconstructed events after passing the full PandaRoot simulation and reconstruction chain. In addition, the continuum sample has to pass the PandaRoot simulation and reconstruction criteria to ensure that the sample underlies the same detector acceptance as the signal. This implies the generation of 1.8 million phase-space distributed events.

Selection Criteria

To determine the spin and parity QN, it is necessary to specify the correct model among a set of tested models. Since the fit is performed with different models, the comparison of the resulting negative log-likelihood value is not possible and thus different criteria to be used for the comparison. In this study the Akaike Information Criterion (AIC) and the Bayesian Information Criterion (BIC) are used. The AIC value is not interpretable by itself since it contains arbitrary units. Therefore, it is rescaled to $\Delta_i = \text{AIC}_i - \text{AIC}_{\min}$ in order to rank the candidate hypotheses, where i is the hypothesis labeling number. According to this the preferred model has $\Delta = 0$, while all others will have $\Delta > 0$. The relative merit is assessed by the following rules: 1) $\Delta_i \leq 2$: model is supported; 2) $4 \leq \Delta_i \leq 7$: model has less support; 3) $\Delta_i > 10$: model is not supported. These rules are based on rules used in Bayesian literature and the confidence level for the rejection of a model with $\Delta_i > 10$ is more than 95%.

Using only the BIC can lead to underfitting, while the usage of only the AIC can lead to overfitting. That implies two possible scenarios for the selection: BIC and AIC prefer the same model or they prefer different models. In the first case the best hypothesis can be selected directly by using the ΔAIC criterion. In the latter case good experiences have been made by using the sum of AIC and BIC for the selection criterion, *i.e.* the models are compared by $\Delta(\text{AIC}+\text{BIC})$.

Results of the Partial Wave Analysis

Systematic studies for the PWA of the $\bar{\Xi}^+ \Lambda K^-$ final state have been performed with the aim to provide information about the feasibility to determine the QN of the Ξ resonances with PAWIAN. The main focus in this report is the feasibility to determine the QN from PANDA data.

Single Resonance Case To investigate the influence of the PANDA detector acceptance, the resolution as well as the full reconstruction efficiency on the fit results, a simplified study of the single resonance case has been performed. The data set generated with PAWIAN was subsequently subject to the PandaRoot simulation and reconstruction chain and the remaining events were analyzed, employing a combined kinematic and geometric fit. For each resonance, signal data sets with different spin and parity QN, *i.e.* $1/2^+, 1/2^-, 3/2^+$ and $3/2^-$, have been generated. About 5% to 6% of the generated events passed the full simulation and reconstruction chain and were used as candidates for the fit. The reconstruction efficiency for generated $J = 3/2$ is slightly higher than for $J = 1/2$. This can be explained by more reconstructed events in the region $0.5 \leq \cos \Theta_{c.m.} \leq 1$ for the $3/2$ hypothesis, where $\cos \Theta_{c.m.}$ defines the angle between the beam axis and the momentum vector of the reconstructed particle in the c.m.-frame. However, the full angular range is covered after the reconstruction, which is mandatory to perform the PWA. Furthermore, the influence of the chosen quantum number hypothesis on the detector resolution has been investigated. The results obtained from the reconstructed events imply that the chosen hypothesis has no influence on the detector resolution.

Finally, the possibility to determine the input spin and parity QN from the fitted models has been investigated. For both resonances, all four quantum number combinations have been fit to each generated data sample. In each case, the best fit result is achieved with the true model, while all other models could be rejected with $\Delta > 96.8$.

Two Resonance Case In the following, the study is extended by considering the case in which two resonances, namely $\Xi(1690)^-$ and $\Xi(1820)^-$, are present. A data set of 600,000 signal events has been generated using a $J^P = 1/2^+$ hypothesis for $\Xi(1690)^-$ and $J^P = 3/2^-$ for $\Xi(1820)^-$. Since nothing is known about the production of Ξ resonances, their contribution was assumed to be equal. The generated data set was then subject to the full simulation and reconstruction chain of PandaRoot and 5.1% of the generated events have been reconstructed. 30,000 events of this reconstructed sample were subject to the multi-dimensional fit procedure with PAWIAN. In total 16 fits have been performed for which the hypotheses are combined by the four QN. The best fit result has been achieved with the true fit hypothesis and the difference of the AIC value to the second best fit is $\Delta\text{AIC} > 150$. By comparing the ΛK^- invariant mass distribution of the

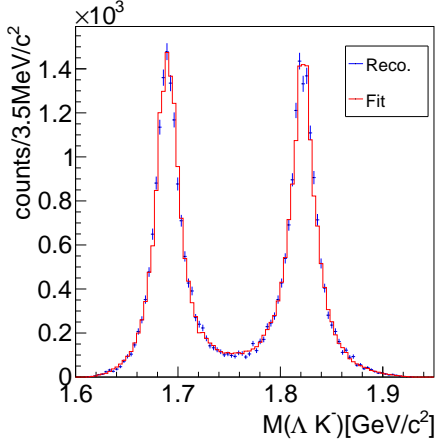


Figure 6: Comparison of the reconstructed (Reco.) and fitted ΛK^- mass distribution.

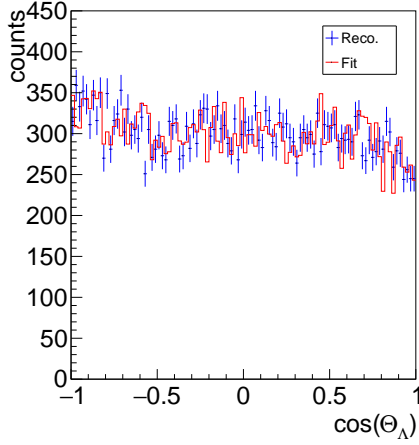


Figure 7: Reconstructed (blue) and fit (red) angular distribution of the Λ in the helicity frame of the Ξ^{*-} for the $1/2^+3/2^-$ hypothesis.

reconstructed sample and the best fit, as illustrated in Figure 6, one sees that both distributions are in agreement. Please note, that the distribution of the fitted sample has been scaled but a factor 1/3 to match the range of the reconstructed distribution. The event generator provided in PAWIAN generated the angular distribution of the Ξ^{*-} system as well as the of the ΛK^- system according to the chosen spin and parity QN. Figure 7 shows the reconstructed and fitted angular distribution for Λ in the helicity frame of the Ξ^{*-} .

Conclusion and Outlook

First results towards the determination the spin and parity QN of $\Xi(1690)^-$ and $\Xi(1820)^-$ have been presented. The QN have been determined by performing a PWA with the PAWIAN framework. Its results are promising and indicate, that the determination of the spin and parity QN of Ξ resonances from PANDA data will be possible. The presented reconstruction efficiency of 5% corresponds to about 18,000 reconstructed events per day assuming a

luminosity of $\mathcal{L} = 10^{31} \text{ cm}^{-2} \text{ s}^{-1}$. This will provide the possibility to collect the needed statistics for this PWA within a few days of data taking during the first phase of the PANDA experiment.

Since the models used in here might be incomplete, it would be appropriate to expand these studies to a wider spectrum of models. Furthermore, a blind analysis of PANDA data should be performed to verify the results obtained in this study.

1.5 Comparison of Track Finding Algorithms for PANDA

Track finding of secondary particles with the Apollonius Triplet Track Finder

To find the flight path of charged particles in a magnetic field is one of the most challenging tasks in the reconstruction process of a particle physics experiment. This task is strongly simplified if one point on the track is already known, *e.g.* for tracks coming from the known primary interaction point. Therefore, many track finding algorithms exist for primary tracks in the PANDA experiment. The situation is more complicated if the interesting particle does not come from the primary interaction point, *e.g.* for the decay products of hyperons, which typically fly several centimeters before they decay. Therefore, a secondary track finder - the ApolloniusTripletTrackFinder - was developed and compared to the currently existing primary track finders, which are the BarrelTrackFinder and the HoughTrackFinder. Additionally, the secondary track finder can be used as an extension after one of the other track finders.

The ApolloniusTripletTrackFinder is an algorithm specifically developed for the Straw Tube Tracker (STT) of the PANDA experiment. The STT measures the track of particles with more than 4200 drift tubes with a tube diameter of 1 cm. A measurement of a single STT tube consist of the tube position and the time for the ionization charge produced by the incident particle to drift to the anode wire. The drift time can be translated into an isochrone ring around the mid-point of the tube giving the minimum distance of the track to the wire. Most of the STT tubes are aligned with the solenoidal magnetic field of PANDA to measure the transversal momentum of the particles. In this projection the charged particles move in circles.

The first stage of the algorithm is to determine all three-hit combinations, so called triplets, which might belong to one track and obey certain selection criteria.

For each triplet there are eight solutions of the Apollonius problem, *i.e.* to find a circle tangent to three other (isochrone) circles. These are shown as yellow circles in Fig. 8. All hits that are close to the Apollonius circles are added to the circles. In a last step only the tracks with the highest number of hits and the lowest χ^2 are selected. In the example in Fig. 8 this circle is shown in red.

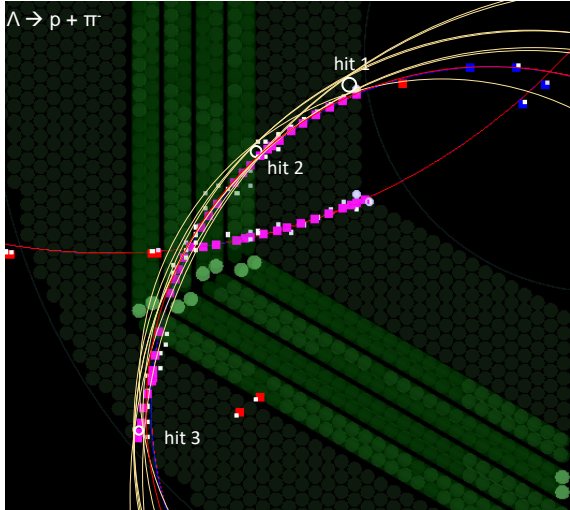


Figure 8: Overview of the working principle of the ApolloniusTripletTrackFinder. The eight possible Apollonius circles are shown in yellow. The chosen Apollonius circle is drawn in red.

In the next stage, the selected solutions for the different triplet combinations are collected into possible events and finally the most probable track candidates are selected.

To compare the quality of the new track finding algorithm with the existing ones a data set ($p\bar{p} \rightarrow \Xi(1820) \rightarrow \Lambda K^-$) with many secondary particles has been chosen. In Fig. 9 the finding rate vs. the distance of the point of closest approach to the interaction point is shown for secondary particles. It is very visible that the finding rate of

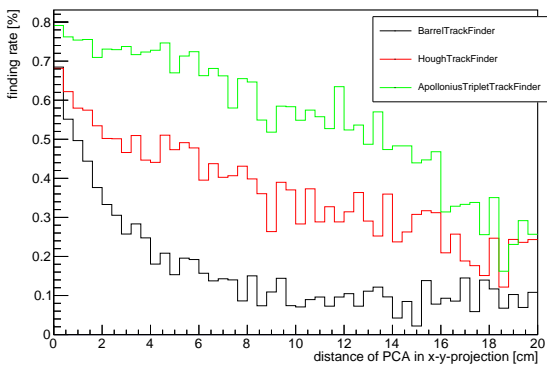


Figure 9: Comparison of finding rate vs. distance of point of closest approach to the interaction point in x-y-projection of the different tracking algorithms.

the BarrelTrackFinder drops dramatically for larger distances to the interaction point. The HoughTrackFinder can handle these cases a bit better. The Apollonius-TripletTrackFinder is the only algorithm designed to find tracks not coming from the interaction point. Therefore, the finding rate for this algorithm is much higher (more than about 20 %-points) compared to the other algo-

ritms. In conclusion the ApolloniusTripletTrackFinder behaves well for particles not coming from the interaction point. An analysis where the algorithms are combined by first using a primary track finder and afterwards finding the secondary particles with the ApolloniusTripletTrackFinder is still under development. The ApolloniusTripletTrackFinder promises to improve the detection rate for hyperons. An application of this algorithm to a physics channel is ongoing.

2 Storage Ring Based EDM Search

The JEDI- and CPEDM-collaborations, aiming to search for electric dipole moments of charged particles (both permanent and oscillating) in storage rings (srEDM), have again been very active in 2021 in spite of the restrictions imposed by the pandemic: The JEDI-collaboration has successfully conducted a second precursor experiment (Precursor-II) at COSY in 2021 to search for the deuteron EDM using the improved conditions of the polarized beam and related instrumentation. A CPEDM-collaboration highlight of 2021 was the publication of the report: *Storage Ring to Search for Electric Dipole Moments of Charged Particles - Feasibility Study*².

Furthermore, the collaboration hosted a (virtual) WE-Heraeus Seminar (# 744, Towards srEDM Measurements), and presented their results at meetings such as the CERN PBC (Physics Beyond Colliders) diversity program, the European JENAA (Joint ECFA-NuPECC-APPEC Activity) initiative and the Snowmass process, which is part of the strategic planning of the US Particle-Physics community. These activities have also been reported in Nuclear Physics News³.

2.1 First Detection of Collective Oscillations

As a scientific milestone, the JEDI collaboration has published an investigation of coherent betatron oscillations of a deuteron beam at COSY, excited by a detuned rf Wien filter (WF)⁴. The beam oscillations were detected by conventional beam position monitors. It was shown that oscillation amplitudes down to 1 μm can be detected. The interpretation of the response of the stored beam to the detuned rf WF is based on simulations of the beam evolution in the lattice of the ring and realistic time-dependent 3D field maps of the WF. Future measurements of the electric dipole moment of protons will, however, require control of the relative position of counter-propagating beams in the sub-picometer range. Since the stored beam

²Storage Ring to Search for Electric Dipole Moments of Charged Particles - Feasibility Study, [CERN Yellow Report: CERN-PBC-REPORT-2019-002](#)

³CPEDM - A Storage Ring Facility for Charged-Particle EDM Searches, [Nuclear Physics News, Vol. 31, No. 2, p.26-29, 2021.](#)

⁴First detection of collective oscillations of a stored deuteron beam with an amplitude close to the quantum limit, [Phys. Rev. Accel. Beams 24, 124601 \(2021\).](#)

can be considered as a rarefied gas of uncorrelated particles, it has been demonstrated that the amplitudes of the zero-point (ground state) betatron oscillations of individual particles are only a factor of about 10 larger than the Heisenberg uncertainty limit. As a consequence of this, it is concluded that quantum mechanics does not preclude the control of the beam centroids to sub-picometer accuracy. The smallest Lorentz force exerted on a single particle that could be determined is 10 aN.

2.2 First Direct Measurement of Deuteron EDM

For an elementary particle, the spin is the only vector defining a direction. A permanent Electric Dipole Moment (EDM) has to be aligned along this axis. If an EDM exists, the spin vector will experience a torque in addition to the one caused by the magnetic moment. For a polarization direction aligned along the momentum vector, this torque causes a polarization component in the vertical direction. The polarization direction can be determined by scattering the beam off a carbon target and analyzing the azimuthal distribution of the scattered particles. Expected EDMs are of the order of $10^{-29} \text{ e} \cdot \text{cm}$. This means that the spin precession due to an EDM is orders of magnitude smaller than the precession caused by the magnetic dipole moment (MDM). The magnetic moment causes a precession of the spins in the horizontal plane as indicated in Fig. 10.

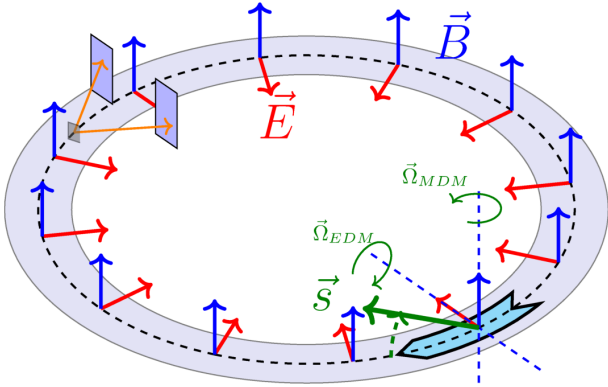


Figure 10: Principle of a storage ring EDM measurement.

Two successful deuteron EDM runs have been performed at COSY in December 2018 and March 2021. Goal of the measurements was the determination of the so-called invariant spin axis \hat{n} , which is directly related to the EDM. The invariant spin axis defines the spin rotation axis. The component of the polarization vector along the invariant spin axis does not rotate. In an ideal accelerator, the invariant spin axis points in vertical direction along the magnetic guiding field, if the particle has only a magnetic dipole moment and no EDM ($\hat{n} \propto \vec{\Omega}_{MDM}$). The presence of an EDM tilts this axis towards the radial direction by an angle $\eta\beta/(2G)$, i.e. $\hat{n} \propto \vec{\Omega}_{MDM} + \vec{\Omega}_{EDM}$. Here η is

a dimensionless factor describing the EDM d ($d = \eta \cdot e \cdot \hbar/(2mc) \cdot S$), β is the velocity in units of c and G the magnetic anomaly of the particle (for deuterons $G = -0.14$). The experiment has been performed with the radio frequency Wien filter causing a build-up of a vertical polarization component, if the invariant spin axis is tilted with respect to magnetic field axis of the Wien filter. Rotating the Wien filter around the beam axis and by adding a solenoidal field the invariant spin axis could be deliberately tilted in radial and longitudinal direction, respectively. Measuring the polarization build-up (in accelerator terminology this means measuring a resonance strength ϵ) as a function of both rotations allows one to measure a two dimensional map.

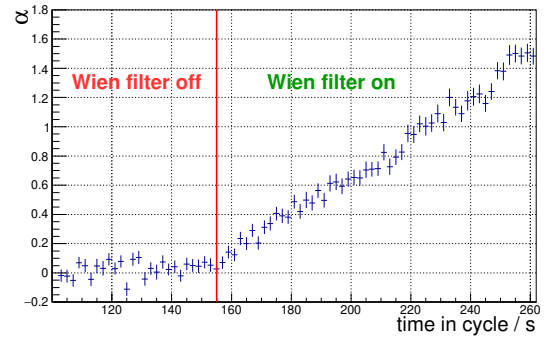


Figure 11: Ratio $\alpha = \arctan(P_v/P_h)$ of vertical to horizontal polarization component as a function of time. The time derivative of the slope is directly related to the resonance strength ϵ .

Figure 11 shows the development of $\alpha = \arctan(P_v/P_h)$ as a function of time for a fixed setting of the Wien filter and the solenoid. Here, $P_{v(h)}$ denotes the vertical (horizontal) polarization component. As soon as the Wien filter is switched on, α , i.e. the vertical polarization starts to raise. The slope is proportional to the resonance strength ϵ . Figure 12 shows the resonance strength as a function of the Wien filter rotation angle Φ^{WF} and the rotation χ^{sol} caused by the solenoidal field. The minimum of the map indicates the position of the invariant spin axis for the Wien filter in its nominal position and no solenoidal field. We observe both longitudinal and radial direction tilts of the order of a few mrad, caused by systematic effects (e.g. misalignments of elements) which are currently under investigation using beam and spin tracking simulations. Note that an offset in radial direction of 1mrad is equivalent to an EDM of $10^{-17} \text{ e} \cdot \text{cm}$.

2.3 The Pilot Bunch Approach

Based on the results of the first precursor run in 2018 and on the spin simulations⁵, the previous implementation (2018) of the phase-lock feedback bear a drawback

⁵Spin dynamics investigations for the electric dipole moment experiment, *Phys. Rev. Accel. Beams*, v. 23, 024601, (2020).

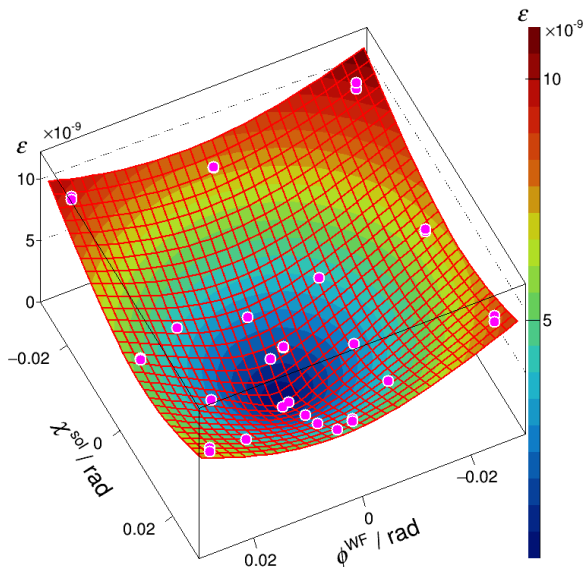


Figure 12: Resonance strength ϵ as a function of the rotation caused by the Wien filter and the solenoid.

and a limitation. The spin tune (and consequently the spin resonance frequency) is measured while simultaneous spin kicks are induced by the Wien filter. In this case, the spin tune is not well-defined. What is measured actually is the running spin tune which may not necessary reflect the idle in-plane spin precession.

With the former implementation of the phase-lock system, the full-oscillations of the vertical spin component cannot be observed. This is related to the fact that the polarization vector will be completely rotated out-of-plane after some time in the cycle. The lack of an in-plane component eliminates the possibility to measure the spin tune and the feedback stops.

Driven by these constraints, an alternative solution has been developed and commissioned in a dedicated beam-time. The new idea is based on multi-bunch spin selective operation. By storing two bunches for instance (more is also an option) in the accelerator, the Wien filter shall be switched off for at least the duration of one bunch. Then within one bunch idle spin precession can be maintained. The spin tune in this case is well-defined and can therefore be measured. This bunch, is called the pilot bunch. Furthermore, an in-plane spin component shall *survive* permitting full vertical spin oscillations which can then be measured. In this way, the WF can be kept in-resonance as long as possible.

Switching the fields of the RF Wien filter (on and off) for at least the duration of a bunch is very challenging. This required the development of novel fast high-power RF

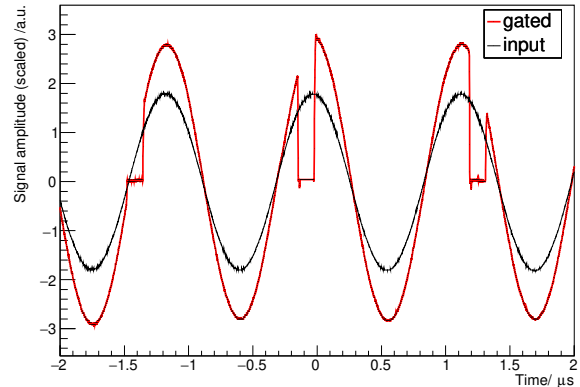


Figure 13: Offline measurement results of one of the fast RF switches. The black and the red graphs denote the (scaled) input and the gated and amplified signals respectively.

switches in close collaboration with barthel HF-Technik GmbH⁶.

The measured switching speed were in the order of 20 ns which is sufficient to prevent fields leakage to the pilot bunch. Very sharp fall and rise of the RF signal could be observed as shown in Fig. 13. Figure 13 refer the off-line (without beam) measurements of one of the switches using relatively high-power levels of 100 W. The black graph denotes the input signal which is a complete sinusoidal one at 871 kHz. Using a TTL signal as a switching signal at the revolution frequency at ≈ 750 kHz, resulted in the red line, after being attenuated correspondingly. Clearly, one can see that the switches fulfilled the design requirements.

One week has been recommended by the CBAC to test this idea with polarized beam. The main test scenario consists of setting up the RF Wien filter in the MDM mode, i.e., with vertical electric field and horizontal magnetic field.

Starting with a vertically polarized beam, the measurement results are shown in Fig. 14. Two bunches are stored in the machine; the red and blue points refer to the vertical asymmetries of the corresponding bunches. The polarization vector of only one bunch oscillates, while the polarization vector of the other bunch (pilot) remains in the vertical plane. This the worldwide first bunch-selective spin manipulation; the analysis is ongoing and the results will be published soon.

2.4 Search for Axion-like Particles at COSY

An experiment to demonstrate the search of axions or Axion-like Particles (ALPs) in storage ring was conducted in COSY and here the result of the preliminary

⁶barthel HF-Technik GmbH, Aachen, Germany, <https://barthel-hf.de>

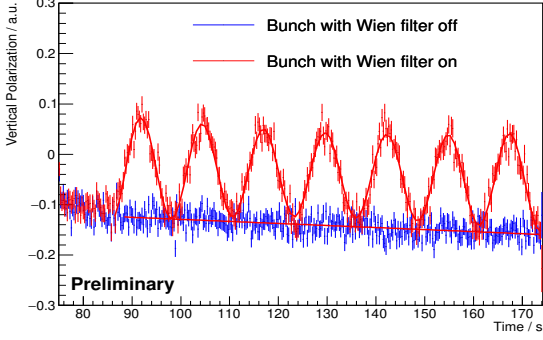


Figure 14: Red graph: vertical spin oscillations of signal bunch "WF off"; blue graph: non-oscillating vertical spin component corresponding to bunch "WF on" (pilot bunch).

sensitivity of the experiment is reported. The experiment is based on the ALP induced oscillations in the nuclear electric dipole moment d_n that can be described as $d_n(t) = d_0 + d_{ac} \cos(\omega_a t + \phi_a)$ where $\omega_a = 2\pi f_a$, ALP induced EDM oscillation frequency, is related to the axion mass m_a by $\omega_a = m_a c^2 / \hbar$ and ϕ_a is the axion primordial phase.

The experiment used the 0.97 GeV/c ($f_{\text{spin}} = 121$ kHz) in-plane polarized deuteron beam to search for the resonance between the spin precession frequency and the EDM oscillation frequency. Since the ALP frequency is unknown, the beam momentum was ramped in steps lasting 135 seconds each. Most of the scans were done with a momentum step of $dp/p = 1.38 \times 10^{-4}$ and the rest at $dp/p = 1.12 \times 10^{-4}$. The expected signal was a vertical polarization jump. Since ϕ_a is unknown, four beam bunches with different polarization directions were stored simultaneously in the ring to ensure that no ALP was missed.

The different polarization directions of the bunches modulate the estimated amplitude \hat{A} of the jumps according to:

$$f(\phi_m) = C_1 \sin x + C_2 \cos x, \quad (1)$$

$$\hat{A} = \sqrt{C_1^2 + C_2^2}, \quad (2)$$

where the ϕ_m is the difference of the polarization phase of bunch m and the ALP phase ϕ_a . A more detailed explanation of the experiment and calculation of the jumps is given in the 2019 and 2020 annual reports.

A sinusoidal fit for \hat{A} in Eq. (2), where \hat{A} represents the coupling between the ALP and the deuteron nucleus, is biased toward more positive values when \hat{A} is close to zero. The Feldman-Cousins analysis method deals with such systematic biases. First consider the probability density function given by

$$f(\hat{A}|A) d\hat{A} = \frac{1}{\sigma^2} e^{-\frac{\hat{A}^2 + A^2}{2\sigma^2}} \hat{A} I_0\left(\frac{\hat{A}A}{\sigma^2}\right) d\hat{A} \quad (3)$$

for the data described by Eq. (2). Here, A is the true value of the signal, \hat{A} is the estimated value of the amplitude from the experiment, σ is the uncertainty in its calculation and I_0 is the modified Bessel function of the first kind. In the next step, a likelihood ratio R defined as

$$R = \frac{f(\hat{A}|A)}{f(\hat{A}|A_{\text{best}})} \quad (4)$$

is calculated. A_{best} is the value of A for which $f(\hat{A}|A)$ has the maximum probability, given the physically allowed region for A . The Feldman-Cousins confidence interval is constructed by adding values of \hat{A} to the region of acceptance of A as values of R decrease. This addition to the band is done until the desired (90%) confidence level is reached. At this point the final value of A is taken to be the amplitude that marks the 90% confidence level boundary below which an ALP might still exist. This value is converted into the EDM limit using $d_{AC} = \lambda A \times 10^{-23}$ e·cm. The coefficient $\lambda = 355$ or 398 for the fast and slow ramp rates, respectively. The coefficient is based on a model of the polarization jump size for a particular ramp rate and distribution of bunch polarizations. Figure 15 provides the upper limit (dark line) for the oscillating EDM and the region excluded by our experiment (filled area). The green and blue areas differentiate the two different ramp rates used in the experiment. This experiment has demonstrated that a horizontally po-

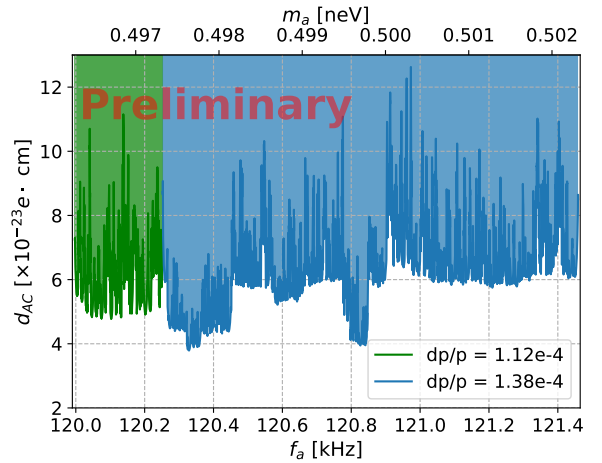


Figure 15: Preliminary 90% confidence level sensitivity for excluding an axion-EDM coupling (e·cm) in the frequency range from 120.0 to 121.4 kHz (mass = 4.95 to 5.02×10^{-9} eV/c²). The green and blue colors show the two scanning ramp rates. The darker colored regions mark sensitivities for individual 2-s time bins during the scan. All colored regions are excluded.

larized beam captured in a storage ring may be used in controlled energy ramps to search for the presence of an axion-like particle. The signal is a jump in the vertical polarization component of the beam at the point where the beam's spin tune frequency is in resonance with the axion

frequency. Test signals generated by an RF Wien filter demonstrated that such signals are detectable. If interpreted as a coupling through an oscillating EDM (purely electromagnetic), the EDM would have to be less than about $7 \times 10^{-23} \text{ e} \cdot \text{cm}$ in the frequency (mass) range of Fig. 15. A greater sensitivity (one or two orders of magnitude yielding $10^{-25} \text{ e} \cdot \text{cm}$ could apply if the axion-quark coupling is through the strong interaction.

2.5 Results of Beam and Spin Tracking Simulations

A whole set of beam and spin tracking simulations have been performed to explain experimental results at COSY, support planned COSY beam times of the JEDI collab., and to advance the design of the prototype EDM ring.

It has been experimentally shown for deuteron beams in COSY that it is possible to achieve a spin coherence time (SCT) of more than 1000 s. Compared to the deuteron, the proton presents a greater challenge because the anomalous moment is larger (and hence the speed of spin precession in the COSY ring), there are more spin resonances, and the chromaticity landscape is more complicated, which can lead to shorter polarization and beam lifetimes. For possible proton EDM experiments at COSY and for the construction of the prototype EDM ring, it is necessary to obtain sufficient proton SCT of roughly 1000 s. The results of detailed beam and spin tracking simulations show that a long spin coherence time with protons cannot be achieved by just minimizing the chromaticities, as is the case for deuteron beams. The second-order momentum compaction factor must be optimized along with the horizontal and vertical chromaticity to achieve a high proton SCT. In addition, simulations show that three families of sextupoles must be used to reach highest SCT. Fortunately, three suitable sextupole families are available in COSY. The optimal theoretical values for the second-order momentum compaction factor and chromaticities have been determined in simulations for COSY and explained in connection with particle orbit lengthening. For the prototype EDM ring, similar studies have been carried out. This storage ring has fourfold symmetry and operates in a frozen spin mode with weak vertical focusing. Two existing sextupole families are used to increase the SCT. In the current design, the maximum value of SCT is about 100 s. The proposed way to increase SCT is to insert the third family of sextupoles to adjust chromaticities and the second order momentum compaction factor to any desired value. All three families should be located at points with different ratios of optical functions and dispersion to reach highest SCT. A racetrack option for the prototype EDM ring with strong focusing has also been investigated and fulfills these requirements. The usage of a third sextupole family in this lattice ensures the increase of the proton SCT to 1000 s. The next step is to prove these theoretical predictions by

beam experiments at COSY. The COSY Beam Advisory Committee has accepted Proposal E009 to perform SCT studies with protons, and the beamtime is scheduled for February 2022.

Beam and spin tracking studies have also been carried out for polarized deuteron beams at COSY to support the analysis of the measured data from the deuteron precursor experiment. An idealized RF Wien filter has been implemented into the COSY lattice and the simulations have been performed with the software toolkit Bmad⁷ for charged particles from Cornell University. The final aim of these kind of studies is to compare the measured and simulated invariant spin axis. The invariant spin axis characterizes the spin motion inside a storage ring and contains information on the size of the EDM, which can finally be extracted by a precise knowledge of the imperfections in the storage ring. The lattice settings used for this study were taken directly from the April 2021 MadX COSY lattice, as this model is updated regularly. The first goal of the implementation of the RF Wien filter was to simulate the invariant spin axis $\langle \vec{n} \rangle$ without magnet imperfections and other systematic errors of COSY. By changing the relative phase of the Wien filter and the current of the solenoidal snake, the EDM resonance strength ϵ^{EDM} could be obtained for an idealized COSY lattice. The minimum of the simulated map indicates the tilt of the invariant spin axis by the EDM rotation (see Fig. 16).

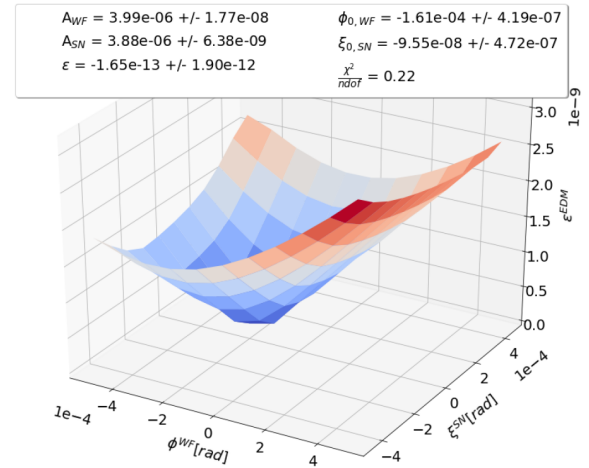


Figure 16: Simulated map of the invariant spin axis using the reference particle. The tilt of the invariant spin axis due to the deuterons EDM rotation and becomes visible at $\Phi^{WF} = 0$.

The next required step is to integrate realistic magnet misalignments, field errors, and other systematic effects into the COSY lattice, since these effects also influence the tilt of the invariant spin axis as the EDM does.

⁷<https://www.classe.cornell.edu/bmad>

More detailed information on the progress of beam and spin tracking simulations can be found in various individual reports.

2.6 Next Steps

2.6.1 Spin Physics Program

The unique global feature of COSY is its ability to accelerate, store and manipulate polarized proton and deuteron beams. In the recent past, these beams have often been used for precision measurements, in particular in connection with the study of charged particle EDMs (Electric Dipole Moment) in storage rings. The role of COSY as a R&D facility and for initial (static and oscillating) EDM measurements can hardly be overestimated. Unfortunately, as a consequence of the strategic decisions of Forschungszentrum Jülich and the subsequent "Trans-FAIR" agreement between FZJ and GSI Darmstadt, it is currently planned to stop the operation of COSY by the end of 2024. The various groups working with polarized beams at COSY felt it important to collect information on essential measurements to be performed until the termination of machine operation. These experiments, briefly described in the CBAC proposal⁸ along with an estimate of the beam time required, serve as pathfinder investigations toward an EDM storage ring and Spin for FAIR. A number of these proposals are related to the investigations in charged particle EDMs. Consequently, the proposed JEDI experiments are either a continuation of existing efforts (axion search, spin tune response to local steerer bumps or preparations for future options (spin coherence time for protons, stochastic beam cooling), that can currently only be done at COSY. In addition, the perspectives for a first direct measurement of the proton electric dipole moment using the RF Wien filter technique is also discussed.

Other proposals deal with a novel technique for the control of particle spins in storage rings called spin transparency, a highly flexible method to manipulate the spin direction in real time, and an experiment on longitudinal spin filtering in order to study the possibility of polarized antiprotons at FAIR. The corresponding beam time request for the proposal: "Proton polarization control at COSY in a Spin-Transparent mode at $\gamma G=2$ integer spin resonance" will be submitted to COSY beam advisory committee in 2022.

2.6.2 Towards an Electric EDM Storage Ring

On the way towards a precision storage ring, a number of technological and metrological challenges need to be mastered, e.g., storage and spin coherence time of the beams, residual radial magnetic fields, which mimic an EDM, or the required precision of beam position monitors. The conclusion of the JEDI- and CPEDM- collabo-

⁸Spin Physics at COSY (2021 - 2024 and beyond) - Pathfinder investigations toward an EDM storage ring and Spin for FAIR, [arXiv:2108.13933 \[physics.acc-ph\]](https://arxiv.org/abs/2108.13933)

rations is that the accomplishment of the task requires a stepwise approach:⁹

- Step-1: Proof-of-capability (ongoing activity). Perform R&D for key components and a first-ever deuteron EDM „precursor experiment“ at the magnetic storage ring COSY-Jülich.
- Step-2: Proof-of-principle (time frame: next 5-10 years). Design, build and operate a prototype ring with beam kinetic energy between 30 and 45 MeV in two steps: (i) an all-electric ring for CW/CCW operation, but not at the magic momentum, and (ii) after complementing the ring complemented with B-fields, for „frozen spin“ operation becomes possible to perform first competitive proton (pEDM) experiment (with a sensitivity similar to the neutron EDM).
- Step-3: Precision experiment (time frame: next 10-15 years). Design, build and operate a dedicated storage ring at the magic momentum (all-electric, beam kinetic energy 232.8 MeV, momentum 700.7 MeV/c) to push the pEDM sensitivity significantly below that of the neutron EDM; the final goal is 10^{-29} e · cm.

The first objective is to convene and combine technological and scientific expertise in accelerator, nuclear/hadron and particle physics for a storage-ring EDM project. The emphasis will be on Step-2 as an inevitable milestone towards Step-3: (i) Prepare a Technical Design Report (TDR) for the prototype ring, then build and operate it. The ring layout should be site independent; (ii) Conduct a pEDM measurement as proof-of-principle and pave the way for the design of the final high-precision ring; (iii) Exploit the prototype ring to conduct a Dark Matter (axions/ALPs) scan by searching for oscillating EDMs. The CPEDM-collaboration is preparing an EU application "Design Study" in frame *Research Infrastructure Concept Development* (HORIZON-INFRA-2022-DEV-01-01) for the project "A Prototype ring for charged particle EDM searches (proEDM)", which is the essential step towards the ultimate EDM storage ring (Step-3).

3 Neutrino Physics

The neutrino group is specialized in low-energy neutrino physics with liquid-scintillator (LS) based detectors. Borexino (Sec. 3.1), the world's radio-purest 280 ton LS detector in the Laboratori Nazionali del Gran Sasso in Italy took data from May 2007 until October 2021, focused on solar neutrinos, geoneutrinos, and searches for rare processes in coincidence with astrophysical events. JUNO (Sec. 3.2) will be the first multi-kton LS detector currently under construction in Jiangmen, China. German groups are leading the construction of the 20 ton

⁹CPEDM - A Storage Ring Facility for Charged-Particle EDM Searches, *Nuclear Physics News*, Vol. 31, No. 2, p.26-29, 2021.

OSIRIS detector (Sec. 3.3) that will monitor the level of radio-purity of the LS during the several months long period of filling the 20 kton JUNO central detector.

3.1 Borexino latest results with neutrinos of solar and astrophysical origin

Due to their very small cross-section, neutrinos provide us with the best sight on otherwise inaccessible processes in the core of the Sun. According to the Standard Solar Model (SSM), the Sun is fueled by two nuclear fusion processes converting Hydrogen into Helium: the dominant proton-proton (pp) chain, responsible for $\sim 99\%$ of the solar energy, and the sub-dominant Carbon-Nitrogen-Oxygen (CNO) cycle, accounting for the remaining $\sim 1\%$. Both processes involve the production of electron-flavour neutrinos, the so-called *solar neutrinos*, whose detection is the main goal of Borexino.

Borexino is a large organic LS detector, designed and built with the primary goal of real-time detection of low-energy solar neutrinos, in the sub-MeV to MeV energy range. The detection material consists of ~ 280 ton of ultra-clean organic scintillator, placed in the Hall C of the Laboratori Nazionali del Gran Sasso (LNGS), in Italy, below a natural shield of about 1400 m of rock (~ 3800 m of water equivalent). The detection of neutrino events is based on scintillation light produced by electrons from the neutrino-electron elastic scattering interaction. The active core of the detector is surrounded by a series of concentric shells made of materials with radio-purity increasing towards the inside, ensuring an unprecedented level of radio-purity in the inner scintillating core. The external surface of the inner detector is equipped with a set of ~ 2000 photo-multiplier tubes (PMTs) to measure the number of detected photons and their arrival times, resulting in a high effective light yield of ~ 500 p.e. at 1 MeV for 2000 PMTs.

In more than ten years of data taking, Borexino has successfully performed a complete spectroscopy of the neutrinos produced in the pp chain¹⁰, and has provided the first observation of solar neutrinos emitted from the sub-dominant CNO cycle¹¹. The European Physical Society has awarded the 2021 Giuseppe and Vanna Cocconi Prize to the Borexino Collaboration for the ground-breaking observation of solar neutrinos that provided unique and comprehensive tests of the Sun as a nuclear fusion engine. Currently, there is an ongoing effort towards an updated CNO measurement. A special review article (invited) on the recent solar and geoneutrino results authored by some Borexino members of the neutrino group has also been published in 2021¹²

¹⁰Comprehensive measurement of pp -chain solar neutrinos, *Nature* 562 (2018) 505.

¹¹Experimental evidence of neutrinos produced in the CNO fusion cycle in the Sun, *Nature* 587 (2020) 577.

¹²Borexino Results on Neutrinos from the Sun and Earth, *Universe* 07 (2021) 231, Special Issue Italian Research Facilities for Fundamental Physics.

First directional measurement of sub-MeV solar neutrinos

In 2021, Borexino has reported the first measurement of sub-MeV solar neutrinos using their associated Cherenkov radiation, providing an experimental proof of principle for the exploitation of directional Cherenkov light signal in future experiments based on liquid scintillator materials. This study has been suggested for a joint publication in *Physical Review Letters*¹³ and *Physical Review D*¹⁴ journals that are currently under review.

The analysis has been conducted in a specific energy region of interest ($\text{ROI} \subseteq [0.54 \text{ MeV} - 0.74 \text{ MeV}]$), selected using the scintillation light spectra, to increase the signal-to-background ratio. In the ROI, the signal is dominated by the electrons scattering off the 0.862 MeV mono-energetic ${}^7\text{Be}$ solar neutrinos ($\sim 90\%$ of signal). The remaining signal is represented by 1.44 MeV mono-energetic pep solar neutrinos and CNO solar neutrinos with an end point at 1.74 MeV. On the other hand, the main backgrounds include radioactive β emitters, such as ${}^{210}\text{Bi}$ ($Q = 1.162 \text{ MeV}$) and ${}^{85}\text{Kr}$ ($Q = 0.687 \text{ MeV}$) in the LS. The amount of emitted Cherenkov photons for electrons in the ROI is $\sim 0.4\%$, disfavours an event-by-event directional reconstruction in Borexino, that is typically possible in Water Cherenkov solar neutrino detectors. Since Cherenkov photons are emitted much faster with respect to isotropic scintillation photons, most of the Cherenkov information is contained in the first few nanoseconds of each event. Therefore, the analysis is done using the 1st and 2nd photon hits. The measurement is performed through a newly developed technique called *Correlated and Integrated Directionality* (CID). In this technique, the directional angle α is measured by correlating the PMT-hit distribution of a given event with the well-known position of the Sun, using the reconstructed vertex of the solar neutrino event and the position of the PMT. Since light emission from background sources in Borexino exhibits no correlation with the Sun position, their CID- $\cos\alpha$ distribution is expected to be flat. On the contrary, the CID distribution of solar neutrinos is expected to have a peak at $\cos\alpha \sim 0.7$ (see Fig. 17). This particular feature can be exploited to disentangle the neutrino signal from the backgrounds present in the ROI. The number of solar neutrinos in the ROI ($N_{\text{solar}-\nu}$) is extracted through a χ^2 -fit of the data hits using the Monte Carlo generated Probability Density Functions (PDFs) of the directional signal and flat background components. The Phase-I dataset of Borexino (May 2007 to May 2010) is used for this analysis. This choice is motivated by the existence of the gamma source calibration data from 2009: these gamma sources have been used to calibrate the wavelength-dependent group velocity of Cherenkov

¹³First Directional Measurement of sub-MeV Solar Neutrinos with Borexino, *arXiv:2112.11816* (2021), and accepted for publication in *Physical Review Letters*.

¹⁴Correlated and Integrated Directionality for sub-MeV solar neutrinos in Borexino, *arXiv:2109.04770* (2021), and accepted for publication in *Physical Review D*.

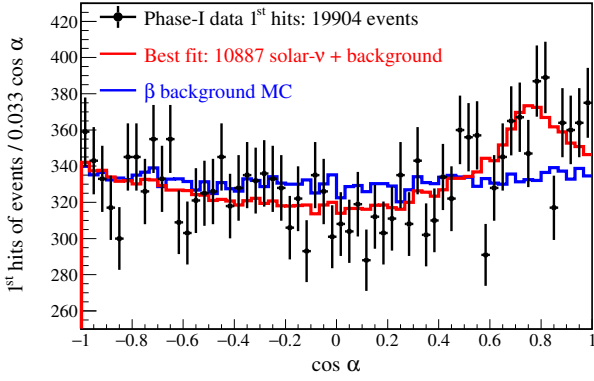


Figure 17: The $\cos\alpha$ distributions of the first hits of all the selected events (black points) compared with the best fit curve (red) for the resulting number of solar neutrinos $N_{\text{solar-}\nu}$ plus background. All histograms are normalized to the data statistics. It can be seen that the data points cannot be explained by the background-only hypothesis (blue).

light, essential for a directional measurement. Fig. 17 shows the measured $\cos\alpha$ data distribution for the first PMT hits, along with the best fit (red curve) and the $\cos\alpha$ PDF of background normalized to the total number of data events (blue curve). It is clear that the data cannot be explained with the background-only hypothesis.

Many possible sources of systematic uncertainties have been considered. The dominant effects limiting the precision of the final result are: (1) the bias between the true and the reconstructed positions of the recoil electron in its direction (left as a free nuisance parameter in the fit) and (2) the large relative uncertainty of 36% on the effective Cherenkov group velocity correction obtained from gamma calibration sources. The best fit result, with the 68% CI for the number of solar neutrino events in the ROI has been measured as $N_{\text{solar-}\nu} = 10887^{+2386}_{-2103}(\text{stat.}) \pm 947$ (syst.) out of 19904 total events. The agreement between data and model is good, as testified both by the $\chi^2/\text{ndf} = 124.6/117$, and the p-value = 0.30.

In Fig. 18, the $\Delta\chi^2$ profile as a function of $N_{\text{solar-}\nu}$ both with and without the systematic uncertainty is shown, along with the 68% confidence intervals for the measured $N_{\text{solar-}\nu}$ and the expected value according to the SSM. The best fit result is well in agreement with the SSM expectation ($N_{\text{SSM}} = 10187^{+541}_{-1127}$), rejecting the hypothesis of no neutrino signal at $> 5\sigma$ confidence level. Furthermore, subtracting the small contributions of *pep* and CNO solar neutrinos according to the SSM prediction, it is possible to convert $N_{\text{solar-}\nu}$ into the interaction rate of ${}^7\text{Be}$ neutrinos in Borexino, resulting in $R_{\text{Be-7}}(\text{CID}) = 51.6^{+13.9}_{-12.5}$ cpd/100 ton. It is well in agreement with both the SSM predictions as well as with the Borexino results from the *standard spectral fit procedure* ($R_{\text{Be-7}}(\text{Standard}) = 47.9 \pm 2.3$ cpd/100 ton). This result is an important proof of principle for the hy-

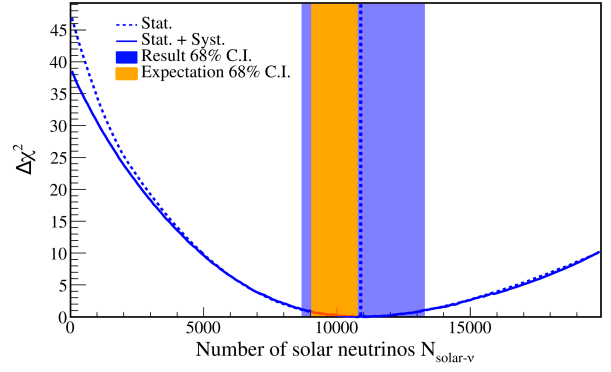


Figure 18: $\Delta\chi^2$ profiles of the first and second hits from the fit as a function of $N_{\text{solar-}\nu}$ with (blue solid curve) and without (blue dotted curve) the systematic uncertainty. The no-neutrino signal hypothesis (pure background, $N_{\text{solar-}\nu}=0$) can be rejected with $\Delta\chi^2 > 25$, thus $> 5\sigma$ confidence level. The 68% confidence intervals for the measured $N_{\text{solar-}\nu}$ and the expected value according to the SSM are shown with blue and orange band respectively.

brid detection of low-energy solar neutrinos using both Cherenkov and scintillation light. Furthermore, the novel CID method is robust and straightforward, and readily applicable to next generation LS-based experiments, that will be able to perform a dedicated calibration of the Cherenkov light and thus substantially reduce the uncertainty on such measurements.

Identification of the cosmogenic ${}^{11}\text{C}$ background

In Borexino, the cosmogenic background is a challenging threat for solar neutrino analysis. Despite the natural rock shield above the detector, that reduces the overall surface muon flux by $\sim 10^6$ orders of magnitude, there is a non-negligible amount of muons reaching the scintillator and producing unstable nuclei in the spallation process, typically on Carbon. The most abundant cosmogenic background is the ${}^{11}\text{C}$ isotope (β^+ , $Q = 960$ keV plus 2×511 keV annihilation gammas), depositing energy in the region of interest for *pep* and CNO solar neutrinos. In Borexino solar neutrino analysis, the ${}^{11}\text{C}$ background is tagged through a specifically designed algorithm called *Three-Fold Coincidence* (TFC), exploiting the spatial and temporal coincidence of the ${}^{11}\text{C}$ decays with the track of the incident muon and the secondary neutrons. Typical ${}^{11}\text{C}$ tagging efficiency is $\sim 90\%$, while the post-tagging exposure is reduced to $\sim 63\text{-}66\%$ of the total exposure.

In 2021, a novel method to further improve the identification of ${}^{11}\text{C}$ events has been proposed by the Borexino collaboration. The study has been published in the Eu-

ropean Physical Journal C¹⁵, and it is potentially adaptable to future liquid scintillator detectors. The new technique, called *Burst Identification* (BI), relies on the tagging of multiple ¹¹C events, so-called *bursts*, that are produced simultaneously by muons, typically those inducing hadronic showers. Large amount of light produced in such processes can deteriorate the performance of muon track and neutrino position reconstructions and thus the effectiveness of the standard TFC algorithm. Burst ¹¹C events are correlated in space and time, providing a tagging technique independent of any prior knowledge on the parent muon and secondary neutrons. This new technique can be combined with the regular TFC algorithm, resulting in a higher fraction of surviving exposure (66.7% to be compared with previous TFC-only 63.6% for Phase-III of Borexino), while maintaining the same tagging efficiency of $\sim 90\%$.

Search for low-energy neutrinos from astrophysical sources

Over the years, the Borexino collaboration has been active in investigating possible neutrino and anti-neutrino signatures from different astrophysical sources, and has also studied the conversion of solar neutrinos into anti-neutrinos in the magnetic field of the Sun. Recently a collaboration paper has been published in the *Astroparticle Physics Journal*¹⁶. Detection of electron anti-neutrinos through the inverse β -decay reaction along with the extreme radio-purity of the Borexino detector has led to new limits on the diffuse supernova neutrino background for $\bar{\nu}_e$ in the previously unexplored region below 8 MeV. Previous results have been improved by a factor of ~ 2.5 , setting a model-independent upper limit on neutrino fluxes from unknown sources in the energy range of 7.8-16.8 MeV.

Since it would be a proof of non-zero anomalous magnetic moment of neutrino, the search of $\bar{\nu}_e$ in the solar neutrino flux is also discussed. Thanks to an almost 5-fold increase in statistics, previous Borexino limits on neutrino to anti-neutrino conversion has been improved by a factor of two. The limit for solar $\bar{\nu}_e$ flux is found to be $384 \text{ cm}^{-2}\text{s}^{-1}$ at 90% C.L., corresponding to a transition probability of $p_{\nu_e \rightarrow \bar{\nu}_e} < 7.2 \cdot 10^{-5}$ (for $E_{\bar{\nu}_e} > 1.8 \text{ MeV}$). Moreover, by analyzing elastic scattering events at low energies, a new limit on ⁷Be solar neutrinos conversion into $\bar{\nu}_e$ is set: $p_{\nu_e \rightarrow \bar{\nu}_e} < 0.14$ at 90% C.L.

Lastly, solar flares as possible neutrino sources have been investigated. Borexino obtained the strongest up-to-date limit on the fluence of neutrinos for all flavors below 3 MeV. Assuming the neutrino flux to be proportional to the flare's intensity, intense solar flare as the cause of the

observed excess of events in run 117 of the CI-Ar Home-stake experiment can be excluded.

Search for Low-Energy Signals from Fast Radio Bursts

Fast Radio Bursts (FRBs) are millisecond radio transients observed at the extra-galactic or cosmological distances, caused by high-energy astrophysical processes yet unclear. The most popular class of models proposed to explain their origins involve the emission of neutrinos (and possibly axions), which could be potentially detected by large-volume Cherenkov or LS detectors. Accordingly, the search for an excess in the number of events produced by neutrino-electron elastic scattering and the inverse beta-decay on protons (IBD) has been performed using the full exposure Borexino data set, between 2007 and 2021. This work¹⁷ is currently under review. The signal has been selected by performing a temporal correlation analysis between events with visible energy above 250 keV within a time window of $\pm 1000 \text{ s}$ and the most intense FRBs. No statistically significant increase in the number of events over the backgrounds was observed. Consequently, it was possible to set the strongest upper limits on the fluences of monochromatic neutrinos of all flavors in the energy range of 0.5 - 15 MeV. Moreover, an alternative approach was used based on the search of the characteristic shape of neutrino-electron scattering spectra in the Borexino data. In particular, two different spectra of incoming neutrinos ($\nu_{e,\mu,\tau}, \bar{\nu}_{e,\mu,\tau}$) were considered for the analysis: the mono-energetic line and the spectrum expected from supernovae. The strongest limits on the fluences of both spectra were obtained, along with a new limit on the $\bar{\nu}_e$ -Fluence from the IBD reaction.

3.2 Towards completion of the JUNO detector

The Jiangmen Underground Neutrino Observatory (JUNO), a 20 kton multi-purpose underground LS detector, was conceived in 2008 with the main goal to determine the neutrino mass ordering (MO) through a measurement of the oscillation pattern of reactor anti-neutrinos. The JUNO complex is currently under construction underground, with a rock overburden of 700 m, located 53 km away from the Yangjiang and Taishan nuclear power plants in south China. The detector construction is scheduled to be completed in 2023. Given the gigantic size and the unprecedented energy resolution requirement of 3% at 1 MeV, JUNO has a vast potential also as an extraordinary astrophysical observatory for solar, atmospheric, geo, and supernovae neutrinos and in the search for various rare processes.

Several technological challenges must be addressed in the design of the detector in order to meet the require-

¹⁵Identification of the cosmogenic ¹¹C background in large volumes of liquid scintillators with Borexino, *Eur. Phys. Journal C* 81 (2021) 1075.

¹⁶Search for low-energy neutrinos from astrophysical sources with Borexino, *Astroparticle Physics* 125 (2021) 102509.

¹⁷Search for Low-Energy Signals from Fast Radio Bursts with the Borexino Detector, [arXiv:2111.14500](https://arxiv.org/abs/2111.14500) (2021), and submitted to the European Physical Journal C.

ments of the challenging physics program. Among these, the properties of the LS are crucial. JUNO will apply LAB-based scintillator, with PPO as a fluor and bis-MSB as a wavelength shifter. The exact LS composition has been optimized in dedicated studies with a 20 ton detector of the Daya Bay experiment focusing on the high light yield, high transparency, low chemical reactivity, and high radio-purity. The results have been published as a collaboration paper in Nuclear Instruments and Methods A¹⁸. Moreover, it is essential to maintain the background count rate — the so-called singles rate — due to the natural radioactivity below 10 Bq. The collaboration has recently published a paper describing the radioactivity control strategy for the detector materials in the Journal of High Energy Physics¹⁹.

A precise knowledge of the detector’s energy scale and its intrinsic non-linearity and non-homogeneity is an important requirement for a successful measurement of the neutrino MO. To achieve this, a complex calibration strategy has been developed and published in the Journal of High Energy Physics²⁰.

Since the last release of the general overview of JUNO’s physics potential in 2015²¹, a lot of progress has been made. The detector design has been further optimized and challenges regarding the detector technologies have been solved with extensive R&D programs. Moreover, physics goals have been either updated or newly established. The final design of the detector and the updated JUNO physics strategy are summarized in a recent review paper in Progress in Particle and Nuclear Physics journal²².

The JUNO collaboration is also releasing detailed studies about the sensitivities to various physics targets. The potential to measure ⁸B solar neutrinos down to an unprecedented 2 MeV threshold has been published in Chinese Physics C²³. A study of the potential to measure medium-energy solar neutrinos (⁷Be, pep, and CNO), completed as a joint effort of the IKP and Milano groups, is currently under collaboration review before publication.

Thanks to its large size, JUNO can also detect atmospheric neutrinos, produced in the interactions of Cosmic Rays in the atmosphere, down to lower energies with respect to the large water/ice Cherenkov detectors as Super-Kamiokande or Ice Cube. This topic is of particular interest for the neutrino group. A paper on the potential measurement of the atmospheric neutrino energy spectrum has been published in the European Physical Jour-

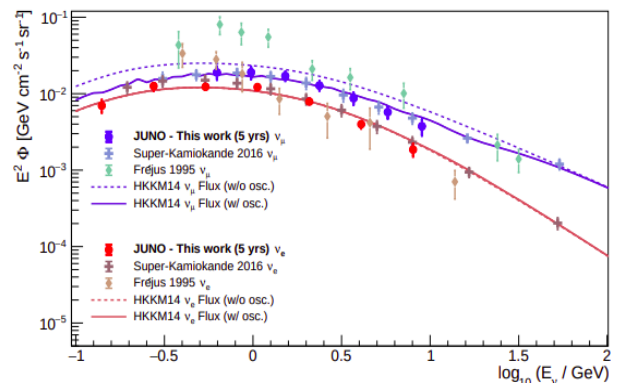


Figure 19: Atmospheric neutrino energy spectra reconstructed by the JUNO detector for ν_μ (blue color) and ν_e (red color), compared with present Super-Kamiokande, and Frejus measurements in the same energy region. The HKKM14 model predictions are also reported, both at the source and including oscillation effects. The fluxes are multiplied by E^2 for illustrative purposes.

nal C²⁴. The JUNO performance in reconstructing the atmospheric neutrino spectrum of ν_e and ν_μ is shown in Fig. 19. A probabilistic unfolding method has been used to infer the primary neutrino energy spectrum from the detector experimental observables. The simulated spectrum has been reconstructed between 100 MeV and 10 GeV, showing a great potential of the detector in the atmospheric low energy region. Further more realistic techniques to reconstruct the energy and directionality of atmospheric neutrinos in the LS are currently under development. These are needed in order to exploit atmospheric neutrinos in a combined analysis with reactor neutrinos in order to boost the sensitivity the neutrino MO.

JUNO can also serve as an outstanding detector for probing the damping signatures of different new physics models as the quantum decoherence, neutrino absorption, ν_3 decay, and wave package decoherence. The phenomenological effects of these models can be characterized by exponential damping factors at the probability level. A collaboration paper has recently been prepared for submission to the Journal of High Energy Physics²⁵, assessing how well JUNO can constrain these damping parameters and how to disentangle the different damping signatures.

Robust and reliable event reconstruction and Monte Carlo simulations are fundamental for accurate analyses. The IKP-2 neutrino group is largely involved in these activities, that included also the development of the event reconstruction techniques based on machine learning. The particular application of the latter on the pulse-shape par-

¹⁸Optimization of the JUNO liquid scintillator composition using a Daya Bay anti-neutrino detector, *Nucl. Instr. Meth. A*, 988 (2020) 164823.

¹⁹Radioactivity control strategy for the JUNO detector, *JHEP11* (2021) 102.

²⁰Calibration strategy of the JUNO experiment, *J. High En. Phys.* 3 (2021) 4.

²¹Neutrino physics with JUNO, *J. Phys. G: Nucl. Part. Phys.* 43 (2016) 030401.

²²JUNO physics and detector, *Progress in Particle and Nuclear Physics*, 103927.

²³Feasibility and physics potential of detecting ⁸B solar neutrinos at JUNO, *Chinese Physics C*45 (2021) 1.

²⁴JUNO sensitivity to low energy atmospheric neutrino spectra, *Eur. Phys. J. C* 81 (2021) 887.

²⁵Damping signatures at JUNO, a medium-baseline reactor neutrino oscillation experiment, *arXiv:2112.14450v1*.

ticle discrimination was a part of the small-group paper prepared together with the colleagues from DESY Hamburg and published in JINST²⁶. Furthermore the neutrino group is involved in the optimization of the energy reconstruction algorithms, with the goal of improving the sensitivity to the neutrino MO.

3.3 Online Scintillator Internal Radioactivity Investigation System (OSIRIS) of JUNO

The success of JUNO in various fields strongly depends on the final level of radio-purity of the liquid scintillator. Levels of 10^{-15} g/g for both ^{238}U and ^{232}Th are needed for the neutrino MO analysis. For solar neutrino measurements, the radio-purity needs to be one magnitude more stringent, i.e. 10^{-16} g/g for both radioactivity chains. In order to ensure these requirements, the Online Scintillator Internal Radioactivity Investigation System (OSIRIS) is being constructed. As a pre-detector of the JUNO central detector, it is designed to monitor the LS purity during the months-long filling of the 20 kton JUNO central detector.

In OSIRIS, the levels of ^{238}U and ^{232}Th contaminations in the scintillator are determined by identifying fast-coincidences of the decays of the isotope pairs ^{214}Bi - ^{214}Po and ^{212}Bi - ^{212}Po , respectively. OSIRIS will also be capable of measuring the ^{14}C concentration in the scintillator, down to a $^{14}\text{C}/^{12}\text{C}$ ratio of $d10^{-17}$ at 90% C.L. Additionally, possible ^{210}Po contamination present in the LS can be detected by measuring ^{210}Po decay rates with a precision of at least 15%. Further studies analyzed the ^{85}Kr concentration in the scintillator to detect air leaks in the purification chain and to extract an upper limit on the ^{39}Ar present in the scintillator.

The OSIRIS detector design consists of two optically separated volumes within a cylindrical stainless steel tank of 9 m height and width. The outer volume is filled with ultra-pure water which serves as a shielding buffer against external radioactive background emanating from the surrounding rock. A stainless steel frame within this volume is used to mount measurement and calibration devices. In order to detect and veto cosmic muons, 12 intelligent PMTs (iPMTs) are used to record Cherenkov light in the outer water volume. The inner volume consists of an acrylic cylinder with a height and width of 3 m that contains the 18 ton LS target. Inlets and outlets equipped with diffusers on top and bottom of the vessel allow a laminar exchange of the scintillator. The vessel is instrumented with 64 iPMTs placed 1.3 m away from the vessel surface.

The iPMTs used within OSIRIS are a novel design combining a regular 20"-PMT with its readout electronics mounted directly on the electrodes of the PMT. In this design, the digitisation of signals is done on the individual iPMT itself, which leads to a drastic reduction of noise

²⁶Particle Identification at MeV Energies in JUNO, JINST 16 (2021) 01016.

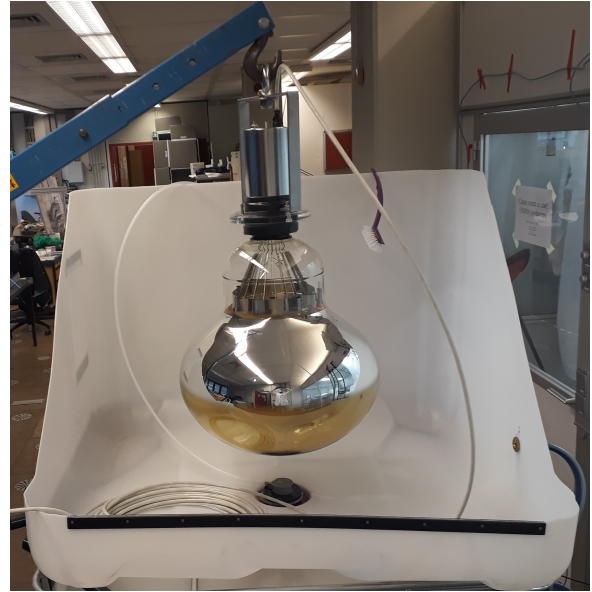


Figure 20: iPMT that will be used in the OSIRIS detector inside a washing station constructed at the RWTH with a major contribution from the IKP-2 neutrino group.

and thus an improved signal quality. A single ethernet cable is sufficient to power and read out the iPMTs via Power-over-Ethernet. The main analog-to-digital converter chip VULCAN was developed at the ZEA-2 institute of FZJ, whereas the development of the readout electronics stack and the actual integration of VULCAN into the stack is led by the OSIRIS hardware group of RWTH Aachen.

Members of the neutrino group supported the working group in Aachen in multiple ways during the last year. Mechanical simulations of the iPMT holding structures were continued, the reinforced design was tested and produced successfully. During the production of the iPMT system, members from the neutrino group offered substantial help in various steps, for example testing of electronic components. To minimize dust contamination in OSIRIS, the iPMT system and other collaboration parts from Germany were cleaned before shipment to China, as shown in Fig. 20. For this purpose, cleaning procedures were developed jointly with RWTH Aachen. A cleaning facility was constructed and successfully used during the production, which was finished in late November 2021.

As every iPMT triggers individually during normal operation, only a software trigger is needed. The data packages from the iPMTs are sorted according to their UNIX timestamps and combined into events for further analysis. The trigger is able to detect low energy-events, namely ^{14}C β -decays with 156 keV end point, while maintaining a reasonable low event rate when taking PMT dark noise into account. Furthermore, to be able to issue fast warnings in case of high-levels of contamination in the scintillator, the collected data needs to be analysed in real time. The neutrino group is strongly involved in the de-

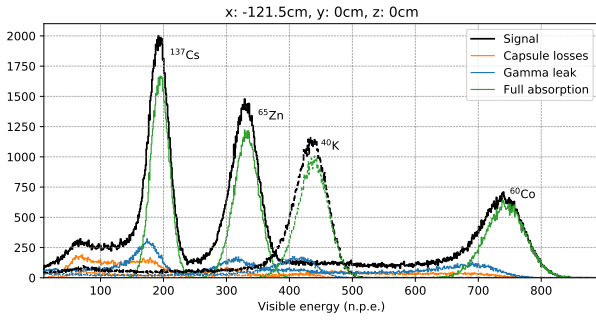


Figure 21: The expected energy spectrum, expressed in number of photoelectrons, of γ 's from the calibration sources placed inside the OSIRIS detector. Each black peak represents the spectrum from one isotope labeled next to it. The coloured lines show different contributions to the black spectrum.

velopment of the trigger, online analysis software, and reconstruction algorithms.

Another responsibility of the neutrino group is the development of the calibration system of OSIRIS, utilizing γ sources to characterize the detector response in terms of position and energy reconstructions and a pulsed LED to calibrate PMT timing and charge reconstructions. Both source capsule and LED will be lowered into the detector along an off-center axis by using an Automatic Calibration Unit (ACU), kindly provided by the Daya Bay collaboration. The expected spectrum of the radioactive sources at one position on the calibration axis in OSIRIS is shown in Fig. 21. Substantial progress has been achieved in planning a calibration with a minimal risk of contaminating the scintillator.

The final design and the sensitivity levels of OSIRIS have been published as a collaboration paper in the European Physical Journal C²⁷. Studies about the usage of the OSIRIS detector, once its main purpose for JUNO has been fulfilled, are ongoing. In the SERAPPIS experiment the upgraded OSIRIS detector is suggested to be used for a high-precision measurement of the low-energy pp solar neutrinos. The respective collaboration paper²⁸ was submitted to the European Physical Journal C.

4 Accelerator Research

4.1 Developments at COSY

Injector

In 2021 cyclotron JULIC together with its polarised and unpolarised sources have been used as injector for COSY

²⁷The Design and Sensitivity of JUNO's scintillator radiopurity pre-detector OSIRIS, *Eur. Phys. J. C* 81 (2021) 973.

²⁸Potential for a precision measurement of solar pp neutrinos in the Serappis Experiment, [arXiv:2109.10782](https://arxiv.org/abs/2109.10782) (2021), submitted to *Eur. Phys. J. C*.

synchrotron and experiments with a low energy beams directly from the cyclotron. Injector team has been working continuously on uninterrupted operation of all the injector systems and their modernisation. The new NMR-probe produce by Metrolab company was tested and in a cooperation with external company optimised for a real cyclotron environment. Quality of the maintenance works, done by the injector group, was confirmed during long beam time for the JEDI experiment in spring 2021, then a Cs-gun of polarised source was continuously operational for more then 50 days.

EPICS Integration of the Injection Beam-line

In the course of EPICS integration at COSY²⁹ progress was achieved with various accelerator sub-systems. Major progress was achieved in power supply control of the injection beam-line (IBL) in collaboration with Cosylab d. d.. This paves the way for the upcoming beam-times focused on machine-learning and significantly helps in routine operation.

Power Supplies The Injection beamline consists of 12 dipole, 43 quadrupole, 13 biaxial and 2 horizontal steerer magnets. These are powered by 48 power supply units utilizing 4 different controller types.

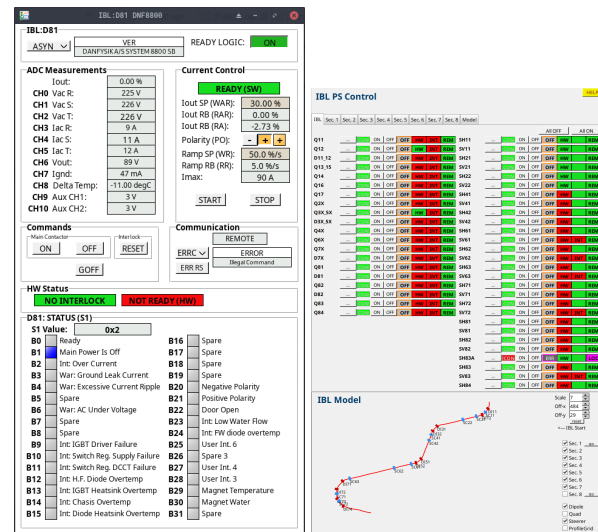


Figure 22: Examples of an engineering (left) and operations (right) graphical user interface implemented on top of the EPICS power supply input-output-controller

Model The IBL model is completely reworked and is now based on MAD-X. A similar approach as for the COSY lattice³⁰ is followed and the model is automatically generated from the corresponding entries in

²⁹I. Bekman et al., *EPICS Integration Status*, Annual Report 2019, IKP - COSY, Jül-4423, pp.107-108, (2019).

³⁰I. Bekman, J. Hetzel, *Model-Related Applications*, Annual Report 2020, IKP - COSY, Jül-4427, pp.99-100, (2020)

the component database. Integration into EPICS is in progress.

IBL Optimization Controlling of the beam will be used in tandem with the diagnostic systems already integrated in EPICS: profile grids, beam cups (with new read-out), phase probes, beam current transformer of COSY. This completes the feedback control loop needed for algorithmic IBL optimization allowing to test machine-learning techniques both based on the beam-line model and unconstrained.

New Beam Diagnostics Tools

Stripline Unit Upgrade In order to excite the beam for different measurements, the excitation signal generated by various systems can be applied in different ways to the 4 stripline electrodes. A new signal distribution and control unit was designed built and put into routine operation. In addition an EPICS IOC and a GUI were developed and commissioned. The new approach allows for the use of two independent signals/frequencies with individual signal level adjustment for beam excitation³¹. The work was carried out by a FZJ trainee.

Bunch Shape Monitor and Continuous Fast Tune Measurement Two systems for further beam inspection were developed. These new tools are based on the fast bunch-by-bunch and raw ADC data provided by the Libera Beam Position Processors. For both methods the data is further processed and displayed to the operator³². Furthermore, the data was used for tomographic reconstruction of the longitudinal phase space evolution at COSY³³.

Improvements of further accelerator sub-systems continued. An additional multi wire proportional chamber (MWPC) was installed and commissioned at the Industrial Irradiation Facility (IBP). Together with the first profile grid (PG1) in the IBL the extraction from the cyclotron JULIC can be optimized with the data obtained from that MWPC. This information additionally speeds up the beam setup during the irradiation beam times. It is also of significant benefit for COSY operations. The drive controllers of the IBL profile grids were modernized and are now seamlessly integrated in the new control system. The readout of the IBL faraday cups and various BI elements in the ion source beam line was modernized. The new hardware provides high resolution data allowing accurate representation of time structure of the beam pulses. The new CSS GUI is put in routine operation as well. Additional process variables were added to

³¹M.Kaczmarek, B.Breitkreutz, K.Reimers, Modernisation of the Stripline Unit Signal Conditioner at COSY, individual contribution in this report

³²P. Niedermayer, B. Breitkreutz, A Bunch Shape Monitor for COSY, individual contribution in this report

³³P. Niedermayer, B. Breitkreutz, Tomographic reconstruction of the longitudinal phase space evolution at COSY, individual contribution in this report

the HV and magnet sub-systems of the 100 kV electron cooler.

Access to Accelerator Related Information

360° photo walk-trough In order to have a 360° photo walk-trough, the entire accelerator complex was photographed with a 360° camera. The photographs were put into a special software to create a walk-through experience. Most of the accelerator, not only COSY but also e.g. the cyclotron or the power supply rooms, are already available. Further descriptions and explanations are being added for public release. This system will significantly improve the experience of visitors who are not allowed to enter certain areas due to accelerator operation or radiation safety restrictions.

COSY Documentation which is still on paper, is being scanned and processed via OCR to be machine readable. Documentation is put on a system hosted by the controls group to have it full text searchable.

4.2 Progress of the HESR

Introduction

IKP is leading the international consortium which is dedicated to build the HESR. It is strongly supported by colleagues from the Central Institutes for Engineering and Analytics (ZEA) of the Research Center Jülich. The investment money either spent or bound by contract did not change much as nearly all items that need to be bought now are already ordered. The remaining money is reserved for items which are due for installation, e.g. dipole power converters, vacuum pumps, and edge valves.

All planning is adjusted to deliver the pre-assembled HESR hardware components with the available personnel to FAIR as soon as possible to the storage hall or in time for the installation dates. Last deliveries are planned to happen significantly before 31-12-2024. There are some exceptions to this date: The site acceptance test of the power supplies for the main dipole magnets can only be done on the installed and wired dipole magnets as no test load is available. Thus this delivery date is depending on the end of installation in the tunnel. The vacuum pumps will only be installed directly in the tunnel after the last transport by truck. Due to guarantee reasons the pumps will be bought as late as possible.

Facing the end of IKP-4 in the Research Centre Jülich at the end of 2024, the available and qualified personnel is slowly decreasing. As a consequence, the possibilities to buffer Corona-induced delays are very limited. The TransFAIR process to migrate personnel from IKP-4 to the HESR group at FAIR is proceeding. Colleagues leaving the HESR team cannot be replaced.

Workpackage Magnets and Pre-assembly

The heating jackets of the special beam pipes in the 4 dipole magnets in the neighbourhood of the SPARC target places turned out to be of critical thickness. Some iterations were necessary to get the first two of these dipole magnets closed and delivered to Weiterstadt. 2 more are still awaiting final pre-assembly.



Figure 23: The first quadrupole unit is assembled and loaded on the truck.

The first quadrupole unit in the arc sections was finalized and sent to Weiterstadt. 6 benches for assembly in parallel have been set up. 38 BPMs are in Jülich and ready for pre-assembly. All quadrupole magnets are now ready for pre-assembly.

All deliveries (magnets and power supplies) from our Romanian partners were delivered and accepted. Post contract support is excellent (exchange of quality documents).



Figure 24: Assembly hall: Benches for quadrupole girders of the arc sections.

Work Package Power Converters

The specification of the 2 main dipole power converters is approved by all relevant working groups. It will be used for the call for tender once we can add a serious date for delivery, i.e. the HESR buildings must be contracted.

EMC measurements for the Romanian power converters are routinely performed. 45 (72 in total) of these power converters are released for installation. Close collaboration with the colleagues of GSI Power Converter Group ensures smooth continuation in case of ACU issues.

The commissioning of the fast temperature interlock system for the septum power converter is postponed until



Figure 25: HESR cavity installed in COSY. Note the fans below each resonator.

installation. This power converter has been released for storage.

Work Package RF System

The HESR cavities are assembled now. One of them is installed in COSY for life tests using the full system including air cooling and solid state amplifiers.

Work Package Injection (Kickers with Pulsers)

The first tank with two magnets installed has been released for storage together with the associated cables and pulsers. The next tank and the next pulsers are being assembled.

Work Package Beam Diagnostics

Beam position monitor (BPM) Up to now 38 beam position monitors (BPMs) are delivered to Jülich. One by one they are being tested and the electrical center measured as this deviates for each unit slightly. Later they will be assembled in the quadrupole units mentioned above. For the comparably small beam currents expected at the HESR, head-amplifiers have to be installed in addition to the FAIR-wide pre-amplifier A110. The design was finished and a preliminary review was performed. The additional head-amplifier will be used not only with the BPMs in the HESR, but also at the CR and some HEBT beamlines. A total of 100 BPMs will be equipped with these devices.

Ion clearing (IC) All the ion clearing chambers (ICCs) were delivered.

Viewer The mechanical design for viewers and beam diffusors was finished. The first unit was build and tested. The production of the series has started.

Ionization beam profile monitor (IPM) The mechanical design is nearly completed. The technological aspects of a very fine mesh being diffusion-welded to a frame are being worked out by ZEA. The mesh is to be put in front of the position sensitive detector of the IPM as well as in front of the UV lamp which is used for detector calibration. The envisaged design review for the beam profile monitor is still pending.

Scraper The scraper has been build and is awaiting mechanical and electrical tests of the stepper motors and vacuum tests.

Measurement of the uncaptured beam in Barrier-Bucket mode Theoretical work was performed in order to find a suitable method for measuring the uncaptured percentage of the beam while in Barrier-Bucket mode, which is used during injection of the HESR. Two methods were reviewed: a Wall Current Monitor (WCM) and of a modified IPM. Unfortunately, the theoretical investigations showed that both methods won't deliver the data needed. Therefore further investigations will be conducted.

Beam Loss Monitor (BLM) For the Beam loss monitor system a test setup was installed at COSY. That included the specified hardware, a scaled down version of the FESA control system as well as a few scintillation detectors. The setup further allows integration tests of other FESA components and knowledge transfer.

Work Package Vacuum, Space Management

The girders for the straight sections are in production. Further heating jackets were ordered. Time consuming tasks are pre-assembly of the quadrupole units which include geodetic measurements and RGA, verifying the quality of delivered components, space management, and mirroring the picture of the HESR in the data bases. The concept for merging the space requests in the tunnel for cabling, connection boxes, installation aids and technical infrastructure is continuously in development.

For the mobile heating system the connection points were fixed. There the mobile racks with control and power circuits will be hooked up. The software for the mobile heating system was tested successfully using a prototype rack. The system will be designed to automatically recognize the details of the vacuum section where it is connected to. Uploading and updating the documentation of individual components to the electronic document management system now is a routine task. The large number of documents (10k) is still a challenge.

Work Package Stochastic Cooling

All stochastic tanks are assembled now. Operation of one complete system is thoroughly tested in COSY. The mode damper beam pipes are released for storage.

Work Package Experiment Integration

The vacuum chambers for the chicane dipole magnets and for the injection dipole have been ordered. The tendering of the compensation solenoid is in preparation. The big magnet in the middle of the PANDA chicane could be contracted together with its power supply.

5 Further Activities

5.1 LHCb-target Development

Over the past 20 years, the Jülich group, together with the INFN Section of Ferrara, has developed a solid and acknowledged experience in the design and construction of storage cells for gaseous targets. The use of this technology has had a significant impact in the field of experimental hadronic physics. Examples of the application of this technology are the target of the HERMES experiment (see Fig. 26) at HERA (DESY), operated from 1995 to 2007, that of the OLYMPUS experiment at DORIS (DESY), operated in the period 2012-2013, and that of the PAX/JEDI experiment, currently in operation at COSY (Forschungszentrum Jülich).

The storage cell, typically made of a 50-200 μm thick layer of aluminum with cylindrical geometry, is placed inside the beam-pipe of the accelerator, coaxially with the beam. The latter then intercepts directly the target gas contained into the cell, without interacting with other materials, as in the case of solid targets. Furthermore, with respect to the more traditional gaseous jet targets, the use of a storage cell allows to reach areal densities of the order of $10^{13} - 10^{14}$ atoms/cm², i.e. up to two orders of magnitude higher.

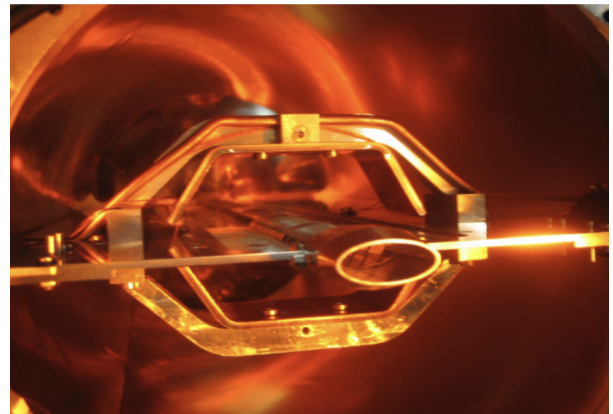


Figure 26: The HERMES storage cell.

The experience acquired in the framework of CSN3 experiments, has recently allowed to develop a storage cell for the LHCb experiment (see Fig. 27) in the framework of the SMOG2 project³⁴.

SMOG2 is a gas target confined within a 20 cm-long aluminium storage cell that is mounted at the upstream edge of the VELO detector, 30 cm from the main interaction point, and coaxial with the LHC beam. The storage cell technology allows a very limited amount of gas to be injected in a well defined volume within the LHC beam pipe, keeping the gas pressure and the density profile precisely controlled, and ensuring that the beam pipe vacuum level stays at least two orders of magnitude below the upper threshold set by the LHC. The cell is made of two halves, attached to the VELO with an alignment precision of 200 μm . Like the VELO halves, they can be opened for safety during LHC beam injection and tuning, and closed for data taking.

The storage cell was successfully installed upstream of the LHCb detector in Summer 2020. Starting from RUN3 (2021), LHCb is therefore the only LHC experiment to be provided with two distinct interaction points and the possibility of operating simultaneously in two collision modes: collider and fixed-target mode. The beam-gas collisions occurs at a center-of-mass energy of 115 GeV for proton beams and 72 GeV for lead beams. SMOG2 will allow to carry out precision studies in the field of QCD and astroparticle physics in essentially unexplored kinematic regions.

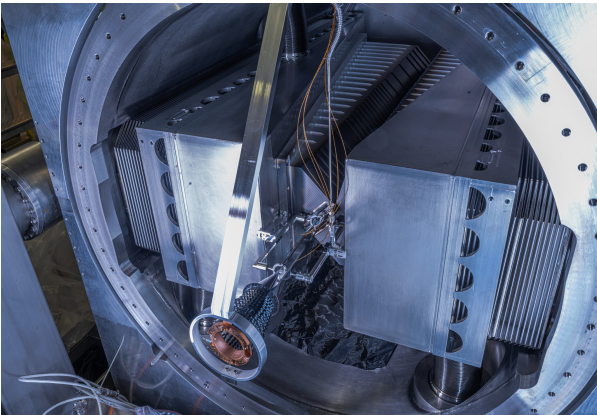


Figure 27: The target cell at the interaction point of LHCb.

The next step of the development is related to the installation of a polarized atomic beam source. The performance of the storage cell for this case is strongly connected with the behavior of the cell surface with respect to recombination and depolarization of the stored polarized atomic hydrogen. Little is presently known about amorphous carbon, which is the only coating admitted for the LHC surfaces directly exposed to the beam. The PAX interaction point at COSY, being equipped with an

atomic beam source, a Breit-Rabi polarimeter and a vertex silicon detector, is the only place worldwide where a characterization of the cell coating can be performed. Such a test can be conducted right after the completion of the longitudinal spin-filtering experiment.

5.2 Spectroscopy with a Sona Transition Unit

In principal, it should not matter if an atom at rest is hit by an electromagnetic wave to induce a transition or if an atom with the velocity v is moving through a static oscillating magnetic field. The only difference is that the corresponding velocity of the magnetic field oscillations is now not the speed of light c but $v \ll c$. In addition, the possible wavelengths are in a range of 1 to several 10 cm. This means that for a beam energy of ~ 1 keV the velocity is about $v \sim 5 \cdot 10^5$ m/s and the time-of-flight through a magnetic field oscillation with a wavelength of 20 cm is $\Delta t = 2.5 \cdot 10^{-7}$ s. Thus, the atoms experience a magnetic field oscillation of $f = 2.5$ MHz or following the Planck-Einstein equation a photon with the energy $E = h \cdot f \sim 10$ neV that can induce magnetic dipole transitions. These transitions between quantum states are found in the Zeeman region of the hyperfine substates of hydrogen atoms

Within the BOB project to measure the helicity of the anti-electron neutrino via the rare β -decay $n \rightarrow H_{2S} + \bar{\nu}$ at the technical university in Munich it is necessary to measure the occupation numbers of the hyperfine substates of these metastable hydrogen atoms. This requires separating the hyperfine α -substates with $m_J = +1/2$ from the β_3 state ($m_J = m_I = -1/2$). A Lamb-shift polarimeter can measure the α states, but it cannot access the β_3 state. Thus, a Sona-transition unit (STU) was designed, built and tested that is similar to those in use at polarized proton sources to exchange the occupation numbers of the α_1 and the β_3 state by inverting the magnetic quantization axes faster than the Larmor precession can do. Tests showed that hydrogen atoms passing through the sinusoidal magnetic fields of the STU experience an oscillating magnetic field that excites non-adiabatic transitions between the hyperfine substates too.

The actual setup (Fig. 28) consists of an ionizer to produce protons and accelerate them to energies of about 1 keV. A Wien filter is used as a velocity filter to decrease the velocity distribution of the protons down to $\Delta v/v \sim 10^{-3}$. By charge exchange with Cesium vapor hydrogen atoms are produced in the metastable state $2S$. A spinfilter, the most important component of an LSP, quenches atoms in 3 out of 4 hyperfine substates into the ground state so that only metastable hydrogen atoms in the α_1 and α_2 states can survive. If atoms in the α_1 state are chosen, the STU will transfer them into the β_3 state. In parallel, corresponding photons are absorbed and can induce transitions directly into the α_2 substate and with absorption of a second photon back into the α_1 state. Even odd multi-photon transitions are possible until the

³⁴The LHC Spin Project, [arXiv:1901.08002 \[hep-ex\]](https://arxiv.org/abs/1901.08002)

sum of the photon energies fits to the energy difference between the states. Following the Breit-Rabi diagram (Fig. 29) the energy difference depends on the magnetic field amplitude that is dominated by the longitudinal field component, but the transitions itself are induced by the radial component. Afterwards, another spinfilter is separating the again occupied α states from each other and the single occupation numbers are measured by quenching the residual metastable atoms into the ground state and counting the produced Lyman- α photons with a photomultiplier as function of the amplitude of the longitudinal magnetic field.

In principal, the measured spectra are perfectly described by solving the time-dependent Schrödinger equation, but this needs an extremely precise knowledge of the magnetic fields in the STU. A simple fit to the measured resonances allows to determine the energy difference between the hyperfine substates with a relative uncertainty of 10^{-3} , i.e. in the order of 10^{-11} eV. Nevertheless, an improved analysis is underway that takes care on the correlation between the different transitions that deforms the Lorentz peaks and the distortion of the x-axis, because the energy difference of the substates is not a linear function of the external magnetic field. When these effects are taken into account to the actual measured data the uncertainty should drop by one order down to 10^{-12} eV.

In parallel, a new proton source is implemented and will increase the beam intensity by more than one order to decrease the statistical uncertainty. Another option for this purpose are more measurements at different beam velocities that will allow many independent measurements of the Breit-Rabi diagram. A new coil setup will improve the static magnetic field so that its shape will come closer to a sinus function. This will help to decrease the uncertainty even further and at the end a statistical uncertainty of 10^{-13} eV seems to be in range. The analysis of the actual data even allowed to identify a first systematic problem, because the necessary different magnetic field settings of the second spinfilter influenced the magnetic

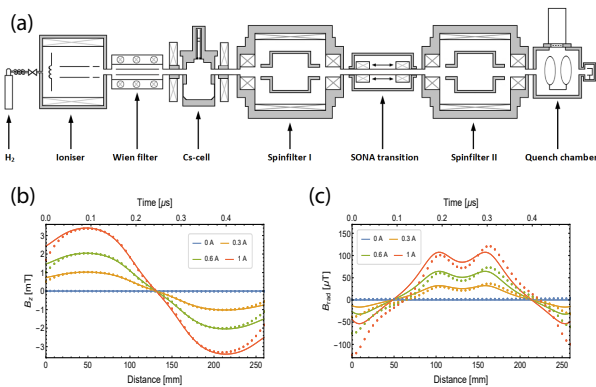


Figure 28: The experimental setup and the corresponding longitudinal and radial magnetic fields of the Sonar transition unit.

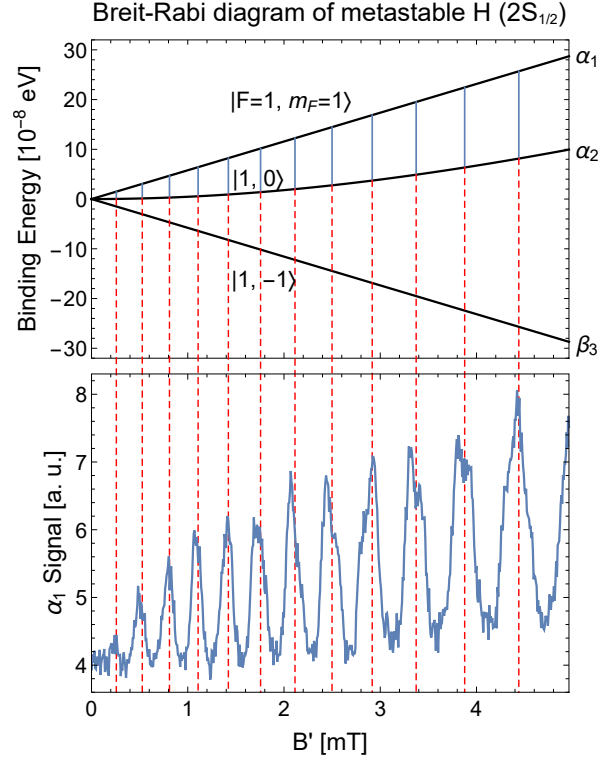


Figure 29: The energy difference between the hyperfine substates of metastable hydrogen atoms as function of an external magnetic field B and the corresponding transitions for odd multiples of the basic photon energy.

field of the STU and produced an offset of less than $1 \mu\text{T}$ that can be easily observed in the data. Further shielding of this region will help to minimize this problem. With this improvements it should be possible to test the modifications predicted due to QED, e.g. the influence of the proton size, in the order of 10^{-12} eV.

Of course, the same method can be used for deuterium atoms. Fig. 30 shows the expected relative occupation numbers for the different metastable α substates with $m_J = +1/2$ that can be separated with the spinfilter. [refer to Ref.³⁵]

5.3 Developments of polarized beams at JuSPARC

Polarized beam developments at JuSPARC include hardware development, beam and spin simulations, as well as experiments.

5.3.1 Polarized ^3He Gas Jets for Laser-Plasma Applications

A target providing nuclear polarized ^3He gas jets for laser-plasma applications has been designed, built, and

³⁵R. Engels et. al., Eur. Phys. J D **75**, 257 (2021).

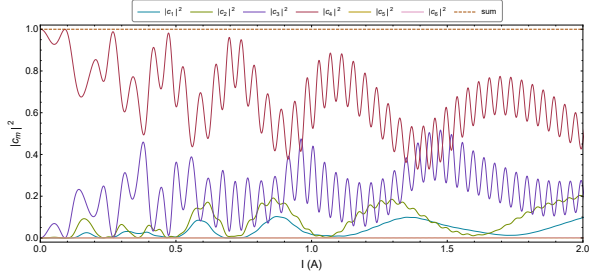


Figure 30: Simulations of the occupation numbers of the different hyperfine substates for deuterium atoms at a beam energy of 1.28 keV passing the STU. At the beginning all atoms will be in the state β_4 (red) and with increasing magnetic fields, i.e. more current in the Sona coils, the α -substates will be populated. Due to the growing energy difference between the states β_4 and α_3 (violet) especially the occupation numbers of these states are oscillating very fast.

tested in the laboratory. Such a target requires a magnetic system providing a permanent homogeneous holding field for the nuclear spins and a set of Helmholtz-like coils for adjusting the orientation of the polarization. Starting from a transport vessel at a maximum pressure of 3 bar, the helium gas is compressed for a short time and can be injected into a laser-interaction chamber through a non-magnetic opening valve and nozzle, thus forming jets with densities of about a few 10^{19} cm^{-3} and widths of about 1 mm. The target comprises a 3D adjustment system for precise positioning of the jet relative to the laser focus. An auxiliary gas system provides remote target operation and flushing of the gas lines with Ar gas, which helps to reduce polarization losses. The measured degree of ^3He polarization is sufficient for proof-of-principle polarization experiments at high-power laser facilities. First such measurements have been carried out in August 2021 at the PHELIX facility, GSI Darmstadt (see Fig. 31). The data are still being analyzed and the results will be reported in a currently prepared publication. This work has been supported by the ATHENA consortium (Accelerator Technology HELmholtz iNfrAs-structure) in the ARD programme (Accelerator Research and Development) of the Helmholtz Association of German Research Centres. W. Heil (retired Professor from Johannes Gutenberg-University Mainz) provided the ^3He polarizer.

5.3.2 Polarized Proton Beams with Multiple GeV Energies

The generation of polarized proton beams with multiple GeV energies upon ultra-intense laser interactions with targets was studied with three-dimensional particle-in-cell simulations. For proton acceleration, a plasma target near critical density with pre-polarized protons and tritium ions (which have a maximum mass-to-charge ratio)

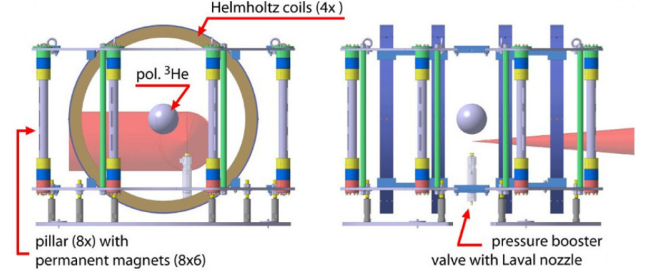


Figure 31: Arrangement of the magnet system with permanent magnets and four concentric coils. The transport vessel with ^3He (gray sphere) can be seen at the center and the compressor below. The PHELIX laser beam is indicated by the red cone.

was considered. The pre-polarized protons are first accelerated by the pressure of the laser radiation before being injected and further accelerated in a bubble-like wakefield. The time dynamics of the proton polarization is followed via the Thomas-Bargmann-Michel-Telegdi equation, and it was shown that the polarization state of the protons can be changed by both the laser field and the magnetic component of the wakefield. A series of simulations was performed to study the polarization dynamics during the acceleration of pre-polarized protons with a modified version of the three-dimensional particle-in-cell (PIC) code EPOCH³⁶. A laser pulse with $\lambda = 0.8 \mu\text{m}$ wavelength and clockwise polarization was propagated in the x direction with a focused transverse Gaussian profile with a pulse duration was $\tau = 20 \text{ fs}$ and a laser intensity $2.14 \cdot 10^{23} \text{ W/cm}^2$. After pre-acceleration by a circularly polarized laser, the protons are trapped in the front region of a wakefield bubble and are further accelerated by the wakefield, where the acceleration gradient is nearly 10^{14} V/m . It was found that the hydrogen-to-tritium ratio in the gas has a strong influence on the proton acceleration in this regime. The radius and the velocity of the accelerating field structure depend critically on the ion ratio. For sufficiently large ratios, a polarized proton beam can be trapped by the wakefield and accelerated to multi-GeV energies. The protons can gain 10 GeV in this field within $100 \mu\text{m}$. The dependence of proton acceleration and polarization on the ion species ratio was determined. It was found that protons can be accelerated efficiently as long as their relative fraction is less than 20%, in which case the bubble size is large enough for the protons to obtain sufficient energy to overcome the bubble injection threshold. In all considered cases the accelerated proton beams maintain more than 40% of their original polarization in the pre-polarized target³⁷.

³⁶Contemporary particle-in-cell approach to laser-plasma modelling, *Plasma Phys. Control. Fusion* **57**, 113001 (2015)

³⁷Polarized proton acceleration in ultraintense laser interaction with near-critical-density plasmas, *Phys. Rev. E* **104**, 015216 (2021)

6 Theoretical Investigations

Introduction

The IKP theory group studies the strong interactions in their various settings — spanning topics in hadron structure and dynamics, the nuclear many-body problem, symmetry tests in Quantum Chromodynamics (QCD), physics beyond the Standard Model and strongly correlated electronic systems. The first focus of the theory group is the formulation and application of effective field theories for precision hadron and nuclear physics based on the symmetries of QCD. The second focus is related to high performance computing in nuclear, hadronic and condensed matter physics, spear-headed by the work on nuclear lattice simulations. Since July 2012, the group is heavily involved in the activities of the collaborative research center “Symmetries and the emergence of structure in QCD” (CRC 110) together with researchers from Bonn University, TU München, Ruhr-Universität Bochum, IHEP/CAS (Beijing, China), ITP/CAS (Beijing, China) and Peking University (China). This CRC is presently in its third and final funding period. A further strengthening of the group was achieved through the ERC Advanced Grant “EXOTIC” that began in November. It focuses on precision calculations in nuclear and hypernuclear physics on the lattice as well as exploring fine-tunings in nuclear reactions and the role of anthropic considerations. Some of the high-lights of all of these activities are discussed in the following.

Wigner SU(4) symmetry, clustering and the spectrum of ^{12}C

Using Nuclear Lattice Effective Field Theory (NLEFT), we had shown earlier that the ground state properties of many light and medium-mass nuclei as well as neutron matter could be well-described by microscopic A -body lattice calculations using a spin- and isospin-independent interaction plus the Coulomb interaction. These spin- and isospin-independent interactions obey Wigner’s SU(4) symmetry. The very simple interactions have only four parameters: the strength of the two-nucleon (NN) interaction, the range of the two-nucleon interaction, the range of the local part of the two-nucleon interaction, and the strength of the three-nucleon interaction. The strength and range of the SU(4)-symmetric local interaction are known to play an important role in the effective interactions between two α clusters and the binding of nuclei with more than four nucleons. An interesting unresolved question is whether or not such simple SU(4)-symmetric interactions can reproduce more than just the average ground state properties of atomic nuclei. It is clear that nuclei with large spin-orbit splittings among nuclear subshells will not be properly described if the nucleonic interactions are independent of spin. However, if we are considering a nuclear system where α clustering is important, then the impact of the spin-orbit interactions might be significantly reduced. But this also raises the possi-

bility that some of the nuclear states are well described while others are not. Therefore, the success or failure of these simple spin-independent interactions in describing the spectrum of a given nucleus provides a useful probe for illuminating the underlying physics. Further, it is known from *ab initio* shell model calculations that the spin-orbit splittings are not strong for ^{12}C . We have therefore focused on the nucleus with perhaps the most interesting and astrophysically important spectrum, ^{12}C . In the case of ^{12}C , there is much evidence of competition between the arrangement of nucleons into shell model orbitals and the grouping of nucleons into α clusters.

Consequently, we have explored the low-lying spectrum of ^{12}C using a simple SU(4)-symmetric interaction with local and non-local terms. By fitting the strength of the interaction and the local smearing parameter to the ground state energies of ^4He and ^{12}C , we have obtained a good representation of the spectrum up to excitation energies of about 15 MeV, see Fig. 32, for the states with definite angular momentum and parity. This was achieved using initial states composed of three α clusters, as well as of shell model orbitals. In particular, we were able to confirm earlier NLEFT results concerning the structure of the Hoyle state and the second 2^+ state. For the Hoyle state, prolate α cluster configurations are very important, and the second 2^+ state is consistent with the interpretation as a rotational excitation of the Hoyle state. Our results provide confirmation that ^{12}C sits at a fascinating balance point where the competition between the shell structure and clustering produces a low-energy spectrum with qualitatively different types of nuclear states. The success of these simple interactions in describing all of the low-lying states of ^{12}C suggests that the tendency towards α clustering is probably not a simple binary attribute that effects some states of ^{12}C and not others. It is clear that the effects of α clustering are very prominent for the Hoyle state and the second 2^+ state, to the extent that their overlap with shell model initial states are so small that they cannot be detected in the lattice Monte Carlo calculations. However, it also appears that spin-orbit interactions are not playing a decisive role for the other ^{12}C states with good overlap with shell model initial states. This implies that either spin-orbit interactions are somewhat weak in the ^{12}C system, or the effects of α clustering are diminishing their influence. It will be very interesting to perform similar studies for ^{16}O and ^{20}Ne to see whether an SU(4)-symmetric interaction can fully describe the low-energy spectra of these nuclei.

Constraints on the Λ -neutron interaction from charge symmetry breaking in the $^4_{\Lambda}\text{He}$ - $^4_{\Lambda}\text{H}$ hypernuclei

The large charge symmetry breaking (CSB) manifested in the differences of the Λ -separation energies of the mirror nuclei $^4_{\Lambda}\text{He}$ and $^4_{\Lambda}\text{H}$ is one of the mysteries of hypernuclear physics. Already experimentally established in the early 1960s, for the ground (0^+) state there is

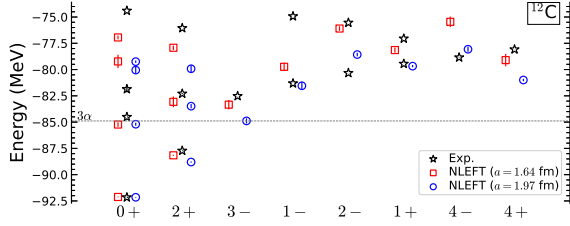


Figure 32: Spectrum of ^{12}C below ~ 15 MeV excitation energy obtained by NLEFT using an SU(4) symmetric NN interaction (for two different lattice spacings) in comparison with experiment (black stars).

still no plausible and generally accepted explanation of it despite of numerous investigations. Indeed, the current separation-energy difference $\Delta E(0^+)$ of 233 ± 92 keV is about one third of the corresponding difference in the mirror nuclei ^3H and ^3He which amounts to 764 keV. However, while in the latter case about 90% of the difference is due to the Coulomb force, its effects are rather small for the $A = 4$ hypernuclei and, moreover, they go into the wrong direction. Thus, most of the CSB seen in the $A = 4$ hypernuclei must come from the strong interaction. The measured separation-energy difference for the excited (1^+) state is $\Delta E(1^+) = -83 \pm 94$ keV.

We performed a study of CSB in the ΛN interaction within chiral effective field theory (EFT). In this approach the long-range part of the interaction (due to exchange of pseudoscalar mesons) is fixed by chiral symmetry. The short-distance part is not resolved and effectively described by contact terms whose strengths, encoded in low-energy constants (LECs), need to be determined by a fit to data. This notion applies to the charge-symmetry conserving as well as to the charge-symmetry breaking part of the interaction. Specifically, for the considered ΛN interaction derived within chiral EFT up to next-to-leading order (NLO) in the power counting, a CSB contact term arises in each of the two S -wave states (1S_0 , 3S_1). The pertinent LECs can be fixed from the $A = 4$ separation energies and then predictions of CSB effects for the elementary Λp and Λn amplitude are possible.

Results for the level splitting are presented in Fig. 33 for two variants of our NLO YN interaction, NLO13 and NLO19. The dependence of the results on the inherent regulator are displayed and the numerical error of the few-body calculations are indicated. One can see that these variations are much smaller than the present experimental uncertainties.

With respect to the ΛN interaction it turned out that the reproduction of the present splittings requires a sizable difference between the strength of the Λp and Λn interactions in the 1S_0 state, whereas the modifications in the 3S_1 partial wave are much smaller. The effects go also in opposite directions, i.e. while for 1S_0 the Λp interaction is found to be noticeably less attractive than Λn , in case of 3S_1 it is slightly more attractive. In terms of the pertinent scattering lengths we predict for $\Delta a^{CSB} = a_{\Lambda p} - a_{\Lambda n}$

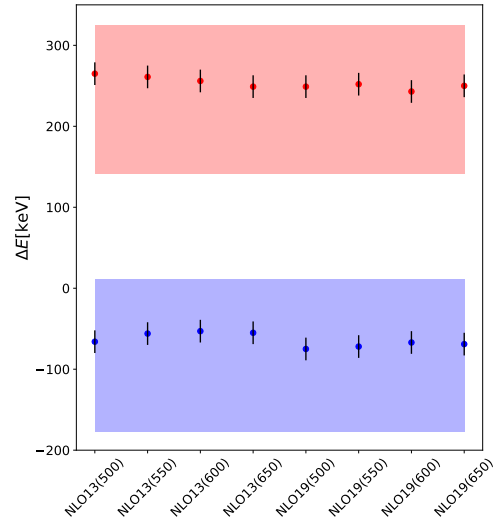


Figure 33: CSB of $^4_{\Lambda}\text{He}/^4_{\Lambda}\text{H}$ in the 0^+ (top, red circles) and 1^+ (bottom, blue circles) state compared to the currently best experimental values (red and blue bands). The error bars reflect the numerical uncertainty.

a value of 0.62 ± 0.08 fm for the 1S_0 partial wave and -0.10 ± 0.02 fm for 3S_1 . Accordingly, the required CSB implies a significantly stronger Λn interaction in the 1S_0 partial wave where the pertinent scattering length of our NLO potentials increases from -2.9 fm to values around $a_s^{\Lambda n} = -3.2$ fm.

Constraining the $\Sigma^+ p$ interaction by measurements of the correlation function

The interactions of hyperons ($Y = \Lambda, \Sigma, \Xi$) with nucleons have been studied for many decades. However, so far only the bulk properties are experimentally established, and first of all those for the ΛN system. More detailed information, specifically about the spin dependence of the YN forces, is completely lacking. The latter is a consequence of the short-lived character of the hyperons so that no proper beams can be prepared in order to perform standard scattering experiments.

Recently, we have pointed out that a separation of the spin states is feasible from measurements of the two-particle momentum correlation function - in combination with cross section data - without any spin-dependent experiment. Such correlation functions can be determined in heavy-ion collisions but also in high-energy proton-proton collisions. The separation is possible in specific cases, namely when the interaction in one of the spin states is attractive while that in the other one is repulsive. In such a situation the contributions of the spin states to the correlation function will partially cancel, because they depend on the sign of the scattering amplitude, whereas they always add up in case of the reaction cross section. This qualitatively different interplay allows one

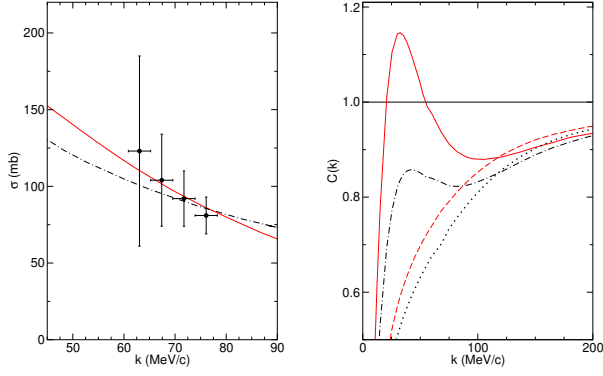


Figure 34: Total cross section (left) and correlation function (right) for the $\Sigma^+ p$ system as a function of the center-of-mass momentum k . Predicted by NLO19 (solid line) and NLO-var (dash-dotted line) are shown. Right: Contributions from the 3S_1 alone are indicated by the dashed (NLO19) and dotted (NLO-var) curves. The used source radius is $R = 1.2$ fm.

to disentangle the spin contributions, provided one has data on the correlation function and on the elastic cross section.

We exemplify this idea for the $\Sigma^+ p$ system, where cross section data at low energies have been available for a long time. At low energies the observables are dominated by the (spin singlet) 1S_0 and (spin triplet) 3S_1 partial waves. There is unambiguous evidence that the interaction in the 3S_1 partial wave is repulsive, say from the analysis of level shifts and widths of Σ^- atoms, but also from lattice simulations. On the other hand, the 1S_0 state is attractive, which is likewise suggested by lattice calculations but also expected from the approximate validity of SU(3) flavor symmetry.

Results are presented in Fig. 34 for our standard YN interaction, derived in chiral effective field theory up to next-to-leading order (NLO19), which predicts 1S_0 (s) and 3S_1 (t) scattering lengths of $a_s = -3.62$ fm, $a_t = 0.49$ fm, and based on a variant (NLO-var) with a somewhat weaker (stronger) 1S_0 (3S_1) interaction: $a_s = -2.39$ fm, $a_t = 0.80$ fm. One can see that there is some change in the reaction cross section. However, the variation in the correlation function $C(k)$, calculated here for a source radius of $R = 1.2$ fm characteristic for measurements in high-energetic proton-proton collisions, is much more drastic. Specifically, for momenta in the range of, say, 25 to 75 MeV/c, there is a pronounced difference for the two scenarios considered. Thus, pertinent measurements should allow one to discriminate between the interactions and, thus, facilitate the determination of the singlet- and the triplet S -wave amplitudes in combination with the measured $\Sigma^+ p$ cross section.

Light $S = -2$ hypernuclei

The baryon-baryon interaction in the strangeness $S = -2$ sector is not well known because of the scarcity of direct scattering data. It therefore remains to a large extent unknown how strongly hyperons contribute to the properties of neutron matter. Such a contribution is possibly sizable and could lead to inconsistencies for the predictions for neutron matter and astrophysical observations. Several experimental facilities, e.g. FAIR, J-PARC and J-Lab, are setting up or extending their experimental program to study interactions of hyperons for this reason.

In view of the difficulties to perform direct scattering experiments, bound states of Λ and Ξ hyperons with nucleons are coming into the focus of these experiments. In order to use such data to constrain hyperon-hyperon (YY) and Ξ -nucleon (ΞN) interactions, we have recently extended the Jacobi no-core shell model (J-NCSM) to $S = -2$ hypernuclei and reported first results for ${}^4_{\Lambda\Lambda}\text{H}$, ${}^5_{\Lambda\Lambda}\text{He}$, and ${}^6_{\Lambda\Lambda}\text{He}$. In a second paper, we have then investigated several baryon number $A = 4$ Ξ hypernuclei, ${}^5_{\Xi}\text{H}$, and ${}^7_{\Xi}\text{H}$.

To obtain converged results within the J-NCSM, the nucleon-nucleon (NN), hyperon-nucleon (YN), YY and ΞN interactions are evolved via similarity renormalization group (SRG). The dependence on the SRG evolution of NN and YN is significant. Based on our previous results, we use the evolution parameters that give the best description of strangeness $S = -1$ hypernuclei. With this additional information used, there is almost no SRG dependence for $\Lambda\Lambda$ - and only a moderate one for Ξ hypernuclei. For the interactions defined in this manner, it is possible to obtain energies with higher accuracy. This is exemplified in Fig. 35 for ${}^5_{\Lambda\Lambda}\text{He}$.

Our first studies are based on realistic chiral baryon-baryon interactions that fulfill all constraints from YN, YY and ΞN data. Reassuringly, these interactions are also consistent with the known binding energy of ${}^6_{\Lambda\Lambda}\text{He}$. Our calculations show that a bound state of ${}^5_{\Lambda\Lambda}\text{He}$ is likely to exist whereas ${}^4_{\Lambda\Lambda}\text{H}$ is probably not bound. These results clearly motivate further experimental searches for ${}^5_{\Lambda\Lambda}\text{He}$ or its isospin partner ${}^5_{\Lambda\Lambda}\text{H}$ since the calculations also indicate that a stronger contribution of the $\Lambda\Lambda$ to ΞN transition than in ${}^6_{\Lambda\Lambda}\text{He}$ can be expected here. The $A = 5$ data will therefore provide additional information on the $\Lambda\Lambda$ interaction.

Recent observations of bound Ξ hypernuclei motivated an extension of this study to $A = 4$ to 7 Ξ hypernuclei. They generally decay via the strong interaction to unbound systems involving $\Lambda\Lambda$ making numerical calculations difficult. Fortunately, several other studies and also predictions based on our chiral ΞN interactions indicate a suppression of this decay channel. Therefore, we devised interactions where ΞN to $\Lambda\Lambda$ transitions are omitted. For such interactions, Ξ -hypernuclei bound state calculations can be performed and the decay width perturbatively estimated. Our results indicate that several $A = 4, 5$ and 7 bound states with different spin/isospin quantum numbers could exist and would be sufficiently stable for

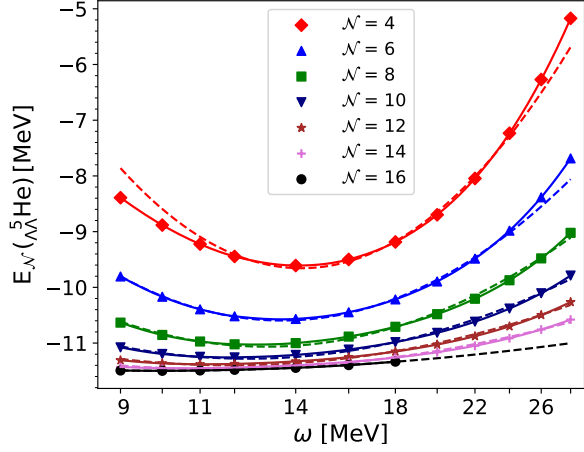


Figure 35: Binding energy of ${}^5_{\Lambda\Lambda}\text{He}$ depending on the harmonic oscillator model space size and frequency.

experimental detection. Our results show that the various ΞN channels give very different contributions to binding so that Ξ hypernuclei should provide valuable information on the spin/isospin dependence of ΞN interactions. Based on upcoming new data and the J-NCSM, we are now well prepared for the development of improved $\Lambda\Lambda$ and ΞN interactions that will be a reliable starting point for a microscopical understanding of the hyperon contribution to neutron matter.

Pion electroproduction off the proton

In the few GeV range of the strong interactions, quark confinement manifests itself in a rich spectrum of resonances. A link between large-scale experimental programs and theory approaches like Lattice QCD, unitarized Chiral Perturbation Theory, or quark models is provided by partial-wave analyses. Our knowledge of the baryon spectrum has rapidly evolved over the last decade, due largely to the refinement of dynamical and phenomenological coupled-channel approaches for the partial-wave analysis of pseudoscalar-meson photoproduction reactions.

The so-called Jülich-Bonn dynamical coupled-channel model describes several pion- and photon-induced reactions. While the description of the hadronic reactions is realized in a field-theoretical framework, the photon-induced reactions are described in a semi-phenomenological approach in order to enable the numerical analysis of the large photoproduction data base ($\sim 10^5$ data points). The hadronic amplitude enters the photoproduction process as final-state interaction.

In a recent work, we extended this semi-phenomenological approach to the “Jülich-Bonn-Washington” model for electroproduction processes, where the hadronic reaction is not induced by a real but a virtual photon. The Q^2 variation of resonance couplings is expected to provide a connection between perturbative

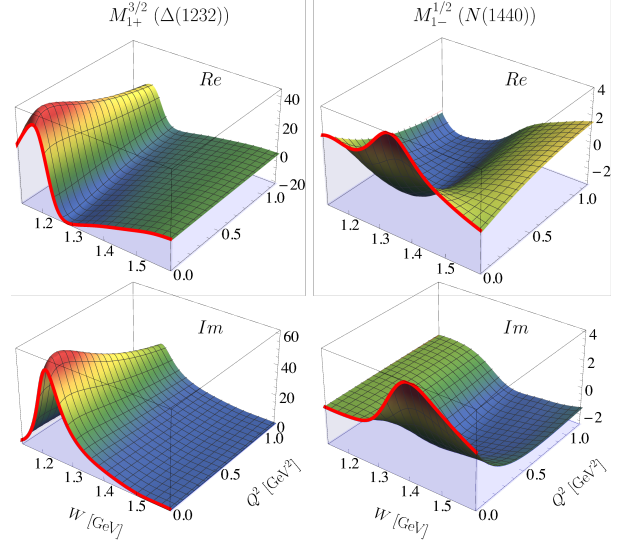


Figure 36: Selected electroproduction results for multi-poles associated with $\Delta(1232)$ (left) and $N(1440)$ (right). All in units of mfm .

QCD and the region where quark confinement sets in. A large amount of high-quality data is already available and awaits a theoretical analysis. In total, almost 80,000 data were analyzed in the present study, including many polarization observables. We performed six different fits to assess systematic uncertainties, some of them up to $Q^2 = 8 \text{ GeV}^2$. In Fig. 36 selected results for one of those fits for the $M_{1+}^{3/2}$ and $M_{1-}^{1/2}$ multipoles are shown, which contain the $\Delta(1232)$ and $N(1440)$ resonances, respectively. At $Q^2 = 0 \text{ GeV}^2$ the solution is constrained by pion-induced and photoproduction data via the Jülich-Bonn model (red lines in Fig. 36). The $\Delta(1232)$ shows a canonical resonance behavior with the resonance shape disappearing at higher Q^2 . In contrast, the “profile” of the enigmatic Roper resonance, $N(1440)$, shows a non-trivial Q^2 behavior, including zero-crossings for the real and the imaginary part.

This work represents a major step towards the first-ever simultaneous analysis of pion-, photon-, and electron-induced reactions with different hadronic final states. Another milestone was achieved very recently with the extension of the Jülich-Bonn-Washington model to eta electroproduction, representing the first joint analysis of pion and eta electroproduction data.

Where is the lightest charmed scalar meson?

The Particle Data Group quotes for the lightest charmed scalar meson without strangeness, $D_0^*(2300)$, a mass of $2342 \pm 10 \text{ MeV}$ and a width of $229 \pm 16 \text{ MeV}$ extracted in Breit-Wigner (BW) fits to production data. In particular the mass value is problematic, as it is located even above the mass of the lightest charmed scalar with strangeness, $D_{s0}^*(2317)$, with a mass of $2317.8 \pm 0.5 \text{ MeV}$, although the addition of a strange quark usually adds in an additional 100-200 MeV.

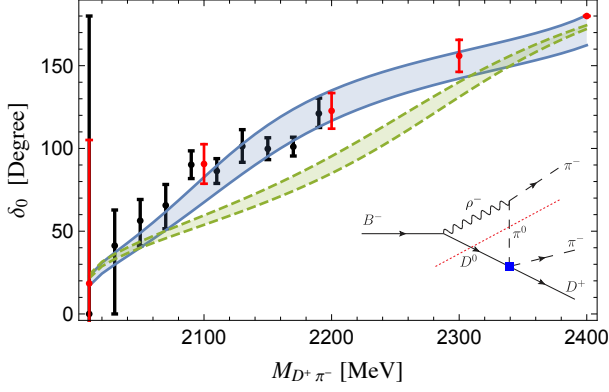


Figure 37: Comparison of the predictions from UChPT (blue) and a BW parametrization (green) for the S -wave phase of the πD production amplitude, δ_0 , with the phases extracted by the LHCb collaboration (red) and our analysis (black) from data on $B^- \rightarrow \pi^- \pi^- D^+$. The inlay shows the evaluated diagram.

The $D_s(2317)$ is an excellent candidate for a DK molecular state. Its properties may be derived using unitarized chiral perturbation theory (UChPT) with parameters fixed from a fit to a few lattice data. The same calculation also predicts, in line with expectations, that the lightest non-strange open charm scalar meson is located at 2105^{+6}_{-8} MeV with a width of 200 MeV. Moreover, also recent lattice data support that the lightest D_0^* is located below 2200 MeV. What is needed is an experimental confirmation of those theoretical findings.

Since πD scattering cannot be realised experimentally, the necessary information needs to be extracted from production experiments. Recently the LHCb collaboration published high quality data on $B^- \rightarrow \pi^- \pi^- D^+$. In particular at a few energies even the phase of the πD S -wave amplitude was extracted from the data (red points in Fig. 37). In our work we first of all demonstrated that from the published moments one can extract the phase at more energies under the well justified assumption that D -waves are negligible and that the P -wave is fully controlled by the D^* resonance. The resulting phases are shown as the black dots in the figure.

It should be stressed that the decay dynamics of the B decay under study strongly favors the transition $B^- \rightarrow \rho^- D^0$ compared to the direct transition to the decay channel. As a result, although in the energy range relevant for this study the πD system by itself is still elastic, the phase of the production amplitude is not equal to that of the scattering amplitude, since additional imaginary parts enter through rescattering as shown as an inlay in the figure. Fortunately this observation does not spoil the mentioned goal, since the diagram can be calculated reliably for both the UChPT and the BW description of the πD system. The results of those calculations are shown as the blue and the green band in Fig. 37, respectively. Clearly the result based on the BW ansatz is at odds with the data. The same UChPT study also shows how it was possible that for so long the D_0^* was believed to be significantly

heavier: The πD spectrum is in fact shaped by two poles. In addition to the one just discussed there is a heavier one located at 2451^{+35}_{-26} MeV. The emergence of two relatively light poles typically in different SU(3) multiplets is a feature common to the scattering of the Goldstone-boson octet off heavy sources. The work presented here provides therefore strong support not only for the low mass of the lightest scalar open charm meson but also for the relevance of the chiral symmetry for the emergence of the hadron spectrum in the scalar sector.

Remarks on the Effective Range Expansion

Weinberg related the parameters of the effective range expansion (ERE) to Z , the probability to find the compact component of a given hadron inside a bound state wave function

$$a = -2 \left(\frac{1-Z}{2-Z} \right) \frac{1}{\gamma}, \quad r = - \left(\frac{Z}{1-Z} \right) \frac{1}{\gamma},$$

where $\gamma = \sqrt{2\mu|E_b|}$ (with $E_b < 0$ for the binding energy) is the binding momentum. The corrections to these expressions may be estimated as $1/\beta$, where β denotes the next momentum scale that is not treated explicitly in the ERE; it is commonly estimated as the mass of the lightest exchange particle. However, it may also be the momentum scale due to the presence of the next closed channel. Clearly, model-independent statements are possible only if $\gamma \ll \beta$. Then one observes that $a \rightarrow -1/\gamma$, $r \rightarrow N_r/\beta$ for a predominantly molecular state ($Z \rightarrow 0$) and $a \rightarrow -N_a/\beta$, $r \rightarrow -\infty$ for a predominantly compact state ($Z \rightarrow 1$), where N_a is expected to be a positive number of the order of 1. In case of a single-channel potential scattering with a finite interaction range and negative potential in the whole space also N_r should be positive and of the order of 1. However, this conclusion does not hold when coupled channels are included.

To extract the ERE parameters from production data for the $\chi_{c1}(3872)$, also known as $X(3872)$, an amplitude inverse proportional to

$$D(E) = E - E_f + \frac{i}{2} (g_1^2 k_1 + g_2^2 k_2 + \Gamma(E))$$

was used. Moreover, $g_1 = g_2 = g$ was chosen to acknowledge that the $\chi_{c1}(3872)$ is an isoscalar state. Here channel 1 (2) denotes the $D^0 \bar{D}^{*0}$ ($D^+ \bar{D}^{*-}$) channel with their on-shell momenta $k_a = \sqrt{2\mu_a(E - \delta_a) + i\epsilon}$. We measure the energy with respect to the neutral channel and thus use $\delta_1 = 0$ and $\delta_2 = M_{D^*} - M_D$. Since the isospin breaking in the masses is small we may choose $\mu_1 = \mu_2$. The term $\Gamma(E)$ is meant to absorb all inelasticities.

When this ansatz was used to analyse the recent LHCb data on $B \rightarrow K \chi_{c1}(3872) \rightarrow K J/\psi \pi \pi$ the parameters g and E_f showed a very strong correlation, see Fig. 38. Not only is a clear linear dependence of g^2 on E_f visible, but also remains the log likelihood, ΔLL , nearly unchanged, when E_f is getting increasingly negative, once it is smaller than -6 MeV (ΔLL reaches 1 for $E_f =$

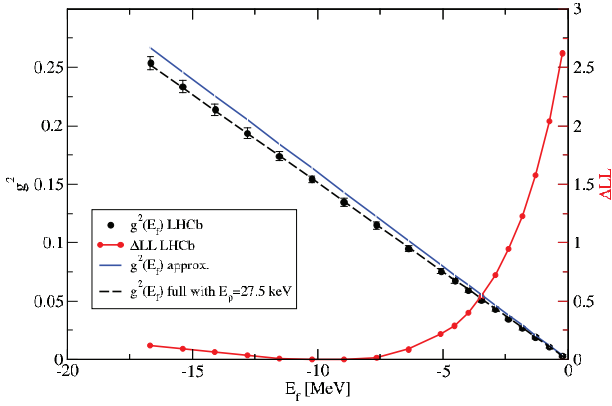


Figure 38: Coupling (black dots with errors) to the elastic $D\bar{D}^*$ channels (g^2) and change in the negative log-likelihood function relative to its minimum (red dots) as function of the Flatté energy E_f . The black dashed line shows the approximate result for $g(E_f)^2$ while for the dashed line the value of E_p was fitted.

-270 MeV, where $g^2 \approx 4$). To allow for a converging fit regardless of the correlation, in the LHCb analysis the value of E_f was fixed to -7.18 MeV which revealed $g^2 = 0.108 \pm 0.003$. With those parameters one finds for the effective range

$$-r = 2/(\mu_1 g^2) + 1/\sqrt{2\mu\delta} \simeq (3.8 + 1.4) \text{ fm} \gg 1/M_\pi.$$

This large (with respect to the range of forces) and negative value was interpreted by some authors as a clear indication for a compact tetraquark structure of the $\chi_{c1}(3872)$. However, we stressed in a follow up publication that the second term should not be included to compare the effective range to that of the Weinberg analysis, since it comes from the charged channel and is thus a part of the isoscalar $\chi_{c1}(3872)$ — in other words, one should take the isospin limit first, which removes the second term, and only then extract the effective range.

Moreover, the parameters extracted from the data should be handled with care because of the mentioned correlation. In fact, what the data are sensitive to is E_p , the real part of the pole location:

$$E_p = E_f + \frac{g^2}{2} \left(\sqrt{2\mu_1 |E_p|} + \sqrt{2\mu_2 (\delta + |E_p|)} \right)$$

which one may rewrite to find an expression for $g^2(E_f)$. The LHCb data are described excellently by the resulting expression when $E_p = -27.5$ keV is used. This is shown as the dashed line in Fig. 38. Moreover, neglecting the small value of E_p vs. δ one gets the parameter free prediction $g^2 = -E_f/\sqrt{\mu\delta}$, which clearly captures the bulk of the correlation as shown by the solid line. Thus one has to conclude that the LHCb data only provided a lower bound for the coupling g^2 and accordingly the data are still consistent with a purely molecular nature of $\chi_{c1}(3872)$. An improved analysis of the LHCb data employing the insights presented here is currently under way.

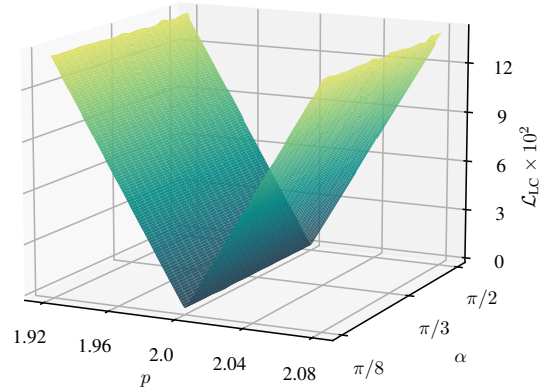


Figure 39: LCLoss for $1/r^p$ potentials over the exponent p and hyperangle α . The lowest losses are aligned at $p = 2$ and take values between $\mathcal{L}_{LC} = 2.332 \times 10^{-4}$ and $\mathcal{L}_{LC} = 9.389 \times 10^{-4}$, suggesting the $1/r^2$ potential to be the desired limit-cycle potential.

Three-body renormalization group limit cycles based on unsupervised feature learning

The interest in renormalization group (RG) limit cycles has steadily increased ever since Wilson has pointed out in 1971 that coupling constants provided by RG equations for field theories of strong interactions do not necessarily flow towards a fixed point. Instead, RG equations may also allow coupling constants to approach periodical trajectories in parameter space, the so-called limit cycle. Both the three-body system and the inverse square potential carry a special significance in the study of renormalization group limit cycles. In a recent work, we have pursued an exploratory approach and address the question which two-body interactions lead to limit cycles in the three-body system at low energies, without imposing any restrictions upon the scattering length, based entirely on machine learning techniques. For this, we train a boosted ensemble of variational autoencoders, that not only provide a severe dimensionality reduction, but also allow to generate further synthetic potentials, which is an important prerequisite in order to efficiently search for limit cycles in low-dimensional latent space. We do so by applying an elitist genetic algorithm to a population of synthetic potentials that minimizes a specially defined limit-cycle-loss (LCLoss). This LCLoss measure the deviation of the coupling constant corresponding to a specific generated potential from the required log-periodic behaviour, thus the LCLoss vanishes if a given potential leads to a true limit cycle. The resulting fittest individuals suggest that the inverse square potential is the only two-body potential that minimizes this limit cycle loss independent of the hyperangle, see Fig. 39. We remark that in the context of RG limit cycles, the inverse square potential has been covered extensively in the literature. Hence, at first sight it is not surprising that the result of our search is at least to some degree related to the inverse square potential. Nevertheless, in contrast to studies of the $1/r^2$ poten-

tials in the two-body sector, we do not consider solutions of the Schrödinger equation, but the low-energy Faddeev equation, instead. Since these two equations of motion are not equivalent, it is all the more remarkable that there turns out to be one unique limit-cycle potential that, in addition, is exactly the inverse square potential. For further investigations it would be of great interest to determine the extent to which our results can be generalized to more complex few-body systems. At this, special attention needs to be paid to whether the found limit-cycle potential again corresponds to the two-body inverse square potential and if the found solution is unique. If for whatever reason several limit-cycle potentials should arise for some few-body system, it would be promising to compare the corresponding bound state spectra and RG flows with each other.

The critical exponents of the Hubbard quantum phase transition on the honeycomb lattice

We have, for the first time, performed a unified, comprehensive treatment of all operators that contribute to the anti-ferromagnetic (AFM), ferromagnetic (FM), and charge-density-wave (CDW) order parameters of the honeycomb Hubbard model. Such an analysis provides a complete picture of the Hubbard phase transition on the honeycomb lattice, including not only its critical coupling (which we recently determined), but also its critical exponents. The latter elucidates which universality class this transition falls under, and potentially provides insights into the nature of systems such as graphene and its many carbon allotropes, including nanotubes, nanoribbons, and fullerenes.

In spite of a long history of theoretical studies of the Hubbard model, surprisingly little is known with certainty of its properties in low-dimensional settings. In particular, a fully-controlled *ab initio* characterization of the semi-metal (SM) to AFM insulating transition was lacking prior to our work. Monte Carlo calculations can address this issue, and we have taken advantage of recent improvements in our grand canonical Hybrid Monte Carlo (HMC) algorithm to perform a precision study of various observables in the honeycomb Hubbard model. In particular, we performed a controlled analysis of the Trotter error, the thermodynamic limit, and finite-size scaling with inverse temperature (which is almost always neglected in the condensed matter community) of all relevant observables.

Building off our recent work in determining the critical coupling $U_c = 3.835(14)$ of the hexagonal Hubbard model that signifies the formation of a Mott insulating gap from a semi-metal state, this past year we performed a systematically controlled treatment of the AFM, FM, and CDW order parameters. We found for the critical exponents $\nu = 1.181(43)$ and $\beta = 0.898(37)$. This represents the first *ab initio* determination of these parameters without resorting to any mean-field approximations.

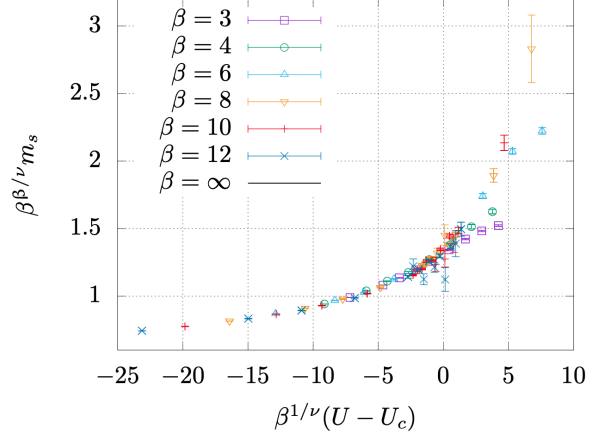


Figure 40: Data collapse plot with the optimal parameters of U_c , ν , and β obtained from a collapse fit to the magnetisation m_s and other order parameters (not shown). The optimal parameters are $\nu = 1.181(43)$, $\beta = 0.898(37)$, and $U_c = 3.835(14)$.

These parameters are consistent with those of the SU(2) Gross-Neveu, or chiral Heisenberg, universality class.

In Fig. 40 we show an example of our MC results for the magnetization m_s scaled by inverse temperature β , critical exponents β and ν , and critical coupling U_c . For appropriately determined parameters ν , β , and U_c , the data obtained for different inverse temperatures “collapse” to a single curve. Similar finite scaling analyses were performed for other order parameters. It was found that the m_s order parameter only vanishes below the critical coupling U_c , whereas FM and CDW order parameters vanished in the thermodynamic limit for all values of the coupling U . This confirms the AFM nature of the Hubbard transition from first principles. Also, we found that the quantum phase transition associated with the SM-AFMI transition coincides with the opening of the single-particle gap Δ , which disfavors the possibility of other exotic phenomena, such as an intermediate spin-liquid phase, as has been proposed by some research groups.

This work resulted from a strong collaborative effort between scientists at IAS-4/IKP-3 and JSC, and used JARA HPC allocations (cjjs37). The favorable computational scaling of our HMC algorithm, developed by scientists at both institutes, enables future extensions of our work to carbon nanotubes, fullerenes, and topological insulators, which we are actively pursuing.

Quantum mechanics of coherent beam oscillations in storage rings

One of grand challenges in particle physics is the search for physics beyond the Standard Model (SM) as we know it. Although there is violation of CP symmetry (with C charge conjugation and P parity) in the flavor-changing, weak-interaction sector of the SM, this symmetry breaking is far too small to allow for the matter-

antimatter asymmetry observed in our Universe at the freeze-out point of radiation or via the bounds of big-bang nucleosynthesis. Moreover, the SM prediction for the permanent electric dipole moment (EDM) of any subatomic particle is at least five orders of magnitude smaller than the existing direct and indirect experimental bounds. Thus there is a window of opportunity: an experimental observation of such an EDM would signal the explicit violation of parity and time reflection (T) symmetries and, according to the CPT theorem, a flavor-conserving CP violation much stronger than the established mechanism of the SM, either resulting from physics beyond the SM or from a – so far not observed – CP violation in the strong-interaction sector of the SM.

While *direct* empirical bounds on the EDMs of charge-neutral particles have been established using traps or atom beams, this is not the case for electrically charged hadrons, such as the proton. Thus, other techniques are required. An interesting but challenging proposal for such an EDM measurement is to search for the buildup of the vertical polarization of horizontally spin-frozen protons stored in an all-electric storage ring. In addition to trapping the protons and to providing a precession mechanism for the proton spins, proportionally to their EDMs, by the bending electric fields, the all-electric rings allow for beams rotating *simultaneously* in *opposite* direction. This would significantly reduce systematic effects, as a sensitivity of $d_p \sim 10^{-29} \text{ e cm}$ is envisaged which is some 15 orders of magnitude smaller than the magnetic dipole moment (MDM) of the proton. One of the crucial tasks is to control the difference of the vertical position of the centers of the two counter-rotating beams to 5 pm precision – along the circumference of the ring – in order to have a handle on the strength of radial magnetic fields acting on the MDM of the proton. The question might arise whether this accuracy would be in contradiction with the Heisenberg uncertainty limit.

The subject of the reported work is the transition from the description of classical mechanics suitable for micrometer amplitudes in this year's COSY experiment on radiofrequency-driven coherent beam oscillations to an obviously deep quantum regime of picometer amplitudes in the proposed ultimate proton EDM experiment. Our main conclusion is that one and the same formula covers the whole range of amplitudes of coherent beam oscillations from large classical ones to well below the one-particle quantum limit. Moreover, neither scattering from the residual gas inside the storage ring nor intrabeam scattering contribute to these *coherent* beam oscillations. Finally, a would-be-EDM signal due to earth's gravity acting on each beam and estimated to be of comparable magnitude, can be separated from an actual signal by invoking the counter-rotation of both beams.

In summary, considerations of the Heisenberg quantum uncertainty do not preclude sub-picometer accuracy in the determination of the coherent beam oscillation amplitude – the challenge lies in improving the sensitivity of the beam position monitors.

A Beam Time at COSY in 2021

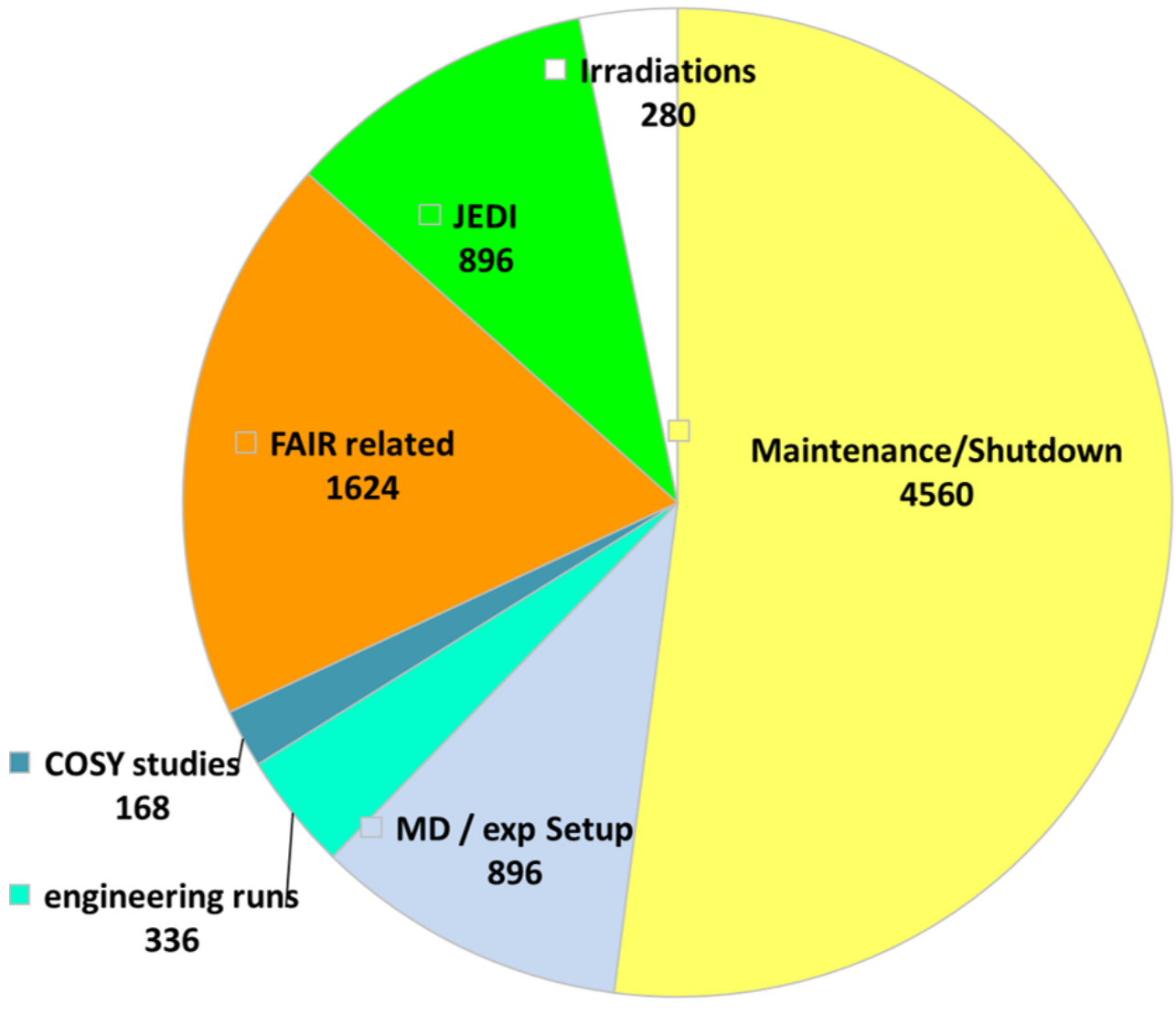


Figure 41: COSY beam-time statistics in 2021.

The distribution of user weeks and maintenance/shutdown periods is listed in Table 1.

Table 1: Overview COSY user beam time and EDM/FAIR weeks in 2021.

Date	Experiment	Duration	Reaction, experiment #
1.01.21.–24.01.21	Maintenance	3 weeks	
25.01.–31.01.	COSY	1 week	engineering run
01.02.–07.02.	COSY	1 week	Orbit feedback Exp. A014.3
08.02.–07.03.	MD/Maintenance	4 weeks	
08.03.–11.04.	EDM (JEDI)	5 weeks	JEDI Wien Filter Exp. E005.7
12.04.–18.04.	MD	1 week	
19.04.–25.04.	COSY	1 week	electron cooling, Exp. A002.7
26.04.–02.05.	FAIR (Clust.)	1 week	FAIR Cluster Jet Target, Exp. D009.5
10.05.–16.05.	COSY	3 days	Stable Quadrupole, Exp. A020
17.05.–23.05.	FAIR (Lumi)	1 week	FAIR Luminosity, Exp. D011.2
24.05.–30.05.	COSY	1 week	Irradiation studies, A019
31.05.–06.06.	MD	1 week	
07.06.–13.06.	FAIR (KOALA)	1 week	FAIR KOALA, Exp. D005.4
14.06.–04.07.	Maintenance	3 weeks	
05.07.–03.10.	shutdown	13 weeks	finance driven shutdown
04.10.–10.10.	MD	1 week	
11.10.–17.10.	COSY	1 week	engineering run
18.10.–24.10.	COSY	1 week	Palmer Pickup Exp. A018.1
25.10.–30.10.	COSY-MD	1 week	Fraunhofer Ges., Irradiation studies
01.11.–07.11.	FAIR (CBM)	1 week	CBM Hades COSY Exp. D004.10
08.11.–14.11.	MD	1 week	Rad.Prot.Exam.
15.11.–21.11.	COSY	1 week	R3B/SFRS GSI, Exp. D015
22.11.–28.11.	FAIR (Lumi)	1 week	FAIR Luminosity, Exp. D011.4
29.11.–31.12.	shutdown	5 weeks	finance driven shutdown
user weeks 2021		17 weeks	
maintenance		6 weeks	
finance driven shutdown		18 weeks	

B Committees

B.1 CBAC – COSY Beam Time Advisory Committee

Prof. K. Aulenbacher	Universität Mainz, Germany
Prof. O. Kester	TRIUMF, Canada
Prof. C.J. Schmidt	GSI Darmstadt, Germany
Prof. T. Stöhlker	HI-Jena, Jena, Germany
Prof. M. Weber (chair)	KIT, Karlsruhe, Germany

B.2 Committee Service

O. Felden	- WTR (Scientific and Technical Council), FZ-Jülich GmbH, Germany
F. Goldenbaum	- Chair of the PANDA at FAIR collaboration board
	- WTR (Scientific and Technical Council), FZ-Jülich GmbH, Germany
	- Scientific Secretary of COSY Beam Advisory Committee (CBAC), FZ-Jülich GmbH, Germany
J. Haidenbauer	- Theory advisory Group PANDA
C. Hanhart	- Theory advisory Group PANDA
	- Particle Data Group
	- Task coordinator (Precision calculations in non-perturbative QCD (I): Effective Field Theories, analyticity and dispersion relations) within STRONG2020
R. Gebel	- International Organising Committee of the International Conference on Cyclotrons and their Applications
V. Hejny	- WTR (Scientific and Technical Council), FZ-Jülich GmbH, Germany
A. Lehrach	- Institutional representative in the European Network for Novel Accelerators (EuroNNAc)
	- Coordination, support and enhancement of training activities for accelerators in Europe in the EU-Projekt ARIES (Accelerator Research and Innovation for European Science and Society)
	- Institutional representative for the FCC (Future Circular Collider), International Collaboration Board
	- Scientific Advisory Board (SAB) of the 12th International Particle Accelerator Conference (IPAC'21), May 24 - 28, 2021, virtual conference
	- Member of the JuDocs Council, FZ-Jülich GmbH, Germany
L. Ludhova	- Institutional Board of Borexino
	- Steering Committee of Borexino
	- Physics Coordinator of Borexino
	- Institutional Board of JUNO
	- Analysis Coordination Committee of JUNO
	- L2 manager of the OSIRIS calibration
	- Member of the International Advisory Committee of Physics In Collision (PIC) conferences

- U.-G. Meißner - Spokesperson DFG Review Board 309 "Particles, Nuclei and Fields"
- Gründungsmitglied der Kommission für Ethik in der Forschung am Forschungszentrum Jülich
- Scientific Advisory Committee of the Collaborative Research Center (SFB) 1245, "Nuclei: From fundamental interactions to structure and stars", TU Darmstadt
- German/DFG delegate of NuPECC
- Project coordinator, Regional Doctoral Program in Theoretical and Experimental Particle Physics (Bonn, Jülich, Siegen Tiflis, Yerevan), funded by Volkswagen Stiftung
- Spokesperson of the Collaborative Research Center SFB/TR-110 "Symmetries and the Emergence of Structure in QCD"
- Theory advisory Group PANDA
- Particle Data Group
- A. Nogga - WTR (Scientific and Technical Council), FZ-Jülich GmbH, Germany
- D. Prasuhn - International Advisory Committee of the COOL Conferences (Beam Cooling)
- J. Ritman - Scientific Coordinator of COSY
- Co-Chair of the MESON biannual conference series
- Chair of the Scientific Advisory Committee for FAIR-CZ
- Co-Spokesperson of KLF (K-Long Facility at Jefferson Lab)
- S. Schadmand - Jefferson Lab User Organization (JLUO) Board of Directors (until June 2020)
- Workshop Program Committee of the APS Topical Group on Hadronic Physics (GHP)
- R. Stassen - Member of the Machine Advisory Committee for NICA (Nuclotron-based Ion Collider Facility), Joint Institute for Nuclear Research (JINR), Dubna, Russia
- T. Stockmanns - Computing coordinator PANDA
- H. Ströher - IAB KIU (International Advisory Board Kutaisi International University, Georgia)
- ISPC (International Spin Physics Committee)
- NuPECC (Nuclear Physics European Collaboration Committee)
- PGSB (Palestinian-German Science Bridge) Advisory Committee

C Publications

C.1 Journal Articles

1. Y. Ünal and U. Meißner
Strong CP violation in spin-1/2 singly charmed baryons
J. High Energ. Phys. **2021** 115 (2021)
2. A. Abusleme *et al.*
Optimization of the JUNO liquid scintillator composition using a Daya Bay antineutrino detector
Nucl. Instr. Meth. Phys. Res. A **988** 164823 - (2021)
3. A. Abusleme *et al.*
Feasibility and physics potential of detecting 8 B solar neutrinos at JUNO
Chinese Phys. C **45** 023004 - (2021)
4. A. Abusleme *et al.*
Calibration strategy of the JUNO experiment
J. High Energ. Phys. **2021** 4 (2021)
5. A. Abusleme *et al.*
JUNO sensitivity to low energy atmospheric neutrino spectra
Eur. Phys. J. C **81** 887 (2021)
6. A. Abusleme *et al.*
Radioactivity control strategy for the JUNO detector
J. High Energ. Phys. **2021** 102 (2021)
7. A. Abusleme *et al.*
The design and sensitivity of JUNO's scintillator radiopurity pre-detector OSIRIS
Eur. Phys. J. C **81** 973 (2021)
8. J. Adamczewski-Musch *et al.*
Production and electromagnetic decay of hyperons: a feasibility study with HADES as a phase-0 experiment at FAIR
Eur. Phys. J. A **57** 138 (2021)
9. S. Adhikari *et al.*
The GlueX beamline and detector
Nucl. Instr. Meth. Phys. Res. A **987** 164807 - (2020)
10. S. Adhikari *et al.*
Measurement of beam asymmetry for $\pi - \Delta + +$ photoproduction on the proton at $E \gamma = 8.5$ GeV
Phys. Rev. C **103** L022201 (2021)
11. M. Agostini *et al.*
Search for low-energy neutrinos from astrophysical sources with Borexino
Astropart. Phys. **125** 102509 (2021)
12. M. Agostini *et al.*
Identification of the cosmogenic ^{11}C background in large volumes of liquid scintillators with Borexino
Eur. Phys. J. C **81** 1075 (2021)
13. M.N. Anwar and Y. Lu
Heavy quark spin partners of the $Y (4260)$ in coupled-channel formalism
Phys. Rev. D **104** 094006 (2021)
14. V. Baru *et al.*
Insights into $Z_b (10610)$ and $Z_b (10650)$ from dipion transitions from $\Upsilon (10860)$
Phys. Rev. D **103** 034016 (2021)
15. G. Barucca *et al.*
Study of excited Ξ baryons with the $\bar{\text{P}}\text{ANDA}$ detector
Eur. Phys. J. A **57** 149 (2021)

16. G. Barucca *et al.*
The potential of Lambda and Xi(-) studies with PANDA at FAIR
Eur. Phys. J. A **57** 154 (2021)
17. G. Barucca *et al.*
PANDA Phase One
Eur. Phys. J. A **57** 184 (2021)
18. C. Broocks *et al.*
g-Factor and static quadrupole moment of ^{135}Pr , ^{105}Pd , and ^{187}Au in wobbling motion
Eur. Phys. J. A **57** 161 (2021)
19. M. Carver *et al.*
Photoproduction of the $f_2(1270)$ Meson Using the CLAS Detector
Phys. Rev. Lett. **126** 082002 (2021)
20. Z.M. Chitgar *et al.*
Theory of circularly polarized harmonic generation using bi-colour lasers in underdense plasmas
Plasma Phys. Contr. F. **63** 035023 - (2021)
21. C. Christian *et al.*
CPEDM: A Storage Ring Facility for Charged-Particle EDM Searches
Nucl. Phys. News **31** 27 - 29 (2021)
22. X. Dong *et al.*
Coupled-Channel Interpretation of the LHCb Double- J/ψ Spectrum and Hints of a New State Near the J/ψ Threshold
Phys. Rev. Lett. **126** 132001 (2021)
23. X. Dong *et al.*
Is the existence of a J/ψ bound state plausible?
Sci. Bull. **66** 2462 (2021)
24. J. Dragos *et al.*
Confirming the existence of the strong CP problem in lattice QCD with the gradient flow
Phys. Rev. C **103** 015202 (2021)
25. M. Du *et al.*
Where Is the Lightest Charmed Scalar Meson?
Phys. Rev. Lett. **126** 192001 (2021)
26. M. Du *et al.*
Revisiting the nature of the Pc pentaquarks
J. High Energ. Phys. **2021** 157 (2021)
27. C. Duchemin *et al.*
Production Cross-Section Measurements for Terbium Radionuclides of Medical Interest Produced in Tantalum Targets Irradiated by 0.3 to 1.7 GeV Protons and Corresponding Thick Target Yield Calculations
Front. med. (Lausanne) **8** 625561 (2021)
28. R. Dupré *et al.*
Measurement of deeply virtual Compton scattering off He 4 with the CEBAF Large Acceptance Spectrometer at Jefferson Lab
Phys. Rev. C **104** 025203 (2021)
29. R. Engels *et al.*
Direct observation of transitions between quantum states with energy differences below 10 neV employing a Sona unit
Eur. Phys. J. D **75** 257 (2021)
30. R.W. Engels
Polarized fuel: A new option for sustained nuclear fusion
Res. Out. **126** 10 (2021)

31. E. Epelbaum *et al.*
Effective Field Theory for Shallow P-Wave States
Few-body systems **62** 51 (2021)
32. J. Haidenbauer, U. Meißner and L. Dai
Hyperon electromagnetic form factors in the timelike region
Phys. Rev. D **103** 014028 (2021)
33. J. Haidenbauer and U. Meißner
On the structure in the ΛN cross section at the ΣN threshold
Chinese Phys. C **45** 094104 - (2021)
34. J. Haidenbauer, U. Meißner and A. Nogga
Constraints on the Λ -neutron Interaction from Charge Symmetry Breaking in the ${}^4\text{He}$ - ${}^4\text{H}$ Hypernuclei
Few-body systems **62** 105 (2021)
35. T.B. Hayward *et al.*
Observation of Beam Spin Asymmetries in the Process $ep \rightarrow e'\pi^+\pi^-X$ with CLAS12
Phys. Rev. Lett. **126** 152501 (2021)
36. A. Hirtl *et al.*
Redetermination of the strong-interaction width in pionic hydrogen
Eur. Phys. J. A **57** 70 (2021)
37. S. Holz *et al.*
Towards an improved understanding of $\eta \rightarrow \gamma^*\gamma^*$
Eur. Phys. J. C **81** 1002 (2021)
38. C. Kannis and T.P. Rakitzis
Macroscopic production of highly nuclear-spin-polarized molecules from IR-excitation and photodissociation of molecular beams
Chem. Phys. Lett. **784** 139092 (2021)
39. S. Karanth *et al.*
Influence of electron cooling on the polarization lifetime of a horizontally polarized storage ring beam
Nucl. Instr. Meth. Phys. Res. A **987** 164797 (2021)
40. B. Kaspchak and U. Meißner
How machine learning conquers the unitary limit
Commun. Theor. Phys. **73** 035101 - (2021)
41. B. Kaspchak and U. Meißner
Neural network perturbation theory and its application to the Born series
Phys. Rev. Res. **3** 023223 (2021)
42. M. Khachatryan *et al.*
Electron-beam energy reconstruction for neutrino oscillation measurements
Nature <London> **599** 565 - 570 (2021)
43. S. Kistryn *et al.*
Experimental Studies of Few-Nucleon Systems
Act. Phys. Pol. A **139** 319 - 322 (2021)
44. I. Korover *et al.*
 ${}^{12}\text{C}(e,e'pN)$ measurements of short range correlations in the tensor-to-scalar interaction transition region
Phys. Lett. B **820** 136523 - (2021)
45. A. Kryjevski, T. Luu and V. Karasiev
Electronic structure of semiconductor nanoparticles from stochastic evaluation of imaginary-time path integral
Phys. Rev. Res. **3** 023173 (2021)
46. S. Kumaran *et al.*
Borexino Results on Neutrinos from the Sun and Earth
Universe **7** 231 - (2021)

47. H. Le *et al.*
S-shell $\Lambda\Lambda$ hypernuclei based on chiral interactions
Eur. Phys. J. A **57** 217 (2021)
48. H. Le *et al.*
 $A = 4 - 7$ Ξ hypernuclei based on interactions from chiral effective field theory
Eur. Phys. J. A **57** 339 (2021)
49. D. Lee *et al.*
Hidden Spin-Isospin Exchange Symmetry
Phys. Rev. Lett. **127** 062501 (2021)
50. Y. Lin, H. Hammer and U. Meißner
High-precision determination of the electric and magnetic radius of the proton
Phys. Lett. B **816** 136254 - (2021)
51. Y. Lin, H. Hammer and U. Meißner
Dispersion-theoretical analysis of the electromagnetic form factors of the nucleon: Past, present and future
Eur. Phys. J. A **57** 255 (2021)
52. J. Lozano *et al.*
Finite volume corrections to forward Compton scattering off the nucleon
Phys. Rev. D **103** 034507 (2021)
53. M. Mai *et al.*
Jülich-Bonn-Washington model for pion electroproduction multipoles
Phys. Rev. C **103** 065204 (2021)
54. N. Marchini *et al.*
SLICES: Spes Low-energy Internal Conversion Electron Spectrometer
Nucl. Instr. Meth. Phys. Res. A **1020** 165860 - (2021)
55. P. Maris *et al.*
Light nuclei with semilocal momentum-space regularized chiral interactions up to third order
Phys. Rev. C **103** 054001 (2021)
56. I. Matuschek *et al.*
On the nature of near-threshold bound and virtual states
Eur. Phys. J. A **57** 101 (2021)
57. N. Miller *et al.*
Scale setting the Möbius domain wall fermion on gradient-flowed HISQ action using the omega baryon mass and the gradient-flow scales t_0 and w_0
Phys. Rev. D **103** 054511 (2021)
58. M. Mirazita *et al.*
Beam Spin Asymmetry in Semi-Inclusive Electroproduction of Hadron Pairs
Phys. Rev. Lett. **126** 062002 (2021)
59. J. Ostmeyer *et al.*
The Antiferromagnetic Character of the Quantum Phase Transition in the Hubbard Model on the Honeycomb Lattice
Phys. Rev. B **104** 155142 (2021)
60. J. Ostmeyer *et al.*
The Ising model with Hybrid Monte Carlo
Comput. Phys. Commun. **265** 107978 (2021)
61. J. Pretz
Oscillations of a suspended slinky
Eur. J. Phys. **42** 045008 (2021)
62. J. Pretz
Anomale Abweichung
Phys. J. **6** 16 (2021)

63. H. Rebber *et al.*
Particle identification at MeV energies in JUNO
J. Instrum. **16** P01016 - P01016 (2021)
64. X. Ren *et al.*
The $\Lambda(1405)$ in resummed chiral effective field theory
Eur. Phys. J. C **81** 582 (2021)
65. M. Rimmner *et al.*
Developments of a multiplexer system for the High-Brilliance Neutron Source HBS
J. Neutron Res. **23** 143 - 156 (2021)
66. J. Rowley *et al.*
Improved Λ p Elastic Scattering Cross Sections between 0.9 and 2.0 GeV/c as a Main Ingredient of the Neutron Star Equation of State
Phys. Rev. Lett. **127** 272303 (2021)
67. M. Schneider *et al.*
Simulating both parity sectors of the Hubbard model with tensor networks
Phys. Rev. B **104** 155118 (2021)
68. C. Seng *et al.*
High-precision determination of the K3 radiative corrections
Phys. Lett. B **820** 136522 - (2021)
69. S. Shen *et al.*
Wigner SU(4) symmetry, clustering, and the spectrum of ^{12}C
Eur. Phys. J. A **57** 276 (2021)
70. Y. Shi *et al.*
Two-meson form factors in unitarized chiral perturbation theory
J. High Energ. Phys. **2021** 86 (2021)
71. Y. Shi and U. Meißner
Chiral dynamics and S-wave contributions in $\bar{B}^0/D^0 \rightarrow \pi^\pm \eta l^\mp \nu$ decays
Eur. Phys. J. C **81** 412 (2021)
72. U. Shrestha *et al.*
Differential cross sections for $\Lambda(1520)$ using photoproduction at CLAS
Phys. Rev. C **103** 025206 (2021)
73. J. Slim *et al.*
First detection of collective oscillations of a stored deuteron beam with an amplitude close to the quantum limit
Phys. Rev. Accel. Beams **24** 124601 (2021)
74. A.K. Spiliotis *et al.*
Ultrahigh-density spin-polarized hydrogen isotopes from the photodissociation of hydrogen halides: new applications for laser-ion acceleration, magnetometry, and polarized nuclear fusion
Light Sci. Appl. **10** 35 (2021)
75. G. Stellin and U. Meißner
P-wave two-particle bound and scattering states in a finite volume including QED
Eur. Phys. J. A **57** 26 (2021)
76. S. van Waasen *et al.*
JUNO physics and detector
Prog. Part. Nucl. Phys. **122** 103927 (2021)
77. L. von Detten *et al.*
On the scalar πK form factor beyond the elastic region
Eur. Phys. J. C **81** 420 (2021)

78. T. Vonk, F. Guo and U. Meißner
The axion-baryon coupling in SU(3) heavy baryon chiral perturbation theory
J. High Energ. Phys. **2021** 24 (2021)
79. T. Wagner *et al.*
Beam-based alignment at the Cooler Synchrotron COSY as a prerequisite for an electric dipole moment measurement
J. Instrum. **16** T02001 - T02001 (2021)
80. J. Wynen *et al.*
Machine learning to alleviate Hubbard-model sign problems
Phys. Rev. B **103** 125153 (2021)
81. H. Xu *et al.*
Measurement of proton-proton elastic scattering into the Coulomb region at Pbeam = 2.5, 2.8 and 3.2 GeV/c
Phys. Lett. B **812** 136022 - (2021)
82. N. Zachariou *et al.*
Double polarisation observable G for single pion photoproduction from the proton
Phys. Lett. B **817** 136304 - (2021)
83. X. Zheng *et al.*
Measurement of the proton spin structure at long distances
Nat. Phys. **9** 873 (2021)
84. Y. Zhou *et al.*
The KOALA experiment for (anti)proton-proton elastic scattering
Nucl. Instr. Meth. Phys. Res. A **1019** 165849 - (2021)

D Talks, Colloquia and Proceedings

D.1 Conference and Workshop Contributions

1. A. Alicke
Track finding for the PANDA detector based on Hough transformations
25th International Conference on Computing in High-Energy and Nuclear Physics, virtual Event hosted by CERN, USA: 2021-05-17 - 2021-05-21
2. I. Bekman and J. Hetzel
COSY Machine-Model Optimization
International Particle Accelerator Conference (12th), Campinas, Brazil: 2021-05-24 - 2021-05-28
3. C. Böhme *et al.*
Libera Hadron Applications and Operational Experience at COSY
Libera Workshop, Solkan, Slovenia: 2021-06-10 - 2021-06-10
4. R.W. Engels, K. Grigoryev and H. Smitmanns
Coating Tests at FZ Jülich
LHCspin meeting, CERN, Switzerland: 2021-02-19 - 2021-02-19
5. R.W. Engels
Polarized H_2 , D_2 and molecules and their possible use to feed a polarized H_2^+ , D_2^+ and HD^+ ion source for stripping injection into storage rings
The 24th International Spin Symposium, Matsue, Japan: 2021-10-18 - 2021-10-22
6. A. Göttel
Data analysis of a low-polonium-field for the discovery of CNO neutrinos in Borexino
XIX International Workshop on Neutrino Telescopes, Padova, Italy: 2021-02-18 - 2021-02-26
7. A. Göttel
JUNO potential in non-oscillation physics
2021 European Physical Society Conference on High Energy Physics, Online (Hamburg), Germany: 2021-07-26 - 2021-07-30
8. A. Göttel *et al.*
Calibrating OSIRIS: A 20-ton radioactivity monitor for JUNO
Deutsche Physikalische Gesellschaft, Online (Dortmund), Germany: 2021-03-15 - 2021-03-19
9. A. Göttel
JUST: a neutrino fit software for JUNO's solar analysis and sensitivity
The 1st INFN International School on Underground Physics, Online, Italy: 2021-06-28 - 2021-07-02
10. A. Göttel
DATA ANALYSIS OF A LOW-POLONIUM-FIELD FOR THE DISCOVERY OF CNO NEUTRINOS IN BOREXINO
XIX International Workshop on Neutrino Telescopes, online, ONLINE: 2021-02-18 - 2021-02-26
11. J. Haidenbauer
Electromagnetic form factors of hyperons in the time-like region
Joint THEIA-STRONG2020 and JAEA/Mainz REIMEI Web-Seminar, Mainz, Germany: 2021-02-24 - 2021-02-24
12. J. Haidenbauer
Flavor hadron interactions from effective field theory
Workshop on Hadron in Nucleus 2020, Kyoto, Japan: 2021-03-08 - 2021-03-10
13. J. Haidenbauer
Hyperon-nucleon interaction in few- and many-body systems
16th International Workshop on Meson Physics, Cracow, Poland: 2021-05-17 - 2021-05-20
14. J. Haidenbauer
Present status and future prospects of chiral EFT interactions with strangeness
Workshop on Strangeness in Neutron Stars - Physics at J-PARC HIHR/K1.1 brems lines, Sendai, Japan: 2021-06-17 - 2021-06-19

15. J. Haidenbauer
Baryon-baryon interaction in chiral effective field theory
 International Workshop on the Extension Project for the J-PARC Hadron Experimental Facility (J-PARC HEF-ex WS), Tokai, Japan: 2021-07-07 - 2021-07-09
16. J. Haidenbauer
NNbar interaction from chiral effective field theory and its application to neutron-antineutron oscillations
 A Virtual Tribute to Quark Confinement and the Hadron Spectrum 2021, Stavanger, Norway: 2021-08-02 - 2021-08-06
17. J. Haidenbauer
NNbar interaction from chiral effective field theory and its application to neutron-antineutron oscillations
 EXA online Conference 2021, Vienna, Austria: 2021-09-13 - 2021-09-17
18. J. Haidenbauer
Strangeness S=-3 and -4 baryon-baryon interactions in chiral effective field theory
 The 10th International workshop on Chiral Dynamics, Beijing, Peoples R China: 2021-11-15 - 2021-11-19
19. C. Hanhart
Dipion transitions and bottomoniumlike states
 The 14th International Workshop on Heavy Quarkonium, UC Davis, USA: 2021-03-15 - 2021-03-19
20. C. Hanhart
Spectroscopy of Heavy Exotics
 The XV International Conference on Heavy Quarks and Leptons, Warwick, Great Britain: 2021-09-13 - 2021-09-17
21. C. Hanhart
Unconventional meson states with two or more heavy quarks
 16th International Workshop on Meson Physics, Cracow, Poland: 2021-05-17 - 2021-05-21
22. P. Kampmann
EVENT RECONSTRUCTION IN JUNO
 XIX International Workshop on Neutrino Telescopes, Online (Padova), Italy: 2021-02-18 - 2021-02-26
23. P. Kampmann *et al.*
Online analysis for the OSIRIS pre-detector of JUNO
 Deutsche Physikalische Gesellschaft, Online (Dortmund), Germany: 2021-03-15 - 2021-03-19
24. P. Kampmann
STATUS AND PHYSICS OF THE JUNO EXPERIMENT
 Nineteenth Lomonosov Conference on Elementary Particle Physics, Moscow, Russia: 2019-08-22 - 2019-08-28
25. P. Kampmann
Physics potential of the JUNO experiment
 The 40th International Symposium on Physics in Collision 2021, Aachen, Germany: 2021-09-14 - 2021-09-17
26. P. Kampmann
EVENT RECONSTRUCTION IN JUNO
 XIX International Workshop on Neutrino Telescopes, Online (Padova), Italy: 2021-02-18 - 2021-02-26
27. C. Kannis *et al.*
NEW APPLICATION OF A SONA TRANSITION UNIT: Observation of direct transitions between quantum states with energy differences of 10 neV and below
 The 24th International Spin Symposium, Matsue, Japan: 2021-10-18 - 2021-10-22
28. S. Kumaran *et al.*
The Low Polonium Field of Borexino and its significance for the CNO neutrino detection
 Rencontres de Moriond 2021, online, online: 2021-03-20 - 2021-03-27
 arXiv:2105.13209

29. S. Kumaran *et al.*
First direct evidence of the CNO fusion cycle in the Sun with Borexino
 Proceedings of 37th International Cosmic Ray Conference – PoS(ICRC2021) - Sissa Medialab Trieste, Italy, 2021.
 - ISBN - doi:10.22323/1.395.1109, Berlin, Germany - Online: 2021-07-12 - 2021-07-23
 Proc. Sci., SISSA 395395 9
30. S. Kumaran
Bi-210 upper limit for the direct evidence of CNO solar neutrinos with Borexino
 DPG Spring Meetings, Dortmund, Germany: 2021-03-15 - 2021-03-19
31. S. Kumaran
The Low Polonium Field of Borexino and its significance for CNO neutrino detection
 55th Rencontres de Moriond 2021, online, France: 2021-03-20 - 2021-03-27
32. S. Kumaran
First direct evidence of the CNO fusion cycle in the Sun with Borexino
 37th International Cosmic Ray Conference, Berlin, Germany: 2021-07-12 - 2021-07-23
33. S. Kumaran
Spectroscopy of geoneutrinos with Borexino
 17th International Conference on Topics in Astroparticle and Underground Physics, Valencia, Spain: 2021-08-30 -
 2021-09-03
34. S. Kumaran
Detecting signals from the deep Earth with Borexino
 Weak Interactions and Neutrinos (WIN) 2021, Minnesota, USA: 2021-06-07 - 2021-06-12
35. S. Kumaran
**Chasing Cherenkov photons in an organic liquid scintillator detector: Directionality of sub-MeV Be-7 solar
 neutrinos in Borexino**
 The 1st INFN International School on Underground Physics (SoUP), online, Italy: 2021-06-28 - 2021-07-02
36. S. Kumaran
**Directional measurement in Borexino: Calibration of Cherenkov photons in a liquid scintillator detector
 using gamma sources**
 17th International Conference on Topics in Astroparticle and Underground Physics (TAUP 2021), Valencia, Spain:
 2021-08-30 - 2021-09-03
37. S. Kumaran
Borexino unravels the Sun and Earth with neutrinos
 Helmholtz Matter Universe Meeting 2021, online, Germany: 2021-11-24 - 2021-11-25
38. S. Kumaran
Spectroscopy of geoneutrinos with Borexino
 17th International Conference on Topics in Astroparticle and Underground Physics, Valencia (online), Spain: 2021-
 08-26 - 2021-09-03
 J. Phys.: Conf. Ser. 2156 012140 -
39. S. Kumaran
**Directional measurement in Borexino: Calibration of Cherenkov photons in a liquid scintillator detector
 using gamma sources**
 17th International Conference on Topics in Astroparticle and Underground Physics, Valencia (online), Spain: 2021-
 08-26 - 2021-09-03
 J. Phys.: Conf. Ser. 2156 012184 -
40. A. Lehrach
Beam and Spin Tracking
 744. WE-Heraeus-Seminar: Towards Storage Ring Electric Dipole Moment Measurements, Online Seminar, Ger-
 many: 2021-03-29 - 2021-03-31
41. R. Liu
JUNO OSIRIS ONLINE TRIGGER
 XIX International Workshop on Neutrino Telescopes, Online (Padova), Italy: 2021-02-18 - 2021-02-26

42. R. Liu
Trigger Studies for the OSIRIS Pre-detector of JUNO
 ISAPP 2021 Valencia “Neutrino Physics, Astrophysics and Cosmology” Online school, Online (Valencia), Spain: 2021-07-21 - 2021-07-30
43. R. Liu *et al.*
Software trigger optimization for the OSIRIS pre-detector of JUNO
 Deutsche Physikalische Gesellschaft, Online (Dortmund), Germany: 2021-03-15 - 2021-03-19
44. R. Liu
JUNO OSIRIS ONLINE TRIGGER
 XIX International Workshop on Neutrino Telescopes, Online (Padova), Italy: 2021-02-18 - 2021-02-26
45. L. Ludhova *et al.*
Solar and geoneutrinos
 17th International Conference on Topics in Astroparticle and Underground Physics, Valencia (online), Spain: 2021-08-26 - 2021-09-03
 J. Phys.: Conf. Ser. 2156 012002 -
46. L. Ludhova
Solar and geo neutrinos
 17th International Conference on Topics in Astroparticle and Underground Physics, Valencia, Spain: 2021-08-30 - 2021-09-03
47. P. Niedermayer *et al.*
Development of a fast betatron tune and chromaticity measurement system
 DPG-Frühjahrstagung 2021, Dortmund, Germany: 2021-03-15 - 2021-03-19
48. P. Niedermayer *et al.*
Development of a Fast Betatron Tune and Chromaticity Measurement System for COSY
 IPAC 2021, Campinas, Brazil: 2021-05-24 - 2021-05-28
49. L. Pelicci
Strategy and data analysis for the discovery of CNO neutrino in Borexino
 LXXI International conference (NUCLEUS 2021) Nuclear physics and elementary particle physics, St. Petersburg, Russia: 2021-09-20 - 2021-09-25
50. L. Pelicci
Data analysis strategy used for the detection of CNO solar neutrinos with Borexino
 17th International Conference on Topics in Astroparticle and Underground Physics, Valencia, Spain: 2021-08-30 - 2021-09-03
51. L. Pelicci *et al.*
Solar neutrino physics below 2 MeV with Juno
 Deutsche Physikalische Gesellschaft, Online (Dortmund), Germany: 2021-03-15 - 2021-03-19
52. L. Pelicci
Data analysis strategy used for the detection of CNO solar neutrinos with Borexino
 17th International Conference on Topics in Astroparticle and Underground Physics, Valencia (online), Spain: 2021-08-26 - 2021-09-03
 J. Phys.: Conf. Ser. 2156 012200 -
53. Ö. Penek *et al.*
Observation of CNO cycle solar neutrinos in Borexino
 17th International Conference on Topics in Astroparticle and Underground Physics, Valencia (online), Spain: 2021-08-26 - 2021-09-03
 J. Phys.: Conf. Ser. 2156 012128 -
54. Ö. Penek
Measurement of pp chain and CNO cycle solar neutrinos with Borexino
 DPG Spring Meetings, Dortmund, Germany: 2021-03-15 - 2021-03-19

55. Ö. Penek
Observation of CNO cycle solar neutrinos in Borexino
 17th International Conference on Topics in Astroparticle and Underground Physics, Valencia, Spain: 2021-08-30 - 2021-09-03
56. Ö. Penek
First Experimental Evidence of CNO Cycle Solar Neutrinos by Borexino
 40th international symposium on physics in collision, Aachen, Germany: 2021-09-14 - 2021-09-17
57. Ö. Penek
SENSITIVITY TO CNO CYCLE SOLAR NEUTRINOS IN BOREXINO
 XIX International Workshop on Neutrino Telescopes, Padova/Venice, Italy: 2021-02-18 - 2021-02-26
58. Ö. Penek
SENSITIVITY TO CNO CYCLE SOLAR NEUTRINOS IN BOREXINO
 XIX International Workshop on Neutrino Telescopes, Online (Padova), Italy: 2021-02-18 - 2021-02-26
59. V. Poncza and A. Lehrach
SIMULATION MODEL IMPROVEMENTS AT THE COOLER SYNCHROTRON COSY USING THE LOCO ALGORITHM
 IPAC 2021, Campinas, Barzil: 2021-05-24 - 2021-05-28
60. J. Pretz
Electric Dipole Moment Measurements at Storage Rings
 Did you mean: spin 2021 japan The 24th International Spin Symposium, Matsue, Japan (online): 2021-10-18 - 2021-10-22
61. F. Rathmann
Prototype Ring Facility for charged-particle EDM search - Toward a Technical Design Report
 Physics Beyond Colliders Annual Workshop, online, Switzerland: 2021-03-01 - 2021-03-04
62. M. Rifai *et al.*
Reconstruction of atmospheric neutrino events with JUNO
 Deutsche Physikalische Gesellschaft, Online (Dortmund), Germany: 2021-03-15 - 2021-03-19
63. M. Rifai
Atmospheric neutrinos in JUNO
 The 1st INFN International School on Underground Physics, Online, Italy: 2021-06-28 - 2021-07-02
64. G. Settanta *et al.*
First detection of CNO neutrinos with Borexino
 55th Rencontres de Moriond 2021, online, online: 2021-03-20 - 2021-03-27
 arXiv:2105.09211
65. G. Settanta
First detection of CNO neutrinos with Borexino
 55th Rencontres de Moriond 2021, online, France: 2021-03-20 - 2021-03-27
66. G. Settanta
ATMOSPHERIC NEUTRINO PHYSICS WITH JUNO
 XIX International Workshop on Neutrino Telescopes, Online (Padova), Italy: 2021-02-18 - 2021-02-26
67. G. Settanta
JUNO Non-oscillation Physics
 17th International Conference on Topics in Astroparticle and Underground Physics (TAUP 2021), Online (Valencia), Spain: 2021-08-26 - 2021-09-03
68. G. Settanta *et al.*
Reconstruction of the atmospheric neutrinos energy spectrum with JUNO
 Deutsche Physikalische Gesellschaft, Online (Dortmund), Germany: 2021-03-15 - 2021-03-19
69. G. Settanta
ATMOSPHERIC NEUTRINO PHYSICS WITH JUNO
 XIX International Workshop on Neutrino Telescopes, Online (Padova), Italy: 2021-02-18 - 2021-02-26

70. G. Settanta
JUNO Non-oscillation Physics
 17th International Conference on Topics in Astroparticle and Underground Physics (TAUP 2021), Online (Valencia), Spain: 2021-08-30 - 2021-09-03
 J. Phys.: Conf. Ser. 2156 012109 -
71. V. Shmakova
The search for electric dipole moments of charged particles using storage rings
 16th International Workshop on Meson Physics, Krakow, Poland: 2021-05-17 - 2021-05-20
72. V. Shmakova
The search for electric dipole moments of charged particles using storage rings
 DPG-Meeting of the Matter and Cosmos Section, Online, Germany: 2021-08-30 - 2021-09-03
73. V. Shmakova
The search for electric dipole moments of charged particles using storage rings
 24th International Spin Symposium, Matsue, Japan: 2021-10-18 - 2021-10-22
74. A. Singhal
Strategy used in CNO solar neutrinos analysis with the Borexino Experiment
 DPG Spring Meetings, Dortmund, Germany: 2021-03-15 - 2021-03-19
75. A. Singhal
First experimental proof of CNO fusion cycle in Sun with the Borexino Experiment
 LXXI International conference (NUCLEUS 2021) Nuclear physics and elementary particle physics, St. Petersburg, Russia: 2021-09-20 - 2021-09-25
76. A. Singhal
Understanding the systematic effects for the directional measurement of Be-7 solar neutrinos with Borexino
 17th International Conference on Topics in Astroparticle and Underground Physics, Valencia, Spain: 2021-08-30 - 2021-09-03
77. A. Singhal
First directional detection of sub-MeV solar neutrinos in the liquid scintillator detector by Borexino
 40th international symposium on physics in collision, Aachen, Germany: 2021-09-14 - 2021-09-17
78. A. Singhal
Understanding the systematic effects for the directional detection of sub-MeV solar neutrinos with Borexino
 17th International Conference on Topics in Astroparticle and Underground Physics, Valencia (online), Spain: 2021-08-26 - 2021-09-03
 J. Phys.: Conf. Ser. 2156 012202 -
79. H. Smitmanns *et al.*
New aspects of storage cell developments for the polarized internal target at LHCb
 The 24th International Spin Symposium, Matsue, Japan: 2021-10-18 - 2021-10-22
80. H. Ströher
Dark Matter Search: CPEDM/JEDI
 First DMLab Meeting: Scientific Kickoff, Zoom, Zoom: 2021-12-09 - 2021-12-10
81. M. Vitz, A. Lehrach and R. Shankar
Simulation and Optimization of the Spin Coherence Time of Protons in a Prototype EDM Ring
 IPAC 2021, Campinas, Brazil: 2021-05-24 - 2021-05-28
82. M.C. Vollbrecht
OSIRIS - An online scintillator radiopurity monitor for the JUNO experiment
 The European Physical Society on High Energy Physics (EPS-HEP), Online (Hamburg), Germany: 2021-07-26 - 2021-07-30
83. M.C. Vollbrecht *et al.*
Radiopurity treatment of the intelligent PMTs for OSIRIS
 Deutsche Physikalische Gesellschaft, Online (Dortmund), Germany: 2021-03-15 - 2021-03-19

84. P. Wintz
Drift chambers, straw tubes, TGC, CSC and other wire chambers
 ECFA Detector R&D Roadmap Symposium of Task Force 1 Gaseous Detectors, Zoom, Zoom: 2021-04-29 - 2021-04-29
85. P. Wintz *et al.*
Hyperon physics at HADES as part of the FAIR Phase-0 program
 19th International Conference on Hadron Spectroscopy and Structure in memoriam Simon Eidelman, Mexico City, Mexico: 2021-07-26 - 2021-07-31

D.2 Colloquia

1. J. Haidenbauer
Two- and three-baryon interactions with hyperons
 Sendai, Japan: 2021-02-16 -
2. L. Ludhova
The new journey to the center of the Earth: geoneutrino measurement with Borexino
 McDonald Institute Queen's University, Kingston, Canada: 2021-02-16
3. L. Ludhova
Latest solar- and geo-neutrino results from the Borexino experiment
 University of Houston ,Houston, USA: 2021-02-23
4. Ö. Penek
Search for Non-Standard Neutrino Interactions in Borexino Phase-II
 London, UK: 2021-01-27
5. J. Pretz
Polarization measurements for Electric Dipole Moment and Axion/ALP searches
 Aspects of Symmetry, online, online: 2021-03-10 - 2021-03-12
6. H. Ströher
The Beauty and Power of Spin
 Student Seminar (online)
7. H. Ströher
The Beauty and Power of Spin
 STRONG 2020

E Academic Degrees

E.1 Dissertation / PhD Theses

1. F. Abusaif
Development of compact, highly sensitive beam position monitors for storage rings
RWTH Aachen
2. D. Alfs
Search for Polarization Effects of Antiprotons Produced in pA Collisions
Ruhr-Universität Bochum
3. Z. Chitgar
Optical control of laser-driven X-ray and XUV radiation sources
RWTH Aachen
4. W.A. Esmail
Deep Learning for Track Finding and the Reconstruction of Excited Hyperons in Proton Induced Reactions
Ruhr-Universität Bochum
5. A. Hützen
Polarized Proton Beams from Laser-induced Plasmas
HHU Düsseldorf
6. L. Huxold
A Lamb-Shift Polarimeter for a Molecular Beam Source and Further Applications
HHU Düsseldorf
7. Ö. Penek
Measurement of pp and CNO cycle solar neutrinos with Borexino
RWTH Aachen
8. V. Poncza
Extensive Optimization of a Simulation Model for the Electric Dipole Moment Measurement at the Cooler Synchrotron COSY
RWTH Aachen
9. M. Rimmler
Development of a Multiplexer System and Measurement of the Neutron Yield for a Low-Energy Accelerator-Driven Neutron Source
RWTH Aachen
10. A. Thampi
Search for Charmonium-like Exotic States in $B \rightarrow J/\psi K$ Decays at Belle
Ruhr-Universität Bochum
11. T. Wagner
Beam-based alignment at the Cooler Synchrotron COSY for an Electric Dipole Moment measurement of charged particles
RWTH Aachen

E.2 Master Theses

1. C.M. John
Investigating Machine Learning methods to replace Hybrid Monte Carlo in simulations of Hubbard Model
Bonn University
2. P. Niedermayer
Development of a Fast Betatron Tune and Chromaticity Measurement System Using Bunch-by-Bunch Position Monitoring
RWTH Aachen
3. S. Siddique
Beam Simulation of a Prototype Proton Electric Dipole Moment Storage Ring
RWTH Aachen
4. R. Similon
Konstruktion eines justierbaren Detektor- und Probenisches für ein Neutronenreflektometer
FH Aachen
5. M. Vitz
Simulation and Optimization of the Spin Coherence Time of Protons in a Prototype EDM Ring
RWTH Aachen

E.3 Bachelor Theses

1. L. Brusa
CNO solar neutrino analysis with Borexino
RWTH Aachen
2. L. Heuser
A Study of the Isoscalar KK Interaction
Bonn University
3. J. Kastell
Comparison of methods to determine the molecular admixture of unstable states
Bonn University
4. A. Mandiwal
Development of a modified Spinfilter for metastable Hydrogen atoms
FH Aachen
5. L. Meyer
Benchmarking Pole Extractions with Pade Approximants on the example of πK scattering
Bonn University
6. F. Neumann
Comparison of methods to determine the molecular admixture of states with unstable constituents
Bonn University
7. P. Schnicke
Optimierung eines Sona-Übergang zur Vermessung des Breit-Rabi-Diagramms von metastabilen Wasserstoffatomen
FH Münster
8. M. Westphal
Improvements of Spin-filter Cavities for a Lamb-shift polarimeter
FH Aachen
9. L. Zhang
Digital Rate Regulation at the Cooler Synchrotron COSY
RWTH Aachen

F Awards

2021 Giuseppe and Vanna Cocconi Prize The European Physical Society has awarded the **2021 Giuseppe and Vanna Cocconi Prize** to the Borexino Collaboration for their ground-breaking observation of solar neutrinos from the pp chain and CNO cycle that provided unique and comprehensive tests of the Sun as a nuclear fusion engine
[FzJ press release](#)
[RWTH press release](#).

Prof. Dr. Dr. Livia Ludhova is highlighted "Physikerin der Woche 2021" (calendar week 50).
Since January 2018, the working group on equal opportunities (AKC) of the German Physical Society (DPG) highlights weekly women in physics in Germany or German women in physics abroad.
[DPG Website](#)
[Twitter](#)
[Facebook](#)
[Instagram](#)

Prof. Dr. Dr. h.c. Ulf-G. Meißner ERC Advanced Grant "Emergence of Complexity from Strong Interactions" (EXOTIC) European Research Council.
[FzJ press release](#)
[Bonner Generalanzeiger](#)

G Third Party Funded Projects

Project	Responsible/Contact	Funded by
Untersuchung von exotischen 4-Quark Zuständen	E. Prencipe	DFG
PGSB: Experimental tests of time-reversal	H. Ströher	BMBF
Bestimmung der Neutrino-Massenhierarchie	L. Ludhova	DFG
SFB/TR 110 Symmetries and the Emergence of Structure on OCQ	U.-G. Meißner	DFG
EXOTIC ERC Advanced Grant	U.-G. Meißner	EU
PANDA/ Straw Tube Tracker	J. Ritman	Industrieprojekt mit der GSI GmbH
PANDA/ Micro Vertex Detector	J. Ritman	Industrieprojekt mit der GSI GmbH
HESR - Dipole und Quadrupole	R. Tölle	Industrieprojekt mit der FAIR GmbH
HESR - sonstige Magnete	J. Böker	Industrieprojekt mit der FAIR GmbH
HESR - Netzgeräte	M. Retzlaff	Industrieprojekt mit der FAIR GmbH
HESR - Hochfrequenz	R. Stassen	Industrieprojekt mit der FAIR GmbH
HESR - Injektion	R. Tölle	Industrieprojekt mit der FAIR GmbH
HESR - Strahldiagnose	V. Kamerzhiev	Industrieprojekt mit der FAIR GmbH
HESR - Vakuum	F. Esser	Industrieprojekt mit der FAIR GmbH
HESR - Stochastische Kühlung	R. Stassen	Industrieprojekt mit der FAIR GmbH
HESR - Panda-Integration	D. Prasuhn	Industrieprojekt mit der FAIR GmbH
HESR - P1SR	R. Tölle	Industrieprojekt mit der GSI GmbH
AVA MSCA ITN	D. Grzonka	EU
Unit Costs TA1	D. Grzonka	EU (STRONG2020)
Travel and Subsistance for Users TA	D. Grzonka	EU (STRONG2020)
Transnational Access to COSY TA1	D. Grzonka	EU (STRONG2020)
JRA12-SPINFORFAIR: Spin for FAIR	F. Rathmann	EU (STRONG2020)
srEDM ERC Advanced Grant Management	H. Ströher	EU
srEDM ERC Advanced Grant Research	H. Ströher	EU

H Collaborations

- ATHENA Accelerator Technology Helmholtz Infrastructure
(https://www.athena-helmholtz.de/home/index_eng.html)
- Belle-II (B(meson) to lepton lepton (v.2))
(<https://www.belle2.org>)
- Borexino (Boron solar neutrino experiment, LNGS, Italy)
(<http://borex.lngs.infn.it>)
- CBM (Compressed Baryonic Matter)
(<https://www.gsi.de/work/forschung/cbmnqm/cbm.htm>)
- CLAS (CEBAF Large Acceptance Spectrometer, JLab, USA)
(<https://www.jlab.org/Hall-B/clas-web>)
- CPEDM (Electric Dipole Moments, CERN)
(<http://pbc.web.cern.ch/edm/edm-org.htm>)
- ELENA (CERN) (Extra Low Energy Antiproton ring)
(<https://espace.cern.ch/elena-project/SitePages/Home.aspx>)
- GlueX (The GlueX experiment, JLab, USA)
(<https://www.jlab.org/Hall-D/>)
- HADES (High Acceptance DiElectron Spectrometer)
(<https://www-hades.gsi.de>)
- HBS (High Brilliance Neutron Source)
(https://www.fz-juelich.de/jcns/jcns-2/EN/Forschung/High-Brilliance-Neutron-Source/_node.html)
- JEDI (Jülich Electric Dipole moment Investigation, COSY)
(<http://collaborations.fz-juelich.de/ikp/jedi>)
- JUNO (Jiangmen Underground Neutrino Observatory, Jiangmen, China)
(<http://juno.ihep.cas.cn>)
- JuSPARC (Jülich Short-Pulsed Particle and Radiation Center)
(<https://jusparc.fz-juelich.de/>)
- KLF (K-long Facility, Jefferson Lab)
(https://wiki.jlab.org/klproject/index.php/December,_2020)
- LENPIC (Low Energy Nuclear Physics International Collaboration)
(<http://www.lenpic.org/>)
- PANDA (Anti-Proton Annihilation at Darmstadt, FAIR)
(<https://panda.gsi.de>)
- PAX (Polarized Antiproton eXperiments, COSY)
(<http://collaborations.fz-juelich.de/ikp/pax>)
- PDG (Particle Data Group)
(pdg.lbl.gov)
- PREFER (Polarization Research for Fusion Experiments and Reaktors)
- STRONG-2020 (The strong interaction at the frontier of knowledge: fundamental research and applications)
(www.strong-2020.eu)
- WASA (Wide Angle Shower Apparatus, FRS)
(<https://www-win.gsi.de/frs/index.htm>)
- WASA (Wide Angle Shower Apparatus, WASA-at-COSY)
(<http://collaborations.fz-juelich.de/ikp/wasa/>)

J Teaching Positions

Institute	Name	University
IKP-1	Prof. Dr. F. Goldenbaum	Bergische Univ. Wuppertal
	Prof. J. Ritman Ph.D.	Ruhr-Univ. Bochum
	Dr. T. Stockmanns	Ruhr-Univ. Bochum
IKP-2	PD Dr. F. Rathmann	RWTH Aachen
	Prof. Dr. L. Ludhova	RWTH Aachen
	Prof. Dr. Dr. h.c. mult. H. Ströher	Univ. zu Köln
	Prof. Dr. J. Pretz	RWTH Aachen
IKP-3/IAS-4	Univ. Doz. Dr. J. Haidenbauer	Univ. Graz
	Prof. Dr. C. Hanhart	Rheinische Friedrich-Wilhelms-Univ. Bonn
	Prof. Dr. T. Luu	Rheinische Friedrich-Wilhelms-Univ. Bonn
	Prof. Dr. Dr. h.c. U.-G. Meißner	Rheinische Friedrich-Wilhelms-Univ. Bonn
	Dr. A. Nogga	Rheinische Friedrich-Wilhelms-Univ. Bonn
	PD Dr. A. Wirzba	Rheinische Friedrich-Wilhelms-Univ. Bonn
IKP-4	Dr. O. Felden	FH Aachen
	Prof. Dr. A. Lehrach	RWTH Aachen

K Personnel

MSc. F. Abusaif (IKP-2, until 31st Oct. 2021)
MSc. A. Alicke (IKP-1)
MSc. A. Andres (IKP-2/ IKP-4)
BSc. A. Asokan (IKP-3/IAS-4)
BSc. S. Aswani (GSI-FFN, since 1st Dec. 2021)
MSc. A. Awal (GSI-HESR, since 1st Oct. 2021)
Dr. I. Bekman (IKP-4)
C. Berchem (IKP-TA)
MSc. P. Bergmann (GSI-FFN, since 15th Sep. 2021)
Dr. E. Berkowitz (IKP-3/IAS-4, since 1st June 2021)
O. Bilen (GSI-FFN, since 1st Sep. 2021)
Dr. C. Böhme (IKP-4)
M. Böhnke (IKP-4)
Dr. J. Böker (IKP-4, until 31st Jan. 2021)
DI N. Bongers (IKP-4)
Dr. B. Breitzkreutz (IKP-4)
P. Brittner (IKP-4)
J. T. Chacko (IKP-3/IAS-4, since 1st July 2021)
W. Classen (IKP-4)
M. Comuth-Werner (IKP-TA/IAS-4)
DI F. U. Dahmen (IKP-4)
C. Deliege (IKP-4)
DI N. Demary (IKP-TA)
MBA A. Derichs (IKP-1)
G. D'Orsaneo (IKP-2)
R. Dosdall (IKP-1)
C. Ehrlich (IKP-4)
Dr. R. Engels (IKP-2)
B. Erkes (IKP-4)
MSc. W. Esmail (IKP-1, GSI-FFN, since 15th Oct. 2021)
DI F.-J. Etzkorn (IKP-4)
J. Fahnenschreiber (IKP-TA, since 1st May 2021)
Dr. O. Felden (IKP-TA)
H. - W. Firmenich (IKP-TA)
Dr. D. Frame (IKP-3/IAS-4, until 31st Oct. 2021)
N.O. Fröhlich (IKP-4, until 30th June 2021)
MSc. C. Gäntgen (IKP-3/IAS-4, since 1st Oct. 2021)
Dr. R. Gebel (IKP-4, GSI-HESR, since 1st Sept. 2021)
M. Ghaly (GSI-HESR, 1st May until 31st Aug. 2021)
J. Göbbels (IKP-TA)
MSc. A. Göttel (IKP-2)
Prof. Dr. F. Goldenbaum (IKP-1)
Dr. K. Grigoryev (IKP-4)
Dr. D. Grzonka (IKP-1)
M. Gülpen (IKP-TA)
D. Gu (GSI-HESR, since 1st Aug. 2021)
T. Hahnrahts-von der Gracht (IKP-TA)
PD Dr. J. Haidenbauer (IKP-3/IAS-4)
A. Halama (IKP-4)
E. Hall-Brunton (IKP-TA)
DI S. Hamzic (IKP-4)
Prof. Dr. C. Hanhart (IKP-3/IAS-4)
Dr. M. Hartmann (IKP-2)
DI R. Hecker (IKP-TA)
Dr. V. Hejny (IKP-2)
Dr. J. - H. Hetzel (IKP-4)
M. Holona (IKP-1)
MSc. O. Javakhishvili (IKP-2)
Dr. A. Kacharava (IKP-2)
Dr. V. Kamerdzhev (IKP-4)
Dr. P. Kampmann (IKP-2, GSI-FFN, since 1st Aug. 2021)
MSc. J. Kannika (IKP-1)
MSc. C. Kannis (IKP-4)
A. Kelleners (IKP-TA)
Dr. I. Keshelashvili (IKP-2, GSI, since 1st Oct. 2021)
A. Kieven (IKP-4)
Dr. J. Kim (IKP-3/IAS-4, since 1st July 2021)
S. Kistemann (IKP-TA)
B. Kuckelkorn-Klimczok (IKP-TA)
M. Kremer (IKP-TA)
DI T. Krings (IKP-TA)
M. Küven (IKP-4)
Dr. P. Kulesa (IKP-1, GSI-FFN, until 30th Sept. 2021)
MSc. S. Kumaran (IKP-2)
Dr. T. Lähde (IKP-3/IAS-4)
K. Laihem (GSI-HESR, since 1st Oct. 2021)
K. - G. Langenberg (IKP-4)
Dr. H. Le Thi (IKP-3/IAS-4)
Prof. Dr. A. Lehrach (IKP-4)
MSc. S. Liebert (IKP-4)
MSc R. Liu (IKP-2)
BSc I. Lomidze (IKP-2, 9th March until 31st Oct. 2021)

MSc. K. Luckas (IKP-1, until 31st Oct. 2021)
 Prof. Dr. L. Ludhova (IKP-2)
 Prof. T. Luu (IKP-3/IAS-4)
 A. Mandiwal (GSI-FFN, 1st April until 31st Oct. 2021)
 M. Manerova (GSI-HESR, since 1st Oct. 2021)
 M. Marzen (IKP-4, since 14th Sept. 2021)
 M. Maubach (IKP-TA)
 Prof. Dr. Dr. h. c. U.-G. Meißner (IKP-3/IAS-4)
 DI A. Messaaf (IKP-4)
 J. Messchendorf (GSI-FFN, since 1st July 2021)
 Dr. B. Metsch (IKP-3/IAS-4, since 1st Dec. 2021)
 MSc. N. Mohan (GSI-FFN, since 1st Nov. 2021)
 Dr. A. Naß (IKP-2)
 MSc. P. Niedermayer (IKP-4)
 Dr. A. Nogga (IKP-3/IAS-4)
 MSc. L. Pelicci (IKP-2)
 Dr. O. Penek (IKP-2)
 MSc. G. Perez-Andrade (IKP-1)
 Dr. A. Pesce (IKP-2)
 BSc J. T. Peters (IKP-4)
 C. Poulwey (IKP-4, until 30th June 2021)
 Dr. D. Prasuhn (IKP-4)
 Prof. Dr. J. Pretz (IKP-2)
 V. Priebe (IKP-TA, since 24th June 2021, GSI-HESR, since 23rd Dec. 2021)
 Dr. J. Pütz (IKP-1, GSI-FFN, since 1st Jan. 2021)
 S. Pütz (GSI-FFN, since 1st Sept. 2021)
 S. Rasalingam (IKP-4, GSI-HESR, since 30th April 2021)
 PD Dr. F. Rathmann (IKP-2)
 MSc S. Rawat (IKP-3/IAS-4, since 1st Jan. 2021)
 BSc. L. Razmadze (IKP-3/IAS-4, until 31st Oct. 2021)
 DI K. Reimers (IKP-4)
 DI M. Retzlaff (IKP-4, until 30th Nov. 2021)
 MSc. M. Rifai (IKP-2)
 A. Rifaie (GSI-HESR, 10th May until 31st Aug. 2021)
 Dr. M. Rimmler (IKP-4, GSI-HESR, since 1st July 2021)
 Prof. J. Ritman Ph.D (IKP-1, GSI-FFN)
 Dr. D. Rönchen (IKP-3/IAS-4)
 G. Roes (IKP-TA)
 D. Ruhrig (IKP-4)
 G. Rupsch (IKP-4)
 J. Salmann (GSI-FFN, since 15th Nov. 2021)
 Ph.D. habil. S. Schadmand (IKP-1, GSI-FFN, since 15th March 2021)
 F. Scheiba (IKP-4)
 Dr. R. Schleichert (IKP-2)
 H. Schiffer (IKP-TA, until 30th June 2021)
 M. Schmühl (IKP-4)
 BSc C. Schneider (IKP-3/IAS-4, since 1st Sept. 2021)
 P. Schnicke (GSI-FFN, 1st April until 30th Sept. 2021)
 M. Schubert (IKP-4)
 Dr. Th. Sefzick (IKP-TA)
 Dr. V. Serdyuk (IKP-1, until 31st March 2021)
 Dr. G. Settanta (IKP-2, until 31st Aug. 2021)
 Dr. S. Shen (IKP-3/IAS-4)
 Dr. V. Shmakova (IKP-2) (until 30th Sept. 2021)
 MSc. N. Shurkhno (IKP-4)
 S. Siddique (IKP-2, GSI-FFN, since 1st July 2021)
 R. Similon (IKP-4, GSI-HESR, since 1st July 2021)
 DI M. Simon (IKP-4)
 MSc. A. Singhal (IKP-2)
 J. Slim (GSI-FFN, since 1st Oct. 2021)
 H. Smitmanns (IKP-2)
 J. Spelthann (IKP-TA, GSI-HESR, since 29th April 2021)
 D. Spölgén (IKP-2)
 Dr. R. Stassen (IKP-4)
 G. Sterzenbach (IKP-1, until 31st Aug. 2021)
 Dr. T. Stockmanns (IKP-1)
 Prof. Dr. Dr. h. c. mult. H. Ströher (IKP-2, until 30th Sept. 2021, GSI-FFN, since 1st Oct. 2021)
 MSc. R. Suvarna (GSI-FFN, since 1st Dec. 2021)
 MSc. A. Thampi (IKP-1)
 MSc. M. Thelen (IKP-4)
 Dr. R. Tölle (IKP-4, GSI-HESR, since 1st April 2021)
 Dr. Y. Valdau (IKP-4)
 DI T. Vashegyi (IKP-4)
 MSc. M. Vitz (IKP-4)
 MSc. C. Vollbrecht (IKP-2)
 MSc L. von Detten (IKP-3/IAS-4, since 1st Jan. 2021)
 Dr. T. Wagner (IKP-2, GSI-FFN, 1st April 2021 until 30th Sept. 2021)
 L. Werth (IKP-TA, until 31st July 2021)

M. Westphal (GSI-FFN, since 1st Aug. 2021)

V. Wettig (IKP-TA, until 31st May 2021)

BSc. A. Weßel (GSI-FFN, since 1st May 2021)

Dr. P. Wintz (IKP-1)

D. Wirtz (IKP-TA)

PD Dr. A. Wirzba (IKP-3/IAS-4)

T. von Witzleben (GSI-FFN, 1st Apr. 2021 until 30th June 2021)

Dr. H. Xu (IKP-1)

H. Zens (IKP-4)

L. Zhang (GSI-HESR, 1st June until 31st Aug 2021)

Dr. Y. Zhou (IKP-1, GSI-FFN, 1st Jan. 2021 until 30th Apr. 2021)

IKP-1 = Experimental Hadron Structure
IKP-2 = Experimental Hadron Dynamics
IKP-3/IAS-4 = Theory of the Strong Interactions
IKP-4 = Large-Scale Nuclear Physics Equipment
IKP-TA = Technical Services and Administration

GSI-FFN = GSI Helmholtzzentrum für Schwerionenforschung, FAIR Forschung NRW
GSI-HESR = GSI Helmholtzzentrum für Schwerionenforschung, Hochenergiespeicherring

L Individual Contributions

Contents

Accelerator Research	60
Test of carbon coated storage cells for the LHC spin project	60
Production of high-density nuclear-spin-polarized ^3He for a laser-induced acceleration experiment at PHELIX@GSI	61
New Spinfilter for Separation of all Hydrogen HFS-Substates	62
Optimization of the magnetic field configuration of a SONA Transition Unit	63
Measurement of the Sona-transition-effect with deuterium	64
A bunch shape monitor for COSY	65
Tomographic reconstruction of the longitudinal phase space evolution at COSY	67
First HESR Cavity prepared for COSY	69
Modernisation of the Stripline Unit Signal Conditioner at COSY	71
The HESR Scraper from Radiation Protection's point of view	72
Measures at the BigKarl -Area for the High Brilliance Neutron Source (HBS)	73
Storage Ring Based EDM Search	74
Toward a direct measurement of the deuteron EDM at COSY	74
Study of Beam dynamics of Prototype Electric Dipole Moment Storage Ring	75
Progress toward a direct measurement of the deuteron Electric Dipole Moment at COSY	76
Orbit response matrix calculation of an idealized COSY model using Bmad	77
Simulation of the spin coherence time for proton beams with BMAD	78
Investigation of the proton Spin Coherence Time (SCT) at storage rings	79
Spin-Tracking simulations in an idealized COSY model using Bmad	80
Injection optimization using machine learning at the Cooler Synchrotron COSY	81
The status of the Pellet target development for the JePo polarimeter at COSY	82
Benchmarking the spin tracking for spin tune mapping with three-steerer vertical orbit bumps	83
FAIR Related Experimental Activities	85
Investigation of the Σ^0 Production Mechanism in p+p Collisions	85
InnerTOF - a Trigger Scintillator for HADES	86
Comparison of Track Finding Algorithms for the PANDA Detector	88
The HADES Straw Tube Stations calibration	90
Track Finding in Hexagonal Geometry Using Language Models	92
The STS Detector for the FAIR Phase-0 Experiment with HADES	93
Neutrino Physics	94
Detecting Neutrino Signals from the Deep Earth with Borexino	94
Data analysis strategy used for the detection of CNO solar neutrinos with Borexino	95
First Experimental Evidence of CNO Cycle Solar Neutrinos by Borexino	96
First directional detection of sub-MeV solar neutrinos in the liquid scintillator detector by Borexino	97
Understanding the systematic effects for the directional detection of sub-MeV solar neutrinos with Borexino	98
Chasing Cherenkov photons in organic liquid scintillator detectors: Directional analysis of sub-MeV ^7Be solar neutrinos in Borexino	99
Directionality measurement in Borexino: Calibration of Cherenkov photons in a liquid scintillator detector using gamma sources	100
Physics potential of the JUNO Experiment	101
Atmospheric neutrinos in JUNO	102
OSIRIS An online scintillator radiopurity monitor for the JUNO experiment	103
JUST: a neutrino fit software for JUNO's solar analysis & sensitivity	104
Trigger Studies for the OSIRIS Pre-detector of JUNO	105

Test of carbon coated storage cells for the LHCspin project

O. Bilen, R. Engels, K. Grigoryev, H. Smitmanns, C.S. Kannis, A. Schweitzer^a

To start spin physics at LHC@CERN it is discussed to implement a polarized target in front of the LHCb detector based on the SMOG2 storage cell. This T-shaped storage cell will be fed with polarized hydrogen/deuterium atoms from a polarized atomic beam source. For this purpose the options for the surface coating of such a cell are limited, because the LHC experts insist on materials like carbon to decrease the secondary electron yield that disturbs the accelerated beam. Thus, it is necessary to investigate if carbon coated storage cells will allow a high polarization of the stored atoms or if it will induce large recombination rates of the polarized atoms into less-polarized molecules.

Simultaneously we will investigate the effect of the Lyman- α radiation emitted by the ABS on target gas recombination. This could be helpful in explaining the formation of interstellar H_2 molecule clouds and the problems in storage cell development.

The measurements will be taken with the already existing apparatus at the Research Center Jülich [1][2]. It consists of a polarized atomic beam source (ABS)[3], a superconducting solenoid containing the storage cell (ISTC chamber) and a Lamb-shift polarimeter (LSP)[4].

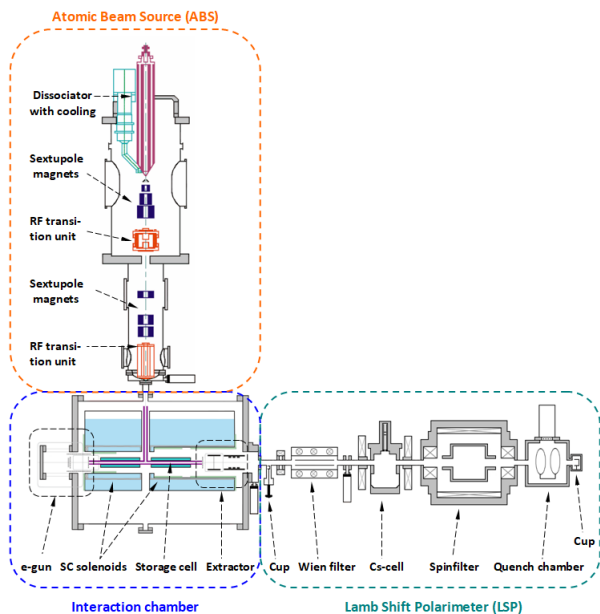


Figure 1: experimental setup (ABS ist mounted on top of the ISTC chamber).

The ABS generates a polarized hydrogen beam via dissociation of H_2 gas (or deuterium beam via dissociation of D_2 gas). The atoms are polarized via the Stern-Gerlach principle using two sets of

sextupole magnets. With 3 transition units the hyperfine states of the atoms can be changed through combination of weak, mean and strong transition fields [3]

The superconducting solenoid of the ISTC chamber generates a strong magnetic holding field to prevent changes in nuclear spin orientation of the stored atoms. These atoms are ionized using an electron gun und guided into the LSP where they are analyzed in regard to their polarization. The LSP consists of a Wien filter for mass separation (to differentiate between single atoms and recombined molecules), a cesium cell to generate metastable hydrogen (or deuterium) using charge exchange, a spin filter and a quenching chamber with a photomultiplier to detect the spin filtered atoms that pass through the LSP.

Unfortunately due to problems with the storage cell coating at CERN, we were not able to conduct our measurements yet. Meanwhile, with the help of A. Schweitzer from ZEA1 we were able to coat storage cells by ourself and will do our first preliminary experiments at end of January 2022. The cell was coated by flooding it with acetone and heating it up until the acetone breaks down and evaporates, leaving a carbon coating on the fused-quartz glass cell.



Figure 2: carbon coated storage cell.

References

- [1] R.W. Engels et.al., Phys. Rev. Lett. **124** (2020) 113003.
- [2] R.W. Engels et.al., Phys. Rev. Lett. **115** (2015) 113007.
- [3] M. Mikirtychians et.al., NIM A **721** (2013) 83.
- [4] R.W. Engels et.al., Rev. Sci. Instr. **85** (2014)

^a Central Institute of Engineering (ZEA1)

Production of high-density nuclear-spin-polarized ^3He for a laser-induced acceleration experiment at PHELIX@GSI

C. S. Kannis^{a,b}, M. Büscher^{c,d}, R. Engels^a, I. Engin^e, P. Fedorets^f,
A. Lehrach^{a,b}, H. Soltner^g, M. Westphal^a and C. Zheng^c

Optical pumping techniques have been successfully applied to produce polarized atoms such as alkali metals and noble gases. In particular, metastability exchange optical pumping (MEOP) is used to achieve high nuclear polarization in ^3He . The process takes place in a homogeneous magnetic field of ~ 1 mT which establishes the quantization axis. The principle of MEOP can be described by the following three steps.

1. A direct transition from ground state to 2S is forbidden so a weak radio frequency discharge is applied instead. This will populate the higher states of ^3He but after a radiative cascade the atoms will deexcite to the metastable 2S state, which plays the role of ground state for optical pumping.
2. Next, circularly polarized light tuned at 1083 nm induces transitions from the m_F substates of 2S to the corresponding substates of 2P. These transitions obey to the selection rule $\Delta m_F = \pm 1$ (the sign depends on right/left circular polarization). However, due to a spontaneous reemission the 2S substates get populated again. For that reason a CW laser is used which depletes one of the 2S substates. This is equivalent to the orientation of the electronic angular momentum. Due to the hyperfine coupling between the electrons and the nucleus, the electronic optical orientation induces nuclear-spin polarization.
3. The last step is to transfer the nuclear polarization from the metastable to the ground state. This is achieved via metastability exchange collisions. During them a polarized metastable atom and an unpolarized ground state atom exchange their electronic states while the nuclear polarization does not get affected. Consequently, nuclear-spin-polarized ground state atoms are produced, but also unpolarized metastable atoms that can be further optically pumped by the CW laser.

Based on the MEOP method a compact ^3He polarizing facility [1] was built at the university of Mainz and was transferred to the Forschungszentrum Jülich. It consists of three parts. The first part consists of the reservoir for the unpolarized ^3He gas and a getter pump for gas purification. The last is necessary because impurities in ppm or higher level reduce the density of metastable atoms and hence the degree of polarization as well as the polarization lifetime. In the second part the MEOP process takes place and polarized ^3He is produced. The third part contains a mechanical piston compressor which preserves the

polarization throughout compression. The gas can be stored into a buffer cell of 6 L volume or further compressed in a detachable transport cell ($V = 1$ L). The maximum polarization that can be attained by the polarizer is 84% in a steady state. For the production of 3 standard liters with $\sim 70\%$ polarization, 5 hours of operation were needed. The polarized gas was used as a target at PHELIX (Petawatt High-Energy Laser for Heavy Ion EXperiments, GSI Darmstadt) for laser-induced acceleration of $^3\text{He}^{++}$ ions [2]. During transportation, the glass cell was stored inside a cylindrical magnetic box which provides a homogeneous magnetic holding field in order to preserve polarization. The polarization degree and the relaxation time were determined by an NMR device before transportation.

The pressure of the glass cells cannot exceed 3 bar leading to insufficient particle density at the interaction point with the laser. To overcome this problem a compressor is developed from non-magnetic materials such as titanium and some aluminum parts. A nozzle is placed on the compressor's exit to shape the beam. This increased the pressure from 3 bar to 18-27 bar. An additional static magnetic field is also necessary to maintain polarization during the experiment (5-6 hours). This is achieved with a magnet system that consists of 48 NdFeB permanent magnets combined in eight vertical columns and four Helmholtz coils.

Finally, the experiment took place in a vacuum chamber, which not only provides good experimental conditions but also allows us to pump and collect the ^3He gas in big tanks in order to transfer it back to the polarizer and reuse it after purifying it.

References

- [1] C. Mrozik et al., J. Phys.: Conf. Ser. 294 (2011) 012007.
- [2] I. Engin, Plasma Phys. Control. Fusion 61 (2019) 115012.

^a Institute for Nuclear Physics, FZ Jülich, Germany

^b III. Physikalisches Institut B, RWTH Aachen University, Germany

^c Peter Grünberg Institut, FZ Jülich, Germany

^d Laser and Plasma Physics Institute, HHU Düsseldorf, Germany

^e Sicherheit und Strahlenschutz (S-A), FZ Jülich, Germany

^f Institute for Theoretical and Experimental Physics named by A. I. Alikhanov of National Research Centre "Kurchatov Institute", Russia

^g Zentralinstitut für Engineering, Elektronik und Analytik (ZEA), FZ Jülich, Germany

New Spinfilter for Separation of all Hydrogen HFS-Substates

M. Westphal, B. Breitzkreutz, R. Engels, C. S. Kannis, A. Mandiwal und H. Soltner^a

There are a couple of experiments which require a Spinfilter to separate the different HFS-states of hydrogen, such as the Sona transition [1] and the Bound-Beta-Decay experiment [2]. But by now these Spinfilter could only separate the $2S_{1/2}$ -alpha substates. To eliminate this limitation a new Spinfilter is needed, which could also separate the $2S_{1/2}$ -beta substates.

The new Spinfilter is capable of separating all four $2S_{1/2}$ -states by using a rectangular shaped cavity inside a solenoid. Due to its form, the cavity can hold two different radiofrequencies, which have an orthogonal polarisation to each other.

The heart of the Spinfilter, the cavity, was build by the workshop out of thick copper plates which are screwed together to allow later access for adjustments of the antennas and to avoid bending and oxidisation during a soldering process. At the top and at the sides of the cavity are additional holes for screws which should be used to adjust the radio frequencies in the cavity.

To proof the quality and the accuracy of the cavity, we made some resonance measurements to find the resonance frequencies. The needed frequencies for our chosen configuration would be $f_1=0,706$ GHz and $f_2=1,412$ GHz. Because frequency f_2 is nearly twice as

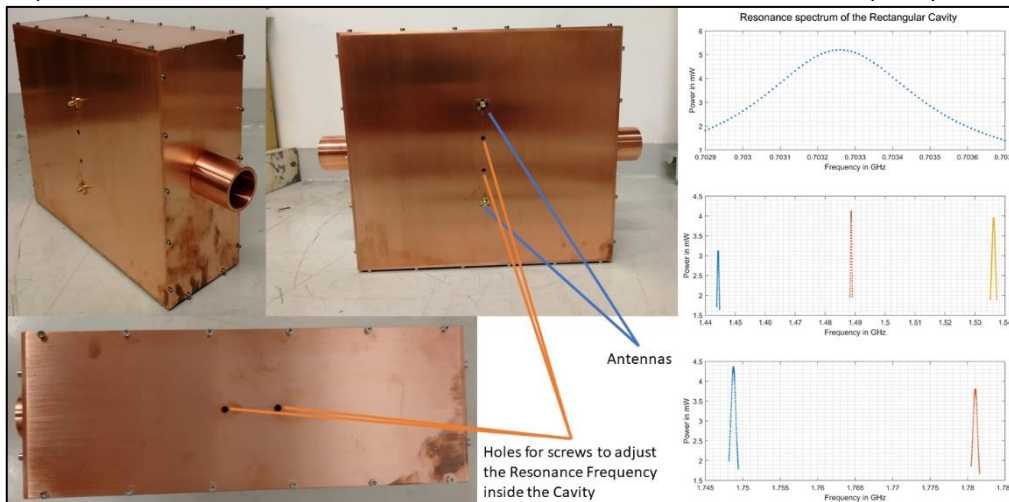


Figure 2: Pictures of the already build rectangular cavity and the measured resonance curves inside it

Depending on the strength of the B-Field of the solenoid, the two radio frequencies can couple strongly or weakly to the different $2S_{1/2}$ -states. If the quality of the cavity is high enough and the B-field has the right strength, one of the radio frequencies couples weakly to two of the $2S_{1/2}$ -states which leads to the de-excitation of these two states. The other radio frequency couples weakly to a third state and strongly to the fourth, which results in the de-excitation of the third and the conservation of the fourth state.

This allows the filtering for a certain HFS-state like shown in the Breit-Rabi-Diagram below.

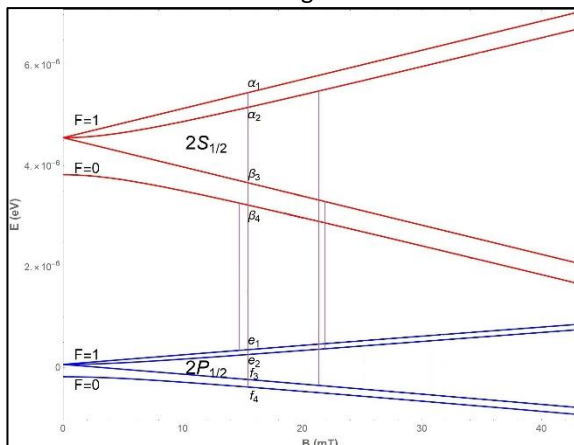


Figure 1: Breit-Rabi-Diagram with the four transitions from the $2S_{1/2}$ - into the $2P_{1/2}$ -states[3]

high as frequency f_1 , f_2 is hard to distinguish from the second harmonic of f_1 . This can be seen in the resonance curves in figure 1, besides some pictures of the already build cavity.

The only thing that is missing now, to bring this new Spinfilter in operation and proof its concept, is the new solenoid. The magnetic field and its producing solenoid were simulated and designed by Aditya Mandiwal in his bachelor thesis [4].

It consists out of three coils, one primary and two secondary coils, which are all connected in series. While the primary coil produces the needed homogenic field, the secondary coils reduce the gradient of the magnetic field at the ends of the coil to prevent the quenching of the atoms by the electric field they experience by entering and exiting the cavity. For thermal stability the coils are cooled by a water loop inside the Wendel [4].

References:

- [1] R. Engels et al.; EPJ D **75**, 257 (2021)
- [2] W. Schott et al.; EPJ Web of Conferences **219**, 04006 (2019)
- [3] C. S. Kannis privat communication
- [4] Bachelor Thesis of Aditya Mandiwal, FH Aachen, 2021

^a Institute for Central Engineering (ZEA1)

Optimization of the magnetic field configuration of a SONA Transition Unit

S. Aswani, R. Engels, C. S. Kannis, J. Salmann, P. Schnicke, H. Smitmanns, and H. Soltner^a

The SONA Transition Unit consists of two oppositely polarized coils that generate an oscillating longitudinal magnetic field inside the device. A metastable atom in a single Zeeman State, passing the SONA unit, would experience an incoming radiofrequency, which can induce a transition into another hyperfine substate, if the longitudinal magnetic fields closely represent a sinusoidal function. The radial field as a result of being a functional derivative of the longitudinal field also resembles a cosine function. These magnetic fields however are susceptible to influence from the two significantly stronger Spinfilter magnetic fields from the two spin filters placed on either side of the SONA Transition Unit. In order to understand the degree of influence an experiment was designed.

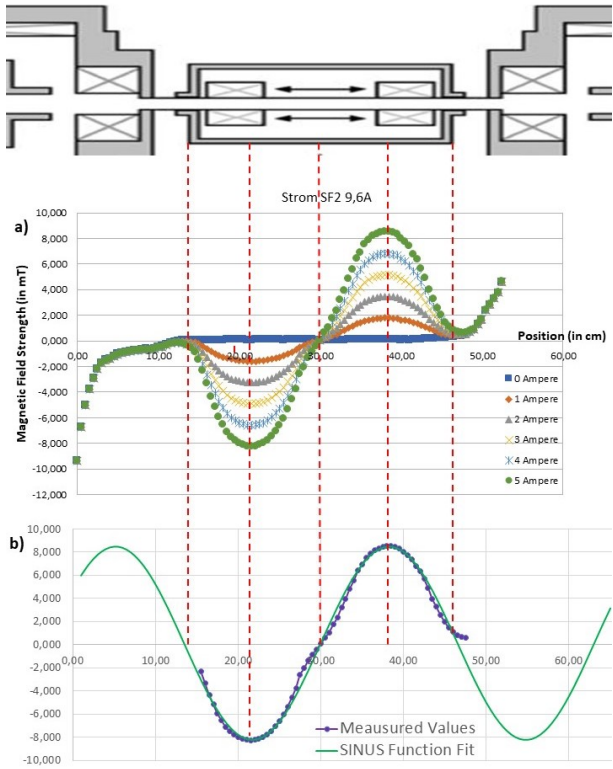


Figure 1: Longitudinal magnetic field distribution inside the SONA Transition Unit.

A probe is introduced through the open end of Spinfilter-2 and pushed to the point from which the quantitative magnetic field measurements were required to understand the influence of the fields on the SONA Unit. Magnetic field values were recorded at a constant Spinfilter-1 current of 8.1 A, for two Spinfilter-2 current settings i.e., 8.6 A and 9.6 A and for six SONA current settings, from 0 A to 5 A. This process was repeated at 115 different points for a length of 57.5 cm. A graphical representation of the

data obtained is represented in Fig. 1. The graphs represent the magnetic field along the length of the SONA Transition Unit. The given graph is then compared to a simulated sinusoidal function that best represents the required magnetic field. From the sinusoidal functions it is evidently clear that a few adjustments to the setup must be made in order to obtain the required magnetic field. A possible solution would be winding oppositely charged coils at the ends of the SONA coils in order to compensate for the magnetic field strength where needed. For this very reason a simulation is being prepared in order to accurately obtain measurements and positions for coil compensation. It is essential to approximate our magnetic field to a sinusoidal function as it helps optimize the wavelength obtained. An increase in the precision of the wavelength would subsequently lead to significantly less variance in energy.

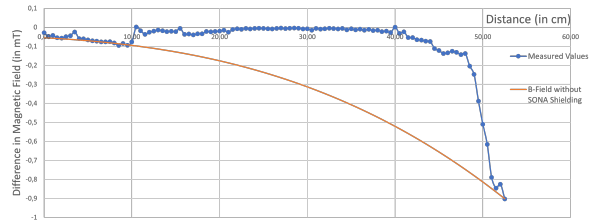


Figure 2: Change in magnetic field strength due to change in Spinfilter current.

From the graphs corresponding to 8.6 A and 9.6 A, a third graph (Fig. 2) is obtained as a difference of the above two graphs. This is done to understand the effect of the changes in current and thus the magnetic field in Spinfilter-2 on the SONA Transition Unit. In this graph we see the simulated difference in fields in absence of shielding around the SONA, as compared to the recorded field difference in the presence of the shielding. Note how the presence of shielding almost suppresses the induced magnetic effect from the strong Spinfilter-2 Magnetic field introducing an only positive offset. This difference increases significantly as the region of the shielding is passed. There is absolutely no influence of the change in SONA current on the differences in field strengths.

References

- [1] R. Engels et al., EPJ. D **75**, 257 (2021).
- [2] Bachelor Thesis of Yuchen Gan, FH Aachen (2017).
- [3] Bachelor Thesis of Philipp Schnicke, FH Münster (2021).

^a Central Institute for Engineering (ZEA 1)

Measurement of the Sona-transition-effect with deuterium

J. Salmann, R. Engels, S. Aswani, C. S. Kannis, and H. Smitmanns

When using a Sona-transition unit unexpected oscillations have occurred. Attempts to explain lead to the discovery, that the hydrogen atoms passing through the Sona-transition experience fields like being exposed to an electromagnetic wave [1]. Its frequency $f = \frac{v}{\lambda}$ is determined by the characteristic wavelength λ of the sine-like magnetic field in the Sona-transition (see figure 1) and the velocity v of the atoms.

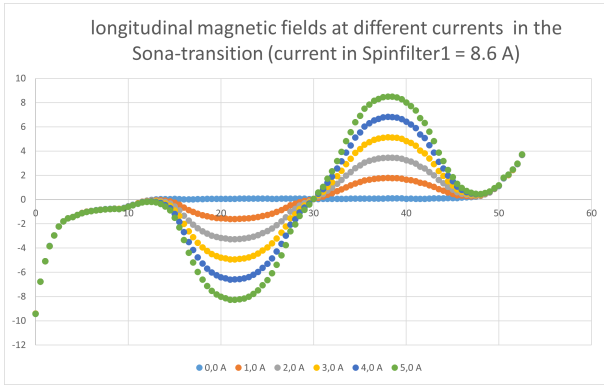


Figure 1: Longitudinal component of the magnetic field in the Sona-transition unit.

Because atoms and electromagnetic radiation usually hit at light speed, the use of much lower velocities enables access to corresponding smaller frequencies and photon energies.

In case of the used hydrogen, one or several of those photons can induce a transition between the Zeeman-states, if their energy equals the corresponding energy difference and if the selection rules allow it (see figure 2). A change of the amplitude of the B-field in the Sona-transition, necessary to change the position on the horizontal axis of figure 2 will not change the characteristic wavelength of the magnetic wave in figure 1, and, therefore, will also not change the energy of the photons determining the positions of the possible transitions. With the position of the peaks one can measure the function of the difference between the energy levels of the Zeeman-states.

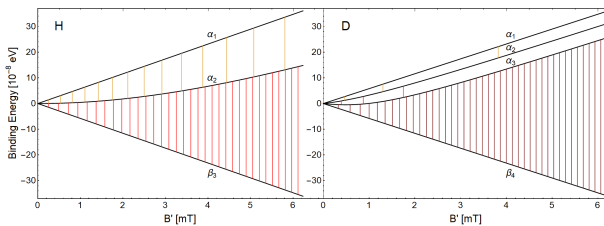


Figure 2: Transitions in the Breit-Rabi-Diagram of hydrogen (left) and deuterium (right).

This experiment has already been done for hydrogen and is supposed to be executed with deuterium. The most significant difference between deuterium and hydrogen is the nuclear spin: $I_H = 1/2 \leftrightarrow I_D = 1$. Therefore, there are different possible total angular momenta of the atom: $F_H = 0, 1 \leftrightarrow F_D = 1/2, 3/2$, causing, instead of 4, there are 6 Zeeman-states of which 4 states are accessible with existing spinfilters and a Sona-transition unit (see figure 2). Due to the existence of an additional α -state and the α -states being closer together the details of the produced spectra will be different. A simulation of the resulting atom distribution between the Zeeman-states of deuterium depending on the B-field in the Sona-transition unit is shown in figure 3 for an input of α_1 -atoms in the Sona-transition. The atoms get transferred to the β_4 -state and can be excited to the other Zeeman-states afterwards.

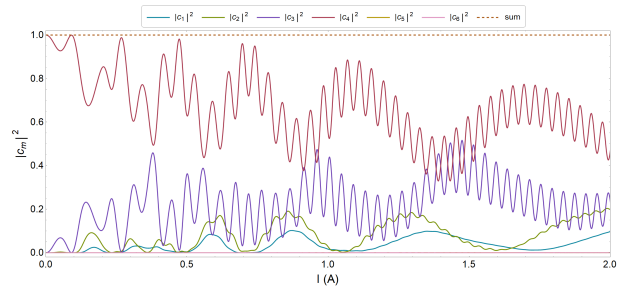


Figure 3: Simulation of the Zeeman-states of deuterium produced in the Sona-transition

In figure 3 one can see the distribution of α_1 - and α_2 -state occurrence in wider and distant peaks, mainly determined by the α_2 - α_1 - and α_3 - α_2 -transitions of small energy (see also figure 2). On the other hand the oscillations of the α_3 - and β_4 -state are much narrower and closer together, because of the larger distance between the α_3 - and β_4 -state energies. Because the atoms in most states stem from one of the other Zeeman-states displayed in figure 3, the occupation numbers are dependent on each other, which can be seen best in the α_2 -line, where the faster oscillation of the α_3 -line can be recognized as well.

References

- [1] Engels, R., Büscher, M., Buske, P. et al. Direct observation of transitions between quantum states with energy differences below 10 neV employing a Sona unit. *Eur. Phys. J. D* **75**, 257 (2021)

A bunch shape monitor for COSY

P. Niedermayer, B. Breitschütz

A bunch shape monitor based on capacitive pick-ups was developed and taken into operation at the Cooler Synchrotron COSY in 2021. The tool allows to monitor the evolution of the longitudinal bunch profile on a variable time-scale ranging from turn-by-turn measurements up to 1 s. Thereby, transient processes like (de-)bunching can be visualized, allowing the COSY operators to adjust and fine tune the RF system.

Implementation

COSY is equipped with 29 beam position monitors (BPMs) consisting of split-plane capacitive pick-ups [1]. In the course of the BPM system upgrade in 2017 [2, 3], LIBERA hadron beam position processors were installed for digitization at 250 MHz and signal processing. With up to 1 second of ADC data stored, the longitudinal signal of every bunch passing the pick-up can be reconstructed.

For processing of the ADC data, the signals of all four pickup plates are summed and the data stream is sub-sampled by selecting single bunch profiles at equal time intervals. Using the wrapped phase $\psi(t)$ and frequency $f(t)$ of the RF as provided by the control system, the bunch profiles are aligned such that the phase $\phi(t) = \psi(t) + \int_{t_0}^t f(\tau) d\tau$ is a multiple of 2π . Compared to a data based alignment, this approach also works during bunching, and allows to quantify bunch oscillations.

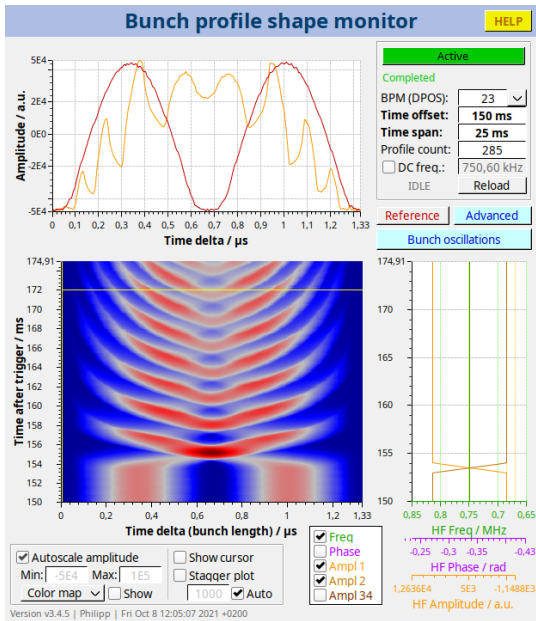


Figure 1: Bunch profiles during merging of two bunches. The upper plot shows the initial profile (red) and at $t = 156$ ms (orange, marker); the right plot the RF frequency and amplitudes.

Using a dedicated GUI (fig. 1), the aligned bunch profiles can be viewed online in a color-coded 2D plot, where the color represents the amplitude from blue (smallest) to red (largest). The bunch shape in the μs -scale is displayed on the x-axis; its evolution over several milliseconds on the y-axis. An adjustable marker can be used to view the bunch profile as waveform in the upper plot and slide through its evolution. On the right, the RF system parameters are plotted. The GUI and data processing is implemented with the Experimental Physics and Industrial Control System (EPICS), allowing for seamless integration into the COSY control system as well as central archiving of the data.

Optimisation of bunching process

Using the new diagnostic tool, the bunching process can be optimized by tuning the RF cavity frequency, phase and amplitude ramps. Fig. 2 shows the bunching process of a proton beam at 45 MeV injection energy for two different RF settings. The initially not well matched RF caused clearly visible distortions of the bunch profile. After measuring the revolution frequency of the coasting beam and adjusting the RF cavity accordingly, the bunch shape is much smoother and the head-tail oscillations are suppressed.

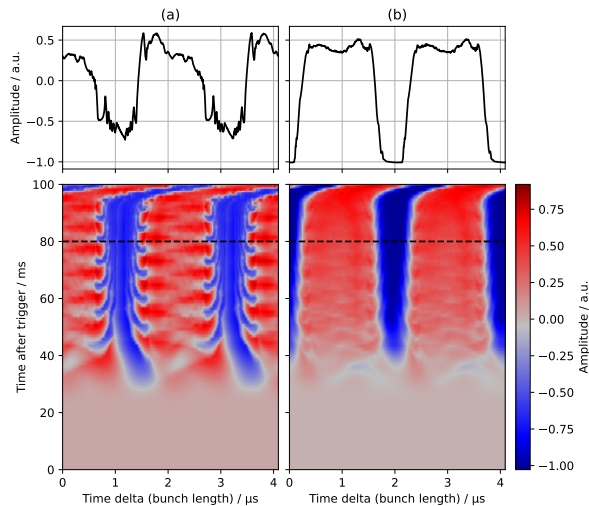


Figure 2: Bunch profiles during bunching at injection energy (a) before and (b) after the RF system was matched to the beam. The upper plots show the profiles at $t = 80$ ms shortly before the acceleration ramp starts. The plots show 2 consecutive turns.

Visualisation of transient processes

The developed bunch profile shape monitor allows to visualize transient processes. Fig. 1 shows the merging of two deuteron bunches at $p = 970$ MeV by switching the RF system from the $h = 2$ harmonic to the base frequency ($h = 1$) within 1 ms. The two bunches perform damped oscillations in the unified bucket.

Fig. 3 shows the transition from acceleration to flat top, where the proton beam is de-bunched at a momentum of $p = 3$ GeV/c. The RF voltage is linearly ramped down between $t = 30$ and 130 ms, causing the circulating beam to slowly become coasting. Thereby the off-momentum particles at the head and tail of the bunch run off in opposite direction. When they meet for the first time at about $t = 160$ ms, the ring is filled completely. The longitudinal intensity interference caused during this process is then slowly washed out over several hundred milliseconds.

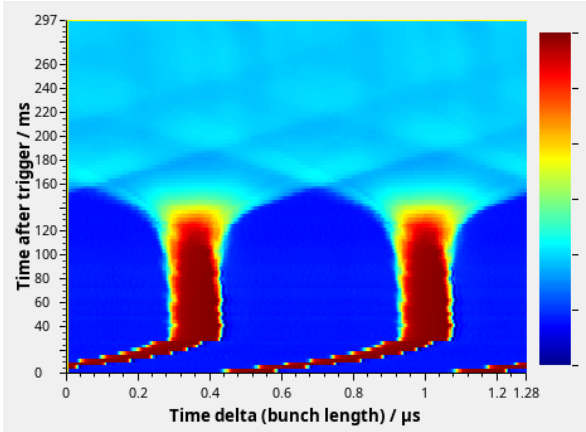


Figure 3: Bunch profiles at the end of the acceleration ramp ($t \leq 30$ ms) and subsequent de-bunching of the beam. The plot shows 2 consecutive turns at once.

Analysis of bunch oscillations

Fig. 4 shows the re-bunching of a $p = 970$ MeV deuteron beam in flat top with a mismatched RF frequency. In addition, the centre of gravity (COG) for the particle distribution in the bunch is plotted over time, and a frequency analysis (FFT) of this data is provided. This shows decaying bunch oscillations with a dominating longitudinal oscillation frequency of $f_s = 100$ Hz.

Outlook

The alignment of the bunch profiles using the analytic frequency integration method needs further improvement during acceleration. As can be seen in fig. 2 and 3, the bunches start to drift as

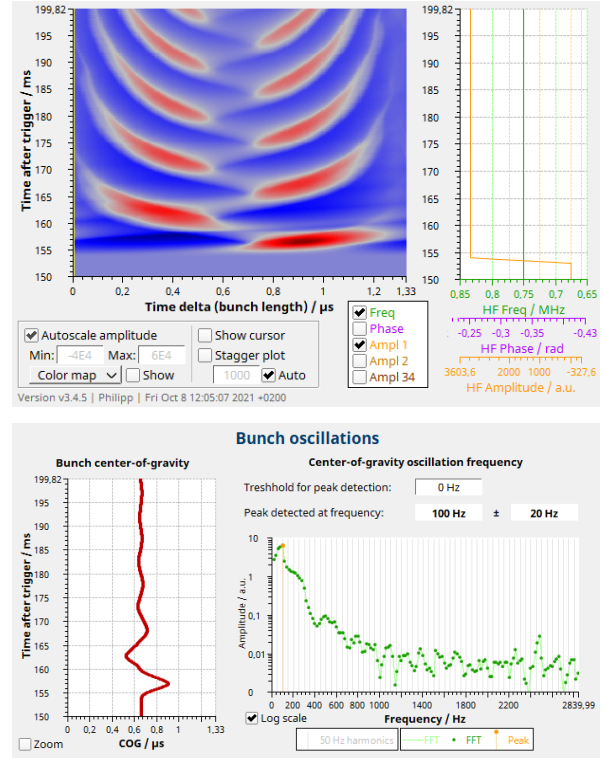


Figure 4: Bunch profiles during re-bunching of a coasting beam with a frequency mismatch (top) and analysis of the bunch oscillations (bottom).

revolution frequency changes rapidly.

Furthermore, it is planned to utilize the acquired bunch profiles and their evolution in time for reconstruction of the longitudinal phase space. Therefore, the method of *phase space tomography* [4, 5], invented by S. Hancock at CERN will be used.

References

- [1] R. Maier et. al.: *Non-Beam Disturbing Diagnostics at COSY-Jülich*. In: Proceedings of EPAC'90, Nice, France. JACoW Publishing, 1990, pp. 800–802. ISBN: 978-2-86332-090-7.
- [2] C. Böhme et. al.: *The upgraded beam position measurement system at COSY*. In: Short Reports, Annual Report 2017, Institut für Kernphysik · COSY, Jülich, 2017
- [3] V. Kamerdzhev et. al.: *BPM System Upgrade at COSY*. In: Proceedings of IBIC'18, Shanghai, China. JACoW Publishing, 2019. DOI: [10.18429/JACoW-IBIC2018-TUPC04](https://doi.org/10.18429/JACoW-IBIC2018-TUPC04).
- [4] S. Hancock et. al: *Tomographic Measurements of Longitudinal Phase Space Density*. In: Proceedings of EPAC'98, Stockholm, Sweden. JACoW Publishing, 1998.
- [5] tomograp.web.cern.ch/tomograp

Tomographic reconstruction of the longitudinal phase space evolution at COSY

P. Niedermayer, B. Breitschütz

The longitudinal charge distribution (bunch profile) and its time evolution can be measured at the Cooler Synchrotron COSY with a newly developed diagnostic tool [1]. Using a hybrid algorithm incorporating tomographic reconstruction and particle tracking [2], the longitudinal phase space is reconstructed as a function of time over the course of the measurement. In this report the phase space reconstruction method is demonstrated for different scenarios in presence of a bunching cavity.

Tomographic reconstruction algorithm

The reconstruction of the longitudinal phase space from measured bunch profiles is performed with a tomography algorithm incorporating particle tracking, which was developed by S. Hancock et al. [2, 3]. For classic algebraic reconstruction techniques [4], projections from different angles are required. The angle determines the projection coefficients for each one-dimensional measurement, which are essential to reconstruct the two-dimensional density distribution by means of an iterative back projection method. However, for the measured bunch profiles the projection angle with respect to the ΔE - Δt -phase space is fixed. Instead, the necessary rotation comes from the synchrotron motion of the particles, which move around the synchronous point in phase space. The method of S. Hancock et al. determines the projection coefficients for all measured profiles by tracking a small number of test particles in phase space and counting them along the Δt axis. While being computationally intense, this has the benefit of correctly dealing with non-linear motion of particles with large synchrotron amplitudes near the separatrix. [2]

Measurement at COSY: Hard bunch merging

During a dedicated beamtime at COSY in January 2021 bunch profile measurements were carried out. Figure 1 shows a measurement of two deuteron bunches being merged at $p = 970$ MeV by switching the COSY RF from the $h = 2$ harmonic to the base frequency ($h = 1$) within 1 ms. The process is purposefully performed in a non-adiabatic manner to initiate strong oscillations of the two bunches in the unified bucket.

The phase space as reconstructed from the measured data with the tomographic algorithm is shown in fig. 2. One can clearly identify the two bunches which are initially separated and start to fray and form filaments while circling around the synchronous point in phase space. The ergodic system eventually reaches an equilibrium state after several hundred synchrotron periods. In the bunch profile mea-

sured about 8 s after the merge (fig. 3, left), a double peak structure with valley is visible. Only the tomographic reconstruction reveals a hollow core in the phase space density distribution (fig. 3, right).

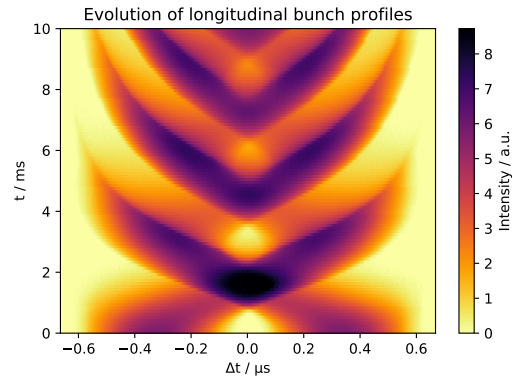


Figure 1: Evolution of the measured bunch profiles after switching the RF system from $h = 2$ to $h = 1$

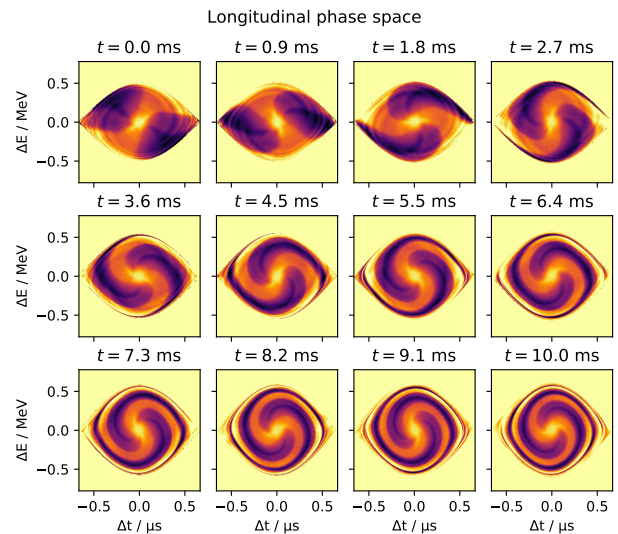


Figure 2: Phase space reconstructions for fig. 1

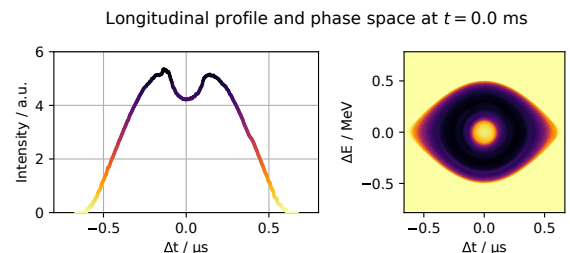


Figure 3: Stable bunch profile and phase space distribution about 8 s after the merge

Measurement at COSY: High gap voltage

In another experiment, the cavity gap voltage is set to $U_{\text{gap}} = 1.5$ kV, which is about twice the nominal value for bunched beam operation at constant energy. Figure 4 shows a bunch profile measurement of a deuteron beam which is bunched in this manner at $p = 970$ MeV. The measurement over a full synchrotron period shows a stable bunch core with pulsing extension at its head and tail.

The reconstruction of the phase space (fig. 5) reveals, that these extensions originate in a class of particles performing non-linear oscillations around the beam core near the separatrix. This asymmetric halo is clearly separated from the core and alternately appears at the head and tail of the bunch profile after every half synchrotron period.

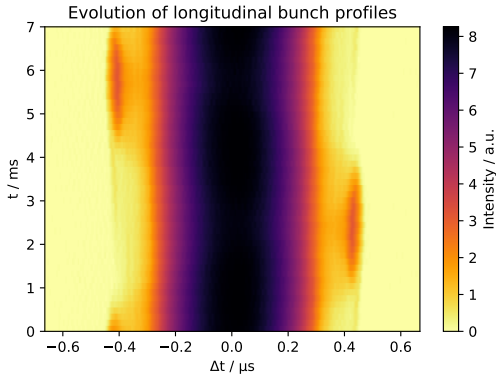


Figure 4: Evolution of the measured bunch profiles

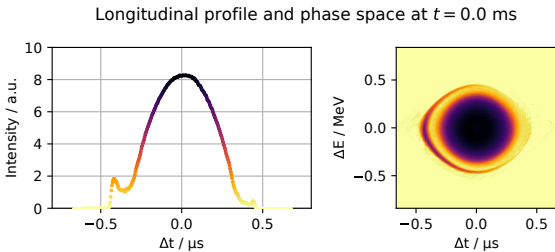


Figure 5: Bunch profile and corresponding phase space distribution

Measurement at COSY: Detuned rebunching

As a third experiment, the effect of a mismatched RF during bunching is demonstrated. Therefore a deuteron beam with momentum $p = 970$ MeV was rebunched with the frequency detuned by 0.2 ‰. This causes strong coherent synchrotron oscillations of about 100 Hz resulting in a distorted bunch shape (fig. 1). In phase space, the strong non-linearity of these oscillations becomes apparent (fig. 2). The particle density is high near the separatrix.

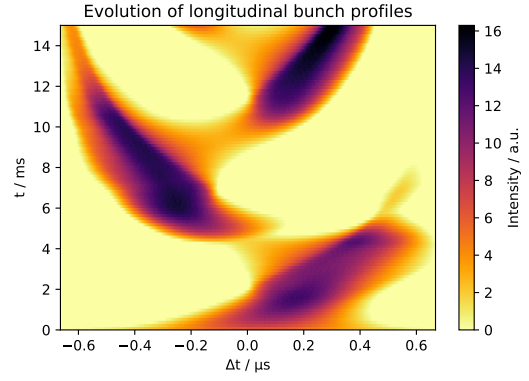


Figure 6: Evolution of the measured bunch profiles

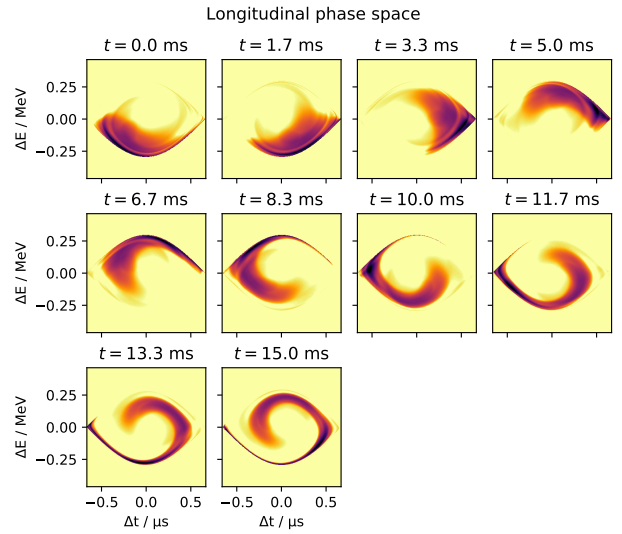


Figure 7: Phase space reconstructions corresponding to different measurement times in figure 6

Summary

The method for tomographic reconstruction of the longitudinal phase space was successfully applied at COSY. In extension to the recently developed bunch shape monitor, the reconstruction allows to visualize and thereby understand the underlying beam dynamic processes in detail.

References

- [1] P. Niedermayer, B. Breikreutz: *A bunch shape monitor for COSY*. In: Annual Report 2021, Institut für Kernphysik · COSY, Jülich, 2021
- [2] S. Hancock et al: *Tomographic Measurements of Longitudinal Phase Space Density*. In: Proceedings of EPAC'98, Stockholm, Sweden. JACoW Publishing, 1998.
- [3] tomograp.web.cern.ch/tomograp
- [4] R. Gordon et al: *Algebraic Reconstruction Techniques (ART) for three-dimensional electron microscopy and X-ray photography*. In: J. theor. Biol. 29, 1970.

First HESR Cavity prepared for COSY

B. Breitschütz, R. Stassen

The concept of the HESR RF-system was changed due to the postponed RESR. The RF-system of the HESR now consists of two identical cavities with a common low-level RF control (LLRF) [1]. Both cavities will be driven by low noise solid state amplifiers and will be cooled by forced air. Each cavity contains one gap and two tanks operating in push-pull mode. Each tank will house 6 ring cores wound of modern magnetic nano-alloy ribbon. Each ring will be separately coupled and fed through the outer conductor. This coupling scheme shows the following advantages:

- The combination of two cores connected to one amplifier gives the best rf-matching condition for all operation modes.
- The rings will only be selected in pairs.
- The influence of the parasitic elements of the rings is reduced. The individual compensation of the rings leads to a higher bandwidth compared to the usual gap coupling.

Further, series compensation has the higher bandwidth. The cavities will be used for acceleration/ deceleration with sinusoidal signals in the frequency range from 440 kHz to 520 kHz as well as barrier-bucket cavity during accumulation and experiment.

The COSY cavity is driven by an old tube amplifier. The tubes are now degrading. That limits the available voltage at the gap and leads to a reduction of the acceleration speed. New tubes would cost € 120,000. This is unprofitable in view of the limited term of COSY. After completing the measurements on the Palmer pick-up for stochastic cooling at CR, there was a possible installation position for the first HESR cavity in COSY. Thanks to the good cooperation between ZEA-1 and IKP-4, the necessary preparations were done in time and the first HESR cavity was installed in COSY during the last shutdown. Before that, the adaptation to the COSY frequency range and the first high-power tests were carried out.

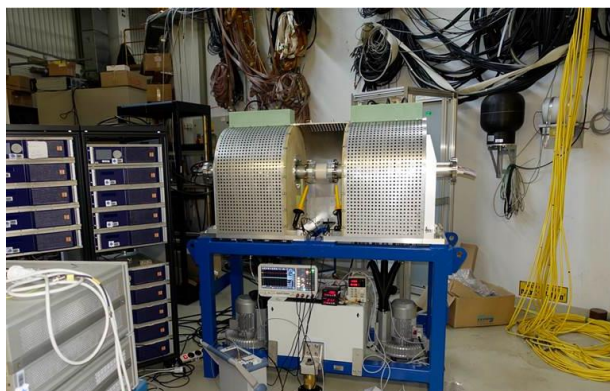


Figure 1: First HESR cavity in the test-field.

At lower frequencies up to 700 kHz the maximum peak to peak voltage was 6 kV while at frequencies above 700 kHz also 7 kV were possible. The limitation is not caused by the cavity but by switching off the amplifiers when the reflected power is too high. The design value to accelerate/decelerate antiprotons (pbars) in the HESR is $V_{pp}=1000V$. The additional

margin will allow a more efficient acceleration of heavy ions in the HESR.

The cavity was tested using the Barrier Bucket signal generator as installed at COSY and synchronized with the COSY RF [2]. A Barrier Bucket signal (BB) was created with a common pre-distortion although the cavity is driven with six independent amplifiers. The first measurement (Fig.3) shows a Barrier Bucket with a width of 20% of the beam revolution time and a peak-peak voltage of $V_{pp}=8.3$ kV. Only 10 harmonics were used and the ripple was lower than 1%. Further improvements are possible by the use of 20 Harmonics. The design value for the BB during the pbar operation at HESR is $V_{pp}=2.5$ kV.



Figure 2: A 20% Barrier-Bucket reaching peak-peak voltage of $V_{pp} = 8.3$ kV. Yellow: Voltage at the upstream-sided rings of the gap (1:1000), green: Voltage at the downstream-sided rings of the gap (1:1000), blue difference of both.

The next measurement was done using a 10% barrier bucket. Such a 10% BB will be used in the HESR during the accumulation of pbars. Here, a voltage of $V_{pp} = 5.6$ kV was reached taking into account 18 harmonics. The ripple is comparable with the 20% BB.



Figure 3: A 10% Barrier-Bucket reaching peak-peak voltage of $V_{pp} = 5.6$ kV. Yellow: Voltage at the upstream-sided rings of the gap (1:1000), green: Voltage at the downstream-sided rings of the gap (1:1000), blue difference of both.

Figure 4 shows the successful acceleration with the HESR cavity to a proton momentum of 531.3 MeV/c. The HESR cavity has enough reserve to operate COSY at its design acceleration rate of 1.15 MeV/c /ms.

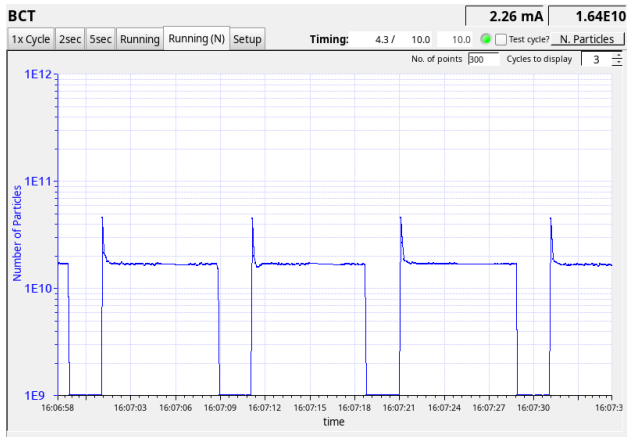


Figure 4: 1.6E10 protons in FT after acceleration to 531.3 MeV/c with HESR cavity.

References:

- [1] R. Stassen et. al.: “Recent Results of the HESR RF System”, Proceedings IPAC14, Dresden, Germany.
- [2] B. Breitkreutz et. al.: “A FPGA-Driven Signal Source for the Barrier Bucket Cavity at COSY”, IKP Annual Report 2017, Juelich, Germany.

Modernisation of the Stripline Unit Signal Conditioner at COSY

M.Kaczmarek, B.Breitkreutz, K.Reimers

The stripline unit [1] is a system for beam excitation transversally in the modes horizontal, vertical and diagonal. The stripline electrodes of the kicker are positioned in a 45° angle to the horizontal or vertical plane (see Figure 1) to maximize horizontal beam aperture. The signal conditioning electronics as well as the RF power amplifiers are located in the COSY hall close to the stripline unit. The input signal is provided by various other systems depending on the purpose of beam excitation. Typical use cases are tune and chromaticity measurements as well as beam extraction onto an internal target.

Motivation and Upgrade

The stripline unit system needed to be upgraded due to reliability issues with the communication to the device and due to the hardware having reached end of life. The need for EPICS integration pushed for the hardware upgrade as well. The new system is built around an ethernet-capable 4-channel attenuator [2].

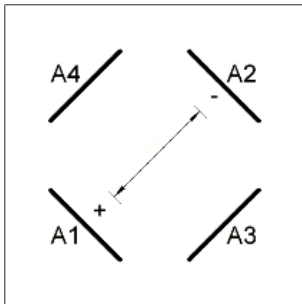


Figure 1: Arrangement of stripline electrodes showing diagonal excitation.

By combining neighbouring electrodes in vertical or horizontal mode and providing band limited white noise signals to these electrode pairs horizontal and vertical beam excitation is achieved.

The four channels of the attenuator provide an attenuation of 0 dB to 95dB independently.

It is a USB powered device with four I/O channels and a build-in network connection with a pre-defined API, hence reducing programming effort and hardware engineering work as well.

The maximum attenuation of up to 95 dB exceeds the electric isolation of RF-relays, having been observed with roughly 70 dB attenuation in open switch mode, is a further benefit.

The stripline unit is provided with two equal rated inputs allowing a choice between two independent signals. The attenuator is embedded in a matrix of splitters, combiners, recovery amplifiers and 180° hybrids [3]. When combining the signals, they can

cancel out or add the counterphase coupling of signals in the hybrids. The intrinsic attenuation by the hybrids, splitters and combiners is compensated by matching recovery amplifiers. The output signals are amplified by four power amplifiers and provide sufficient signal power to the electrodes. The new stripline unit set up (see Figure 2) is integrated into the EPICS control system of COSY [4] and has already been used successfully for different tune measurement settings.

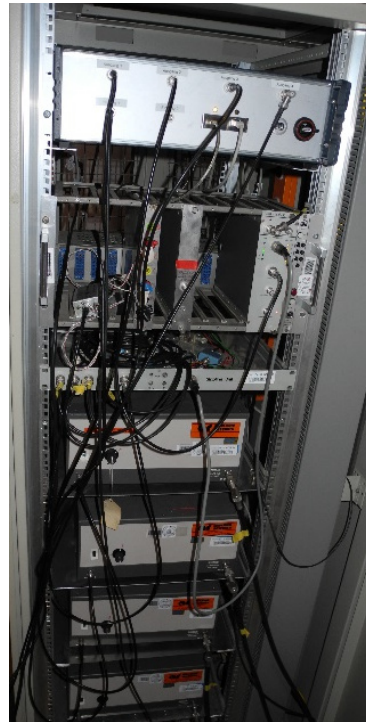


Figure 2: The complete rack with the new signal conditioner on the top, the old one in the middle and 4 power amplifiers below

References

- [1] Stripline unit website: <https://gitlab.cce.kfa-juelich.de/BCC/strip-line-unit/gui-stripline/-/wikis/Help-Stripline-Unit>
- [2] Attenuator data sheet: <https://www.minicircuits.com/WebStore/dashboard.html?model=RC4DAT-6G-95>
- [3] Minicircuits products Website: <https://www.minicircuits.com> - splitters, combiners, attenuators, small signal amps, hybrids, phase shifters
- [4] assignment of channels in GUI: <https://gitlab.cce.kfa-juelich.de/BCC/strip-line-unit/gui-stripline/-/wikis/New-assignment-ATT-channels-of-SU>

The HESR Scrapper from Radiation Protection's point of view

N.Guirgues, O.Felden

In the HESR synchrotron, the scraper device is implemented to create a more focused particle beam by degrading particles that travel with large amplitudes along the central beam axis. This will be achieved once these particles collide with scraper's metal rods, depositing a part of their energy in the rods, which slides in from each side (right, left, up, down) towards the beam. Thus, these particles leave the rods with a lower kinetic energy, which in turn sends them to a dispersive trajectory and finally they will collide with the beam pipe. This energy deposition within the rods causes activation of the material producing radioactive isotopes. These isotopes will later decay with their half lives emitting ionizing radiation giving a dose field around the scraper which can be harmful to personal working in this area. To get an overview of the doses to be expected and to take necessary measures for safe working conditions simulation of the scraper have been performed. Figure 1 shows a simplified model of the scraper and rods and their position relative to the circulating beam.

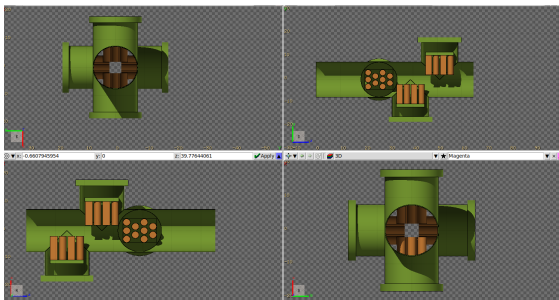


Figure 1: opened Scraper; All rods are slid into the beampipe but giving an open space in the middle of the beampipe for the circulating beam

In FLUKA-simulations radiation protection related questions like remanent dose rate near the scraper device or activation in view of releasing the scraper from the controlled area after HESR decommissioning, were analyzed. In the simulation a 3%-loss of the beam particles was assumed. The analysis showed that the remanent equivalent dose rate due to

activation (figure 2) is $\sim 0,5\text{mSv/h}$ in 1m distance from the scraper immediately after an experimental run. This high dose rate is mostly driven by short lived isotopes, which will decay very fast after stopping the beam. Looking at the remanent dose rate at different times after shutting down the beam, it shows that the dose rate will reduce fast, down to a value in the $\mu\text{Sv/h}$ -range within a day.

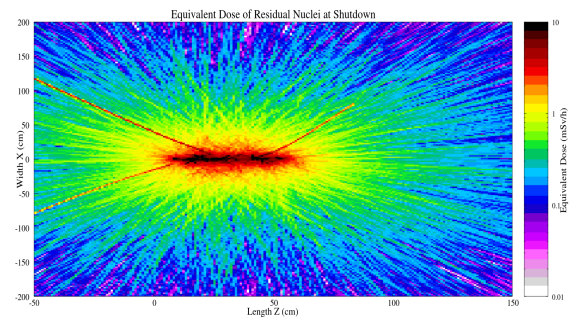


Figure 2: Remanent dose rate after an experimental run. The dose rate in 1m distance is $\sim 0.5\text{mSv/h}$

Another important question are the radioactive nuclides, produced during an assumed operation of the scraper of 30 years. The activity of the different isotopes will give the criteria if the scraper can be released from radiation protection areas when decommissioning HESR. The Fluka simulation show, that most of the nuclides we don't have to pay much attention when decommissioning HESR but Co-60. It will take 15-20 years to under come the threshold, given by German law, to release the rods from radiation-protected areas.

Energy loss, particle production and activation in the HESR SCRAPER, Bachelor thesis
M.T.W.G. Guirgues, 2021

Measures at the BigKarl -Area for the High Brilliance Neutron Source (HBS)

M.Rimmler, O.Felden

After first successful neutron related experiments at NESP in the BigKarl-Area of COSY the idea invoked to set up a Target-Moderator-Prototype (TMR, fig.1) for testing different target materials, handling of activated targets or different cooling schemes of the target e.g..

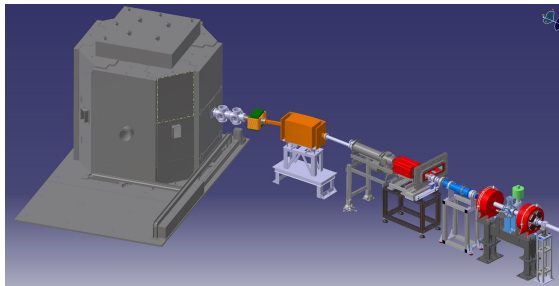


Figure 1: TMR (left) with NESP-Beamline

The TMR can be equipped with different experimental setups to optimize the interplay between neutron production and measurement at the experiment. To achieve these goals the beam intensity needs to be increased. Due to the actual shielding of BigKarl area beam intensity is limited to 10nA. To increase it by a factor of 1000 to 10μA additional shielding is needed. With FLUKA dose rate simulations at BigKarl area, building 07.2 and the surrounding was performed (Fig2). Two loss scenarios have been looked at: left part of the picture shows the full loss of

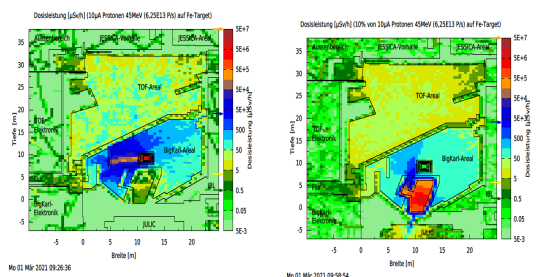


Figure 2: Dose rate simulations with beam losses at TMR (left) and in the beamline towards the TMR (right) the 10μA-beam inside the TMR while the right side shows a 10%-beam loss at the beam line from the cyclotron vault towards the TMR. It shows that shielding the beam line with a new bunker by wall thicknesses of 1m and the actual TMR shielding design will be sufficient to stay below the dose-rate thresholds given by law outside the restricted areas.

At the later to build HBS-facility the proton beam will go with different time structures and repetition rates to 3 different target stations. Therefore, a 3-field multiplexing magnet was designed.

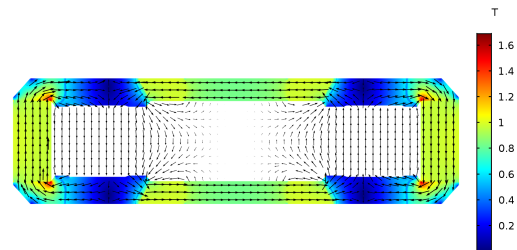


Figure 3: 3-field multiplexing magnet

This multiplexer magnet is made from permanent magnetic material with 3 field regions (fig. 3), deflecting the proton beam to the left or right direction or without deflection going straight. To prove this concept a 3-field multiplexing magnet with smaller deflecting ratios was designed and build. Figure 3 shows

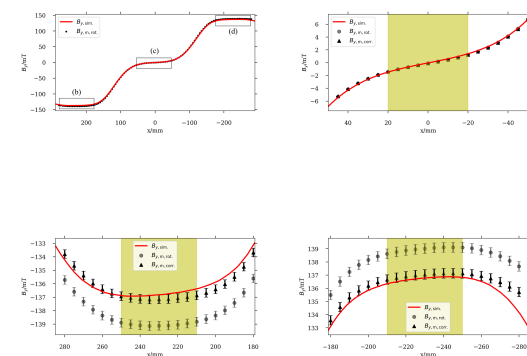


Figure 3: 3-Field-Magnet with measured and calculated field strengths.

the magnetic field calculations (red line) in comparison to the magnetic field strength measurements (black crosses) which match very well. By inserting iron plates, the field strength can be enlarged but not affecting the homogeneity in these regions.

Development of a multiplexer system and measurement of the neutron yield for a low-energy accelerator-driven neutron source, M.-Rimmler, Phd thesis, 2021

Toward a direct measurement of the deuteron EDM at COSY

V. Shmakova on behalf of the JEDI collaboration

The Standard Model (SM) of Particle Physics cannot explain the matter-antimatter asymmetry in the Universe. Therefore, the search of physics beyond the SM is required and one way to achieve it is to strive for the highest precision in the search for electric dipole moments (EDMs). Permanent EDMs of particles violate both time reversal and parity invariance, therefore, with CPT conserved, EDMs violate also the CP-symmetry. Finding an EDM would be a strong indicator for physics beyond the SM. This report presents preliminary results of the precursor experiment which is the first stage of the experimental program to determine the EDMs of proton and deuteron using storage ring [1], [2]. The Thomas-BMT equation describes the spin motion in a ring with radial electric \vec{E} and vertical magnetic field \vec{B} [3], [4],

$$\begin{aligned} \frac{d\vec{S}}{dt} &= \Omega \times S = \\ &= -\frac{q}{m}(G\vec{B} - (G - \frac{1}{\gamma^2 - 1})\vec{\beta} \times \vec{E}) + \frac{\eta}{2c}(\vec{E} + c\vec{\beta} \times \vec{B}) \end{aligned}$$

An EDM causes the invariant spin axis in the ring to tilt in the radial direction. In reality, however, there are additional magnetic misalignments, which is why the invariant spin axis is tilted in both radial and longitudinal directions. The direction of the invariant spin axis provides an experimental access to the EDM.

To induce the vertical polarisation oscillation, the

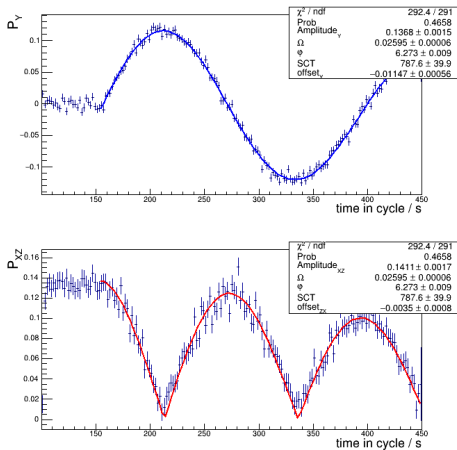


Figure 1: Combined fit of the vertical p_y (up) and horizontal p_{xz} (down) polarization for Wien filter rotated to $\phi^{\text{WF}} = -2$ deg, snake on $\chi^{\text{sol}} = -0.89$ deg (2 A).

RF Wien filter [5] was operated on one of the harmonics of the spin precession frequency [2]. The fast

switches allowed us to gate one of the bunches in the ring from the Wien filter RF, so that only one of the two bunches (signal bunch) was effected by the Wien filter field, the second bunch (pilot bunch) was used for the feedback phase locking. The polarization oscillation frequency is obtained by a combined fit of the time dependencies of both vertical p_y and horizontal p_{xz} polarizations, an example of such a fit is shown on the Fig.2. This frequency is related to the EDM resonance strength via $\epsilon^{\text{EDM}} = \frac{\Omega^{p_y}}{\Omega^{\text{rev}}}$. Measurements were performed for several rotation angles around the beam direction of the RF Wien filter (ϕ^{WF}) and for several magnetic field settings of the Siberian snake (χ^{sol}) on the opposite side of the ring, to rotate the invariant spin axis in the longitudinal direction. An example of the resulting map for the resonance strength versus Wien filter and snake angles is shown in Fig.2. The minimum of the map determines the orientation of the invariant spin axis.

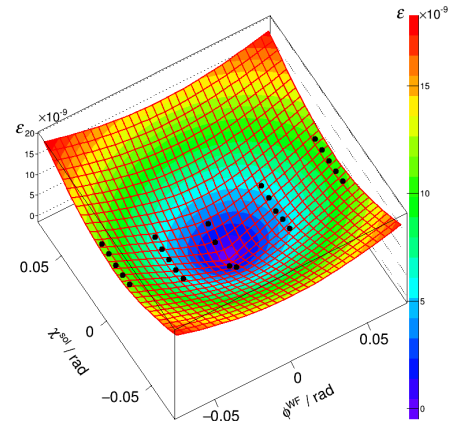


Figure 2: The map of the resonance strength ϵ^{EDM} for various Wien filter angle ϕ^{WF} and Sibirien snake spin rotation angle χ^{sol} .

References

- [1] F. Abusaif *et al.*, Storage ring to search for electric dipole moments of charged particles: Feasibility study, arXiv:1912.07881v3.
- [2] F. Rathmann, N.N. Nikolaev, J. Slim, Phys. Rev. Accel. Beams 23 (2020) 024601.
- [3] T. Fukuyama and A. J. Silenko, Int. J. Mod. Phys. A28 (2013) 1350147.
- [4] A. Saleev *et al.*, Phys. Rev. ST Accel. Beams 20 (2017) 072801.
- [5] J. Slim *et al.*, Nucl. Instrum. Methods Phys. Res. A 828 (2016) 166.

Study of Beam dynamics of Prototype Electric Dipole Moment Storage Ring

S. Siddique for the JEDI Collaboration

This report covers beam simulations of a prototype EDM storage ring. Four different lattices with different focusing strengths ($\beta_y = 33, 100, 200, 300$) were generated by Bmad studied in context of beam losses. Analytical calculations were performed for four major effects of beam losses under two different scenarios, with residual gas and with a polarimeter target to measure the beam polarization.

The objective of these calculations is to find an optimise lattice with minimum systematic effects and maximum beam lifetime. Four major beam loss processes named as Hadronic interactions, Coulomb scatterings, Energy loss straggling and IntraBeam scatterings (IBS) were studied and applied analytically. The basic beam loss rate formula for hadronic and coulomb scatterings is

$$1/\tau = n\sigma_{tot}f_{rev}, \quad (1)$$

where n is the particle density and σ_{tot} is total cross section and f is the revolution frequency of the proton beam which is 0.726 MHz in this case.

The nitrogen equivalent pressure is $3.73 \cdot 10^{-9}$ Pa and the mixture of two gasses H_2 and N_2 in ratio of 80 : 20 with density of $5.30 \cdot 10^5$ atoms/cm³. The total cross section was taken from [1] for hadronic interactions and Rutherford formula was considered for coulomb scatterings

$$\sigma = 4\pi \frac{Z_1^2 Z_2^2 r_p^2}{\beta^4 \gamma^2 \theta_{cut}^2}, \quad (2)$$

where Z_1 and Z_2 are charge numbers of target and projectile and $r_p = 1.525 \cdot 10^{-18}$ m the classical proton radius and θ_{cut} is acceptance angle which depends on the ring acceptance A_{acc} and betafuncions β_x, β_y as

$$\theta_{cut} = \sqrt{\frac{A_{acc}}{\beta_{\perp}}}. \quad (3)$$

Initially calculations were performed with hydrogen pellet with target thickness of $4.0 \cdot 10^{13}$ atoms/cm² to scatter the polarized beam to measure the polarization. However at given beam energy, the precise polarization measurement are only possible with carbon targets, therefore later a carbon target with thickness of around $1.6 \cdot 10^{12}$ atoms/cm² was used to get beam loss estimations. In the presence of a target, the effects of the residual gas on the beam are negligible because the thickness of the target is much greater than the integral density of the residual gas over the circumference of the ring.

The beam loss rate due to energy loss straggling is close to zero because of low beam energy and high longitudinal acceptance. After a small energy loss,

the particles remain in stable part of longitudinal bucket and are not lost. The fourth effect of beam loss plays an important role.

The Touchek effect is a special case of IBS. Strong coulomb scattering within the beam causes a change in particle's direction and ultimately particles start to slip away from their stable region. This effect depends on beam density and longitudinal momentum acceptance of beam and its emittance [1]. The calculations show that coulomb scattering effect is most dominating effect which causes beam loss followed by IBS effect

$$1/\tau = \frac{N\sqrt{\pi}cr_p^2}{4\beta^3\gamma^3 \langle \sqrt{\beta_{\perp}} \rangle C\epsilon_{\perp}^{3/2}}, \quad (4)$$

where N is beam density, ϵ is beam emittance and $\gamma\beta$ are lorentz factors and $\langle \sqrt{\beta_{\perp}} \rangle$ is the average of betatron functions. C is ring length and c is speed of light and r_p is radius of proton.

Hence, the total beam lifetime due to effects discussed above is shown in plot for both targets. It can be seen that a carbon target causes more beam losses than a hydrogen target. One of the reason is the charge number of target. However, further investigations are being performed by considering a software named BETACOOOL [2] for beam losses and emittance growth rate.

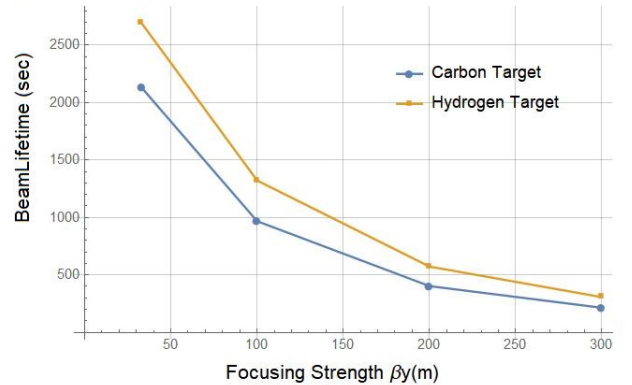


Figure 1: Beam lifetime vs lattice focusing strength, where carbon effective thickness is $1.6 \cdot 10^{12}$ atoms/cm² and for hydrogen is $4.0 \cdot 10^{13}$ atoms/cm²

References

- [1] F. Hinterberger, *Beam-target interaction and intrabeam scattering in the HESR ring*, tech. report.
- [2] A. Sidorin *et al.*, *BETACOOOL program for simulation of beam dynamics in storage rings*, (2006).

Progress toward a direct measurement of the deuteron Electric Dipole Moment at COSY

A. Andres for the JEDI Collaboration

This report covers the current progress of the analysis of the Precursor II 2021 Run at COSY for the search of Electric Dipole Moments of deuterons carried out by the JEDI Collaboration.

The Standard Model of elementary particle physics and cosmology cannot explain the matter-antimatter asymmetry in the universe. According to A. Sakharov, CP violating phenomena are needed to understand the matter-antimatter asymmetry. Permanent Electric Dipole Moments (EDMs) of subatomic elementary particles violate both time reversal and parity asymmetries. Their existence also violates CP symmetry if the CPT-theorem holds.

The collective spin motion of a polarized particle bunch inside a storage ring can be characterized by the so-called invariant spin axis \vec{n} , defined by the rotation axis around which the polarization precesses. The existence of an EDM would tilt the invariant spin axis from initially vertical in radial direction in an ideal storage ring. The goal of the experiment is to measure the direction of the invariant spin axis. However, magnetic misalignments lead to additional tilts in longitudinal and radial direction. Therefore, the results need to be compared to a full simulation model of COSY to disentangle the true EDM signal from signals caused by magnetic misalignments.

During the experiment, a new method for measuring the orientation of the invariant spin axis is used. This method is based on two bunches in the machine. One of the bunches (signal bunch) is affected by the RF Wien Filter which is operated on one of the harmonics of the spin precession frequency (≈ 871 kHz). The second bunch (pilot bunch) is not influenced by the Wien Filter fields and used to run the phase feedback system. It can be shown, that the vertical polarization of the pilot bunch starts to oscillate with

$$p_y(t) = a \sin(\phi_{\text{rel}}) \cdot \sin(\omega \cdot t) \cdot \exp(-\text{SCT} \cdot t), \quad (1)$$

where ϕ_{rel} denotes the fixed relative phase between Wien Filter RF and spin precession. An example of signal and pilot bunch along with a least square fit according to equation (1) is shown in Figure 1. The main observable of the experiment is the oscillation frequency of the vertical polarization ω . In addition, an exponential decay function takes depolarizing effects (Spin Coherence Time) of the particle bunch into account. Knowing the oscillation frequency, the resonance strength ε can be determined using

$$\varepsilon = \frac{\omega}{2\pi f_{\text{rev}}}. \quad (2)$$

The resonance strength ε , plotted as a function of Wien Filter rotation angle ϕ^{WF} and spin rotation

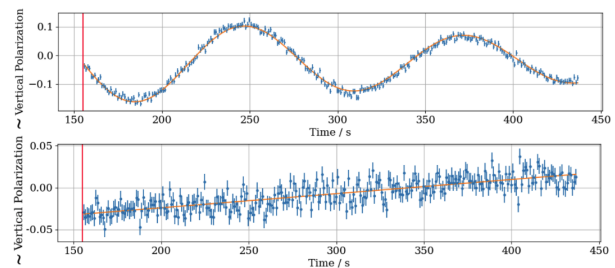


Figure 1: **Top Panel:** Oscillation of the vertical polarization p_y of the signal bunch with a least square fit according to Eq. 1. **Lower Panel** Vertical polarization of the pilot bunch not affected by the Wien Filter fields.

angle ξ^{SOL} caused by the Siberian Snake is shown in Figure 2 along with a paraboloid fit [1]

$$\varepsilon = \left[A_{\text{WF}}^2 (\phi^{\text{WF}} - \phi_0^{\text{WF}})^2 + A_{\text{Sol}}^2 \left(\frac{\xi_0^{\text{Sol}} - \xi^{\text{Sol}}}{2 \sin(\pi \nu_{s,0})} \right)^2 \right]^{\frac{1}{2}}. \quad (3)$$

The minimum of the surface denotes the orientation of the invariant spin axis. The current results read

$$\phi_0^{\text{WF}}/\text{mrad} = -2.05 \pm 0.02, \quad (4)$$

$$\xi_0^{\text{SOL}}/\text{mrad} = 4.32 \pm 0.06. \quad (5)$$

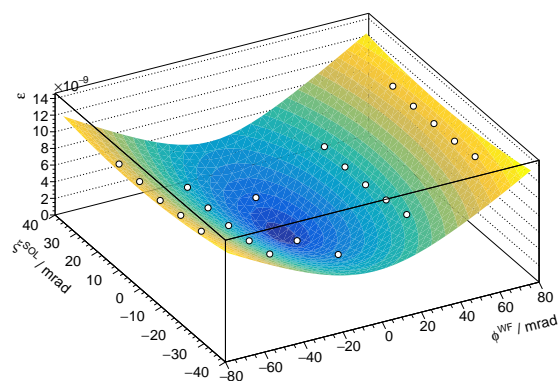


Figure 2: EDM Resonance Strength ε as a function of Wien Filter rotation angle ϕ^{WF} and spin rotation angle caused by the Siberian Snake ξ^{SOL} .

References

- [1] F. Rathmann, N. Nikolaev, and J. Slim, Spin dynamics investigations for the electric dipole moment experiments, Physical Review Accelerators and Beams, 23 (2020).

Orbit response matrix calculation of an idealized COSY model using Bmad

M. Manerova on behalf of the JEDI Collaboration

This report includes the implementation of the orbit correction, namely by calculating the orbit response matrix (ORM) of COSY using Bmad. For the analysis two data sets for the field strength of the quadrupole magnets were used, from February and April 2021, as well as the settings for the correcting magnets from April 2021.

The orbit response matrix in theory only depends on the beta functions and phases of the betatron at the beam position monitors (BPM). However, optical errors such as quadrupole strength, magnet misalignment or roll angles are also to be considered. Taking these errors into account, it is possible to acquire information about the field deviations, which cause the discrepancy between the measured and the desired orbit. To get closer to the target orbit, a correction system has to be implemented. In order to manipulate the orbit, corrector magnets are used. They are needed to influence the orbit locally or the beam focusing to correct the alignment errors of the main magnets. It is important to know the impact of each individual correcting magnet on the orbit in order to find their best field strength configurations. The ORM has proven to be a useful tool for conducting required analyses.

Given m BPMs and n steerer magnets in horizontal and vertical position and θ_x, θ_y represent the strengths of the corrector kicks in both directions, the closed orbit position is denoted by \vec{x} and \vec{y} . The orbit response can therefore be written as

$$\begin{pmatrix} \Delta \vec{x} \\ \Delta \vec{y} \end{pmatrix} = \mathbf{R} \begin{pmatrix} \Delta \theta_x \\ \Delta \theta_y \end{pmatrix}. \quad (1)$$

The resulting $m \times n$ dimensional matrix \mathbf{R} is the orbit response matrix describing the BPM responses $i = 1, \dots, m$ to a perturbation at steerer magnet $j = 1, \dots, n$.

Given the Twiss parameters and the betatron tune Q of the accelerator on the beam position monitors and the corrector magnets, the elements of an ORM can be calculated as

$$R_{ij} = \frac{\sqrt{\beta_{x,i}\beta_{x,j}}}{2 \sin(\pi Q_x)} \cos(\phi_{x,i} - \phi_{x,j} - \pi Q_x) - \frac{D_i D_j}{(\alpha_p - \frac{1}{\gamma^2} C)} \quad (2)$$

$$R_{ij} = \frac{\sqrt{\beta_{y,i}\beta_{y,j}}}{2 \sin(\pi Q_y)} \cos(\phi_{y,i} - \phi_{y,j} - \pi Q_y) \quad (3)$$

for horizontal and vertical components, respectively.

With Bmad it was possible to calculate the matrix for COSY with settings for both the

main quadrupoles as well as for the correcting magnets, using data obtained in April 2021. The calculated ORM is displayed in figure 1.

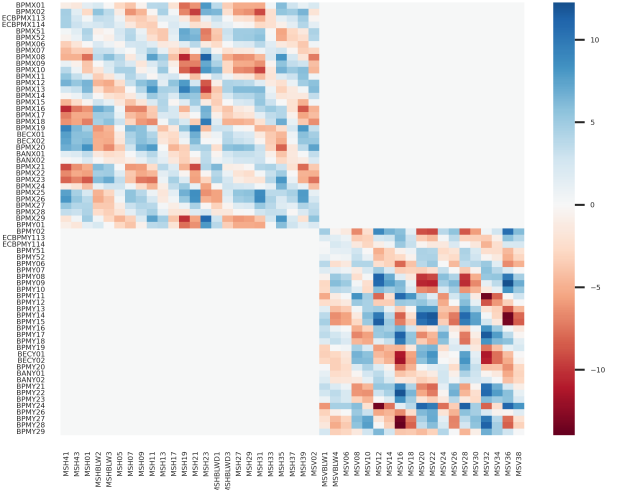


Figure 1: Orbit response matrix \mathbf{R} .

The matrix calculation will further contribute to the orbit matching procedure, i.e. calculation of the excitation strengths θ of the correctors using a singular value decomposition method. The routine for orbit matching has yet to be implemented.

References

- [1] Hoffstaetter, G.H., Keil, J. and Xiao, A., *Orbit-response matrix analysis at HERA*, 8th European Particle Accelerator Conference, 2002
- [2] Weidemann C., Bai, M., Hinder, F., Lorentz, B., *Model Driven Machine Improvement of COSY Based on ORM Data*, 7th International Particle Accelerator Conference, 2016
- [3] Zimmermann, F., *Measurement and correction of accelerator optics*, Joint US-CERN-Japan-Russia School on Particle Accelerators: Beam Measurement, 1998

Simulation of the spin coherence time for proton beams with BMAD

Daoning Gu on behalf of the JEDI Collaboration

Optimization of the Spin Coherence Time (SCT) plays a central role in storage ring EDM experiments, since a large SCT is required to achieve the statistical sensitivity for an EDM measurement. The larger gyromagnetic anomaly indicate that for proton beams, the optimization procedure to realize long SCT is more difficult than for deuteron beams. Therefore, spin tracking simulations were performed with the software library BMAD.

In an idealized COSY lattice from the second precursor run for deuterons, where misalignments of the magnets are not taken into account, the transverse betatron tunes are ($Q_x=3.63$, $Q_y=3.72$) and the natural chromaticities are ($\xi_x=-4.25$, $\xi_y=-3.94$) when all sextupoles are turned off. As the length of SCT depends on the beam parameters, simulations were performed to vary the emittance in a range of 1 to 6 mm mrad for the horizontal and vertical planes. The results in Figure 1 clearly show that there are linear relations between the emittances and the reciprocal of SCT.

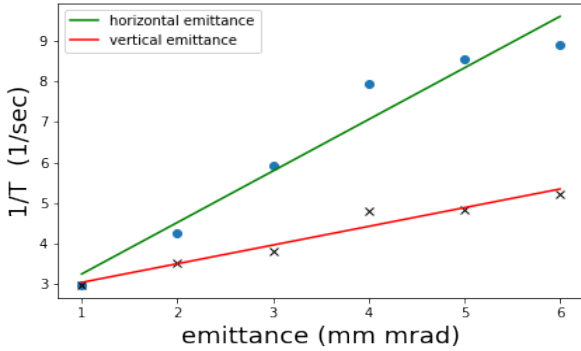


Figure 1: Simulated results for spin coherence time and emittances.

Spin tune spread leads to a shorter SCT. The main contributions to this are average path length change due to betatron and synchrotron motions as well as intrinsic resonances. The fraction of the betatron motion component can be expressed by the following equation [1]:

$$\langle \left(\frac{\Delta C}{C_0} \right)_\beta \rangle = -\frac{\pi}{C_0} (\varepsilon_x \xi_x + \varepsilon_y \xi_y).$$

In order to find the possible chromaticity (ξ_x, ξ_y) values, a 3D scan routine [2] for adjusting the sextupoles settings is used. The three groups of sextupole (MXS, MXL and MXG) in COSY are located at the large places of β_x , β_y and dispersion in the arc parts, respectively [3]. After two iterations to find a specific chromaticities setting. First do a rough scan to locate approximate ranges. Then the second iteration uses these ranges to perform a finer scan.

The results of scanning and spin tracking simulations as well as second order momentum compaction factor α_1 are shown in the Table 1:

Table 1: Scanning and spin tracking results

(ξ_x, ξ_y)	(0,0)	(0,-1)	(-1,0)	(1,0)	(0,1)
SCT (s)	0.54	0.71	0.81	0.80	0.76
α_1	-5.60	-3.19	-1.94	0.99	1.92

It can be seen, that zero chromaticity is not the point where the SCT is maximum. The smaller the α_1 in the vicinity the longer the SCT.

Instead of performing a full chromaticity scan, which would consume too much computing time, the sextupole settings of the minimum spin-tune spread ($\Delta\nu_s$) can be found from the relationships between $\Delta\nu_s$ and the beam parameters. For a single particle with a horizontal or vertical offset, you can change the settings of the MXG sextupoles, while all other groups of sextupoles are set to zero. The difference between spin tune of a offset particle and the reference particle is calculated. The optimized settings for minimum $\Delta\nu_s$ can be obtained by flattening the resulting parabolas (see Figure 2). This was inspired by Aleksei Melnikov's optimization work with another simulation code package COSY Infinity. My next step is to implement the approach in BMAD and complete the corresponding optimizer.

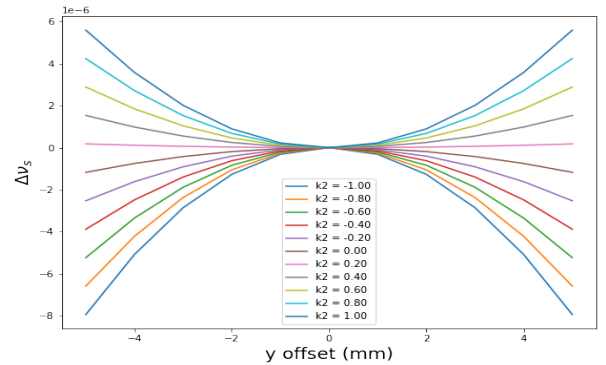


Figure 2: Spin-tune shift for a particle with vertical offsets relative to the reference particle at different sextupole settings.

References

- [1] M. Rosenthal. PhD thesis, RWTH Aachen University, 2016.
- [2] M. Vitz. Master thesis, RWTH Aachen University, 2020.
- [3] G. Guidoboni et al., Phys. Rev. Accelerators and Beams 22 (2018) 024201.

Investigation of the proton Spin Coherence Time (SCT) at storage rings

A. Melnikov on behalf of the JEDI Collaboration

This report covers the studies of methods to increase the proton SCT at PTR (Prototype EDM Ring) and COSY storage ring. Sufficient SCT is obligatory for the planned charge particle Electric Dipole Moment (EDMs) measurement experiments at storage rings. Optimization of SCT in proton case is much more challenging than for the deuteron due to higher anomalous magnetic moment and therefore needs detailed investigation. It has been shown that the second order momentum compaction factor – α_1 has to be optimized along with chromaticities to get high SCT. Three families of sextupoles have to be used.

The first step in optimization of SCT, referring to [1], is inserting an RF cavity to suppress the first order spin-decoherence. In the case of PTR it helped to increase SCT from 0.01 to 10 s.

In the presence of an RF cavity longitudinal motion is nonlinear in general case. The solution of nonlinear equations for the principle of synchronous acceleration gives the rise of average energy level [1]. It can be related to $\Delta\delta_{eq}$:

$$\Delta\delta_{eq} = \frac{\gamma_s^2}{\gamma_s^2\alpha_0 - 1} \left[\frac{\delta_m^2}{2} \left(\alpha_1 + \frac{3}{2} \frac{\beta^2}{\gamma^2} - \frac{\alpha_0}{\gamma_s^2} + \frac{1}{\gamma_s^4} \right) + \left(\frac{\Delta L}{L} \right)_\beta \right], \quad (1)$$

where

$$\left(\frac{\Delta L}{L} \right)_\beta = -\frac{\pi}{L_0} [\epsilon_x \xi_x + \epsilon_y \xi_y]. \quad (2)$$

From (1) and (2) it can be seen that ξ_x, ξ_y, α_1 have to be optimized to influence nonlinear longitudinal and spin motion. For the PTR case, the optimization of two arc sextupole families gives a maximum SCT of about 150 s. But with two sextupole families it is not possible to optimize all three parameters – ξ_x, ξ_y, α_1 . For this reason, a racetrack option of PTR was proposed (figure 1), where three families of sextupoles are used. They are located at points with different optical functions and dispersion. From figure 1 and relations (3-5) it is evident that the first sextupole family is efficient for control of ξ_x , second – ξ_y , third – α_1 . In a racetrack PTR option, three families of sextupoles allow to achieve the proton SCT of about 1500 s, which is sufficient for EDM experiments.

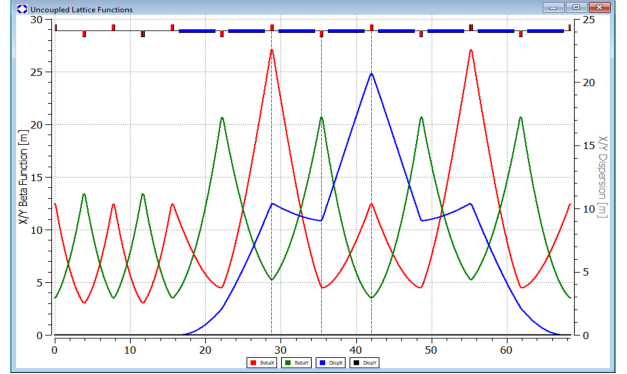


Figure 1: Layout of one superperiod of a racetrack option of PTR with optical functions. Dashed lines indicate the locations of three sextupole families.

$$\xi_x = -\frac{1}{4\pi} \oint \beta_x (k - m\eta_x) dz, \quad (3)$$

$$\xi_y = +\frac{1}{4\pi} \oint \beta_y (k - m\eta_x) dz, \quad (4)$$

$$\Delta\alpha_1 \sim \eta_x^3. \quad (5)$$

Optimization of these three parameters is equivalent to the procedure of flattening spin-tune parabolas in (x-x'), (y-y') and (l- δ) planes. As it was found out, spin-tune in each of the transverse planes depends linearly on ξ_x and ξ_y only, and for longitudinal plane – on α_1 . That allows to write a general relation between SCT and lattice parameters:

$$\frac{1}{\tau} = A|\xi_x - \xi_x^0|\epsilon_x + B|\xi_y - \xi_y^0|\epsilon_y + C|\alpha_1 - \alpha_1^0|\sigma_D^2, \quad (6)$$

where the influence of the last term is predicted to be small for a cooled beam and comes into play when chromaticities are optimized. Therefore, the task of the SCT optimization is equivalent to manipulating three sextupole families to find optimal ξ_x^0, ξ_y^0 and α_1^0 .

These results are also relevant for the COSY ring due to similarity of COSY and racetrack PTR design option and can be used for the SCT optimization during the JEDI beamtime in February 2022.

References

- [1] Y. Senichev, R. Maier, D. Zyuzin, and N. V. Kulabukhova, *Spin Tune Decoherence Effects in Electro- and Magnetostatic Structures*, in Proc. 4th Int. Particle Accelerator Conf. (IPAC'13), Shanghai, China, May 2013, paper WEPEA036, pp. 2579–2581.

Spin-Tracking simulations in an idealized COSY model using Bmad

M. Vitz on behalf of the JEDI Collaboration

This report covers the implementation of an idealized RF Wien Filter into the COSY lattice and the simulations with deuterons using Bmad. The lattice settings as well as the lattice itself used for this investigation were directly obtained from the Madx COSY lattice from April 2021 as this model is regularly updated.

The objective of the implementation of the RF Wien Filter is the measurement of the invariant spin axis $\langle \vec{n} \rangle$. The invariant spin axis characterizes the spin motion inside a storage ring as it is defined as the rotation axis around which the spin of a particle precesses. In an idealized storage ring an EDM of a particle would tilt the invariant spin axis in radial direction. This can be directly demonstrated in a simulation by comparing the spin rotation between successive turns. The calculation method for this approach is described by equation 1 and a simulation result for an artificial EDM signal is shown in figure 1:

$$\langle \vec{n} \rangle = \frac{1}{n-1} \sum_{i=1}^{n-1} \left(\frac{\vec{s}_i \times \vec{s}_{i+1}}{|\vec{s}_i \times \vec{s}_{i+1}|} \right) \quad (1)$$

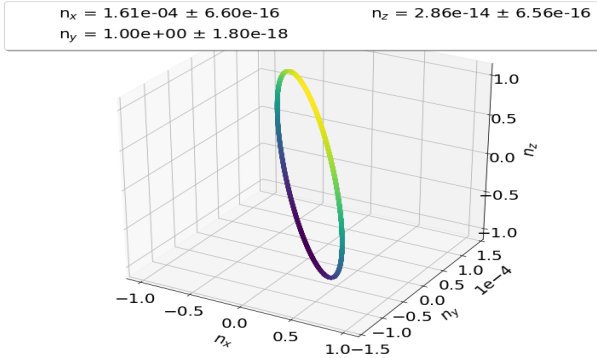


Figure 1: Direct measurement of the invariant spin axis using single particle tracking for 10^4 revolutions in the Bmad COSY model. The tilt of the invariant spin axis due to the deuterons EDM signal becomes visible in the radial n_x coordinate.

Although this approach yields a result, which is in agreement with the theoretical prediction, it can not be applied in a real experiment. For this reason the RF Wien Filter and the so-called Snake solenoid were implemented. The Lorentz force inside the Wien Filter is cancelled by choosing the appropriate ratio of electric and magnetic field while the Snake solenoid provides a longitudinal magnetic field. The Wien Filter operates on one of the harmonics of the spin precession frequency (871 kHz) so a particle passing through the device

gets a spin kick in the same direction every turn. This induces a build up of the vertical polarization over time. By changing the relative phase of the Wien Filter one can obtain a EDM resonance strength ϵ_{EDM} via this vertical build up. The EDM resonance strength can be measured for a variety of Wien Filter rotations and Snake Solenoid currents. The data achieved with this method can be summarized in a resonance map, where the minimum indicates the tilt of the invariant spin axis. Such a simulated map is shown in figure 2; the function to fit for the minimum is displayed in equation 2:

$$\epsilon_{EDM} = \left[A_{WF}^2 (\phi_{WF} - \phi_{WF,0})^2 + A_{SN}^2 \left(\frac{\xi_{SN} - \xi_{SN,0}}{2 \sin(\pi \nu_{s,0})} \right)^2 \right]^{1/2} + \epsilon_0 \quad (2)$$

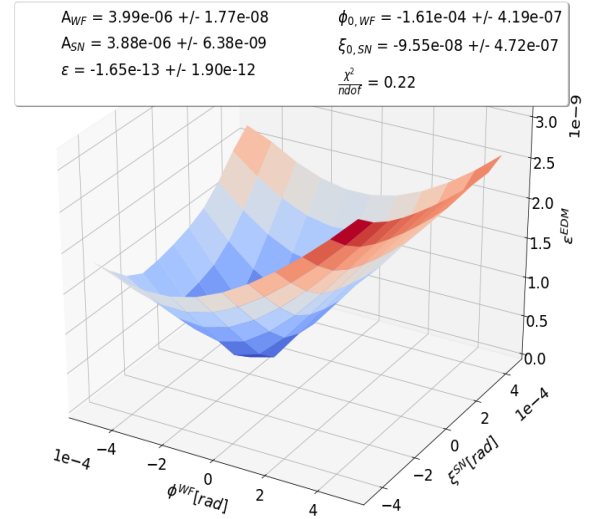


Figure 2: Map measurement of the invariant spin axis using single particle tracking of the reference particle. The tilt of the invariant spin axis due to the deuterons EDM signal becomes visible in the $\phi_{WF,0}$ parameter.

As the results of both methods for an idealized COSY lattice are consistent, it can be assumed, that the implementation of the RF Wien Filter was successful. Further steps will be the integration magnet misalignments and other systematic effects as these effects also tilt the invariant spin axis.

References

- [1] F. Rathmann, N. Nikolaev and J. Slim, *Spin dynamics investigations for the electric dipole moment experiment*, Physical Review Accelerators and Beams, 23, 2020

Injection optimization using machine learning at the Cooler Synchrotron COSY

A. Awal for the JEDI Collaboration

During operation, it is usually desired to have a particle beam in COSY with high intensity and small emittance. In order to achieve this, it is required to successfully transfer the particles from the cyclotron through the Injection Beam Line (IBL) and inject them into COSY. Tuning the IBL demands carefully adjusting many parameters in a complex and non-linear way. Currently, balancing the configurations of the IBL and optimizing the injection into COSY is done manually. The operators usually spend between several hours to a few days to accurately optimize the IBL. Machine learning methods exhibit promising algorithms to effectively address this challenge of optimizing the IBL setup and this has been demonstrated eg. at GSI[2].

Bayesian optimization is a machine learning method that optimizes an objective function to find the optima using limited observations. The objective function to be optimized is a black-box continuous function which means it is costly to evaluate and/or is difficult to differentiate. It is therefore seen as a promising method to optimize the complex parameters of the IBL. Bayesian optimization works by defining and computing two functions, a surrogate function and an acquisition function. The surrogate function approximates the objective function using the observations. It is computed first to model the probability distribution of the objective function in the unexplored space of parameters. Gaussian processes is a widely used surrogate function and it is the method used in the experiments. In Bayesian optimization, the surrogate function is then used to find the most promising parameters to explore. This is achieved through computing the acquisition function. The acquisition function adopted in the experiments is the Expected Improvement (EI). EI is a widely used method that computes the expected value of improvement compared to the current best observation from the objective function. It is defined as

$$EI(x) = \begin{cases} (\mu(x) - \mu^+ - \varepsilon)\Phi(Z) + \sigma(x)\phi(Z) & ,\text{if } \sigma(x) > 0 \\ 0 & ,\text{if } \sigma(x) = 0 \end{cases}$$

$$Z = \frac{\mu(x) - \mu^+ - \varepsilon}{\sigma(x)} \quad (1)$$

where μ & σ are the mean and standard deviation of the probability distribution computed by the surrogate function, μ^+ is the best observed point, $\phi(\cdot)$ and $\Phi(\cdot)$ are the probability density function

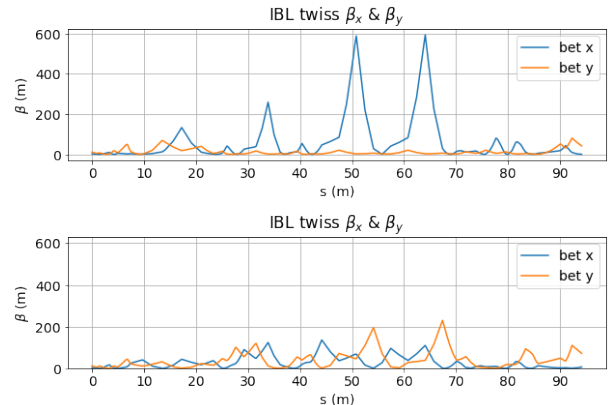


Figure 1: Beam Beta functions of the initial configuration (top) and after Bayesian optimization (bottom).

(PDF) and cumulative distribution functions (CDF) of Gaussian distribution respectively. ε determines the amount of exploration during the optimization with higher ε leading to more exploration. EI is computed over the parameters space and the point with the maximum EI is sampled and is then used to compute the objective function.

Simulating the IBL with Bayesian optimization is conducted using the accelerator simulation software MAD-X[1]. The setup of the source particles is initialized with a relatively wide distribution. The used initial configurations yielded a 16.2% efficiency. Simulating the acquired parameters from the Bayesian optimization achieved 71.5% efficiency and improved profile (Fig 1). These configuration parameters were tested with COSY during the operational run on 21.1.2022. Although the optimized parameters deviate significantly from the conventional settings, the beam was detected at a beam cup near the end of the IBL and after some manual adjustment the efficiency measured was around 80%. This demonstrates the potential of using this method in automating the optimization of the IBL. An online Bayesian optimization is planned to be implemented and tested during a dedicated beamtime in March.

References

- [1] Laurent Deniau et al. “The MAD-X Program (Methodical Accelerator Design)” (2002).
- [2] Sabrina Appel et al. “Optimization of Heavy-Ion Synchrotrons Using Nature-Inspired Algorithms and Machine Learning” (2019). DOI: 10.18429/JACOW-ICAP2018-SAPAF02.

The status of the Pellet target development for the JePo polarimeter at COSY

O. Javakhishvili and I. Keshelashvili for the JEDI collaboration

One of the key elements of the JEDI experiments at COSY is the new polarimeter (JePo)[1]. The JePo consists of a modular inorganic LYSO crystals and ΔE scintillators [2]. One crucial part of the polarimeter is the target system. In storage ring EDM (srEDM) measurements the requirements for the target are minimal influence on beam particles and vacuum system. Most of the traditional target systems are not suitable for srEDM experiments. Considering all the drawbacks of different types of targets we developed new concept of the ballistic carbon pellet target[2]. The idea is to shoot a small (tens of micron) carbon pellet through the beam (see Figure 1). The shooter and catcher mechanisms will oscillate the pellet and make it to cross the beam. By controlling the movement of the pellet it will be

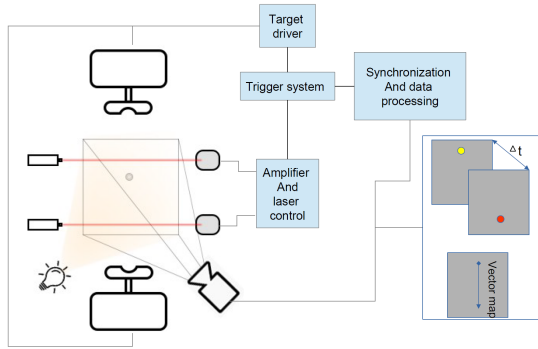


Figure 1: Block diagram of the pellet target system possible to even scan the beam profile at desired position if the DAQ will be synchronized with the pellet movement. Anything using electrical and magnetic fields must be avoided not to disturb the beam. Frequency and speed of the oscillation must be variable to achieve the desired effective target density. The proper monitoring system must be developed.

The system is controlled by FPGA, a TOF (time of flight) system which consists of lasers and photo diodes give us precise trigger and time information. The output of the diodes are amplified and converted to a digital signal which is fed into the FPGA (see Figure 2). To get pellet tracking information, camera signals are fed in to the FPGA, which performs image processing and object tracking. Two main IP(Intellectual Property) for FPGA were developed, one for detecting edges from each input frame (CANNY edge detection) and the other for detecting objects in image and track them (Center of Gravity method). These IPs perform the most hard work in the system, processed data are transferred to CPU, which does easy calculations and data exchange through serial interface and network. For better performance and resource utilisation, several

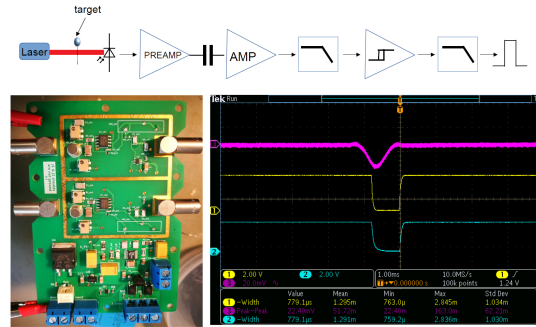


Figure 2: The TOF unit, diagram(up), physical board(left), test figure(right): purple - amplified analog signal, yellow and blue - digital outputs

parameters can be adjusted from CPU in image processing IPs using the AXI interface during run-time. Beside of image processing, TOF IP was also developed for precise triggering and measurement of flight time of the pellet and speed calculation. The simplified design of the FPGA system can be seen on Figure 3

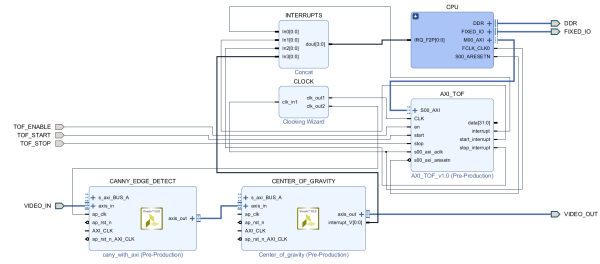


Figure 3: Simplified design of the FPGA system

The TOF system hardware and FPGA IP has been developed and tested. The image processing, object detection and tracking part is also finished, they were tested using generated test signals from PC. Now we are working on combining these different systems into one, integrating it with detector signals and making a user friendly control interface. This project was supported by Shota Rustaveli National Foundation of Georgia (SRNSFG) JFZ_18_01

References

- [1] F. Müller, O. Javakhishvili, D. Shergelashvili, I. Keshelashvili, D. Mchedlishvili et al., "A new beam polarimeter at COSY to search for electric dipole moments of charged particles", JINST 15, P12005 (2020)
- [2] I. Keshelashvili et al., "A new approach: LYSO based polarimetry for the EDM measurements", J. Phys. Conf. Ser. 1162, 012029 (2019)

Benchmarking the spin tracking for spin tune mapping with three-steerer vertical orbit bumps

A. Saleev for the JEDI Collaboration

In-plane magnetic fields have two origins: one is the radial focusing fields of the quadrupoles and vertical steerers to control the beam on a closed orbit. Another one is imperfection fields produced by the uncontrolled alignment errors of the magnets. The spin rotations in the in-plane fields are non-commuting with the spin rotations around the vertical field of the dipoles. This leads to complex dependence of invariant spin axis \vec{c} on the position of viewpoint in the ring, s . However, unlike $c_{x,z}^{\text{ndm}}$, the EDM contribution to \vec{c} is *invariant* along the orbit. It gives possibility to disentangle the EDM and Magnetic Dipole Moment (MDM) effects if non-invariant part of $\vec{c}(s)$ can be described.

In the JEDI experiment E010 in August – September 2020, we tested a demerit of spin rotations, a "commutation failure", by creating a controlled closed orbit distortion over 1/8 part of the ring circumference - a vertical closed orbit bump. It was made by three steerers MSV18, MSV20 and MSV22 for a special period in time of the beam storage cycles (see measured orbit difference on Fig. 1).

An ideal model of COSY ring, set up in beam and spin tracker COSY-Infinity ([2]), allows to predict $\vec{c}(s)$ for any closed orbit. The orbit bump simulation is shown on Fig. 1 by green curve. In order to determine the dependence of projection c_z on the bump amplitude in the experiment, we used a special method called "spin tune mapping" [4]. This method is based on the outstanding ability to determine the spin tune with a relative error of 1×10^{-10} during a 100 s long beam cycle at COSY from the time dependence of horizontal polarization [3]. For the same period of time in the cycles when the bump appears, two static solenoids, one in the target telescope, and one in the cooler telescope, were switched on. The spin tune was measured on the grid of solenoid currents $I_{1,2}$ applied at the fixed amplitude of the bump. Parabolic dependence of the spin tune shifts $\Delta\nu_s$, which are calculated as a change of spin tune relative to the baseline spin tune value ν_s , given at the moment of time in cycle when the solenoid current and the bump amplitude were zero, fits non-lattice model where c_z (at $s = 16.27$ m $c_z = c_{\text{sol}}$ for the 2 MeV e-cooler compensation solenoid in target telescope and at $s = 126.13$ m $c_z = c_{\text{snake}}$ for superconducting snake solenoid at cooler telescope) and solenoid's current-to-spin-kick calibration $k_{1,2}$ are free parameters:

$$-\pi\Delta\nu_s = (\cos a \cos b - 1) \cot \pi\nu_s - c_{\text{sol}} \sin a \cos b - c_{\text{snake}} \cos a \sin b - \frac{\sin a \sin b}{\sin \pi\nu_s}, \quad (1)$$

where

$$a = \frac{k_1 I_1}{2} \quad \text{and} \quad b = \frac{k_2 I_2}{2}. \quad (2)$$

In fit results of such spin tune maps, the values of c_z are determined with angular precision $\sigma_{c_{\text{sol}}} = 6.9 \mu\text{rad}$ at the 2 MeV e-cooler solenoid and $\sigma_{c_{\text{snake}}} = 3.6 \mu\text{rad}$ at superconducting snake. The relative error on the spin tune shift $\Delta\nu_s$ is $\sigma_{\Delta\nu_s} = 3.7 \times 10^{-9}$. When two static solenoids located at COSY telescopes are used, position dependence of $\vec{c}(s)$ is only partly uncovered. Nevertheless, fit results for spin tune maps at all of the measured bump amplitudes are in good agreement with the model prediction for dependence of c_z projections at solenoids from the central steerer setting (see slope parameter $p1$ in Fig. 2). The values of central steerer (MSV20) that correspond to the same amplitude of the bump in the model (in mrad) and measurement (in %) were chosen as a reference ones. The settings for MSV18 and MSV22 were scaled accordingly to fulfill the condition of closed orbit bump, which is derived from the simulated (in case of model) and measured (in experiment) orbit response matrix. It means as a matter of fact, that *we created local orbit distortion by horizontal magnetic fields in the ring and described the resulting beam and spin dynamics*. Note that an offset parameter $p0$ at Fig. 2 is non-vanishing in case of measured c_{sol} and c_{snake} due to the presence of alignment errors in the ring, which contribute to the tilt of invariant spin axis towards z-axis. Few data points were also found for bump made by MSV08, MSV10 and MSV12, and the measured spin tune shifts are also in agreement with the same approach to model the bump in COSY-Infinity.

A new spin-tune mapping scheme with a global vertical orbit correction was also proposed (see ref.[1]). The currents in all vertical steerers, except of those needed to keep the orbit fixed at solenoids, polarimeter and RF cavity, will be gradually scaled down to zero in the successive measurements of spin tune maps. This would allow us to witness the impact of the applied vertical orbit correction at COSY on the observed tilt of the invariant spin axis (the measured parameter $p0$ in Fig. 2 for the z -projection of \vec{c}).

The quantitative understanding of the local sources of the imperfection fields and their active compensation is indispensable for disentangling the EDM effect from the EDM-like background from interactions of the vastly larger magnetic dipole moment with the in-plane magnetic fields. The study presented hereby is an important connecting step to test the model predictions for pure electrostatic lattice, preceding the measurements at strictly frozen spin condition.

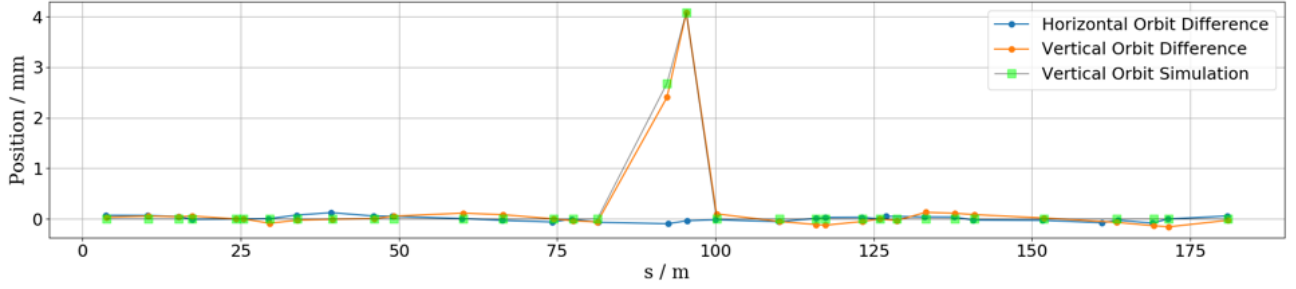


Figure 1: Modelled (green) ideal vertical orbit and measured (orange-vertical, blue-horizontal) orbit difference between 85 (no bump) and 115 (bump applied) seconds in the beam cycle. Horizontal orbit in the simulation was zero, hence it is not shown on the graph.

References

- [1] Spin tune response to vertical orbit correction (JEDI Proposal, 2019) https://www.ikp.fz-juelich.de/CBAC/documents/CBAC13/E010.1_spintune_responce.pdf
- [2] Berz, M.: Computational aspects of optics design and simulation: COSY INFINITY. Nucl. Instrum. Meth. **A298**, 473–479 (1990). DOI 10.1016/0168-9002(90)90649-Q
- [3] Eversmann, D., et al.: New method for a continuous determination of the spin tune in storage rings and implications for precision experiments. Phys. Rev. Lett. **115**, 094801 (2015). DOI 10.1103/PhysRevLett.115.094801
- [4] Saleev, A., et al.: Spin tune mapping as a novel tool to probe the spin dynamics in storage rings. Phys. Rev. Accel. Beams **20**, 072801 (2017)

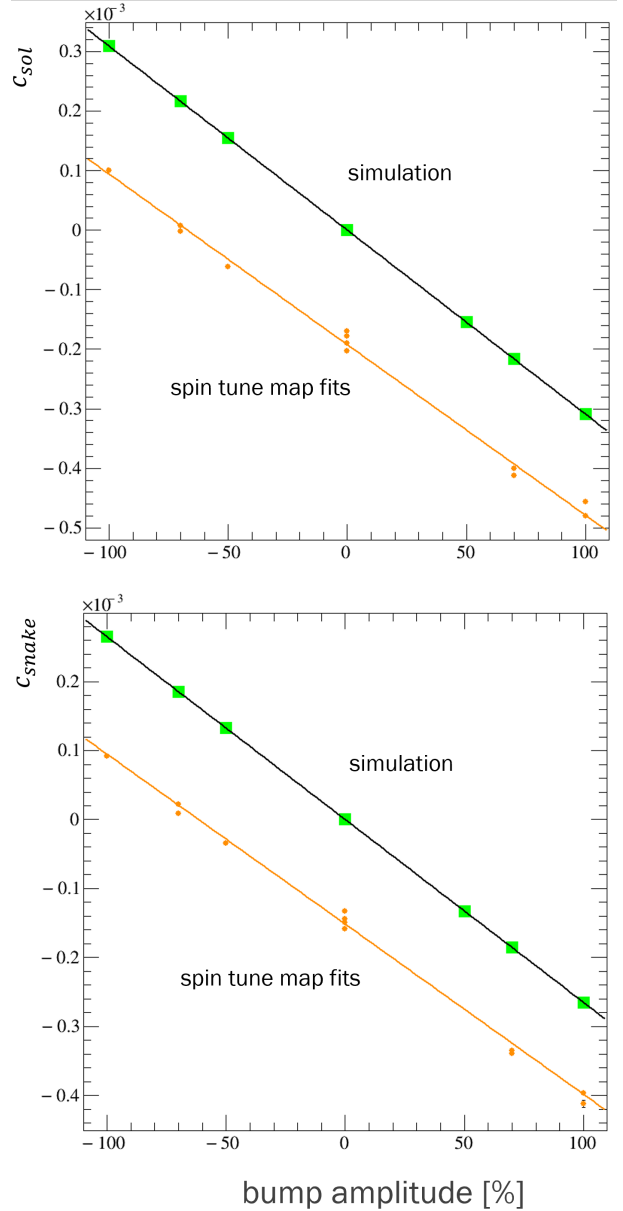


Figure 2: Dependence of the fit parameters c_{sol} (top) and c_{snake} (bottom) on the bump amplitude and comparison to simulation results. Value +100% corresponds to the bump amplitude of 4.08 mm, shown on Fig. 1.

Investigation of the Σ^0 Production Mechanism in p+p Collisions

Waleed Esmail and James Ritman

Hyperon production in proton induced reactions at beam energies of a few GeV serves as a tool to study the strong interaction at the non-perturbative energy regime. The production of the Σ^0 hyperon in p+p reactions at a beam energy $T=3.5$ GeV was investigated via the exclusive reaction $pp \rightarrow pK^+\Sigma^0$ with the HADES detector. The Σ^0 hyperon decays electromagnetically with a branching ratio $BR(\Sigma^0 \rightarrow \Lambda\gamma) \approx 100\%$, where the daughter photon is identified as a missing particle. In order to reconstruct the Σ^0 events, two data-sets have been identified.

The **HADES** data-set, where all the final state charged particles ($2p$, π^- and K^+) are required to be within the acceptance of the main HADES setup. In this data-set, the daughter Λ was reconstructed from its decay products, then off-vertex cuts were defined and applied to enhance the S/B ratio. Finally, events in the range $MM^2(pp_{\text{had}}\pi^-)[\text{GeV}^2/c^4] > 0.2$ were selected. In the **Wall** data-set, only three charged particles ($1p$, π^- and K^+) are required to be within the main HADES acceptance and one hit in the forward wall. Events fulfilling the following kinematical conditions were selected: (a) $-0.02 < MM^2(pK^+p_{\text{wall}}\pi^-)[\text{GeV}^2/c^4] < 0.01$ and (b) $MM^2(pp_{\text{wall}}\pi^-)[\text{GeV}^2/c^4] > 0.2$. A kinematic refit is then applied for the **HADES** and **Wall** data-sets separately, which constrains the secondary proton and the pion to the Λ mass and the overall missing mass to the photon mass. In total 2613 Σ^0 events were extracted from the missing mass $MM(pK^+)$ spectrum.

The total production cross section was determined to be $\sigma = 18.7 \pm 1.0(\text{stat}) \pm 1.7(\text{syst}) \mu\text{b}$. The dynamics of the $pp \rightarrow pK^+\Sigma^0$ reaction were investigated by studying the angular distributions in the CMS, G-J and helicity frames. The angular distributions in the CMS of the Σ^0 hyperon and the proton show anisotropies, where the anisotropy is more pronounced in the case of the proton. This is a clear indication that the reaction proceeds dominantly via the pion exchange mechanism. The G-J angle of the kaon in the $K^+\Sigma^0$ frame tends to be asymmetric, which can be caused by the excitation of nucleon resonances decaying into the $K^+\Sigma^0$ channel. All the helicity angular distributions are non-isotropic, which indicates significant resonant contributions.

In order to provide a better description of the angular distributions and to estimate the contributions of nucleon resonances, the Bonn-Gatchina Partial Wave Analysis (Bo-Ga PWA) tool has been employed. Nucleon resonances (either $I=1/2$ N^* or $I=3/2$ Δ^*)

with a measured $K^+\Sigma^0$ branching ratio have been included as resonant components. Bo-Ga PWA framework performs an unbinned fit, where the fit quality is determined by a log-likelihood value. However, due to the limited statistics, an unambiguous determination of the relative contributions was not possible. Nevertheless, resonances $N^*(1710)$ ($J^P = 1/2^+$), $N^*(1900)$ ($J^P = 3/2^+$) and $\Delta^*(1900)$ ($J^P = 1/2^-$) are certainly required by the fit. Figure 1 shows a comparison between the pure phase space description and the best PWA solution in the CMS, Gottfried-Jackson and helicity angular distributions.

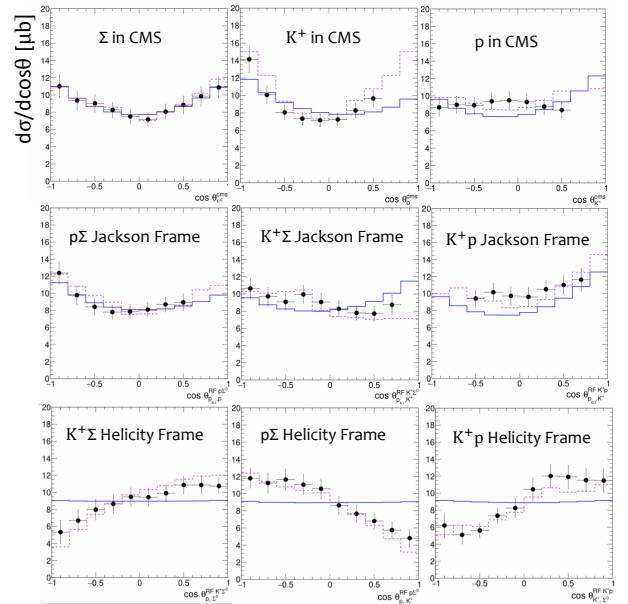


Figure 1: Angular distributions in the CMS frame (top row), Gottfried-Jackson frames (middle row) and helicity frames (bottom row). The experimental data are shown by the black points, where the error bars are the square root of the quadratic sum of the statistical and systematic uncertainties. The blue lines indicate the phase space simulation and the dotted pink lines indicate the best partial wave analysis solution.

The upcoming proton beam time in February 2022 with the upgraded HADES setup including the new forward detector offers the opportunity to improve the mass resolution in the forward detector. In addition, it will provide sufficient statistics to extract quantitative contributions of the different nucleon resonances.

InnerTOF - a Trigger Scintillator for HADES

P. Bergmann, D. Grzonka, P. Kulesa, J. Ritman, T. Sefzick

A new trigger scintillator, called InnerTOF (iTOF), has been built for the HADES experiment at GSI. This detector is placed in front of the first MDC layer of HADES, see Fig.1. It consists of six modules with a trapezoidal shape (height ~ 730 mm, long side ~ 700 mm, short side ~ 90 mm) covering the six MDC sectors and each module includes three separate plastic scintillator plates (BC408¹) with a nominal thickness of 6.4 mm, that are read out by SiPMs. The structure of the modules is sketched in the lower part of Fig.1 with the three scintillators S-A, S-B and S-C in one Al-frame.

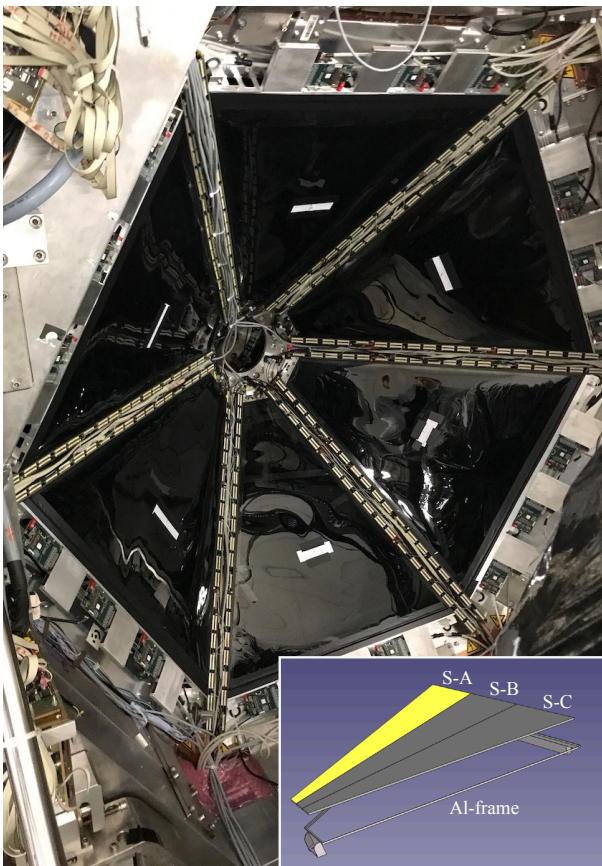


Figure 1: Photo of the InnerTOF modules mounted at the HADES MDC with a sketch of the module-structure in the lower part.

SiPMs of the type MFC-60035² with an active area of 6×6 mm² are used. The SiPMs are soldered to a printed circuit board equipped with FFC-sockets which are used to connect via FFC-cables to an adapter-board for the connection to PADIWA-boards³, see Fig.2. At each scintillator, three boards

¹<https://www.crystals.saint-gobain.com>

²<https://www.onsemi.com>

³<http://trb.gsi.de>

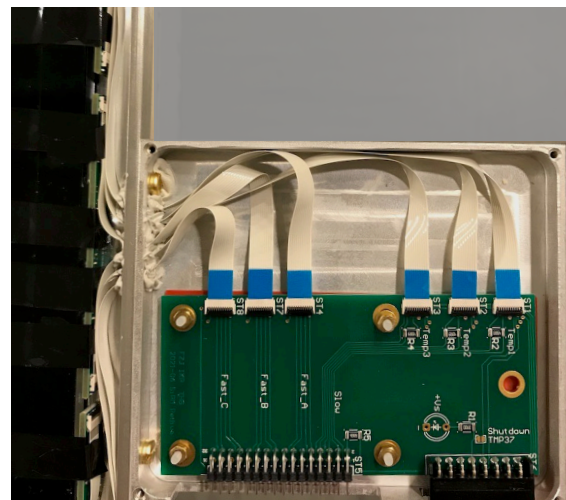
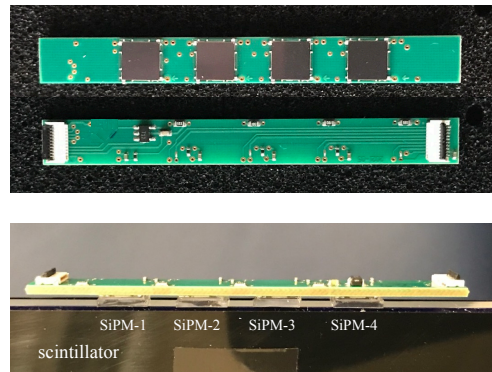


Figure 2: SiPM board with four SiPMs on the frontside and FFC-sockets on the backside (top). Three boards are attached to each scintillator coupled via silicon pads as shown in the middle part and in the lower part with the connection to an adapterboard. The PADIWA-board is connected to the lower left plug.

with four SiPMs each are attached and coupled via silicon-pads resulting in 12 separate signals. The SiPM type used delivers in addition to the standard slow (FWHM ~ 150 ns) output signal a fast (FWHM ~ 10 ns) output which is used as the detector signal. In Fig.3 typical SiPM signals from a ⁹⁰Sr-source are shown with an amplitude in the order of 5 mV. These are direct signals from the SiPM-board without amplification connected to a scope with 50 Ohm termination. The PADIWA-board amplifies the signals by about a factor 10, includes discriminators and delivers LVDS signals to extract the time and amplitude via time over threshold. For the detection of a particle passage through the scintillator a certain

multiplicity of fast SiPM signals will be used for the trigger signal generation. As additional information the sum of the four slow signals from every SiPM-board will be registered.

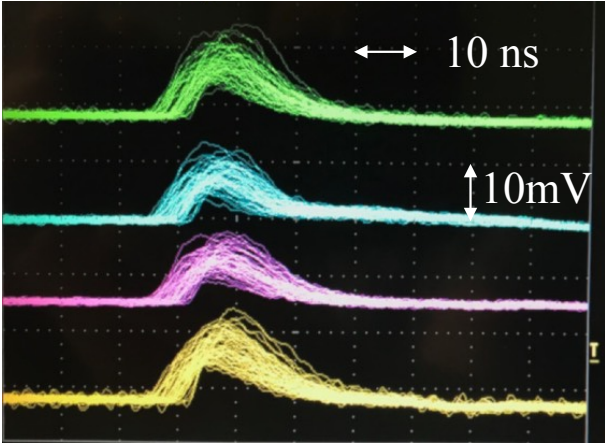


Figure 3: Direct fast SiPM signals from a ^{90}Sr -source for the four SiPMs of one board. The scope was triggered by SiPM-1 (yellow trace) in persistence mode to get a mean signal distribution.

All InnerTOF detector modules were tested with ^{90}Sr -source, cosmics and 2.74 GeV/c proton beam from COSY which is close to minimum ionizing particles. For the tests with beam particles the modules were arranged in a frame as shown in Fig.4 with the beam coming from the side passing through all modules. By varying the frame position the whole area of all scintillators was covered by the beam.

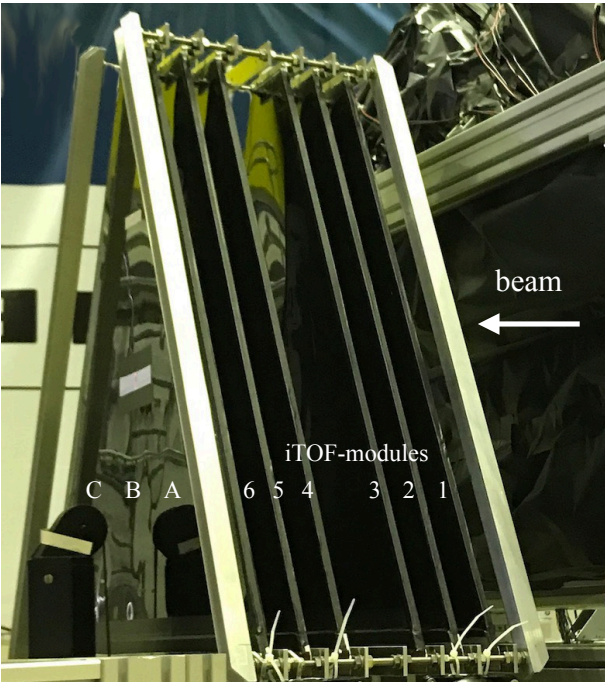


Figure 4: Setup for the tests with COSY-beam and cosmics with all six InnerTOF modules.

For all beam positions a rather high signal multiplicity was achieved with mostly a signal from all 12 SiPMs in each event. Therefore we expect a close to 100% detection efficiency for minimum ionizing particles. Similar results were achieved with cosmics as shown in Fig.5. Here the frame was rotated by 90 degree and events were selected with a multiplicity of 12 in the upper and lower module. This measurement gives the mean multiplicity distribution over the whole scintillator area. The numbering of InnerTOF modules and scintillators is given in Fig.4.

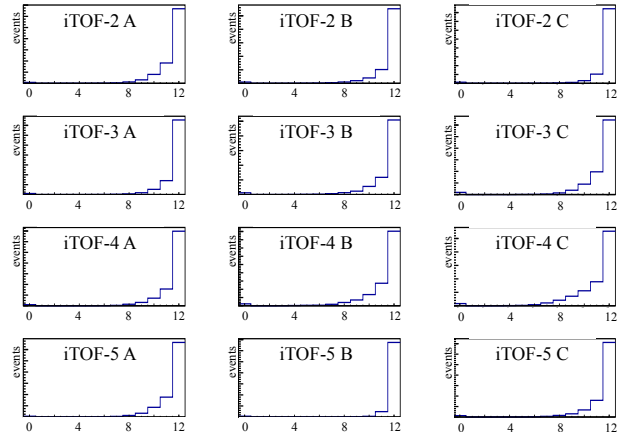


Figure 5: Multiplicity distribution of the SiPM-signals resulting from the passage of cosmic particles through the InnerTOF-modules for the units 2 to 4 for the separate scintillators A, B, C, see Fig.4 for the numbering. Events with a multiplicity of 12 in modules 1 and 6 were selected for the plot.

The InnerTOF modules are now in operation at HADES for a beam time in February 2022 of proton induced hyperon production studies where it will allow a higher selectivity of real events and an improved background reduction.

Comparison of Track Finding Algorithms for the PANDA Detector

A. Aliche, T. Stockmanns, J. Ritman

Introduction

The main tracking detector for the barrel part of the PANDA detector is the Straw Tube Tracker (STT). It consists of over 4200 gas filled drift tubes arranged in a dense packing. The STT provides a coarse position information of the anode wire in the middle of each tube and a precise drift time information of the electrons to the anode. This drift time information results in a cylinder (isochrone) around the anode wire, to which the particle track must be tangent. [1] Taking the additional time information into account is essential for tracking algorithms in PANDA because it significantly improves the hit resolution of the STT. For a more precise position information around the interaction point the innermost tracking detector is the Micro-Vertex-Detector (MVD) with a high spatial resolution to detect displaced vertices [2]. For the forward boosted tracks the outermost tracking detector in PANDA's barrel part are the Gas-Electron-Multiplier plates (GEM).

Tracking in PANDA

There are two different approaches for tracking algorithms in PANDA. The first approach is a global tracking approach where the algorithm takes all detector hits into account without any preference for one detector type. In contrast, the second (local) approach starts with one detector to get a track assumption and adds the other detector hits afterwards. To compare tracking algorithms, quantities must be specified that describe the key requirements for a track finding algorithm. Here the finding rate for primary and secondary particles will be compared as well as the number of multiple found tracks (clones) and the number of wrongly found tracks (ghosts). Additionally, the runtime of the algorithms is taken into account.

Three algorithms are compared. The first one is the currently used tracking algorithm (BarrelTrackFinder). It is a global tracking algorithm which is designed to find primary particles. [5] The second algorithm (HoughTrackFinder) is also a global tracking algorithm designed to find primary particles, which is based on Hough transformations. A detailed description can be found in [3] and [4]. The third algorithm (ApolloniusTripletTrackFinder) is a local track finder designed to find both primary and secondary particles. Additionally, it can be used as an extension after one of the other track finders.

Porting the HoughTrackFinder to GPUs

One of the main advantages of the HoughTrackFinder in comparison to the BarrelTrackFinder is that it promises to be extendable to also find secondary particles. A challenge for the algorithm, however, is the high combinatorics, which makes the algorithm slow. This gets even worse for the secondary extension. To solve this problem the algorithm was ported to a GPU. A GPU has the advantage that it can handle many small calculations in parallel. Where a CPU has only 4, 8 or 16 cores to parallelize calculations, a GPU has thousands of cores which are called threads. Since the calculations are all independent, they can easily be parallelized by calculating one combination per thread. The HoughTrackFinder is divided into different parts: the Apollonius calculation, the filling of the Hough space, the maximum finding in the Hough space and a merging procedure as last step [6]. The runtime improvement for the different parts of the HoughTrackFinder when porting the algorithms to a GPU are summarized in Table 1. The table shows that the calculation of the Apollonius circles per combination indeed gains a large speed up of a factor of 85 times faster. This calculation is a well parallelizable calculation with a small memory usage of 50 % for 10,000 events at a medium class GPU (NVIDIA GeForce RTX 2060) with only 4 GB GPU memory. So, the Apollonius calculation itself can significantly be improved by using GPUs. The other parts however are much more memory intensive. Here the GPU gains only a speed up of 2-3 times faster and is therefore still not as fast as the BarrelTrackFinder. An extension to secondary particles will only be reasonable when the memory problem on the GPU is solved.

	Speed up	memory	used blocks
Apollonius	85	50 %	256 · 393812
Hough space	3	100 %	256 · 125
Maximum finding	2.6	100 %	256 · 125
Merging	2.5	100 %	256 · 8

Table 1: Speed up and GPU parameters for the different parts of the HoughTrackFinder.

Secondary Finding with the Apollonius-TripletTrackFinder

The ApolloniusTripletTrackFinder is a secondary track finder that can determine the true particle track by using only a few hit combinations. For this a set of inner, mid, and outer hits with maximum

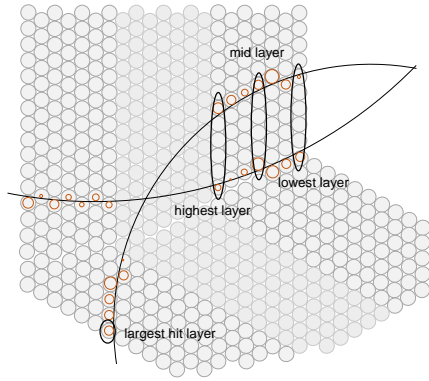


Figure 1: Basic working principle of the triplet generation of the ApolloniusTripletTrackFinder.

distance between each hit is combined. The basic principle of the triplet generation is shown in Figure 1. To reduce the processing time it is important to reduce the number of possible triplet combinations. For this purpose, all combinations that are already contained in one of the previously found tracks are discarded. For each triplet the eight Apollonius circles tangent to the hits are calculated. All hits that are close to the Apollonius circles are added to the circles. In a last step only the tracks with the highest number of hits and the lowest χ^2 are selected.

For a comparison of the ApolloniusTripletTrackFinder a data set ($p\bar{p} \rightarrow \Xi(1820)^-\bar{\Xi}^+ \rightarrow \Lambda K^-\bar{\Lambda}\pi^+$) with many secondary particles is used. In Figure 2 the finding rate vs. the distance of the point of closest approach to the interaction point is shown for secondary particles. Here it is clearly visible that the

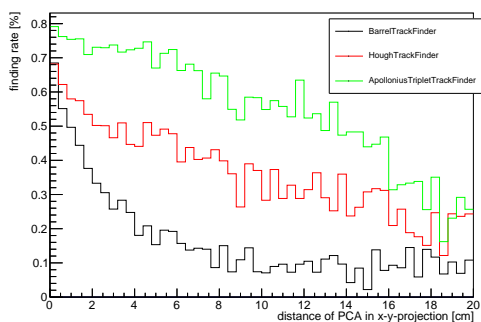


Figure 2: Comparison of finding rate vs. distance of point of closest approach to the interaction point in the x-y-projection.

finding rate of the BarrelTrackFinder drops dramatically for larger distance to the interaction point. The HoughTrackFinder can handle these cases a bit better. The ApolloniusTripletTrackFinder is the only algorithm designed to find tracks not coming from the interaction point. Therefore, the finding rate for

these particles is much higher (about 20 %-points) than for the other algorithms. Nevertheless, the finding rate decreases for larger distances. The reason for this is being further investigated.

Summary and Outlook

This analysis showed that the HoughTrackFinder has a slightly larger finding rate for primary particles than the BarrelTrackFinder and is more robust for particles not coming from the interaction point. The speed of the HoughTrackFinder could be improved by a factor of two by using GPUs. Nevertheless, the algorithm is still not as fast as the BarrelTrackFinder.

The ApolloniusTripletTrackFinder behaves well for particles not coming from the interaction point and increases the finding rate for secondary particles by about 20 %-points. An analysis where the algorithms are combined by first using a primary track finder and afterwards finding the secondary particles with the ApolloniusTripletTrackFinder is still under development. The ApolloniusTripletTrackFinder promises to improve the reconstruction rate for hyperons. A combination of the algorithms is ongoing.

References

- [1] Erni, W., Keshelashvili, I., Krusche, B. et al. Technical design report for the PANDA (AntiProton Annihilations at Darmstadt) Straw Tube Tracker. Eur. Phys. J. A 49, 25 (2013). <https://doi.org/10.1140/epja/i2013-13025-8>
- [2] PANDA Collaboration, W. Erni, I. Keshelashvili, B. Krusche et al. (2012). Technical Design Report for the PANDA Micro Vertex Detector. <http://doi.org/10.15161/oar.it/1446204374.75>
- [3] A. Scholl, T. Stockmanns and J. Ritman, A PANDA Track Finding Algorithm Based on Hough Transformations, in Annual Report 2019 - Institut für Kernphysik, Forschungszentrum Jülich
- [4] A. Scholl, T. Stockmanns and J. Ritman, Quality and Runtime Optimization of a PANDA Track Finding Algorithm based on Hough Transformations, in Annual Report 2020 - Institut für Kernphysik, Forschungszentrum Jülich
- [5] R. Karabowicz, *Global Track Finder for PANDA experiment*, in GSI Scientific Report 2010 - GSI, Darmstadt, Germany, p. 117 (2011).
- [6] A. Aliche, T. Stockmanns and J. Ritman, Track Finding for the PANDA Detector Based on Hough Transformations. EPJ Web Conf. 251 (2021). <https://doi.org/10.1051/epjconf/202125104002>

The HADES Straw Tube Stations calibration

G. Perez-Andrade, P. Wintz and J. Ritman

Introduction

The High Acceptance Di-Electron Spectrometer (HADES) is a fixed-target experiment where hadronic matter is studied through pion, proton and heavy ion induced reactions [1]. HADES operates at the SIS18 accelerator at GSI in Darmstadt, Germany, and is part of the new Facility for Antiprotons and Ions Research (FAIR), under construction at GSI. As part of the FAIR Phase-0, the HADES spectrometer and data-acquisition systems were upgraded, and new components were integrated. In particular, a Forward Detector (FD) consisting of two Straw Tracking Stations (STS1, STS2) and a Forward Resistive Plate Chamber (fRPC) for time-of-flight measurements, and an inner Time of Flight detector (iTOF) were installed [2]. The FD increases the HADES angular acceptance to the region from $\theta = 0.75$ to 7° , which is crucial for the FAIR phase-0 program, including hyperon reconstruction [3].

The Straw Tube Stations (STS)

Each STS station is composed of four double layers of gas-filled straws. The gas mixture used is Ar/CO₂ (90:10) operated at 1 bar over-pressure. The straws design is based on the Straw Tube Tracker [4] and Forward Tracker of the PANDA experiment [5, 6]. The double layers are arranged in four azimuthal orientations for a full 3D track reconstruction and to resolve ambiguities in multi-track events. The charge signals from the ionization electrons in the straws are amplified and shaped in front-end mounted electronic boards. The leading and trailing edge time are measured in multi-hit TDCs [7, 8]. A spatial resolution of 0.13 mm (σ) has been achieved in pre-commissioning tests [6].

The STS is one of the PANDA systems in early operation during the FAIR Phase-0, and will become part of the PANDA FT at the start of FAIR Phase-1.

HADES Commissioning Beamtime

The STS was installed at HADES at the end of 2020. A dedicated commissioning beamtime was carried out in February 2021, in which the newly added detectors and the upgraded DAQ system were tested under experimental conditions. The SIS18 delivered proton beams with $T = 2$ and 4.2 GeV kinetic energy with particle rates of up to 10^8 p/s onto the LH2 target. The STS showed stable operation with no failures and the collected data was used to develop its calibration method.

STS Calibration

The STS raw hit detection time (t_{rawTDC}) includes an offset arising from *e.g.* electronic components, and the particle's time of flight (ToF) to the STS measured by the fRPC:

$$t_{rawTDC} = dt + t_{Offset} + ToF \quad (1)$$

The calibration aims to identify and correct such effects, thereby obtaining the drift time (dt) for the track reconstruction. The calibration consists of i) offset determination/correction and ii) parametrization of the isochrone radius - drift time relation.

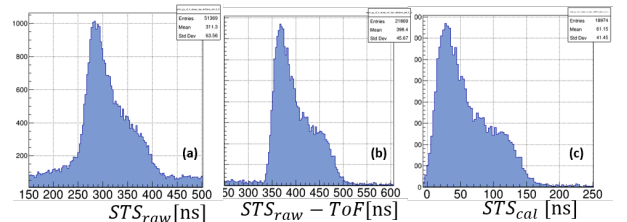


Figure 1: STS raw hit detection times for a single channel (a), after vector candidates selection and time of flight correction (b) and after offset correction (c)

The raw time spectrum corresponding to a sample of ~ 10 million events is shown in Figure 1 (a) for a single straw of STS1. The shape and range of a typical dt spectrum are visible on top of some background. The first calibration step consists of determining the offsets to shift the spectra to 0 ns. However, at this point the background and broadness of the leading edge prevent a precise determination of the starting point of the distribution. Cleaner spectra are obtained by selecting events containing *vector candidates*. These are found through a low resolution track reconstruction [3] in which at least one hit per double layer in the STS (16 in total) is required. The vector candidates also require a hit in the fRPC, associated to the STS by a distance constraint. The STS hit times are then corrected by the track-specific ToF. This event selection suppresses random coincidences contributing to the background.

A time spectrum after the event selection and time of flight correction is shown in Figure 1 (b). The sharper leading edge time and uniform background lead to a better-defined starting point of the distribution. The offset is calculated as the average time between 15% and 70% of the maximum of the distribution (channel-specific). The method is sensitive to the amount of statistics and can thus fail for poorly illuminated channels. An average value of the time offset derived from the high-statistics channels

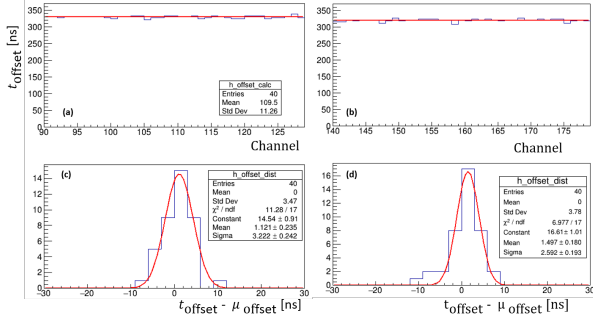


Figure 2: Calculated offsets for the highly illuminated regions of straws in one double layer of STS1 (a) and STS2 (b), together with the linear fit used to determine the mean offset μ_{offset} . Distribution of the differences between the channel specific offset and $\mu_{offset, STS1} = 329.2$ ns for STS1 in (c) and $\mu_{offset, STS2} = 320.2$ ns for STS2 in (d).

is used for those channels. Figure 2 (a),(b) shows the calculated offsets of the highly illuminated regions of straws in the first double layers of STS1,2. The difference of time offsets between STS1,2 is explained by the different signal cable length for the two systems. Variations in single channel offsets can be attributed to different front-end boards or uncertainties in the ToF FRPC calibration. All histograms were produced with 3 ns bin size, reflected in the steps of the offset values. Figure 2 (c),(d) shows the distribution of the differences between the mean offset and the channel-specific offsets together with an estimate of the accuracy of the method given by $\sigma_{STS1, STS2} = 3$ ns.

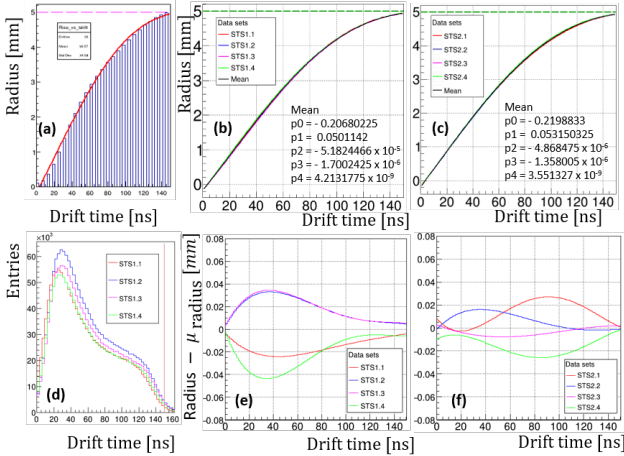


Figure 3: (a) Running integral and isochrone parametrization of the first double layer of STS1. (b),(c) Isochrone parametrization for all double layers of STS1, STS2. (d) dt spectra of all double layers in STS1. (e), (f) Difference between the mean and double-layer specific parametrization of STS1, STS2.

After the offset correction (Figure 1 (c)), the particles dt (t) and the shortest distance from their

track to the wire (r) are correlated by a running integral over the drift time distribution. The $r(t)$ relation is parametrized by a 4th-order polynomial as $r(t_i) = \sum P_i \times t^i$ [8], shown in Figure 3 (a). The $r(t)$ is used for the track reconstruction to calculate the isochrone circle radius from the measured dt. The track is defined by fitting a line tangent to all isochrones. The maximum dt (around 150 ns) and the shape of the distribution are similar among the channels and double layers (Figure 3 (d)), therefore a common parametrization is obtained for each double layer. As shown in Figure 3 (b), (c), taking a mean $r(t)$ for STS1 or STS2 introduces only a minor systematic $r(t)$ shift of $\leq 20 \mu\text{m}$ on average, and 30 - 40 μm maximum in the region < 50 ns. The isochrone parameters are currently being implemented into the HADES software framework called Hydra [9] to perform a High Resolution track reconstruction [3].

Summary

The STS was successfully installed and tested during a commissioning beamtime at GSI in February 2021, showing a stable operation. With the collected rich database, the STS calibration method was developed. The upgraded HADES is now being used for production beamtime. The calibration method of the STS described above is included in Hydra and is the first step in the track reconstruction for physics analyses.

References

- [1] The HADES Collaboration., Agakichiev, G., Agodi, C. *et al.* The high-acceptance dielectron spectrometer HADES. *Eur. Phys. J. A* **41**, 243–277 (2009).
- [2] InnerTOF - a Trigger Scintillator for HADES, D. Grzonka, *et al.* Annual Report 2021 Institut für Kernphysik/COSY
- [3] J. Adamczewski-Musch, *et al.* Production and electromagnetic decay of hyperons: a feasibility study with HADES as a phase-0 experiment at FAIR. *Eur. Phys. J. A*, **21**, (2021) no 4, p. 1-21.
- [4] Erni, W. *et al.*, Technical design report for the PANDA Straw Tube Tracker *Eur. Phys. J. A*, **49** (2013) no. 2.
- [5] PANDA Collaboration, TDR for the PANDA Forward Tracker (2018).
- [6] J. Smyrski *et al.*, Pressure stabilized straw tube modules for the PANDA Forward Tracker, *JINST*, **13**, (2018).
- [7] D. Przyborowski, *et al.* Development of a dedicated front-end electronics for straw tube trackers in the PANDA experiment. *JINST*, **11** (2016) no.08.
- [8] G. Perez-Andrade *et al.* Pre-commissioning of the STS1 straw detector for the phase-0 experiment with the HADES spectrometer. Annual Report Institut für Kernphysik/COSY (2020).
- [9] D. Belder *et al.*, The HADES RPC inner TOF wall. *Nucl. Instrum. Methods. A* **602**, 687 (2009)

Track Finding in Hexagonal Geometry Using Language Models

J. Kannika, T. Stockmanns and J. Ritman

A language model is a probability distribution over sequences of discrete values such as words, integers and so on. One of the well-known applications that the language model use to perform pattern recognitions is word prediction, see Figure 1. The word prediction is an application that helps users by providing choices of possible words determined by probabilities recorded inside the language model. Whenever the users are typing on their phones, the application will collect the data, count word frequencies, calculate probability distribution, then finally update the language model.

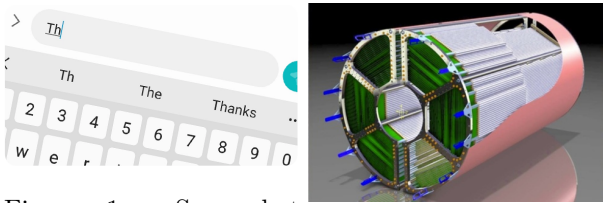


Figure 1: Screenshot

of word prediction application shown in Tracker (STT) from www.samsung.com.

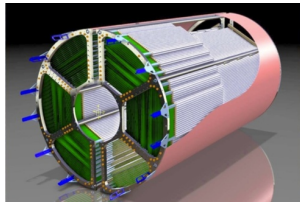


Figure 2: Straw Tube Tracker (STT) from PANDA experiment.

We are developing language models that can be used for tracking particles in a straw-tube-based tracker, in this case, the Straw Tube Tracker (STT) in the PANDA experiment, see Figure 2. The challenges of applying language models to this type of application involve designing the data representations and facing technical issues and limitations of the particle detectors.

We wrote a toy data generator that can generate data similar to the one from the STT. The generator can create tracks in hexagonal geometry within a confined rectangular space, see Figure 3. Each track contains a series of hits, where each hit provides information such as hit position and isochrone radius. Position, in this case, means the center of the tube that was hit, and isochron radius, which is the distance between the center of the tube and minimal distance to the particle's trajectory. Moving direction is one of the feature that we trained, it is defined as $\Sigma = \{30, 90, 150, 210, 270, 330\}$, these are the possible angles for moving from one tube to another ad-

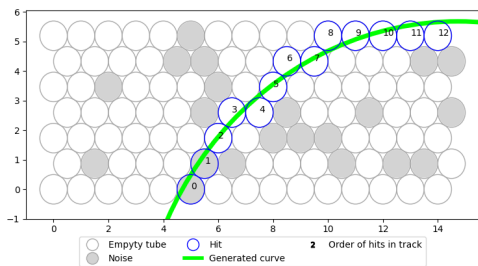


Figure 3: Track generated on hexagonal geometry by the toy data generator.

acent tube. In the training we generate tracks then convert them into moving directions then count word frequencies and finally calculate the probability distribution. Figure 4 shows how the track completeness progresses during the training. The higher gram model is more accurate than the lower ones since they use a longer history to predict the next words.

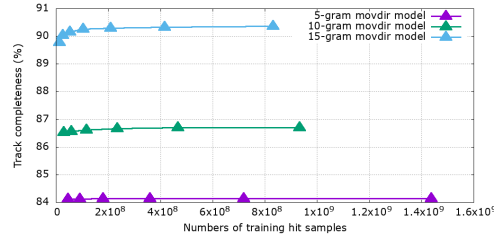


Figure 4: The accuracies of language models are increasing during the training

Currently, we are working on training language models using data generated from PandaRoot software. This software is the main tool used for doing physics analyses in the PANDA research. Similar to the toy data generator, each hit here also contains hit position and isochrone radius. The values of both parameters are more realistic since PandaRoot generates tracks with physical interactions taken into account. We train the language using data on STT. The STT can be categorized into two parts (see Figure 5), the first part consists of groups of axial layers (shown as green color in the Figure 5), the second part consists of groups of skewed layers (shown as red and blue colors in the Figure 5). The tubes in the axial layers can provide XY information when particles are detected, but for the skewed layers, they are designed for detecting particles in the Z direction. However, approximate XY positions can be calculated from finding a point of closest approach of two skewed tubes, see Figure 6. We use XY information from both axial and skewed layers for training our language models to minimize ambiguities in the testing. For future works, we will evaluate the performance of the tracking models using multiple tracks events, explore technical issues and improve tracking efficiency.

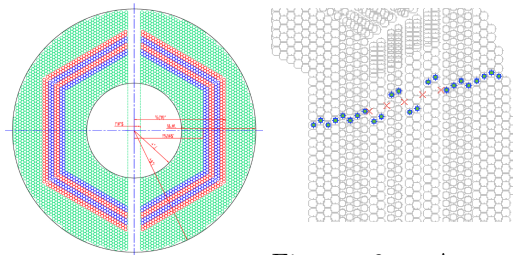


Figure 5: STT shown in the XY-plan. Figure 6: Approximate XY positions shown as red crosses.

The STS Detector for the FAIR Phase-0 Experiment with HADES



G. Perez-Andrade^{1,3}, P. Wintz² and J. Ritman^{2,1,3} for the PANDA@HADES Collaboration
¹Institute for Nuclear Physics of the Research Center Jülich
²GSI Helmholtz Centre for Heavy Ion Research
³Ruhr University Bochum



The HADES Experiment

HADES (Fig. 1) studies the **properties of baryonic resonances** produced in proton or pion induced reactions [1]. The spectrometer is now being upgraded to enable the experiments included in the **FAIR Phase-0 program**, such as **measurements of hyperon radiative decays** [2].

The newly installed forward detectors are two **new Straw Tracking Stations (STS1 - STS2)** and a Forward Resistive Plate Chamber (FRPC). These increase the HADES angular acceptance to low polar angles between $\theta = 0.5$ and 7° (Fig. 2).

Figure 1. HADES spectrometer

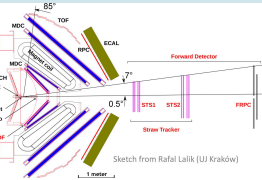
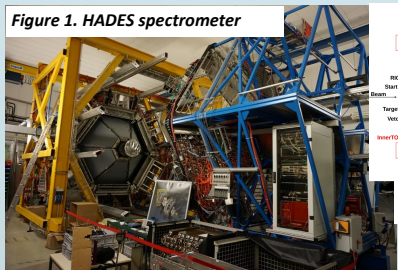


Figure 2. Schematic overview of the HADES spectrometer, including the newly added FD components. The STS(2) shown in magenta.

HADES Forward Detector for FAIR Phase-0

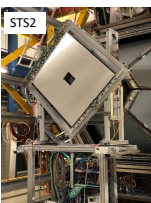


Figure 3. STS1(2) installed at HADES (Coll. with PANDA@FAIR, $\sigma(x) \sim 150 \mu\text{m}$)

Figure 4. Two of four sectors of FRPC installed at HADES $\sigma(\text{TOF}) \sim 100 \text{ ps}$

- No magnetic field \rightarrow No direct momentum measurement
- Path length and time of flight to calculate **velocity** and **particle identification**
- Track reconstruction **combines** information from **STS** and **FRPC**
- Daughter baryon from the hyperon decay is **strongly forward peaked** in the lab frame due to fixed target kinematics: **FD is crucial for hyperon reconstruction**

Forward Detector Tracking

- Low-resolution (LR): **Identify** and **associate** hits within **STS** and **FRPC** to form a track
- High-resolution (HR): **Refit** tracks using **drift time** and **isochrone radius** information from straws

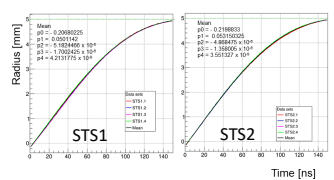


Figure 5. STS(2) Isochrone parameterization

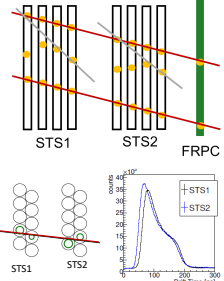


Figure 6. LR (top) and HR (bottom, left) track reconstruction. STS1(2) Drift time spectra (bottom, right)

STS Detector System

Each station with four double layers of **self-supporting gas-filled straws**. Each straw (10 mm diameter) is made of 27 μm thin Al-Mylar film tube with a 20 μm thin W/Re gold-plated wire.

Station	STS1	STS2
No. Straws	704	1024
Straw length	76 cm	125 cm
Orientation (φ)	$0^\circ, 90^\circ, 90^\circ, 0^\circ$	$0^\circ, 90^\circ, 45^\circ, -45^\circ$
Beam opening	$8 \times 8 \text{ cm}^2$	$16 \times 16 \text{ cm}^2$
Distance to target	$\sim 3.50 \text{ m}$	$\sim 5.50 \text{ m}$

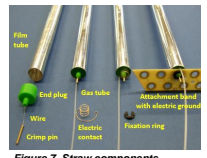


Figure 7. Straw components

A charged particle traversing a straw produces **ionization electrons** which drift towards the wire and generate an electric signal (Fig. 8).

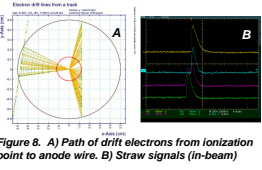
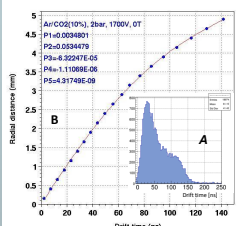


Figure 8. A) Path of drift electrons from ionization point to anode wire. B) Straw signals (in-beam)

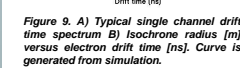


Figure 9. A) Typical single channel drift time spectrum B) Isochrone radius [m] versus electron drift time [ns]. Curve is generated from simulation.

By collecting **all signals** delivered by the STS the particle track is reconstructed: a **straight line** is fitted **tangentially** to the isochrones (Fig. 10).

A **calibration curve** (Fig. 9) is generated to relate the isochrone radius $r(t_i)$ and the electrons drift time t_i : $r(t_i) = \sum P_i \times t^i$

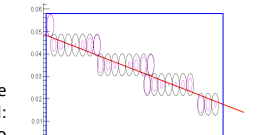


Figure 10. Typical track reconstruction with several layers of straws (testbeam data)

HADES Commissioning Beamtime (February 2021):

- SIS18 delivered **proton beam** with $T = 2 \text{ GeV}$, 4.2 GeV
- STS operation was **stable**
- Very low noise** was observed

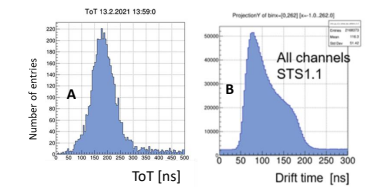
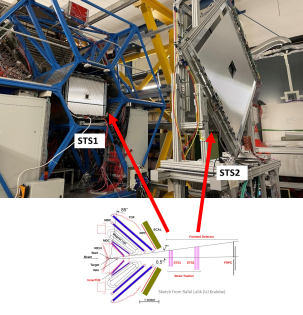


Figure 11. A) ToT online check of STS1. B) Drift time spectrum from first double layer of STS1

Figure 12. STS installed at HADES



Summary and Outlook

- STS station and readout system was **successfully tested** under experiment conditions
- A **rich data base** is **now available** for analysis
- Data offline analysis, development of calibration and tracking algorithms for STS is in progress.
- A four week experiment beamtime with the **upgraded HADES** is scheduled for **February 2022**.

References

[1] Agakichiev, G., et al. The high-acceptance dielectron spectrometer HADES. Eur. Phys. J. A 41, 243(277) (2009).
 [2] Adamczewski-Musch, J., et al. "Production and electromagnetic decay of hyperons: a feasibility study with HADES as a phase-0 experiment at FAIR." The European Physical Journal A 57.4 (2021) 1.
 [3] G. Perez-Andrade et al., Self-calibration Method for the In-Beam Test of the PANDA STT, Annual Report 2019 Institut für Kernphysik/ COSY.



Interdisciplinary Colloquium, November 30th 2021, Ruhr-Universität Bochum

Member of the Helmholtz Association



DETECTING NEUTRINO SIGNALS FROM THE DEEP EARTH WITH BOREXINO

Sindhujha Kumaran^{1,2} for the Borexino Collaboration



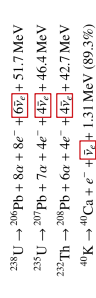
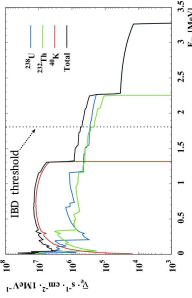
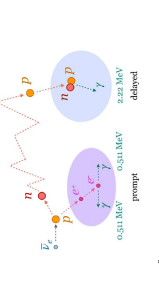
Updated statistics and improved analysis techniques

~18% precision in Borexino's geoneutrino measurement

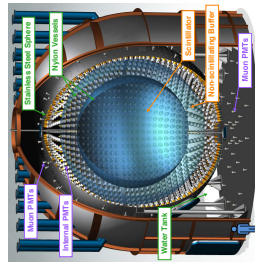
no-mantle signal rejected at 99% C.L.

INTRODUCTION

Inverse Beta Decay (IBD)



Measured in Terrestrial Neutrino Units (TNU), 1 TNU corresponds to 1 antineutrino event detected via IBD over 1 year by a detector with 100% detection efficiency containing 10^{30} free target protons (roughly corresponding to 1 ton of H₂O)

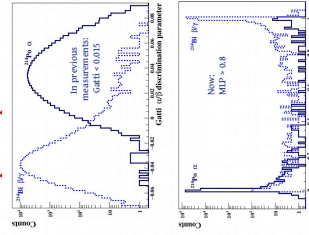


ANALYSIS TECHNIQUES

Selection cuts

- Charge of prompt: 408 p.e. ($2 \times 511 \text{ keV } \gamma$ s)
- Charge of delayed: n-capture on H \rightarrow 700 - 1300 p.e. **enhanced**
- dt: 5 times τ capture time **low**
- dt: 2-12.5 μ s (double cluster events) **low**
- dt: < 1.3 ns between prompt and delayed **enhanced**

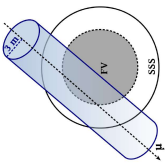
Better pulse shape discrimination



- Cosmogenic veto: **improved**
- 2 s, 1.6 s and 2 ms after internal muons
- 2 ms after external muons
- 3 m cylindrical veto for one category of internal muons
- Dynamic fiducial Volume (DFV) cut **enhanced**
- distance of prompt to inner vessel > 10 cm
- Pulse shape discrimination **improved**
- Multi-Layer Perceptron (MLP) > 0.8 deep learning technique to reject α -like delayed
- Multiplicity cut to reject neutrons 2 ms before or after prompt or 2 ms after delayed

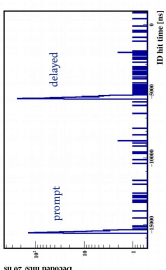
Improved cosmogenic vetoes

In previous measurements \rightarrow 10-11% exposure loss
Now \rightarrow 2.2% exposure loss



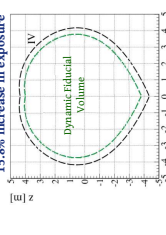
Inclusion of double cluster events

3.8% increase in efficiency

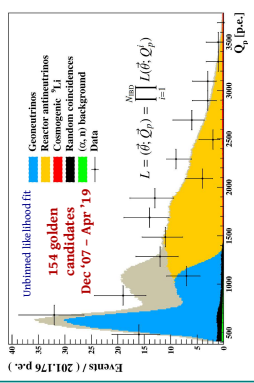


Enlarged fiducial volume

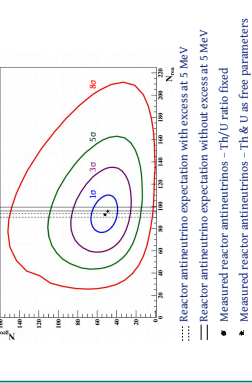
Distance to prompt: 30 cm \rightarrow 10 cm
15.8% increase in exposure



RESULTS



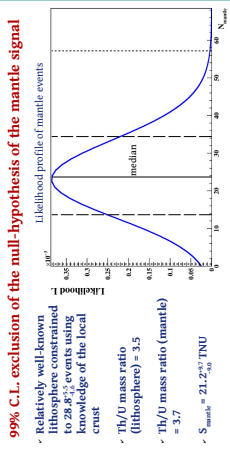
Reactor antineutrino background



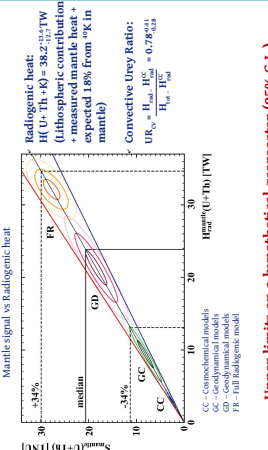
Other backgrounds

Background type	No. of events
^238U background	3.6 ± 1.0
Untagged muons	0.023 ± 0.007
Fast n's (from rock)	-0.013
Fast n's (from WT)	-1.43
Accidental coincidences (α, n) in scintillator	3.846 ± 0.01
(α, n) in buffer	0.81 ± 0.13
(γ, n)	-2.6
Fission in PMTs $^{238}\text{U}, ^{210}\text{Po}$	-0.057
TOTAL	8.28 ± 1.01

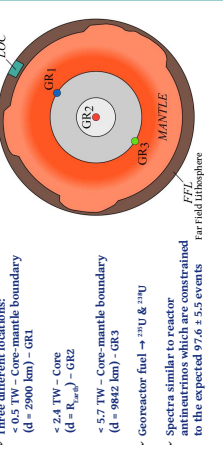
INTERPRETATIONS



2.40 tension with Earth models that predict lowest amount of heat-producing elements inside the mantle



Upper limits on a hypothetical georeactor (95% C.L.)

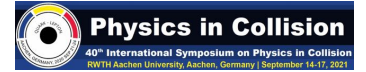




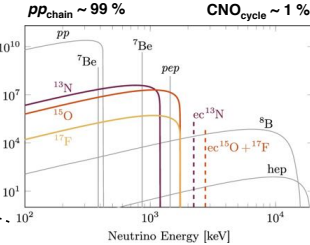
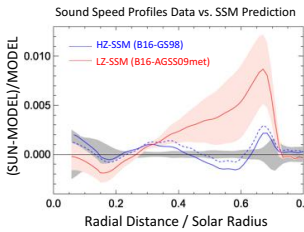
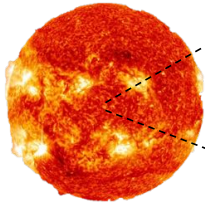
First Experimental Evidence of CNO Cycle Solar Neutrinos by Borexino

Ömer Penek¹ on behalf of the Borexino Collaboration

¹ Institut für Kernphysik, IKP-2, Forschungszentrum Jülich GmbH, 52425 Jülich, Germany



The Sun & the Metallicity Problem

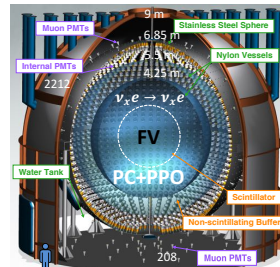


Solar Metallicity = Input to the Standard Solar Model (B16-SSM)
(Z/X) = Surface-Metal-to-Hydrogen Ratio
High-Metallicity HZ-SSM ⇔ (Z/X) = 0.0229
Low-Metallicity LZ-SSM ⇔ (Z/X) = 0.0178

Solar Metallicity Problem:
Helioseismology consistent with older HZ (B16-GS98) but in tension with newer LZ (B16-AGSS09met) description

CNO-ν can unravel metallicity problem!

The Borexino Detector @ LNGS, Italy



- Detection Principle: ν Elastic Scattering off e⁻
- Eff. Light Yield: 500 p.e./MeV in 2000 PMTs
- Energy Resolution: 6% @ 1 MeV
- Position Resolution: 11 cm @ 1 MeV
- Threshold: 50 keV (Hardware)
- Fiducial Vol. (FV): R[m]<2.8, -1.8<z[m]<2.2
- FV mass: 71.3 ton from 280 ton (total)
- Radiopurity Levels: ²³⁸U chain (τ = 6×Gy) < 9.5×10⁻²⁰ g/g (95% C.L.), ²³²Th chain (τ = 20×Gy) < 5.7×10⁻¹⁹ g/g (95% C.L.)
- Ultra Radiopure Detector

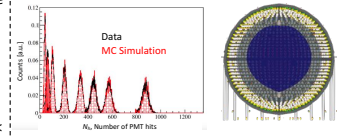
Calibrations and Monte Carlo Simulations

Calibration Campaign ~2009

Isotope	Type	Energy (keV)
⁵⁵ Co	γ	122
¹³⁶ Ce	γ	165
²⁰³ Hg	γ	279
⁸⁵ Sr	γ	514
⁵⁴ Mn	γ	834
⁶⁰ Zn	γ	1115
⁶⁰ Co	γ	1173 - 1332
⁸⁹ K	γ	1460
²²⁸ Rn	α/β	0 ± 3200
¹³⁷ Cs	β	0 ± 156
²⁴¹ Am- ²⁴¹ Pu	n	~0 ± 10000
Ext. ²²⁸ Th	γ	2615

- Placement of sources inside the detector
- Energy + Position Reconstruction
- Detector Response
- Energy Scale

Monte Carlo Simulations

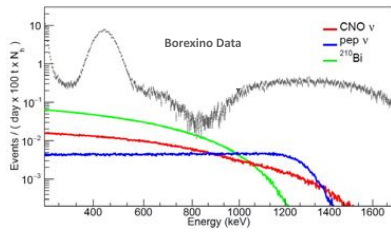


Geant4 simulation of the detector, electronics, and physics processes tuned on calibration data

Observation of CNO Cycle Solar Neutrinos in Borexino

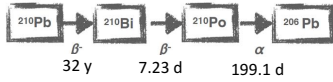
Challenges

Spectral Correlations between CNO, pep, ²¹⁰Bi

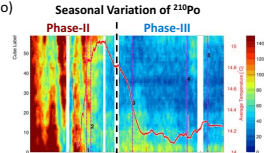


pep-ν rate can be constrained with ~1.4% precision
→ Global Analysis of Solar Neutrino Data + Luminosity constraint (Bergström et al., JHEP, 2016:132, 2016)
Result: (2.74±0.04) counts/day/100t (HZ-SSM ≈ LZ-SSM)

²¹⁰Bi(β⁻) from ²¹⁰Po(α)



Secular Equilibrium: Rate(²¹⁰Bi) = Rate(²¹⁰Po)
Alpha Selection in Borexino: possible on Event-by-Event Basis (Multilayer Perceptron Variable = MLP)
Borexino Situation:
Additional Source of ²¹⁰Po from Inner Vessel + Temperature Gradients
→ Convective Currents
→ Rate(²¹⁰Bi) ≠ Rate(²¹⁰Po)

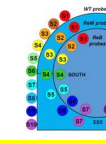


Thermal Stabilization

Towards stopping the Convective Currents



- Thermal Insulation
Double Layer of Mineral Wool installed around ~2015
- Active Temperature Control System
66 Temperature probes (buffer, external tank, different levels)
→ Resolution 0.07 °C

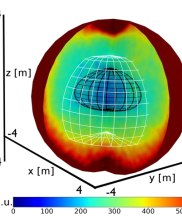


Achieved: excellent temperature stability with the establishment of a stable positive vertical gradient

Low ²¹⁰Po Field + ²¹⁰Bi Constraint

Low Polonium Field (LPoF)

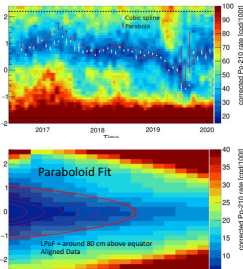
⇔ 20 ton in Bx-Phase-III



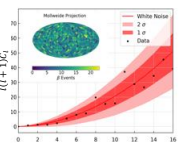
Data alignment → Bias Reduction
→ Bias Reduction (two methods)
1) Fit ellipsoid+spline monthly
2) Extract z-position vs. time (z₀)
3) Create "aligned" dataset ⇔ shift data according to z₀ from previous month
4) Fit aligned dataset

$d^2R(\text{Po}_{\text{min}}) = R(\text{Po}_{\text{min}}) \epsilon_{\text{Bic}} \text{MLP} + R_{\beta}$
 $\times \left(1 + \frac{\beta^2}{a^2} (x - x_0)^2 + \frac{\beta^2}{b^2} (y - y_0)^2 \right)$

ε_{Bic}: ε_{MLP} efficiency
R_β: beta rate after α selection



From 20 ton to 71.3 ton (FV Mass)
→ β rate homogeneity + systematics on ²¹⁰Bi constraint
Angular ±0.59 cpd/100t
Radial ±0.52 cpd/100t



R (Po _{min})	σ _{fit}	σ _{mass}	σ _{bin}	σ _{geom}	σ _{radial}	σ _{ang}	σ _{tot}
11.5	0.88	0.36	0.31	0.59	0.52	0.30	1.30

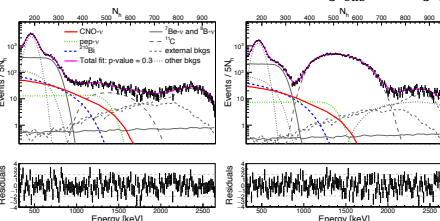
add all systematic uncertainties in quadrature

Bismuth-210 Upper Limit Determination
 $R(\text{Po}_{\text{min}}) = R(\text{Bi}) + R(\text{PoV}) \geq R(\text{Bi})$

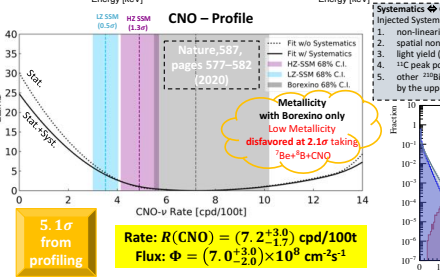
²¹⁰Bi Upper Limit
≤ (11.5 ± 1.3) counts/day/100t

CNO Fit + Significance

Multivariate Fit: $\mathcal{L}_{MV}(\vec{\theta}) = \mathcal{L}_{11C-sub}(\vec{\theta}) \mathcal{L}_{11C-tag}(\vec{\theta}) \mathcal{L}_{radial}(\vec{\theta})$



- pep-ν constraint = symmetric Gaussian
- ²¹⁰Bi constraint = semi-symmetric Gaussian (upper limit)



Systematics → Create distorted Toy Datasets w/w/o signal injected Systematics:

- non-linearity of the energy scale (0.4%)
- spatial non-uniformity z-axis (0.28%)
- light yield (0.22%)
- ¹²C peak position
- other ²¹⁰Bi spectral shapes (18%) (area of ²¹⁰Bi is constrained by the upper limit)

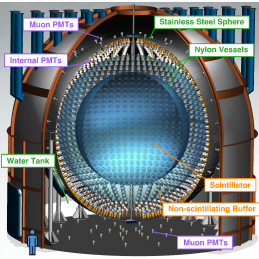
5.0σ from ToyMC (@ 99% C.L.)

Member of the Helmholtz Association

References: 1. M. Agostini et al. (Borexino Collaboration), Experimental evidence of neutrinos produced in the CNO fusion cycle in the Sun, *Nature*, **587**, pages 577–582 (2020), Contact: o.penek@fz-juelich.de
2. M. Agostini et al. (Borexino Collaboration), Sensitivity to neutrinos from the solar CNO cycle in Borexino, *Eur. Phys. J. C* **80**:1091 (2020)



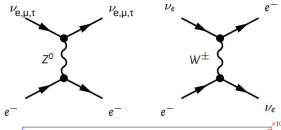
1. INTRODUCTION



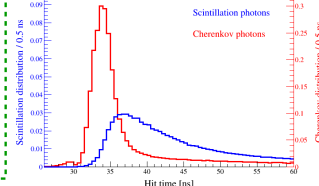
Features of the Detector

- The most radio-pure liquid scintillation detector in the world.
- ~280 tons of liquid scintillator
- Cosmic Muon flux suppression by $\sim 10^6$
- With ~2000 Photomultiplier tubes (PMTs):
- Effective Light Yield: 500 photoelectrons/MeV.
- Energy resolution: 5% @ 1 MeV
- Position resolution: 10cm @ 1 MeV
- Pulse shape discrimination methods available (e^-/α , α/β)
- Calibration with γ radioactive sources.

Neutrinos detected via elastic scattering off electrons



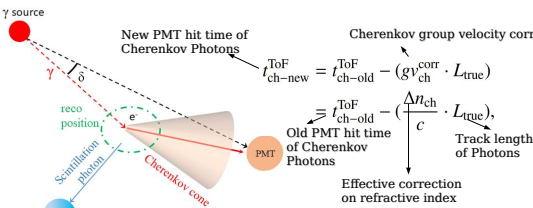
- Dominance of isotropic Scintillation light.
- Forward scattering of electrons.
- Cherenkov photons contribute < 1% and are produced in a cone (in the direction of scattered e^-).
- Most of the Cherenkov photons are emitted earlier than scintillation photons.
- Cherenkov photons are emitted by electrons with energy threshold of 0.16 MeV.



3. CALIBRATION

Effective Correction on Refractive Index for Cherenkov Photons:

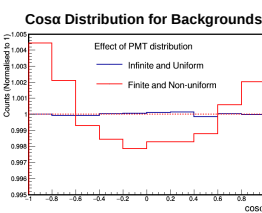
- Essential to calibrate relative time difference between Cherenkov and scintillation photons in MC.
- No dedicated e^- Cherenkov source. Use γ radioactive sources (^{54}Mn , ^{40}K).
- Fitting of $\cos \theta$ distribution of calibration data and MC PDFs with different group velocity corrections (and hence, refractive index) for Cherenkov photons.
- Systematic correction of direction mis-reconstruction is applied using ^{54}Mn on ^{40}K - 36% systematic error (0.039 ns/m).
- Best value of group velocity correction (gv_{ch}^{corr}) is $(0.108 \pm 0.006(stat) \pm 0.039(syst.))$ ns/m.** (2% correction on refractive index @ 400nm).
- Treated as **gaussian pull term** in the final fit.



4. SYSTEMATIC EFFECTS

$\cos \alpha$ distribution distortion for Backgrounds:

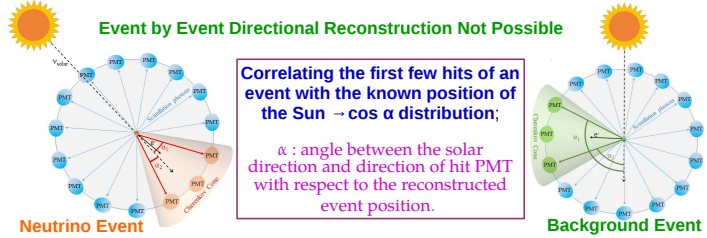
- Due to asymmetric Fiducial volume cut \rightarrow selected spherical FV.
- Due to finite number of PMTs and their non-uniform distribution in the detector \rightarrow Highly dependent.
- MC follows distribution of live channels same as of data.
- Due to non-uniform distribution of events \rightarrow negligible for non-uniformity at the level of Phase-1 data.



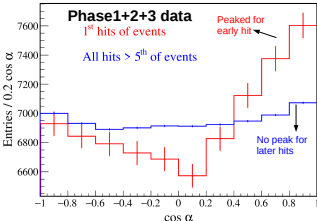
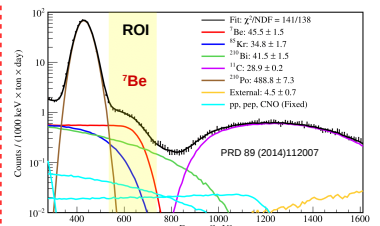
Contributing Systematic Sources:

- Choice of binning of distribution, hits of an event, selection of PMTs with Data-MC agreement \rightarrow 6.9% error.
- Uncertainties on Exposure (dominated by error on position reconstruction) and MLP efficiency are $\pm 4.6\%$ and $\pm 1.0\%$, respectively.
- CNO and pep neutrinos interaction rate using SSM HZ prediction is $+2.9\%$ and -1.5% .

2. CORRELATED AND INTEGRATED DIRECTIONALITY



- #### Data Selection:
- Phase-1 Data (May 2007-May 2010).
 - Spherical Fiducial Volume ($R < 3.3\text{m}$)
 - Energy variable: Geometrically normalised number of hits (N_{ch}^{geo}).
 - Region of Interest (ROI): $225-305 N_{ch}^{geo}$.
 - α/β pulse shape discrimination cut to remove ^{210}Po events with 99% efficiency.
 - Signal: Be7 (89% of solar neutrinos in ROI) + CNO + pep neutrinos
 - Background: ^{210}Bi + ^{85}Kr



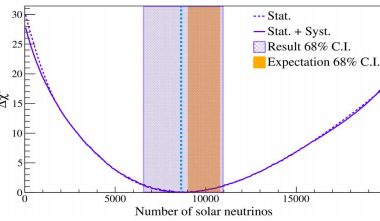
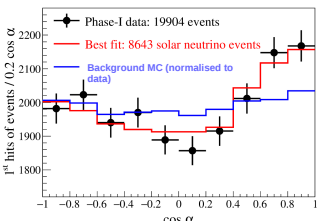
- #### N^{th} hit Analysis Strategy:
- Differences in Time of Flight (ToF) corrected hit time distribution of data and MC at early times.
 - Photons are sorted in time after subtracting ToF for each event.
 - Look at relative ordering of hits in time.
 - Construct $\cos \alpha$ distributions for $1^{\text{st}}+2^{\text{nd}}+\dots+N^{\text{th}}$ hit for all events.
 - N is chosen to maximise amount of Cherenkov photons. Using MC studies, best value of N is 2.

5. RESULTS

$$\chi^2(N_{\text{solar-}\nu}) = \sum_{i=1}^N \sum_{j=1}^l \left(\frac{((\cos \alpha)_{n,i}^D - (\cos \alpha)_{n,i}^M (N_{\text{solar-}\nu}, \Delta t_{\text{dir}}, gv_{ch}^{corr}))^2}{(\sigma_{n,i}^D)^2 + (\sigma_{n,i}^M)^2} + \frac{(gv_{ch}^{corr} - 0.108 \text{ ns m}^{-1})^2}{(0.039 \text{ ns m}^{-1})^2} \right)$$

- $(\cos \alpha)^D$ and $(\cos \alpha)^M$: $\cos \alpha$ distributions of data and MC respectively.
- $N_{\text{solar-}\nu}$: Number of solar neutrino events: free parameter.
- gv_{ch}^{corr} : group velocity correction from γ radioactive sources = (0.108 ± 0.039) ns/m: Gaussian pull term

- Δt_{dir} : bias in direction reconstruction of e^- : nuisance free parameter.
- Cannot be corrected without e^- Cherenkov calibration.
- A bigger mis-reconstruction increases the slope at $\cos \alpha < 0$ and decreases the actual Cherenkov peak around $\cos \alpha = 1$



Measured number of solar neutrinos:
8643 $^{+2171}_{-1989}$ (stat) \pm 597 (syst.)

Extracted ^7Be interaction rate after fixing CNO, pep ν rate to SSM predictions:

39.7 $^{+12.0}_{-11.0}$ (stat.+syst) counts per day/ 100 tons.

> 5 σ detection of sub-MeV solar neutrinos (from ROI) using their directional Cherenkov photons.

Measurement of ^7Be neutrinos rate in agreement with SSM predictions and Borexino Phase-1 spectral fit results.

Can help boost sensitivity for rare processes like CNO solar neutrinos.

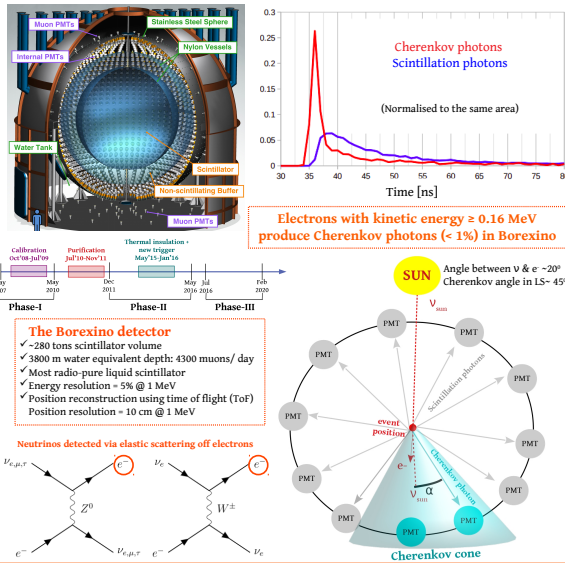
For future detectors: dedicated e^- Cherenkov calibration essential.

Chasing Cherenkov photons in organic liquid scintillator detectors: Directional analysis of sub-MeV ^7Be solar neutrinos in Borexino

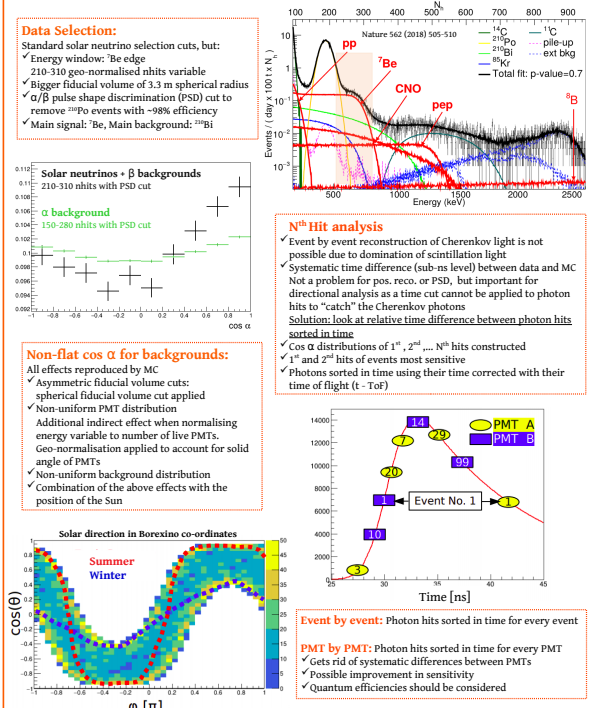
Sindhujha Kumaran^{1,2}, for the Borexino collaboration



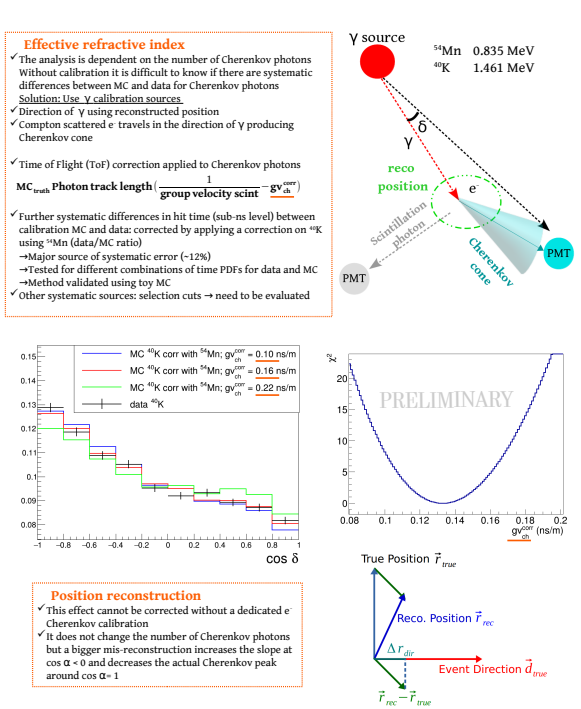
INTRODUCTION



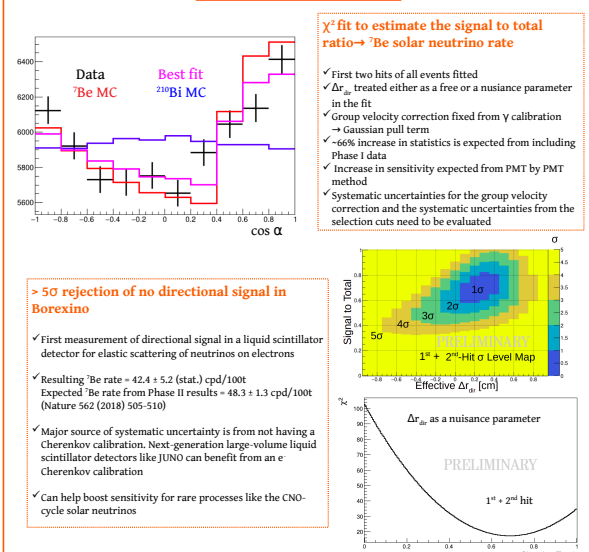
ANALYSIS STRATEGY



SYSTEMATIC EFFECTS



RESULTS



Member of the Helmholtz Association

Contact: s.kumaran@fz-juelich.de

¹IKP-2, Forschungszentrum Jülich, 52428, Jülich, Germany

²Physikalisches Institut III B, RWTH Aachen University, 52062, Aachen, Germany

Directionality measurement in Borexino: Calibration of Cherenkov photons in a liquid scintillator detector using gamma sources

Sindhujha Kumaran^{1,2} and Johann Martyn³ for the Borexino collaboration

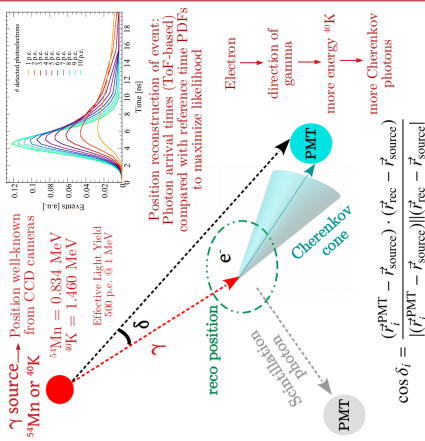


The Borexino detector and Directionality measurement

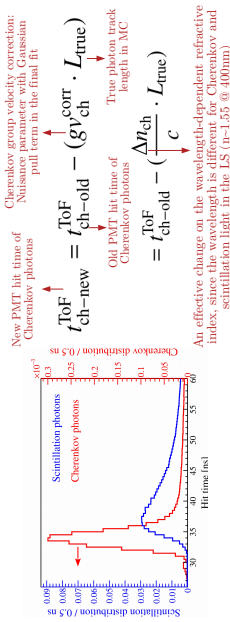
- Cherenkov photons in Borexino**
 - Borexino: liquid scintillator detector: < 1% Cherenkov photons → no event-by-event directional reconstruction
 - Cherenkov photons emitted faster than scintillation
 - Correlated and Integrated Directionality (CID): Correlate the first few hits of an event with the known position of Sun w.r.t. reconstructed event position → Integrate all the hits to produce an angular distribution
- Absolutely essential: Cherenkov calibration**
 - To calibrate the relative time differences between scintillation and Cherenkov photons in Monte-Carlo (MC) simulation → effective correction
 - Applied only on Cherenkov photons in MC using gamma calibration sources → minimal change
 - Does not change the absolute number of Cherenkov photons, but makes them faster or slower with respect to scintillation photons at earlier times

Calibration campaign: 2009

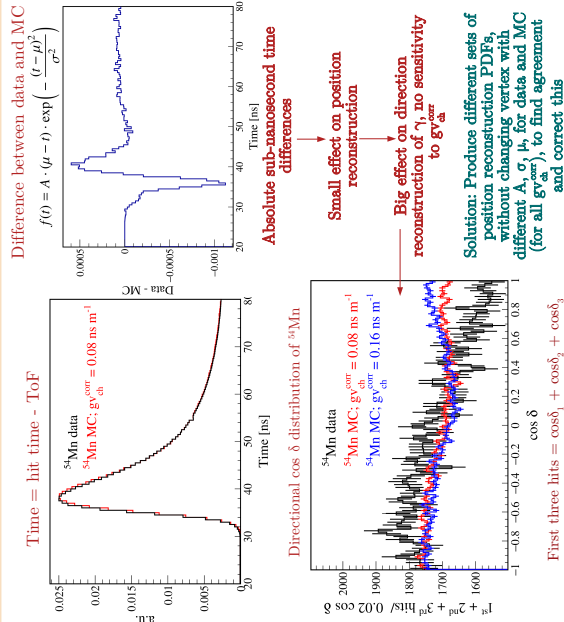
H Beck et al., 2012, JINST 7, P10018



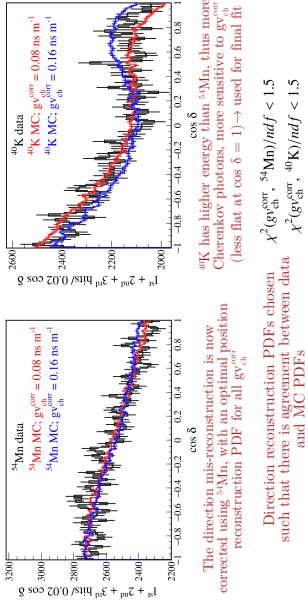
Cherenkov group velocity correction



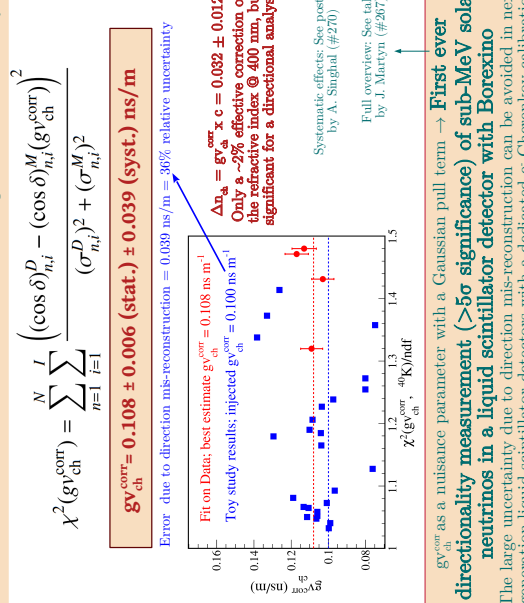
Challenge: Systematic sub-nanosecond time differences between data and MC



Corrected direction mis-reconstruction



Results on the Cherenkov group velocity



¹KP-2, Forschungszentrum Jülich, 52428, Jülich, Germany

²Physikalisches Institut III B, RWTH Aachen University, 52062, Aachen, Germany

Member of the Helmholtz Association

³Institute of Physics and Excellence Cluster PRISMA+, Johannes Gutenberg-Universität Mainz, 55099 Mainz, Germany



Physics potential of the JUNO Experiment

Philipp Kampmann on behalf of the JUNO collaboration
GSI Helmholtzcentre for Heavy Ion Research and Forschungszentrum Jülich, IKP-2

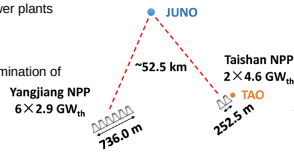


JUNO Experiment (Jiangmen Underground Neutrino Observatory)

- Next-generation multi-purpose detector
- Major goal: Determination of the Neutrino Mass Ordering**
- Under construction near Kaiping, Guangdong province, China
 - Start of data-taking expected in 2023

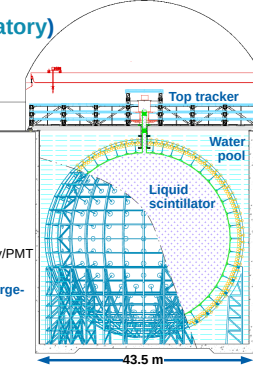
JUNO site

- Adjacent to 2 strong nuclear power plants
 - total 26.6 GW_{th} (~60 ν̄_e/day) (world reactors: ~2 ν̄_e/day)
- Distance optimized for the determination of the Neutrino Mass Ordering
- ~1800 m w.e. overburden



Central Detector

- 20 kt of liquid scintillator (LAB)
 - High photon yield (~10k/MeV)
 - High radiopurity (<10⁻¹⁵ g/g U/Th)
 - Largest LS target in the world!
- Dense PMT instrumentation
 - 17,612 large 20"-PMTs
 - 25,600 small 3"-PMTs
 - 78% coverage
 - ~28.7% photon detection efficiency/PMT
- See poster by B. Jelmini et al.: Characterization of the JUNO Large-PMT readout electronics
- Energy resolution of <3% at 1 MeV



Veto systems

- Water pool - muon veto
 - 2400 20" PMTs - 99.5% μ-detection efficiency
- Top Tracker for muon tracking
 - Plastic scintillator strips
- Other detectors of JUNO
 - TAO (Taishan Antineutrino Observatory)
 - Precision measurement of the reactor-ν̄_e spectrum at 30 m baseline
 - 3t liquid scintillator detector
 - <2% energy resolution at 1 MeV!
 - OSIRIS (Online Scintillator Internal Radioactivity Investigation System)
 - Monitors radiopurity during filling
 - 18t liquid scintillator detector
 - Sensitive to U/Th-contaminations
 - See poster by O. Pilarczyk: The JUNO OSIRIS Detector

Neutrino Oscillation Physics with reactor anti-neutrinos

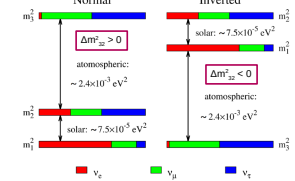
Neutrino oscillations

Electron neutrino survival probability:

$$P(\bar{\nu}_e \rightarrow \bar{\nu}_e) = 1 - \sin^2 2\theta_{12} \cos^4 \theta_{13} \sin^2 \frac{\Delta m_{21}^2 L}{4E} - \sin^2 2\theta_{13} \left[\cos^2 \theta_{12} \sin^2 \frac{\Delta m_{31}^2 L}{4E} + \sin^2 \theta_{12} \frac{\Delta m_{32}^2 L}{4E} \right]$$

with $\Delta m_{ij}^2 \equiv m_i^2 - m_j^2$

Neutrino Mass Ordering: Normal Ordering or Inverted Ordering?



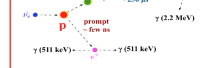
Main Goal: Neutrino Mass Ordering

- Important for the search for
 - Lepton CP-violating phase $P(\alpha-\beta)\neq P(\bar{\alpha}-\bar{\beta})$
 - 0νββ-decay (Majorana nature of the neutrino)
 - Octant of θ_{13}
- Measuring the vacuum oscillation profile
 - Other experiments focus on the measurement via matter effects (e.g. KM3Net, PINGU) (see [3,4])
 - Great potential in combination due to different systematics!
- Estimated sensitivity: $\Delta\chi^2_{\text{Min}} = |\chi^2_{\text{Min}}(\text{NO}) - \chi^2_{\text{Min}}(\text{IO})| \approx 10$ (6 years data-taking, ~100,000 IBDs)

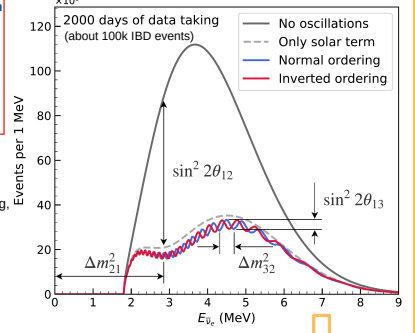
Precision measurement of the Neutrino Oscillation parameters

Relative Precision (%)	$\sin^2 \theta_{12}$	Δm_{21}^2	$\sin^2 \theta_{13}$	$\Delta m_{31}^2 / \Delta m_{32}^2$
Global fit (NuFit 5.0)	4.0	2.8	2.8	1.1
JUNO (6 years)	0.5	0.3	12	0.2

Reactor anti-neutrino detection Inverse beta-decay (IBD)



Expected reactor anti-neutrino spectrum in JUNO

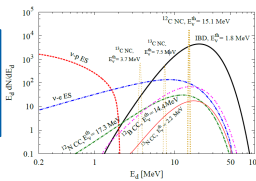


Galactic Supernova Burst-ν's

- High number of detected neutrinos in short time
 - for 10 kpc: ~5000 IBD events expected (among other channels)
 - Nearly background-free
- Aids understanding of Supernova explosion mechanism
- JUNO will be part of SNEWS (SuperNova Early Warning System)

Special low-energy trigger system

Possibility to observe low-energy ν-events (e.g. CEvNS on ¹²C) and pre-burst neutrinos!

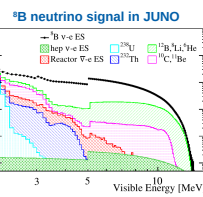


Solar neutrinos

- Detection via elastic ν-e scattering
- High energy solar neutrinos - ⁹B [5]
 - Measuring the MSW-transition region
 - Low detection threshold of 2 MeV!
 - Simultaneous determination of $\sin^2 \theta_{12}$ and Δm_{21}^2 with reactor and solar neutrinos!

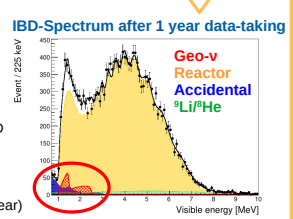
Potential to measure low energy solar neutrinos!

- pp, ⁷Be, CNO, pep neutrinos are under investigation
- Possibility depends largely on liquid scintillator radiopurity



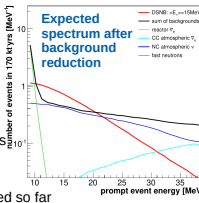
Geo-neutrinos

- Goal: Understand the radiogenic heat distribution in Earth
- Detection via IBD
- Benefit: Large Detector
 - High statistics (400 events/year)
 - Outnumbers the current world sample in short time
- Drawback: Large reactor neutrino background
- Crucial input: Estimated signal from the local crust!
 - Studies on local geology are performed [7,8]



Diffuse Supernova neutrino background

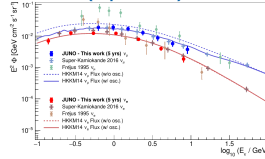
- DSNB
 - isotropic flux of neutrinos from extra-galactic supernovae
 - Detection would give limits on astrophysical parameters (e.g. stellar formation rate)
- Discovery potential!
 - DSNB has not been detected so far
 - JUNO expects a sensitivity of about 3σ in 10 years (model-dependent!)
- JUNO expects a few IBD events/year
- Challenge: Large background of NC atmospheric neutrinos
 - Reducible via differences in scintillation profiles
 - small detection window above reactor spectrum



Atmospheric neutrinos

- Large range of energies (0.1 GeV - 10 TeV) and baselines (~15 km - 13000 km) for measuring neutrino oscillations
- Complementary Neutrino Mass Ordering measurement (via matter effects on neutrino oscillations)
 - Sensitivity boost via combined fit with reactor neutrinos
- Possibility to go to lower energies than Cherenkov detectors! [9]
- Sensitivity for θ_{23} -octant and CP-violating phase (δ_{CP})

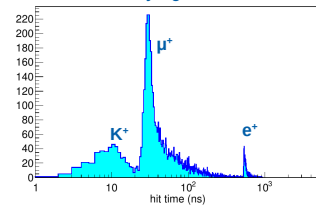
Reconstructed νμ and νe spectra (expectation)



Proton decay

- Detection channel: p → K⁺ν (SUSY-preferred)
- Kaon is under Cherenkov threshold!
 - Scintillation light allows Kaon detection!
- Sensitivity: 8.34×10²³ years (90% C.L. upper limit) after 10 years measurement

Proton decay signature in JUNO



Further potential goals

- Indirect dark matter search [10]
- JUNO as 0νββ detector? [11,12]

References and further reading

- JUNO Physics overview: arXiv:2104.02565
- Yellow Book: J. Phys. G: Nucl. Part. Phys. 43 (2016) 030401
- NMO with JUNO+IceCube: PhysRevD.101.032006
- NMO with JUNO+KM3Net: arXiv:2108.06293
- Solar ⁹B neutrinos: Chin. Phys. C 45 (2021) 1
- Geo-neutrinos: Chin. Phys. C 40.3 (2016) 033003
- Local geology: JGR Solid Earth 124.4 (2019) 4231
- Local geology: Phys. Earth and Planetary Int. 299 (2020) 106409
- Atmospheric ν's, low-energy: arXiv:2103.09908
- Dark matter: JCAP 01 (2016) 039
- 0νββ with JUNO: Chin. Phys. C 44 (2020) 031001
- 0νββ with JUNO: Chin. Phys. C 41 (2017) 053001

Atmospheric neutrinos in JUNO

Mariam Rifai^{1,2}, Giulio Settanta¹ and Livia Ludhova^{1,2}

1.Forschungszentrum Juelich - Institute for Nuclear Physics, IKP-2, Juelich, Germany
2.III.Physalisches Institute B, RWTH Aachen University, Aachen, Germany



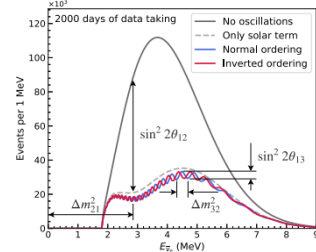
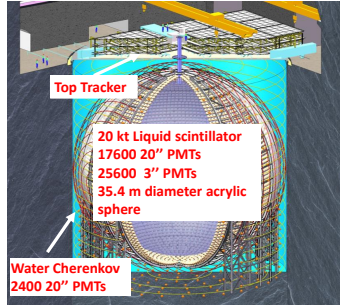
1. Why atmospheric neutrinos in JUNO?

- To enhance JUNO sensitivity to neutrino mass ordering (MO) via combined analysis with reactor anti-neutrinos.
 - To provide the first measurement with a large liquid scintillator detector and thus, down to the sub-GeV energy region.
 - To measure neutrino oscillation parameters θ_{23} and eventually CP violating phase.
 - Accessible from the first year of data taking, with ~15 events/day.
 - A spectrum energy analysis has been established before, without oscillation effects at the detector simulation level [1].
- This poster describes the first step - energy reconstruction with full electronics simulation - towards a sensitivity study.

[1] Measuring low energy atmospheric neutrino spectra with the JUNO detector, arXiv:2103.09908 (2021)

2. JUNO Experiment

- JUNO is a "medium-baseline" (53km) reactor neutrino experiment located in China, construction is ongoing and will be completed in 2022. It aims to determine the MO with more than 3σ in 6 years.



The expected antineutrino energy spectrum with and without oscillation for normal ordering (NO) and inverted ordering (IO)

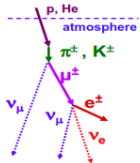
[2] Neutrino physics with JUNO, J.Phys.G 43 030401 (2016)

[3] JUNO Physics and Detector, DOI: 10.1007/JHEP03(2021)004. (2021)

3. Monte Carlo simulation

3.1 Atmospheric-ν flux

ν_e, ν_μ generated by cosmic ray interactions in the atmosphere

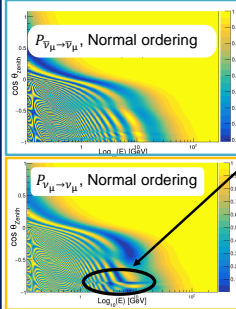


Flux model: HKKM14 for JUNO location

[4] Atmospheric neutrino flux calculation using the NRLMSISE-00 atmospheric model, Phys. Rev. D92, 023004 (2015)

3.2 Atmospheric-ν oscillation

Oscillation calculated with Prob3++ Tool [5], without CP violation (CP=0)



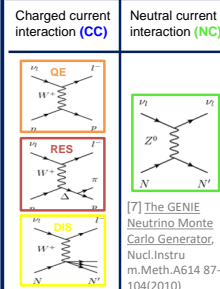
Vacuum oscillations
Neutrinos propagate through the Earth without interaction.
• Identical for ν_α (IO) and $\bar{\nu}_\alpha$ (NO)

Matter effects
Neutrinos interact with the Earth density [6]. Matter effects modify the oscillation pattern.
• identical for ν_α (NO) and $\bar{\nu}_\alpha$ (IO)

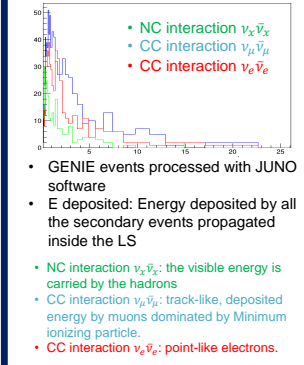
• Matter effects depend on energy and direction of the atmospheric neutrinos
[5] Prob3++: <http://www.phy.duke.edu/~raw22/public>
[6] PREM12, DOI: doi:10.17611/DP/991844

3.3. ν - interaction

- Cross-section calculated with GENIE V3.0.6 for JUNO LS

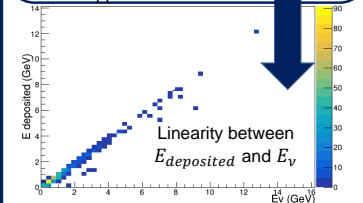


3.4. Detector simulation

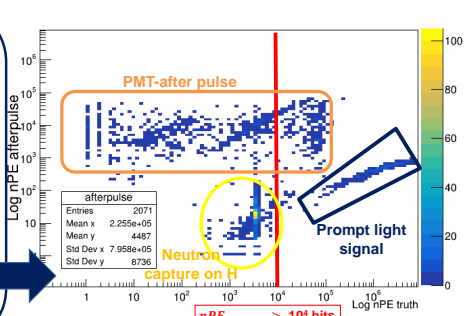


4. Energy reconstruction: Exploit the linearity between $E_{deposited}$ and the total charge seen by JUNO

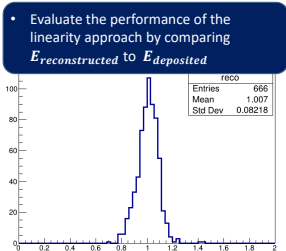
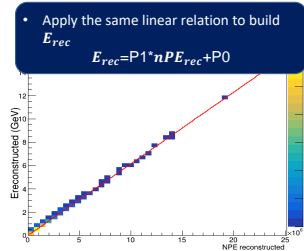
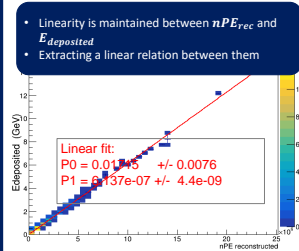
- Selection of fully contained (FC) $\nu_\mu, \bar{\nu}_\mu$ events.
 - Selection cut: $nPE_{MC}^{WaterPool} < 50$ hits.
 - The FC events guarantee the linearity between $E_{deposited}$ and E_ν .



- Removal PMT after pulse related triggers
 - One physical event is split into several readout event
 - Readout event with $nPE_{MC}^{truth} > 10^4$
 - prompt light signal
 - Readout event with $10^2 < nPE_{MC}^{truth} < 10^4$:
 - cloud of events dominated by after pulse and neutron capture on H
 - Readout event with $nPE_{MC}^{truth} < 10^2$
 - Cloud of events dominated by after pulse
- Selection cut: $nPE_{MC}^{truth} > 10^4$ hits
- Correlate all the $nPE_{reconstructed}$ to the same physical event



5. Results



6. Conclusion

The energy evaluated by a linear approach can be reconstructed within 8%

Next Plan:

- Refine the energy reconstruction algorithm.
- Study the direction reconstruction capability of JUNO for track-like ν_μ CC events.
- Evaluate the improvement on the sensitivity of JUNO to MO, thanks to atmospheric neutrinos

OSIRIS – An online scintillator radiopurity monitor for the JUNO experiment

Cornelius Vollbrecht^{1,2} on behalf of the JUNO collaboration

Jiangmen Underground Neutrino Observatory (JUNO)

- 20 kton liquid scintillator (LS) detector in Southern China
- Construction to be completed in 2022
- Main goal: Determination of neutrino mass hierarchy via oscillation patterns of reactor antineutrinos with 53 km baseline
- Vast variety of other topics in (astro-) particle physics
- LS volume monitored by 17612 20"-PMTs and 25600 3"-PMTs [3]
- Excellent energy resolution of 3% at 1 MeV [3]
- Radiopurity requirement for both ^{238}U / ^{232}Th : 10^{-16} g/g for reactor measurements; 10^{-16} g/g for solar measurements [4]

Intelligent PMTs (iPMTs)

- Novel design combining 20"-PMT with readout electronics
- Digitization and waveform reconstruction possible directly on PMT
- Single Cat5e cable for data and power transfer
- Readout chip: VULCAN of ZEA-2, Forschungszentrum Jülich
- Highly configurable electronics, also after assembly
- Self-triggering during normal operation

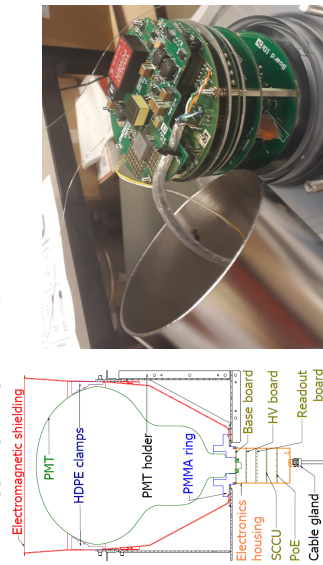


Figure 1: Crosssection of the iPMT assembly.

Data acquisition and RunControl

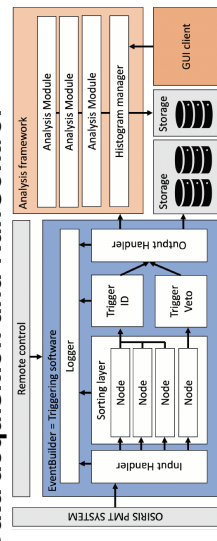


Figure 3: Data acquisition schematic.

Online Scintillator Internal Radioactivity Investigation System (OSIRIS)

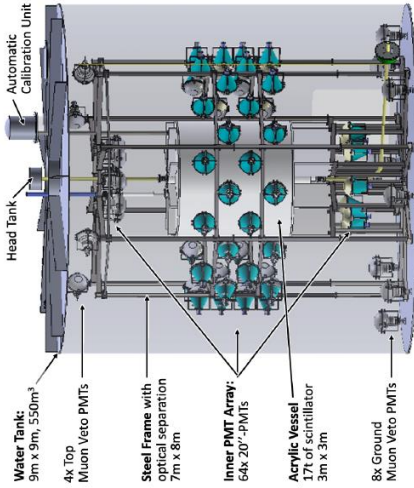


Figure 4: Overview of the OSIRIS detector [4].

- Scintillator radiopurity monitoring during months-long filling of JUNO
- Detection of air leaks and malfunctions in LS purification process
- Optimised for ^{214}Bi , ^{214}Po / ^{212}Bi , ^{212}Po coincidence decays in ^{238}U / ^{232}Th decay chains [4]
- Measurements performed with 76 intelligent PMTs

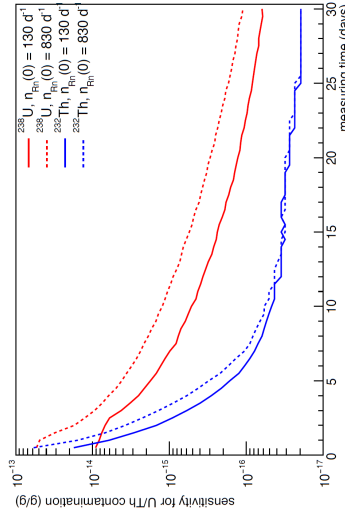


Figure 5: Contamination sensitivities against measuring time for ^{238}U / ^{232}Th in batch mode operation [4]. The time needed to verify the LS radiopurity requirements varies between a few days and a month, depending on the initial radon contamination (dashed / solid lines).

Calibration systems

- ACU (Automatic Control Unit) from Daya Bay experiment
- Calibration of energy / vertex reco / PMT charge / PMT timing
- Insertion of capsules into LS along off-center vertical axis
- One capsule with ^{137}Cs , ^{65}Zn , ^{60}Co sources (0.66 - 2.5 MeV, several kBq)
- Permanently immersed ^{40}K source for continuous monitoring of LS properties (1.46 MeV, < 1 Bq)
- 435 nm-LED-capsule for PMT timing and charge calibration
- ACU capsule positions verified by IR-CCD camera system

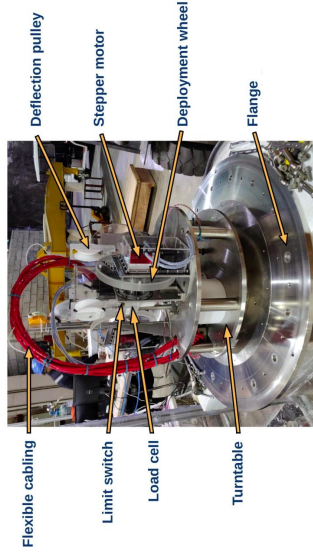


Figure 6: View inside the open ACU [5].

- 420 nm-LASER system for redundancy in PMT timing and charge calibration
- Light distributed by optical fibres and diffusers in OSIRIS
- Longer calibration durations at beginning and after changes; shorter weekly calibrations during normal operation

References

- [1] Forschungszentrum Jülich GmbH, Nuclear Physics Institute IKP-2, Jülich, Germany
- [2] III. Physikalisches Institut B, RWTH Aachen University, Aachen, Germany
- [3] A. Abusleme et al (13 Mar 2021), "JUNO Physics and Detector", to appear in Progress in Particle and Nuclear Physics, arXiv:2104.02565
- [4] A. Abusleme et al. (31 Mar 2021), "The Design and Sensitivity of JUNO's scintillator radiopurity pre-detector OSIRIS", accepted by European Journal C, arXiv:2103.16900
- [5] Graphic of Dr. Christoph Genster, Forschungszentrum Jülich, Germany



JUST: a neutrino fit software for JUNO's solar analysis & sensitivity

Alexandre S. Göttel^{1,2}, Livia Ludhova^{1,2}, Anita Meraviglia^{3,4}, Luca Pelicci^{1,2}, Giulio Settanta¹

¹Forschungszentrum Jülich GmbH, Nuclear Physics Institute IKP-2

²RWTH Aachen University Physics Institute 3.b.

³INFN Milano, ⁴Università degli Studi di Milano



a.gottel@fz-juelich.de

JUNO

- The Jiangmen Underground Neutrino Observatory is currently under construction in Guangdong Province, China
- The detector is expected to be completed in 2022

J. Zhu et al., Event Display in the JUNO Experiment, Journal of physics: conf., 1085 (2018)

- JUNO holds 20 kton of liquid scintillator in a 35.4 m diameter acrylic sphere submerged in a water pool
- It is equipped with a dual calorimetry system: 17612 20" and 25600 3" PMTs
- In total, JUNO can reach an unprecedented 3% resolution at 1 MeV

Motivation

- JUNO's high statistics will allow precise solar neutrino measurements through elastic scattering, assuming backgrounds are kept in check
- Discriminate solar metallicity models
- Test standard solar models through predicted neutrino flux

D. D'Angelo, Recent Borexino results and prospects for the near future, EPJ Web Conf. 126 (2014)

Analysis strategy

Signal and background

- In this analysis, the signal consists of the elastic scattering spectra of solar neutrinos in JUNO's liquid scintillator
- The background mainly consists of intrinsic radioactive decays e.g. ²³²Th or ²¹⁰Po, and of cosmogenic isotopes like ¹¹C
- External background can be completely removed using a fiducial volume cut

Generate Toy Datasets

- Use Monte-Carlo generated PDFs for each fit contribution (signal and background)
- Random generation based on different background assumptions
- Different exposures (e.g. 1 yr*10 kton fiducial volume)
- Distribute events according to TFC cut assumptions
- Spectrum in reconstructed number of photo-electrons
- Each dataset is created on-the-fly to be fitted individually
- Statistical variations are simulated using a Poisson distribution

Sensitivity study

- Event-by-event discrimination impossible
- Fit each dataset to disentangle species
- Generate N >> 1 datasets
- Calculate sensitivity to solar neutrinos from the fit's discriminatory power
- Optimize strategy
- Study possible biases / correlations

Juno nUsol Sensitivity Tool

Goals

- Perform binned extended likelihood fits on multiple data histograms
- C++ 14 compiled through cmake makes installation possible everywhere
- Highly customizable & modular for easy integration of prospective features
- Built for speed & long-term continuous development
- Maximal automation for minimal risk of human error
- Meaningful error handling to avoid erroneous outputs
- Usage of continuous integration tools (gitlab) for seamless parallel development

Design

- Parse config files and cmd args
- Read necessary data from input ROOT files, convert TH1 histograms to c++ vectors, for factor 3-4 speedup
- Thanks to Ö. Penek for the idea! (optional) Use PDFs and rate/exposure assumptions to generate toy data. Alternative is to fit pre-existing data
- Configure and call TMinuit
- Extract relevant physical quantities
- Produce plots and create output files

Configuration

The software is run with command line arguments specifying two (or three) configuration files. Below is an example of a two-histogram fit to existing data

GeneralOptions.cfg

Tell the fitter how to fit

```

1 # Data properties
2 PDFsRootfile data/All PDFs noElec.root
3 DataRootfile data/Data 2histos.root
4 HistOne Pseudodataset_Sub
5 HistTwo Pseudodataset_Tag
6
7 # Fit properties
8 Lifetime 100
9 TargetMass 10.2987
10 emax 3980
11 emin 650
12 ToyData 0
13 Likelihood poisson
        
```

Where to find data, PDFs. Order of histograms important

Exposure

Fit range

How many toy-data fits to do (0: use existing data)

Switch between different likelihoods

SpeciesList.dat

Tell the fit what to fit

```

1 # pdf name species lower upper step fixed list id def
2 Bp7 Bp7 400 0 100 10 0 1 0.6
3 C11 C11 1800 0 165 10 0 1 0.12
4 C11 C11 2 1800 0 165 10 0 2 0.08
        
```

The name of the PDF in the file

Initial guess for the fitter, as well as lower and upper limits, and estimated uncertainty

Total efficiency for the parameter

Parameter names. If duplicates are found the software fits all connected PDFs and Histograms with a single shared variable

Encode the parameter status
0: free
1: fixed
2: constrained

In which histogram should this PDF be considered?

All units in JUNO relevant counts per day per kton

Fit results

- Simultaneously fit TFC-subtracted and TFC-tagged datasets
- Results verified to 10⁻⁴ by independent team/software
- Bias to injected values below a few percent for neutrino species with our current configuration
- Example bias ¹¹C bias plot:

Outlook

Software/analysis in development with future goals in the pipeline:

- Fit N histograms
- More automation in toy-data generation
- Quality-of-life improvements
- Update results with simulation progress
- Facilitate systematic studies

References:

- Fengpeng An et al 2016 J. Phys. G: Nucl. Part. Phys. 43 030401
- J. Zhu et al., Event Display in the JUNO Experiment, Journal of physics: conf., 1085 (2018)
- D. D'Angelo, Recent Borexino results and prospects for the near future, EPJ Web Conf. 126 (2014)

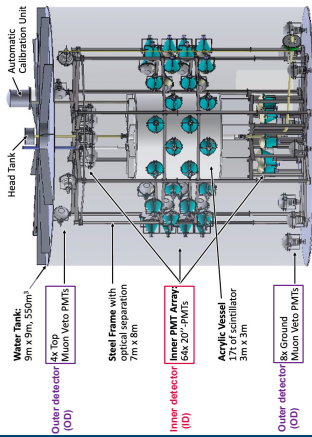
Runxuan Liu^{1,2}
¹Forschungszentrum Jülich - Institute for Nuclear Physics, KP-2, Jülich, Germany
²RWTH Aachen University - Physics Institute III B, Aachen, Germany

I. About JUNO

- JUNO (Jiangmen Underground Neutrino Observatory) is a 20 kt liquid scintillator (LS) detector under construction in Jiangmen, China.
- Construction is planned to be completed in late 2022.
- Main goal: to determine the neutrino mass hierarchy via oscillation pattern of reactor $\bar{\nu}$ at 53 km baseline.
- JUNO has a large potential in a variety of (astro-) particle physics topics.
- Contamination level limits of U and Th in the LS are: Reactor antineutrino-based physics: $\leq 10^{-15}$ g/g Solar neutrino detection: $\leq 10^{-16}$ g/g

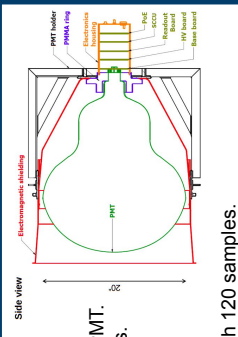
II. What is OSIRIS?

- The **OSIRIS** (Online Scintillation Internal Radioactivity Investigation System), a pre-detector of JUNO, will monitor the radiopurity of LS during the several months of filling the large volume of JUNO.
- OSIRIS can hold 18 ton LS.
- Searching for the fast coincidence decays of ^{214}Bi - ^{214}Po and ^{212}Bi - ^{212}Po in the decay chains of ^{238}U and ^{232}Th , respectively.
- Determination of the ^{14}C and ^{210}Po concentrations in the JUNO LS.
- Fast detection of air leaks at vales and connections via fast coincidences from ^{85}Kr and ^{222}Rn .



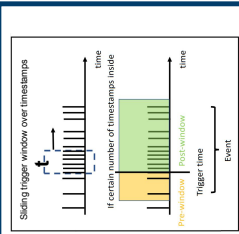
III. IPMTs (intelligent PMTs)

- OSIRIS uses 20"-Hamamatsu PMTs.
- Dark count rate is 15.4 ± 2.6 kHz per PMT.
- Digitization is directly at the PMT bases.
- Each PMT will provide a data-stream composed of the digitized PMT pulses, each contains a timestamp.
- The PMT readout window is 240 ns with 120 samples.



IV. Trigger logics

- OSIRIS will use software coincidence trigger based on timestamps.
- Trigger condition (t, n) is defined as a minimal multiplicity of timestamps n in a time window t .
- Event contains all PMT readout windows from:
 - a **pre-window** before the trigger time
 - to a **post-window** after the trigger time
- ^{14}C (β^- , $Q = 156$ keV) will dominate the low-energy end of the OSIRIS event spectrum and the overall trigger rate.
- Simulation data of ^{14}C and cosmic muons are used for the trigger studies.
- Trigger conditions for inner and outer detectors are tuned as an optimal trade-off between maintaining a low rate of dark noise event and keeping a low energy threshold for detecting ^{14}C events (in **inner detector**) and high muon trigger efficiency (in **outer detector**).



VI. Outer detector trigger conditions

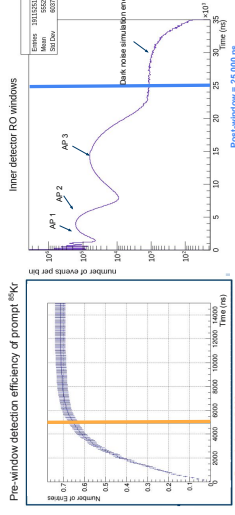
- Outer detector** has 12 IPMTs to veto muons.
- Cosmic muon rate is 0.39 s^{-1} .
- Multiplicity $n > 4$: to have dark-noise event rate < 10 times smaller than the muon rate.
- Trigger conditions **ID (70 ns, 5)** and **OD (150 ns, 5)** give muon trigger efficiencies:

Trigger Window Time (ns)	Multiplicity	Efficiency (%)
100	1.4	1.4
150	1.5	2.2
200	2	2.2
250	2	2.2
300	2	2.2
350	2	2.2
400	2	2.2
450	2	2.2
500	2	2.2
550	2	2.2
600	2	2.2
650	2	2.2
700	2	2.2
750	2	2.2
800	2	2.2
850	2	2.2
900	2	2.2
950	2	2.2
1000	2	2.2
1050	2	2.2
1100	2	2.2
1150	2	2.2
1200	2	2.2
1250	2	2.2
1300	2	2.2
1350	2	2.2
1400	2	2.2
1450	2	2.2
1500	2	2.2
1550	2	2.2
1600	2	2.2
1650	2	2.2
1700	2	2.2
1750	2	2.2
1800	2	2.2
1850	2	2.2
1900	2	2.2
1950	2	2.2
2000	2	2.2
2050	2	2.2
2100	2	2.2
2150	2	2.2
2200	2	2.2
2250	2	2.2
2300	2	2.2
2350	2	2.2
2400	2	2.2
2450	2	2.2
2500	2	2.2
2550	2	2.2
2600	2	2.2
2650	2	2.2
2700	2	2.2
2750	2	2.2
2800	2	2.2
2850	2	2.2
2900	2	2.2
2950	2	2.2
3000	2	2.2
3050	2	2.2
3100	2	2.2
3150	2	2.2
3200	2	2.2
3250	2	2.2
3300	2	2.2
3350	2	2.2
3400	2	2.2
3450	2	2.2
3500	2	2.2
3550	2	2.2
3600	2	2.2
3650	2	2.2
3700	2	2.2
3750	2	2.2
3800	2	2.2
3850	2	2.2
3900	2	2.2
3950	2	2.2
4000	2	2.2
4050	2	2.2
4100	2	2.2
4150	2	2.2
4200	2	2.2
4250	2	2.2
4300	2	2.2
4350	2	2.2
4400	2	2.2
4450	2	2.2
4500	2	2.2
4550	2	2.2
4600	2	2.2
4650	2	2.2
4700	2	2.2
4750	2	2.2
4800	2	2.2
4850	2	2.2
4900	2	2.2
4950	2	2.2
5000	2	2.2
- OD = **94.7%**; **ID|OD = 95.1%**.
- All muons that cross the LS get triggered.
- Most OD muons (69%) also get ID triggered.
- The OD dark noise trigger rate under these trigger conditions is $2.0 \cdot 10^{-3} \text{ s}^{-1}$.
- Enlarging OD trigger window does not give much improvement on muon trigger efficiency.
- Event merger window = 200 ns is used to merge ID and OD trigger events for muons triggering both detectors.

VII. Pre-window and post-window

- Pre-window = 5,000 ns**: determined by coincidence search of minor decay branch of ^{85}Kr :

$$^{85}\text{Kr} \rightarrow ^{85m}\text{Rb} + e^- + \bar{\nu}_e, ^{85m}\text{Rb} \rightarrow ^{85}\text{Rb} + \gamma$$
- Post-window = 25,000 ns**: optimized to catch all PMT afterpulses (APs) at 1.02 μs , 4.0 μs , and 14.1 μs with Gaussian distributions ($\sigma = 70$ ns, 1140 ns, 2440 ns)



V. Inner detector trigger conditions

- Inner detector (ID)** has 64 IPMTs.
- Optimize ID trigger conditions assuming ^{14}C contamination in the LS of 30.0 Bq and **dark noise** in ID of 15,600 kHz.
- Applying (t, n) = (70 ns, 5), we have:
 - ^{14}C event rate of **22.5 s^{-1}**
 - pure dark noise event rate of **2.9 s^{-1}**
 - Trigger efficiency reaches 90% at 36.0 keV.**

